Alternating amphiphilic polymers: from gels and micelles to translocation through lipid membranes

Von der Fakultät für Mathematik, Informatik und Naturwissenschaften der
RWTH Aachen University zur Erlangung des akademischen Grades einer Doktorin der
Naturwissenschaften genehmigte Dissertation

vorgelegt von

Ekaterina Kostyurina, M.Sc.

aus

Pawlowskij Posad, Russland

Berichter: Universitätsprofessor Dr. rer. nat. Stephan Förster
              Universitätsprofessor Dr. rer. nat. Walter Richtering

Tag der mündlichen Prüfung: 21.08.2023
Diese Dissertation ist auf den Internetseiten der Universitätsbibliothek verfügbar.

Die vorliegende Dissertation entstand im Zeitraum von September 2018 bis Oktober 2022 im Arbeitskreis von Prof. Dr. Stephan Förster am Institut für Neutronenstreuung (Jülich Centre for Neutron Science/JCNS-1) des Forschungszentrums Jülich in Kollaboration mit Prof. Dr. Walter Richtering am Institut für Physikalische Chemie der RWTH Aachen unter Supervision durch Dr. Jürgen Allgaier und Dr. Henrich Frielinghaus.

Eidesstattliche Erklärung

Ich, Ekaterina Kostyurina, erkläre hiermit, dass diese Dissertation und die darin dargelegten Inhalte die eigenen sind und selbstständig, als Ergebnis der eigenen originären Forschung, generiert wurden.

Hiermit erkläre ich an Eides statt

1. Diese Arbeit wurde vollständig oder größtenteils in der Phase als Doktorand dieser Fakultät und Universität angefertigt;
2. Sofern irgendein Bestandteil dieser Dissertation zuvor für einen akademischen Abschluss oder eine andere Qualifikation an dieser oder einer anderen Institution verwendet wurde, wurde dies klar angezeigt;
3. Wenn immer andere eigene- oder Veröffentlichungen Dritter herangezogen wurden, wurden diese klar benannt;
4. Wenn aus anderen eigenen- oder Veröffentlichungen Dritter zitiert wurde, wurde stets die Quelle hierfür angegeben. Diese Dissertation ist vollständig meine eigene Arbeit, mit der Ausnahme solcher Zitate;
5. Alle wesentlichen Quellen von Unterstützung wurden benannt;
6. Wenn immer ein Teil dieser Dissertation auf der Zusammenarbeit mit anderen basiert, wurde von mir klar gekennzeichnet, was von anderen und was von mir selbst erarbeitet wurde;
7. Teile dieser Arbeit wurden zuvor veröffentlicht und zwar in:

- Kostyurina, E.; De Mel, J. U.; Vasilyeva, A.; Kruteva, M.; Frielinghaus, H.; Dulle, M.; Barnsley, L.; Förster, S.; Schneider, G. J.; Biehl, R.; Allgaier, J. *Macromolecules* **2022**, *55*, 5, 1552–1565.
- Kostyurina, E.; Allgaier, J.; Kruteva, M.; Frielinghaus, H.; Csiszár, A.; Förster, S.; Biehl, R. *J. Am. Chem. Soc.* **2022**, *144, 33,* 15348–15354.

Datum   Unterschrift

Abstract

Amphiphilic polymers possess both hydrophobic and hydrophilic properties, which make them able to self-assemble in aqueous solutions, be surface active and have simultaneous solubility in polar and non-polar solvents. Therefore, they find various applications, also in industry, in different areas like detergency, agriculture, food, material engineering or pharmaceutics. In experimental studies, statistical copolymer or block copolymer architectures are usually investigated, because of their ease of synthesis or their structural analogy to surfactants. A copolymer structure that links the two architectures is an alternating copolymer, which is easily accessible by polycondensation reactions. Using alternating hydrophilic and hydrophobic building blocks with varying lengths allows a systematic variation between statistical and multi-block architectures. In this project, the alternating amphiphilic polymers (AAP) were broadly and systematically studied with respect to their thermodynamic characteristics and structure formation in water and in an application to translocation through lipid membranes.

Most of the AAPs used in this work were synthesized as polyesters from hydrophobic dicarboxylic acids and hydrophilic polyethylene glycol (PEG) units. These polymers possess a lower critical solution temperature (LCST) behavior in water, where the critical temperature can be varied in the range from 0 to 100°C by adjusting the lengths of hydrophobic and hydrophilic units. Moreover, the same LCST, which can be used as a measure for the overall polymer polarity, can be achieved by different combinations of unit lengths. In this way, the polarity profile along the polymer chain can be changed from a more homogeneous to a more alternating one. Depending on the overall polarity and on the polarity profile the AAPs can be dissolved in water as free chains, form micelles, gels, or ordered crystalline phases. These structures were investigated by small angle x-ray and neutron scattering and a qualitative phase diagram which represents the structures as a function of the hydrophobic and hydrophilic unit lengths was constructed. The micelles formed by the AAP have a pronounced core constructed by the hydrophobic domains embedded in a PEG rich and water poor matrix, whereas the micellar shell consists of a smaller number of PEG end groups or internal PEG units forming loops. Such micelles differ structurally from micelles formed by block copolymers or surfactants, where the core is formed exclusively by the hydrophobic units. The AAP gels are formed by interconnected micellar structures, which make the gel mechanically stable and can arrange in a crystalline order at high concentrations. The ability to tune the AAP polarity allows achieving polymers which are simultaneously soluble in water and non-polar environments as, for example, the interior of lipid membranes. Water

soluble AAPs having such a balanced polarity can passively translocate lipid membranes, which was extensively studied in this thesis. The translocation properties were systematically studied by time-resolved Pulsed Field Gradient (PFG) NMR using large unilamellar vesicles (LUV) as model membranes. The restricted LUV inner volume allows to access independently adsorption and desorption rates, as well as the concentration of the translocating species in the membrane. It was found that the translocation process consists of a relatively fast membrane saturation with the polymers and a slow desorption process. The translocation time varies from minutes to hours depending on polymer and lipid composition, polymer molecular weight, and temperature. On the basis of these measurements a basic thermodynamic model of the translocation process was developed. Neutron reflectometry (NR) measurements proved that the AAP having short hydrophobic/hydrophilic units are located mainly in the hydrophobic interior of the membrane. The concentration in the membrane calculated from the NR study was similar to the one obtained by PFG NMR. Using fluorescent microscopy on giant unilamellar vesicles the ability of transferring a hydrophobic molecule through lipid membranes was proved. The ability of the AAPs to translocate and transfer molecules through lipid membranes can be important for biomedical applications. Therefore, potential cell toxicity properties of the AAPs were tested with living HeLa cells. The AAPs synthesized as polyesters showed no visible effect on the viability of these cells. Therefore, as the next step, in vivo translocation studies were performed using a fluorescently labeled AAP. The translocation through the plasma membrane of four different cell types was proved in a series of fluorescence microscopy measurements. The ability to tune the AAP composition in a wide range by still maintaining the translocation properties makes these polymers very interesting for biomedical applications.

Zusammenfassung

Amphiphile Polymere besitzen sowohl hydrophobe als auch hydrophile Eigenschaften, wodurch sie in wässrigen Lösungen selbstorganisierende Systeme ausbilden können, oberflächenaktiv sind und gleichzeitig in polaren und unpolaren Lösungsmitteln löslich sind. Daher finden sie auch in der Industrie vielfältige Anwendungen in verschiedenen Bereichen wie Waschmitteln, Landwirtschaft, Lebensmittel, Werkstofftechnik oder Pharmazie. In experimentellen Studien werden in der Regel statistische Copolymer- oder Blockcopolymer-Architekturen untersucht, da sie leicht zu synthetisieren sind oder eine strukturelle Analogie zu Tensiden aufweisen. Eine Copolymerstruktur, die die beiden Architekturen verbindet, ist ein alternierendes Copolymer, das durch Polykondensationsreaktionen leicht zugänglich ist. Die Verwendung alternierender hydrophiler und hydrophober Bausteine mit unterschiedlichen Längen ermöglicht eine systematische Variation zwischen statistischen und Multiblock-Architekturen. In diesem Projekt wurden die alternierenden amphiphilen Polymere (AAP) umfassend und systematisch im Hinblick auf ihre thermodynamischen Eigenschaften, Strukturbildung in Wasser und in einer Anwendung zur Translokation durch Lipidmembranen untersucht.

Die meisten der in dieser Arbeit verwendeten AAPs wurden als Polyester aus hydrophoben Dicarbonsäuren und hydrophilen Polyethylenglykoleinheiten (PEG) synthetisiert. Diese Polymere zeichnen sich durch eine untere kritische Lösungstemperatur (LCST) in Wasser aus, wobei die kritische Temperatur durch Anpassung der Längen der hydrophoben und hydrophilen Einheiten im Bereich von 0 bis 100°C variiert werden kann. Darüber hinaus kann die gleiche LCST, die als Maß für die Gesamtpolarität des Polymers verwendet werden kann, durch verschiedene Kombinationen von Längen der hydrophoben und hydrophilen Einheiten erreicht werden. Auf diese Weise kann das Polaritätsprofil entlang der Polymerkette von einem eher homogenen zu einem eher alternierenden Profil verändert werden. Je nach Gesamtpolarität und Polaritätsprofil können die AAPs in Wasser als freie Ketten gelöst werden, Mizellen, Gele oder geordnete kristalline Phasen bilden. Diese Strukturen wurden mittels Röntgenkleinwinkel- und Neutronenstreuung untersucht und ein qualitatives Phasendiagramm erstellt, das die Strukturen in Abhängigkeit von der Länge der hydrophoben und hydrophilen Einheiten darstellt. Die von den AAPs gebildeten Mizellen haben einen ausgeprägten Kern, der aus hydrophoben Domänen besteht, die in eine PEG-reiche und wasserarme Matrix eingebettet sind. Die Mizellenhülle besteht aus einer geringeren Anzahl von PEG-Endgruppen oder internen PEG-Einheiten, die Schleifen bilden. Solche Mizellen unterscheiden sich strukturell von Mizellen, die aus

Blockcopolymeren oder Tensiden gebildet werden und bei denen der Kern ausschließlich aus den hydrophoben Einheiten besteht. Die AAP-Gele bestehen aus miteinander verbundenen mizellaren Strukturen, die das Gel mechanisch stabil machen und sich bei hohen Konzentrationen kristalline anordnen können.

Durch die Möglichkeit, die Polarität der AAPs einzustellen, können Polymere hergestellt werden, die gleichzeitig in Wasser und in unpolaren Umgebungen, wie z. B. dem Inneren von Lipidmembranen, löslich sind. Wasserlösliche AAPs mit einer solchen ausgewogenen Polarität können passiv Lipidmembranen durchdringen, was in dieser Arbeit eingehend untersucht wurde. Die Translokationseigenschaften wurden systematisch mit zeitaufgelöster Pulsed Field Gradient (PFG) NMR unter Verwendung großer unilamellarer Vesikel (LUV) als Modellmembran untersucht. Das begrenzte Innenvolumen der LUV ermöglicht es die Adsorptions- und Desorptionsraten sowie die Konzentration der Polymers in der Membran zu bestimmen. Dabei stellte sich heraus, dass der Translokationsprozess aus einer relativ schnellen Sättigung der Membran mit den Polymeren und einem langsamen Desorptionsprozess besteht. Die Translokationszeit schwankt zwischen Minuten und Stunden, je nach Polymer- und Lipidzusammensetzung, Polymermolekulargewicht und Temperatur. Auf der Grundlage dieser Messungen wurde ein einfaches thermodynamisches Modell des Translokationsprozesses entwickelt. Untersuchungen mittels Neutronenreflektometrie ergaben, dass sich die AAP mit kurzen hydrophoben/hydrophilen Einheiten hauptsächlich im hydrophoben Inneren der Membran befinden, und zwar in einer Konzentration, die der durch PFG-NMR ermittelten entspricht. Mit Hilfe der Fluoreszenzmikroskopie an Giant Unilamellar Vesikels wurde die Möglichkeit des Transports von hydrophoben Molekülen durch die Lipidmembran nachgewiesen. Die Fähigkeit der AAPs, Moleküle durch Lipidmembranen zu transportieren, kann für biomedizinische Anwendungen von Bedeutung sein. Daher wurden die potenziellen zelltoxischen Eigenschaften der AAPs an lebenden HeLa-Zellen getestet. Die als Polyester synthetisierten AAPs zeigten keine sichtbaren Auswirkungen auf die Lebensfähigkeit dieser Zellen. Daher wurden in einem nächsten Schritt in vivo Translokationsstudien mit fluoreszenzmarkierten AAPs durchgeführt. Die Translokation durch die Plasmamembran von vier verschiedenen Zelltypen wurde in einer Reihe von Fluoreszenzmikroskopie-Messungen nachgewiesen. Die Möglichkeit, die AAP-Zusammensetzung in einem weiten Bereich einzustellen und dabei die Translokationseigenschaften beizubehalten, macht diese Polymere für biomedizinische Anwendungen sehr interessant.

Contributions

The results of this thesis are presented in four chapters.

The results of **chapter 4** have been published in *Macromolecules* and the chapter is presented very similar to this publication:

Kostyurina, E.; De Mel, J. U.; Vasilyeva, A.; Kruteva, M.; Frielinghaus, H.; Dulle, M.; Barnsley, L.; Förster, S.; Schneider, G. J.; Biehl, R.; Allgaier, J. Controlled LCST Behavior and Structure Formation of Alternating Amphiphilic Copolymers in Water. *Macromolecules* **2022**, *55*, 5, 1552–1565. https://doi.org/10.1021/acs.macromol.1c02324

I synthesized, fractionated and characterized two polymers under supervision of Jürgen Allgaier. I carried out and analyzed all the experiments related to the formation of micelles and gels with support of Jürgen Allgaier, Ralf Biehl and Martin Dulle. I carried out some DLS experiments and analyzed all the data related to the solubility and thermal behavior of polymers in water with support of other co-authors. I wrote parts of the manuscript related to solubility and thermal behavior of polymers in water and to the formation of micelles and gels with support of Jürgen Allgaier and Ralf Biehl, and prepared the manuscript for publication.

The results of **chapter 5** have been published in *Journal of American Chemical Society* and the chapter is presented very similar to this publication:

Kostyurina, E.; Allgaier, J.; Kruteva, M.; Frielinghaus, H.; Csiszár, A.; Förster, S.; Biehl, R. Passive Macromolecular Translocation Mechanism through Lipid Membranes. *J. Am. Chem. Soc.* **2022**, *144, 33,* 15348–15354. https://doi.org/10.1021/jacs.2c06659

I synthesized, fractionated and characterized some of the polymers under supervision of Jürgen Allgaier. I carried out and analyzed all the experiments with support of Margarita Kruteva, Ralf Biehl and other co-authors, except for the cell viability test which was performed by Agnes Csiszár. I wrote the first version of the manuscript and prepared the manuscript for publication.

The results of **chapter 6** are planned to be submitted to *Biomacromolecules* similar to the chapter. I synthesized, fractionated and characterized some of the polymers under supervision of Jürgen Allgaier. I carried out and analyzed all the experiments with support of Jürgen Allgaier, Ralf Biehl, Margarita Kruteva, Henrich Frielinghaus, Alexandros Koutsioumpas and Stephan Förster. I wrote the manuscript with support of Jürgen Allgaier and Ralf Biehl.

Chapter 7 was prepared in close collaboration with Agnes Csiszár from the Institute of Biological Information processing - Mechanobiology (IBI-2) at Forschungszentrum Jülich using the expertise of the institute on the field of cell biology and imaging. I prepared the polymer samples, participated in the in vivo measurements, performed the measurements with esterase enzyme together with Jürgen Allgaier, and wrote the chapter.

Table of contents

1   Introduction

Amphiphilic polymers own both hydrophobic and hydrophilic properties which lead to their interfacial activity, complex self-assembly behavior in aqueous media, and simultaneous solubility in polar and non-polar solvents. Because of their interfacial activity, amphiphilic polymers are widely used as emulsifiers, detergents, and wetting agents.[1–3] The self-assembly phenomenon of these polymers is used to form stimuli-responsive surfaces and particles which find their applications in the fields from electronics to pharmaceutics.[4–8] Simultaneous solubility in water and hydrophobic environments such as the interior of lipid membranes allows them to interact with cell membranes and enter it with the hydrophobic part. This can modify the biological response of the cells, which can be very desirable for biomedical applications.[9] Therefore, studies of amphiphilic polymer self-assembly and interfacial properties, including interaction with biological membranes, have impact for application of these.

So far, the focus was mainly on diblock- and triblock- along with comb-shaped polymers,[10,11] while alternating amphiphilic polymers (AAPs) have obtained much less attention. However, they provide a unique opportunity to systematically vary the polymer architecture between nearly a homopolymer and multiblock copolymer by varying the length of hydrophobic and hydrophilic units. If the hydrophilic units dominate, water-soluble polymers are obtained, which often show a lower critical solution temperature (LCST) behavior.[12–14] Generally, the LCST depends on the polymer composition and can be used as a measure for AAP hydrophilicity. Unlike for the homopolymers with a fixed LCST behavior, such as PNIPAM or polyethylene glycol, the LCST of the AAP can be tuned and depends on the hydrophobic and hydrophilic unit lengths. This property allows to design a polymer having similar solubility in water and in a non-polar environment as the lipid membrane interior. Such polymers were theoretically predicted to passively translocate lipid membranes.[15,16] Otherwise, translocation of macromolecules across the bilayer mostly occurs via pore formation involving a strong local disruption of the cellular membrane, or via endocytosis, which requires the second translocation step – endosomal escape.[17,18] Passive macromolecular translocation through lipid membranes is highly desirable for biomedical applications but rare. There are only a few synthetic macromolecules reported to do so.[19,20] The ability of the AAPs to cross lipid membranes, together with the possibility of tuning their hydrophilicity opens new opportunities for drug delivery applications.

This work is aimed at a wide and systematic study of AAPs from the perspectives of thermal behavior, structure formation in water and translocation through lipid membranes. Most of the AAPs studied in this project are synthesized as polyesters using hydrophobic dicarboxylic acids ($C_4 - C_{20}$) and hydrophilic polyethylene glycol (PEG) units ($EG_3 - EG_{1000}$). The results of this work are presented in four chapters. Firstly, thermal behavior and structural properties of the AAPs in water are widely investigated as a dependence of the AAP unit lengths, molecular weight, and concentration. Structures of the free polymer chains, micelles and gels are characterized by small angle x-ray and neutron scattering allowing detailed investigations in the mesoscopic length scale. Secondly, the translocation of the AAP through model lipid membranes is proven and studied in detail by kinetic pulsed-field gradient (PFG) NMR. Separate adsorption and desorption steps of the AAP translocation process as well as the AAP concentration in the membrane are accessed by the method and studied as a function of temperature, concentration, AAP and lipid properties to obtain a general understanding of the macromolecular translocation mechanism through lipid membranes. The ability of the AAPs to solubilize and translocate hydrophobic molecules through the lipid membrane is examined by confocal fluorescence microscopy as a first step towards drug delivery applications. In the next chapter the focus is on the influence of the AAP properties on translocation. Especially, the polymer hydrophilicity and hydrophobic/hydrophilic unit length on translocation are examined to understand sensitivity of the translocation phenomenon to the macromolecular properties. Last but not least, the translocation phenomenon as well as cytotoxicity of the AAPs are tested on living cells, providing another step toward applications.

References

[1]   I. Kralova, J. Sjöblom, *Journal of Dispersion Science and Technology* **2009**, *30*, 1363–1383.

[2]   K. Kita-Tokarczyk, M. Junginger, S. Belegrinou, A. Taubert, *Adv. Polym. Sci.* **2011**, *242*, 151–201.

[3]   K. Fukazawa, K. Ishihara, *Colloids Surfaces B Biointerfaces* **2012**, *97*, 70–76.

[4]   T. Hu, P. Jiang, L. Chen, K. Yuan, H. Yang, Y. Chen, *Org. Electron.* **2016**, *37*, 35–41.

[5]   N. Vanparijs, L. Nuhn, B. G. De Geest, *Chem. Soc. Rev.* **2017**, *46*, 1193–1239.

[6]   X. Hu, X. Jing, *Expert Opinion on Drug Delivery* **2009**, *6*, 1079–1090.

[7]   H. Takahashi, G. A. Caputo, K. Kuroda, *Biomater. Sci.* **2021**, *9*, 2758–2767.

[8]   S. R. Mane, A. Sathyan, R. Shunmugam, *ACS Appl. Nano Mater.* **2020**, *3*, 2104–21117.

[9]   E. V. Batrakova, A. V. Kabanov, *J. Control. Release* **2008**, *130*, 98–106.

[10]   S. J. Holder, N. A. J. M. Sommerdijk, *Polym. Chem.* **2011**, *2*, 1018–1028.

[11]   R. Lund, L. Willner, M. Monkenbusch, P. Panine, T. Narayanan, J. Colmenero, D. Richter, *Phys. Rev. Lett.* **2009**, *102*, 188301.

[12]   M. Rackaitis, K. Strawhecker, E. Manias, *Journal of Polymer Science: PartB: Polymer Physics* **2002**, *40*, 2339–2342.

[13]   N. A. Hadjiantoniou, A. I. Triftaridou, D. Kafouris, M. Gradzielski, C. S. Patrickios, *Macromolecules* **2009**, *42*, 5492–5498.

[14]   N. A. Hadjiantoniou, T. Krasia-Christoforou, E. Loizou, L. Porcar, C. S. Patrickios, *Macromolecules* **2010**, *43*, 2713–2720.

[15]   M. Werner, J.-U. Sommer, V. A. Baulin, *Soft Matter* **2012**, *8*, 11714.

[16]   M. Werner, J. U. Sommer, *Biomacromolecules* **2015**, *16*, 125–135.

[17]   N. J. Yang, M. J. Hinner, *Methods Mol. Biol.* **2015**, *1266*, 29–53.

[18]   D. Pei, *Acc. Chem. Res.* **2022**, *55*, 309–318.

[19]   T. Goda, Y. Miyahara, K. Ishihara, *J. Mater. Chem. B* **2020**, *8*, 7633–7641.

[20]   F. Mathot, A. Schanck, F. Van Bambeke, A. Ariën, M. Noppe, M. Brewster, V. Préat, *J. Control. Release* **2007**, *120*, 79–87.

2 Theoretical background

2.1 Basics of polymer physics

The following chapter is a summary of various textbooks and journal articles about polymer physics. For further details, the reader is referred to the original literature. [1–6]

2.1.1 Polymer models

The simplest model to describe polymers mathematically is the freely jointed chain model, which is also called the ideal chain model. The polymer here consists of N links having length b_0 connected with each other such that each link can freely rotate in any direction. A useful parameter characterizing a polymer size is the end-to-end distance $R_{ee} = \sqrt{<\vec{R}_{ee}^2>}$ with end-to-end vector $\vec{R}_{ee} = \vec{R}_N - \vec{R}_0 = \sum_{n=1}^{N} \vec{r}_n$ (Figure 2.1A). For the freely joined chain $R_{ee} = \sqrt{N}b_0$ where $Nb_0 = L_0$ is the polymer contour length. The relation $R_{ee} \sim \sqrt{N}$ holds for more general models as well. Hans Kuhn showed that the real polymer chain can be divided into N segments which are not correlated with each other anymore and can therefore be treated with the freely jointed chain model. The segment length b, in this case, is called Kuhn length, and for $N \gg 1$ $R_{ee} = \sqrt{N}b$. One way of describing a semi-flexible polymer whose length does not allow to use the simple Kuhn approach is using a worm-like chain (WLC) model. It represents the polymer chain as a flexible isotropic rod with a certain persistence length (P) describing the local chain stiffness resulting in correlation between neighboring segments (Figure 2.1B). The limiting cases of the WLC model are the rigid rod which occurs when $P \gg L_0$ and a Kuhn chain when $P \ll L_0$. The general equation for R_{ee} of the WLC is

$$R_{ee} = \left[2PL_0 \left[1 - \frac{P}{L_0} \left(1 - e^{-\frac{L_0}{P}} \right) \right] \right]^{1/2}$$

Which gives $R_{ee} = \sqrt{2PL_0}$ in the limit $P \ll L_0$, and $R_{ee} = L_0$ in the limit $P \gg L_0$. It additionally shows that the Kuhn length is equal to twice the persistence length of the WLC.

The other step towards a general polymer model is considering the volume of chain segments. It leads to a steric repulsion within the chain and, consequently, a more swollen polymer with $R_{ee} \approx bN^{\nu}$, where ν = 3/5. This effect is called the excluded volume effect.
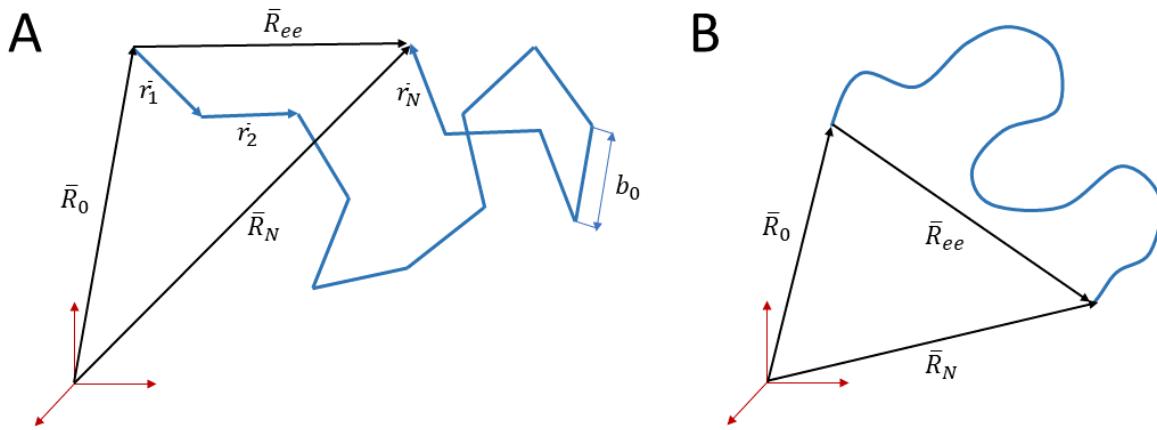
Figure 2.1. Schematic illustration of polymer models. A: Freely joint chain model, B: Worm-like chain model

2.1.2 Measuring polymer chain dimensions

The end-to-end distance is a good measure for polymer size, however, it is difficult to access experimentally. Moreover, it is not defined for polymers with specific architecture, like rings that have no chain ends or branched polymers that have too many chain ends. A more useful quantity is the radius of gyration (R_g) which is defined as a root-mean-square distance between the chain segments and the chain center of mass. Therefore, R_g^2 is the second moment around the center of mass of the chain:

$$R_g^2 = \frac{1}{N+1} \sum_{i=0}^{N} \left(\vec{R}_i - \vec{R}_{cm} \right)^2$$

where $\vec{R}_{cm} = \frac{1}{N+1} \sum_{i=0}^{N} \vec{R}_i$ is the position vector of the polymer center of mass. The Lagrange theorem allows rewriting the equation for R_g^2 as

$$R_g^2 = \frac{1}{2(N+1)^2} \sum_{i,j=0}^{N} \left(\vec{R}_i - \vec{R}_j \right)^2$$

This formula does not assume any specific polymer model and, therefore is valid for any polymer conformation and for any particle in general, if calculating $\vec{R}_i$ as a position of very small particle volume. For the ideal chain $R_g = R_{ee}/\sqrt{6}$. For the real chain, this ratio calculated by Flory and gives a similar result

$$\frac{6R_g^2}{R_{ee}^2} = 0.952$$

R_g can be measured by scattering techniques. Static light scattering allows obtaining R_g which are larger than 1-2% of the incident light wavelength. To get R_g of smaller molecules and the information about their internal structure, small angle X-ray or neutron scattering techniques

can be used. More detailed information on those methods is described in the chapter on experimental methods.

Another useful size measure that can be obtained experimentally is the hydrodynamic radius (R_H). It is calculated from the measured diffusion coefficient by the Stokes-Einstein equation assuming a spherical particle:

$$R_H = \frac{k_B T}{6\pi\eta_s D}$$

So the polymer chain with hydrodynamic radius R$_H$ diffuses the same as the sphere of the radius R$_H$. The hydrodynamic radius can be obtained by experimental methods which can measure the diffusion of molecules, like Dynamic Light Scattering (DLS) or Pulsed Field Gradient (PFG) NMR. For linear polymers, R_{ee}, R_g, and R_H are proportional to each other.

2.1.3 Polymers in solution

When a polymer is dissolved in some solvent, its conformation is additionally influenced by the interaction energy of polymer segments with solvent molecules. In all kinds of solvents, the general relation $R_{ee} \approx bN^\nu$ holds, and the value of the exponent ν which is called the Flory exponent depends on the solvent quality. In good solvents the polymer-solvent interaction is energetically favorable, so the polymer coil will tend to expand due to excluded volume effect, which leads to ν=3/5. In bad solvents the interactions between the polymer segments are getting more preferred than the polymer-solvent interaction, therefore, the polymer chain will tend to more compact conformation. In the limiting case, the polymer will form a globule with ν≈1/3 like for a packed sphere. In the case of a bad solvent, the positive interactions between polymer segments and the excluded volume effect cause an opposite effect on conformation. The solvent where these effects balance out is called θ-solvent. The polymers there can be described by the freely jointed chain model and, therefore, ν=1/2. So, in the range from bad to good solvents ν changes from 1/3 to 3/5. The solvent quality depends not only on the chemical composition of the polymer and solvent molecules but also on temperature. The temperature where the θ-condition is satisfied for a given solvent-polymer system is called θ-temperature. The overview of polymer conformations in solvents with different qualities and the corresponding dependence of R_{ee} is presented in Figure 2.2.

As R_g and R_H are proportional to R_{ee}, they show the same dependence on N. This can be used to determine the solvent quality and, therefore, a polymer conformation, by measuring the molecular weight dependence of R_g or R_H.

$$R_{ee} = bN^{1/3} \qquad R_{ee} = bN^{1/2} \qquad R_{ee} = bN^{3/5}$$

Figure 2.2. Schematic representation of polymer conformation in solvents of different quality, and the corresponding dependence of R_{ee} on polymer length.

2.1.4 Polymer thermodynamics

The simplest approach to describing the thermodynamics of polymer solutions is the Flory-Huggins solution theory. Here the sample volume is divided into *n* equally small sites. One site corresponds by size to one solvent molecule and one polymer occupies *N* sites (Figure 2.3).
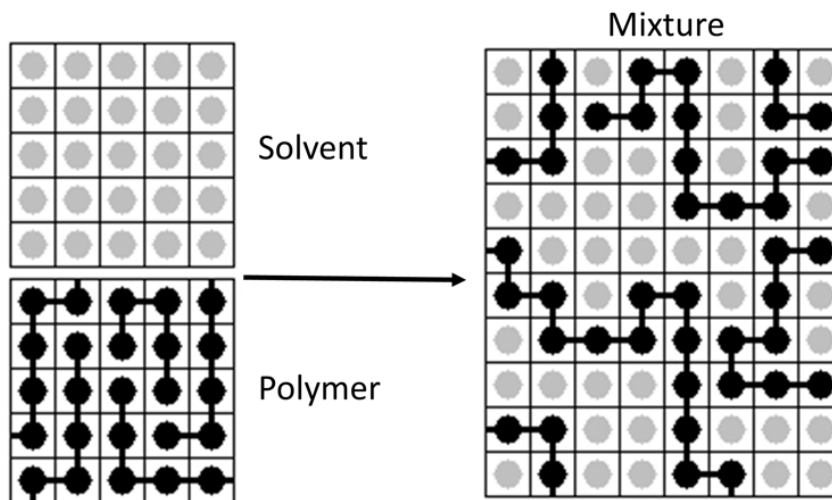
Figure 2.3. Illustration of Flory-Huggins solution theory (adapted from Wikimedia Commons[7])

The entropy of mixing in this model can be written as

$$\Delta S_{mix} = -k_B\big[n_s \ln(c_s) + n_p \ln(c_p)\big]$$

where n_s is the number of solvent molecules, n_p is the number of polymer molecules, and their concentrations are $c_s = \frac{n_s}{n}$, $c_p = \frac{n_p N}{n}$. Using these equations for concentration and *n* = N_a, one could rewrite ΔS_{mix} as

$$\Delta S_{mix} = -R \left[c_s \ln(c_s) + \frac{c_p}{N} \ln(c_p) \right]$$

The enthalpy of mixing can be written as

$$\Delta H_{mix} = RT \chi c_s c_p,$$

with the interaction parameter χ. Therefore, the free energy of mixing $\Delta G_{mix} = \Delta H_{mix} - T\Delta S_{mix}$ can be written as

$$\frac{\Delta G_{mix}}{RT} = \chi c_s c_p + \frac{c_p}{N} \ln(c_p) + c_s \ln(c_s)$$

A polymer is miscible with a solvent if $\Delta G_{mix} < 0$, what happens when $T\Delta S_{mix}$ exceeds ΔH_{mix}. For long polymers the entropy of mixing is quite small so miscibility is governed by the interaction changes upon mixing, i.e. by enthalpy. The interaction parameter χ which determines the enthalpy change is defined as

$$\chi = Z \left[\varepsilon_{PS} - \frac{\varepsilon_{PP} + \varepsilon_{SS}}{2} \right] / k_B T$$

where ε_{PS}, ε_{PP} and ε_{SS} are the interaction energies of polymer-solvent (P-S), polymer-polymer (P-P) and solvent-solvent (S-S) interactions respectively, and Z is the number of contacts per lattice site. The term in the brackets corresponds to the change in interaction energy per one polymer-solvent contact. Very generally, the positive value of χ corresponds to the situation when P-S contacts are less preferred compared to the P-P and S-S contacts. The negative χ, on the opposite, means that the polymer-solvent contacts are preferred, which promotes the solvation of a polymer.

To learn how different the polymer solution is from the ideal solution one could compare its osmotic pressure with the osmotic pressure of the ideal solution. In linear approximation the chemical potential difference of the solvent molecule between the solution with polymer and without $\Delta \mu_s$ is connected with the osmotic pressure Π in the simple relation:

$$\Delta \mu_s = -\Pi v_s$$

where v_s is the solvent molar volume. $\Delta \mu_s$ can be calculated as

$$\Delta \mu_s = \frac{\partial \Delta G_{mix}}{\partial n_s} |_{p,T,n_p} = RT \left[\ln(c_s) - \left(1 - \frac{1}{N} \right) c_p + \chi c_p^2 \right]$$

where p is pressure in solution. For dilute solutions where $c_p \ll 1$,

$$\ln(c_s) = \ln(1 - c_p) \approx -c_p - \frac{c_p^2}{2} + \cdots$$

therefore, the osmotic pressure can be written as

$$-\Pi v_s = RT \left[\frac{c_p}{N} - \left(\frac{1}{2} - \chi \right) c_p^2 + \cdots \right]$$

The first term RTc_p/N is equal to the osmotic pressure of the ideal solution, and the other terms describe deviations from ideal behavior. The polymer solution is closest to the ideal solution when $\chi = 1/2$. It is the thermodynamic definition of Θ-condition. When $\chi > 1/2$ the osmotic pressure exceeds one of the ideal solution. It means that the solvent molecules are suppressed from the polymer resulting in a polymer shrinking, which is typical behavior in a bad solvent. In contrast, $\chi < 1/2$ means reduced osmotic pressure due to polymer swelling in a good solvent. The described behavior is presented in Figure 2.4.

Thermodynamics of block copolymers can be described similarly but considering the mixing of three components (two different polymers plus solvent) to calculate polymer enthalpy.[6]
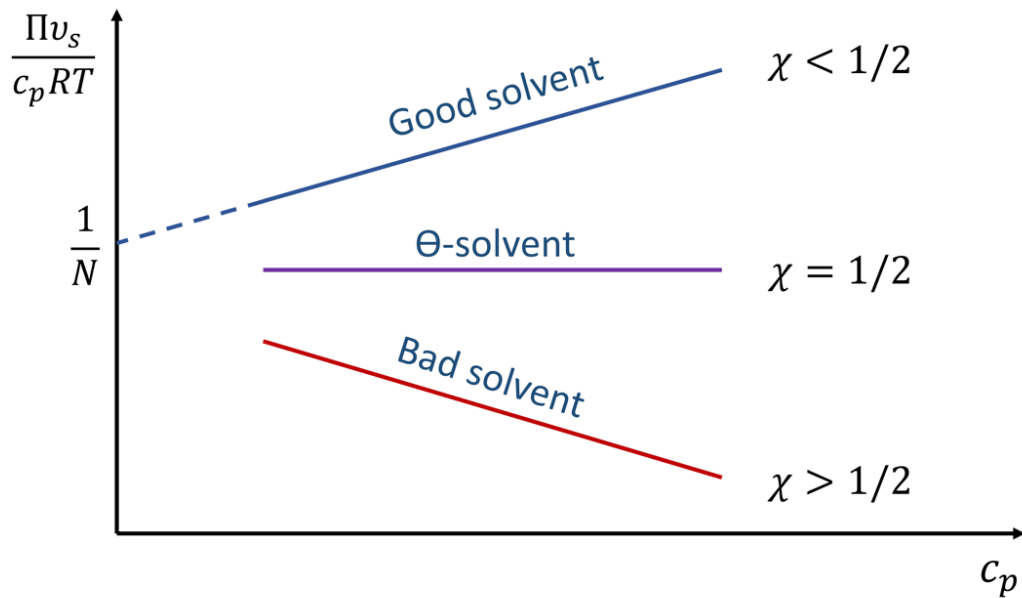

Figure 2.4. Dependence of osmotic pressure on polymer concentration c_p and interaction parameter χ.

2.1.5 Temperature behavior of polymer solutions

The solvent quality, or χ, for a given polymer can be changed by changing temperature or concentration. In Flory-Huggins theory $\chi \sim 1/T$ so the system of polymer and solvent meets the miscibility criteria $\Delta G_{mix} < 0$ only at higher temperatures. In other words, there is a critical temperature above which the polymer is miscible with the solvent. However, the real phase diagrams of polymer solutions cannot be described by Flory-Huggins theory very well, and some polymer solutions show even opposite behavior with temperature, being soluble only at low temperatures. One of the reasons is that volume changes due to mixing are not taken into account by Flory-Huggins theory. These changes lead to changes in polymer mobility and

flexibility and therefore influence polymer entropy. The phase behavior can be better described if the interaction parameter χ is assumed to comprise both enthalpic (χ_H) and entropic (χ_S) contributions:

$$\chi = \chi_S + \chi_H = A + \frac{B}{k_B T}$$

Where χ_H and χ_S are defined as

$$\chi_H = -T\frac{d\chi}{dT} = \frac{B}{k_B T}, \quad \chi_S = \frac{d(\chi T)}{dT} = A = -\frac{\Delta S}{k_B}$$

With this description of χ two scenarios can happen. If χ decreases with increasing temperature ($B > 0$), the miscibility criteria is met at high temperatures, like in Flory-Huggins theory. The critical temperature is called upper critical solution temperature (UCST). In this case mixing leads to an increase in volume, which increases the local movement of the chains and, therefore, entropy. So χ_S is negative and decreases with temperature. In contrast, if χ increases with increasing temperature ($B < 0$), the miscibility criteria is met at low temperatures. The critical temperature below which the polymer is soluble is called lower critical solution temperature (LCST). The volume of such systems decreases after mixing leading to a decrease of entropy and positive χ_S increasing with temperature. The effect gets more pronounced at higher temperatures. Polymer-solvent mixtures have an LCST behavior when short-range attractive interactions between polymer and solvent weaken with temperature, for example in hydrogen bonds. This is the case for polyethylene glycol and its copolymers in water. Some specific polymer solutions might have both LCST and UCST at the same time, for example, polystyrene in cyclohexane. Both LCST and UCST of polymer solutions also depend on the molecular weight because of the polymer length dependence of polymer entropy. The typical phase diagram for LCST and UCST behavior is shown in Figure 2.5. In the metastable region, it is possible to obtain a single-phase mixture by a slow influence on the system.
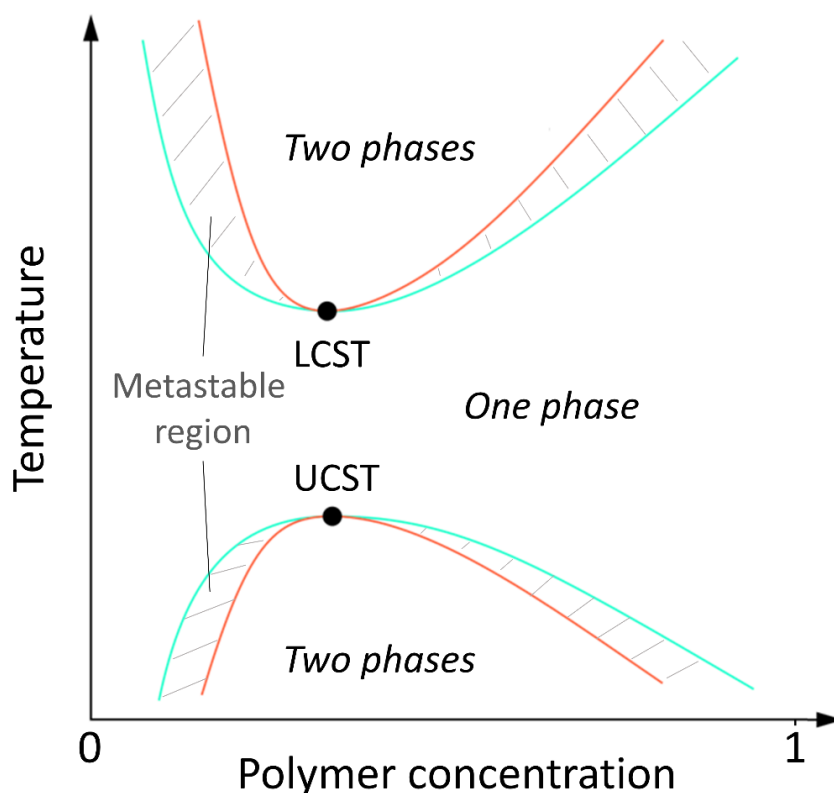
Figure 2.5. Phase diagram of polymer-solvent mixtures having LCST and UCST phase behaviors.

2.2   Amphiphilic polymers and their structure formation in water

Amphiphilic polymers contain both hydrophobic and hydrophilic segments which can exist as di-blocks or triblocks. Alternatively, the segments can be arranged in a random or alternating order. Due to the tendency of hydrophobic blocks to phase separate in water, amphiphilic polymers might form various structures. In general, the structural behavior is determined by the interplay between entropies and enthalpies of each block.

2.2.1   Micelle formation

Di-block copolymers

Di-Block copolymers are the most common block copolymers. In water, they usually have a critical micelle concentration (CMC). Below CMC they solubilize as single chains and above the CMC they form micellar structures where the hydrophobic blocks microscopically phase separate. The driving force for micellization is the reduction of entropy of water molecules due to restrictions of their orientational freedom at the hydrophobic surface. It leads to the minimization of the contact area between water and hydrophobic blocks and, consequently to the aggregation of the latter. Below the CMC the mixing entropy of single polymers with water dominates the total entropy loss of water molecules and, therefore, polymers solubilize as free

chains. Above CMC the system still contains some constant number of free polymers which are in equilibrium with micelles (Figure 2.6). However, the CMC is often rather low and the contribution from free polymers can be neglected. The Gibbs free energy of micellization can be approximated as

$$\Delta G_{micellization} \approx RT\ln(CMC)$$

The value of CMC and the exact structure being formed are affected by many parameters such as all types of interaction in the system and entropic penalties due to aggregation. All of that can be also influenced by temperature or salt concentration. Some theoretical approaches to predict micellar structure are based on Flory-Huggins solution theory.[8–10] However, more advanced studies also exist, for example for star-like micelles.[11,12]
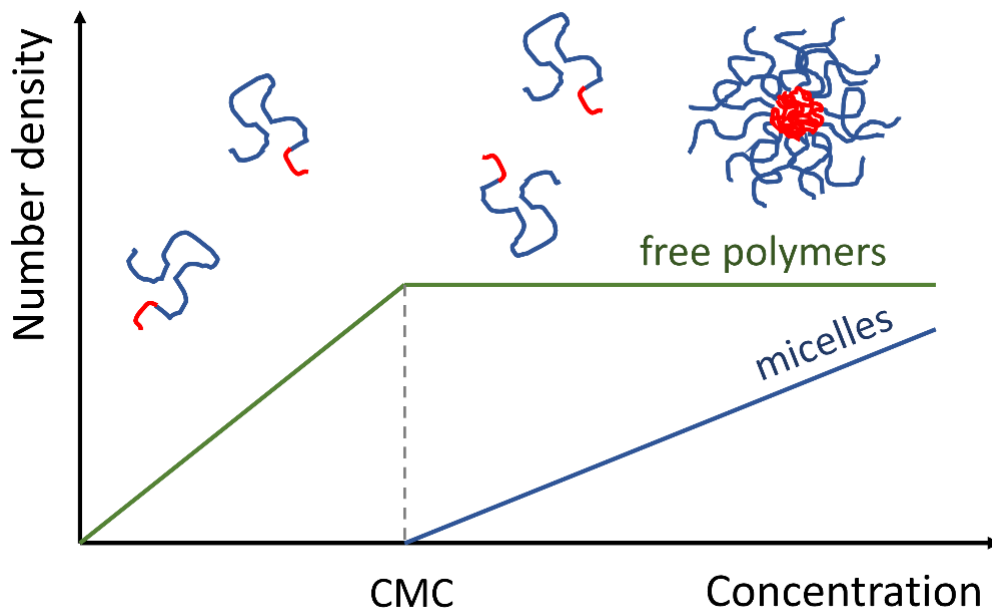

Figure 2.6. Dependence of number density of free polymers and micelles on overall polymer concentration.

Triblock copolymers

Triblock copolymers can have two basic configurations having differences in thermodynamics. Copolymers consisting of two hydrophilic blocks and one hydrophobic behave very similarly to di-block copolymers in terms of thermodynamics and structures being formed. The triblock copolymers having one hydrophilic block and two hydrophobic behave more complex. To form a micelle where all the hydrophobic blocks microscopically phase separate in the micelle core, the polymers must form loops (Figure 2.7). The ability to form loops is related to the change in free energy which can be estimated[13] as

$$\Delta G \approx aRTln(n) - bRTm$$

where n is the length of the hydrophilic block, m is the length of the hydrophobic chain ends, and parameters *a* and *b* are constants for a given system. The first term is attributed to the entropy loss of the hydrophilic chains due to the loop formation, and the second term describes the gain in free energy when the hydrophobic tails associate. When the hydrophilic block is long enough the entropy term dominates which leads to free polymer chains. At longer hydrophobic blocks and/or shorter hydrophilic, when the second term dominates, strong hydrophobic interactions lead to the formation of stable flower-like micelles. It was reported[14] that in the intermediate state when the entropy term dominates but the formation of loops still has a reasonable probability, the micelle formation takes place but not all of the hydrophobic chain ends are located in the micellar core. In such systems the hydrophobic chain ends can also act as a bridge between two micelles, leading to the formation of gels.
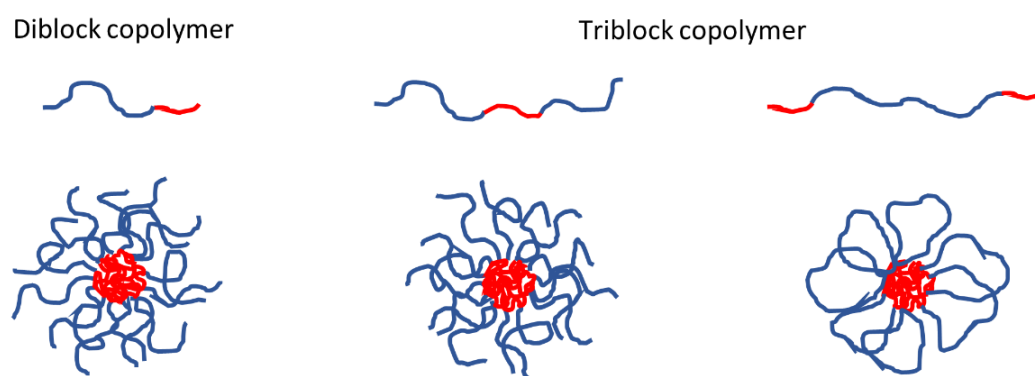

Figure 2.7. Micelles formed by di- and tri- block copolymers

Multi-block copolymers

With the increasing number of blocks, flower-like micelles can be formed similarly to tri-block copolymers. For various alternating amphiphilic polymers such structures were reported.[15–23] However, a large number of blocks allows a larger variety of structures to be formed. Many of the possible structures so far were predicted in simulation studies but have not been proved experimentally. Depending on the segment lengths, their ratio, the solvent quality and other criteria such polymers can solubilize as free chains, form globular structures, multi-core micelles, flower and multi-flower micelles, worm-like micelles, micellar chains and many others.[24–28]
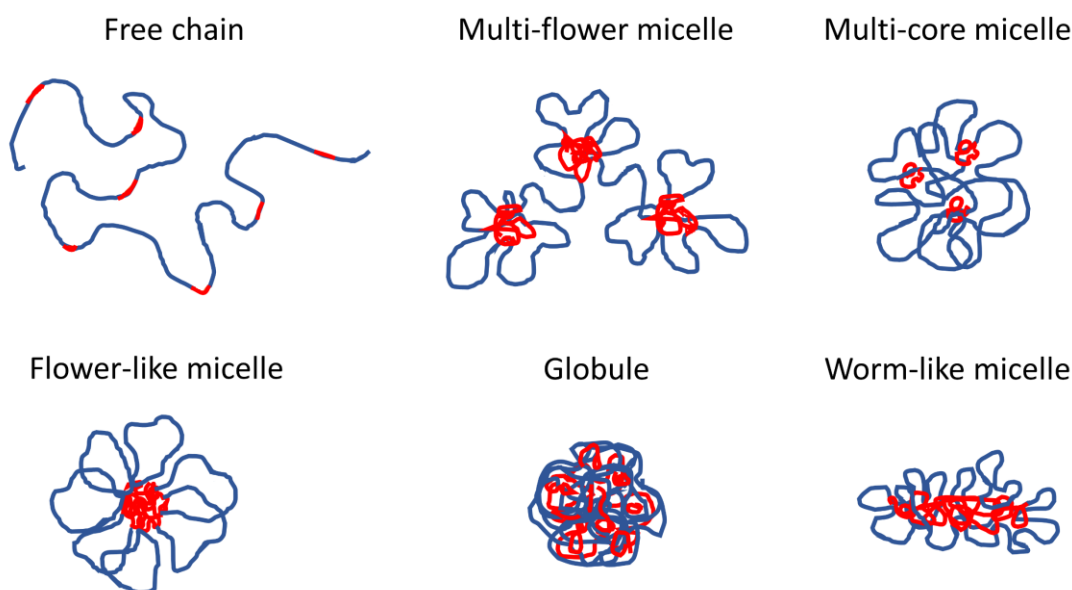
Free chain   Multi-flower micelle   Multi-core micelle

Flower-like micelle   Globule   Worm-like micelle

Figure 2.8. Some of the possible structures created by amphiphilic multiblock copolymers in water.

2.2.2 Gel formation

Increasing concentration of amphiphilic polymers often leads to gel formation. In IUPAC terminology gel is defined as a non-fluid colloidal or polymer network that is expanded throughout its whole volume by a fluid.[30] Gels which are swollen with water are called hydrogels. The network can be formed by crosslinking polymers, by physical aggregation of polymer chains due to, for example, hydrogen bonds or crystallization, by lamellar structures made of surfactants, or by many other systems which can form "junctions". Gels can be also formed by micelles if they can physically or chemically connect. For example, it is possible in the case of triblock copolymer micelles having two hydrophobic chain ends, because of bridging chains between two micelles (Figure 2.9).
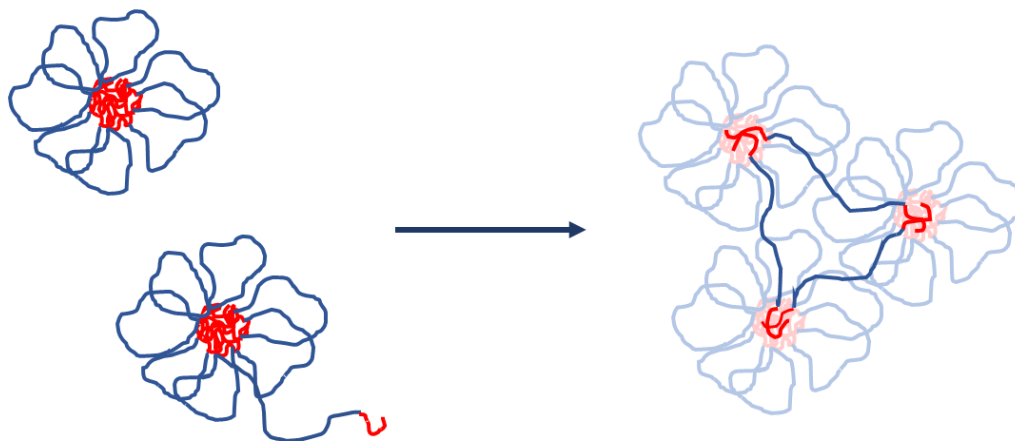
Figure 2.9. Principal of gel formation in triblock copolymer micelles

2.3   Lipid membranes

2.3.1   Biological membranes

The cell is the basic structural and functional unit of life. There is a huge variety of cells in nature, having different compositions and consequently functions.[31,32] In common, they all have a plasma membrane that separates the cell content from the outer environment. The inner part of the cell is called cytoplasm. For more simple prokaryotic cells that are all bacteria and archaea, the cytoplasm consists of DNA, ribosomes and various inclusions. The cytoplasm of eukaryotic cells is highly organized and contains various organelles (Figure 2.10). Some organelles have their own membrane which separates them from the cytoplasm. Such organelles are called membrane-bound organelles and include the nucleus, mitochondria, vacuoles, and vesicles. All plasma membranes and organelle membranes are formed by lipid molecules which consist of hydrophilic head groups and hydrophobic tails. The structure of the most common lipids is shown in Figure 2.11.[33] The lipid tails can have different lengths and saturation degrees. The fraction of lipids in biological membranes rarely exceeds 80%, and the rest is a large amount of various proteins which are involved in many critical cell functions such as transport, signaling, catalyzation of chemical reactions and so on.[34] Lipid composition and the number of proteins in the membrane vary in a wide range depending on the cell type or the organelle. The human body consists of about 230 cell types.
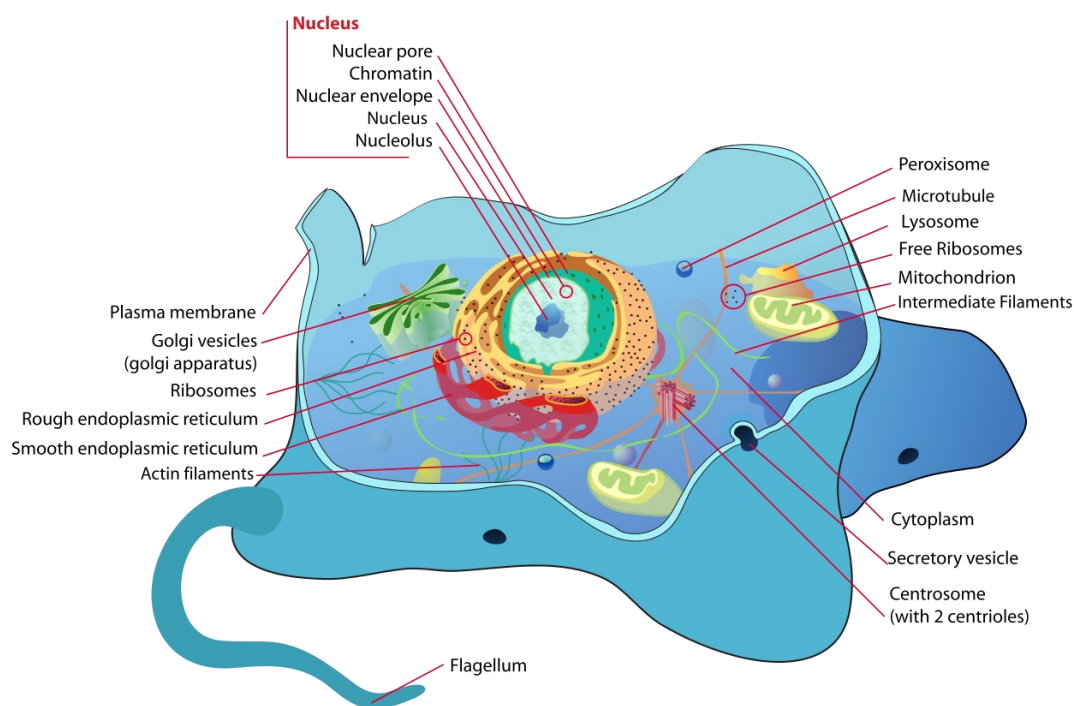

Figure 2.10. Typical diagram of an animal cell.[35]
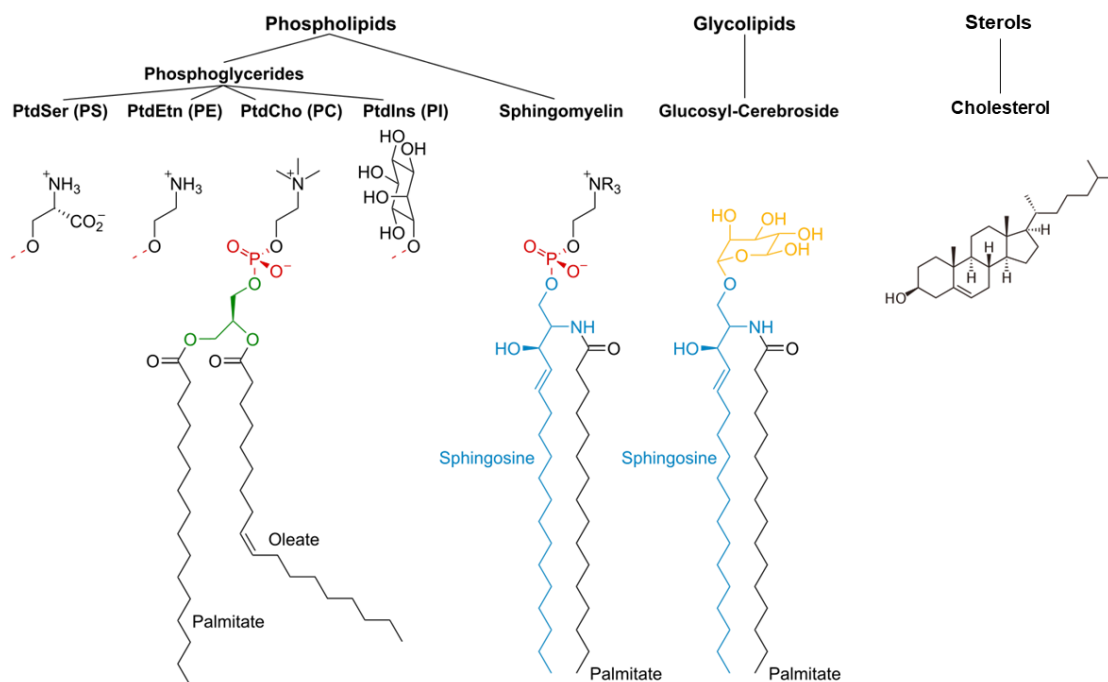
Figure 2.11. Structure of the most common cell lipids (adapted from Wikimedia Commons[36])

2.3.2   Model membranes

Because of the complexity of biological membranes and many limitations in working with real cells, it is common to use model membranes in experimental studies. Such membranes can be composed of only one lipid type, or of the lipid mixture extracted from real cells, and normally the lipid composition is well defined. In terms of shape, they are usually made as lipid vesicles of various sizes, supported lipid bilayers (SLB), bicelles or nanodiscs (Figure 2.12). Systematic variation of membrane composition allows to understand membrane mechanics and thermodynamics as well as the interaction mechanisms with other molecules like proteins or drugs.

Figure 2.12. Examples of model lipid membranes

2.3.3 Lipid phase behavior

Lipid phase behavior in biological membranes is very complex. Model membranes consisting of only one lipid type generally have a gel phase L_β which transits to the li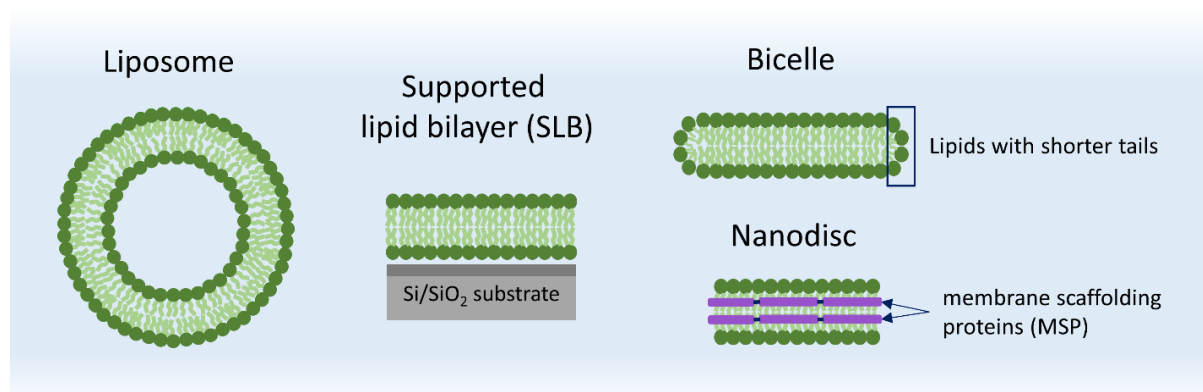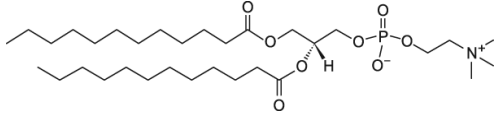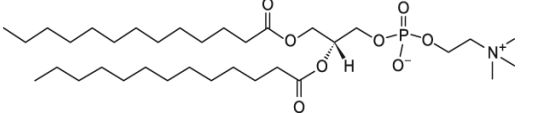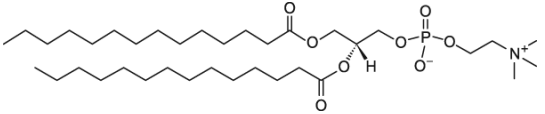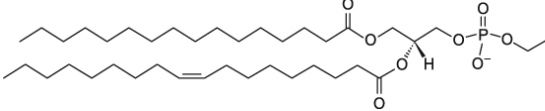quid phase L_α at a melting temperature T_m.[37] Although, one must notice that there are a few different gel phases that are determined by temperature and lipid composition. The common point of the gel phases is that lipid tails there are stretched and therefore well ordered. In contrast, lipid tails in the fluid phase are more disordered, which leads to their smaller viscosity as well as a smaller thickness.[38] The value of T_m depends mostly on the length of the hydrocarbon lipid tails and on their saturation state.[39] The structures and melting temperatures of lipids used in this work are presented in Table 2.1. With increasing the tail length T_m also increases, whereas with increasing number of unsaturated groups in the tails T_m decreases depending on the position of double bonds. This is a result of the angle change created in the chain by the double bond makes packing of the tails more difficult.

Table 2.1. Lipid structures and melting temperatures for the lipids used in this work

Lipid	Chemical structure	T_c, °C
12:0 PC (DLPC)		-2
13:0 PC		14
14:0 PC (DMPC)		24
16:0-18:1 PC (POPC)		-2

A Typical phase diagram for lipids in water is shown in Figure 2.13 for the example of DMPC. In lipid mixtures the phase diagram is more complicated. In some cases different lipids can phase separate into domains in the membrane. In general, the T_m in lipid mixtures is in between the T_m values of each lipid type, and an increasing number of lipid types leads to a broader transition. Cholesterol which is present a lot in cell membranes strongly changes the phase behavior and generally increases the melting temperature.[40]
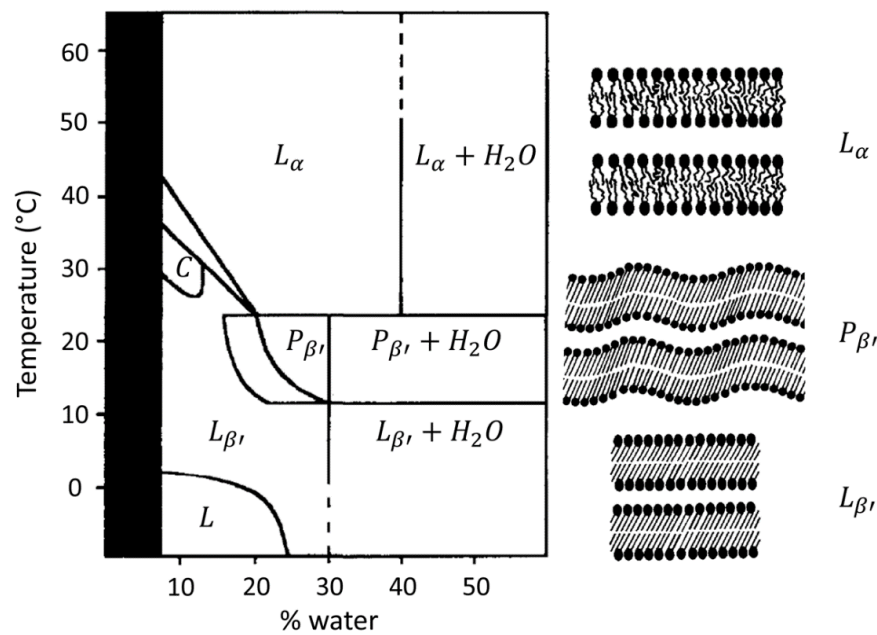
Figure 2.13. Phase diagram of DMPC lipid in water.[41,42]

2.4   Translocation of molecules through lipid membranes

Living cells developed various mechanisms to transport molecules through their plasma membrane (Figure 2.14). The transport mechanisms can be divided into active and passive processes, where the first ones require cell energy and the latter ones do not.
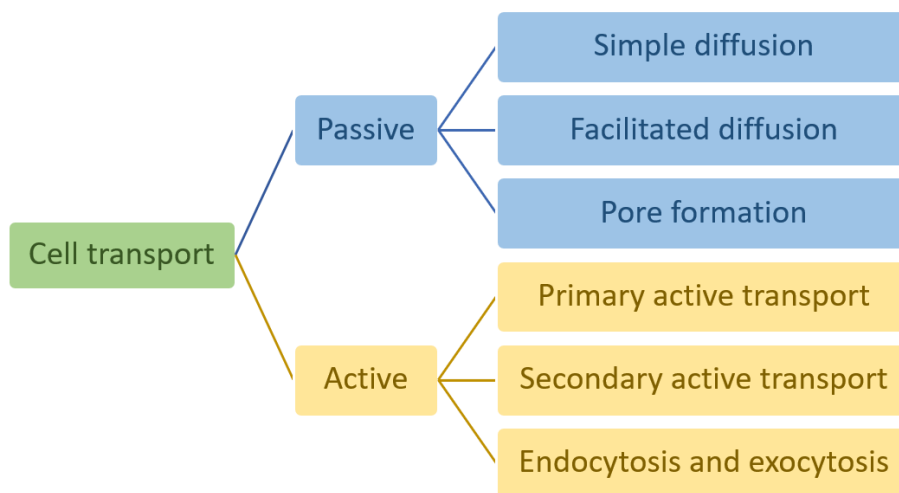
Figure 2.14. Classification of cell transport mechanisms

Small molecules of moderate polarity are usually able to cross plasma membrane by simple diffusion which is driven by the concentration gradient and governed by the molecular solubility in the membrane interior, the size of the molecule, temperature and other parameters. There is an empirical rule formulated by Christopher A. Lipinski in 1996, for predicting passive

translocation of molecules by diffusion.[43] He analyzed existing drug molecules and based on their chemical composition and properties made a prediction that a molecule is likely to have poor adsorption and permeation if it has:

- more than 5 hydrogen bond donors (the total number of nitrogen–hydrogen and oxygen-hydrogen bonds)

- more than 10 hydrogen bond acceptors (all nitrogen or oxygen atoms)

- a molecular mass of more than 500 g/mol

- the octanol-water partition coefficient (log P) that exceeds 5

There are many exceptions to this rule but it gives an impression of what is important for simple diffusion through the cell membrane. There are only a few large molecules that are reported to passively translocate plasma membranes. One interesting and well-studied example is Cyclosporin A, which is a cyclic peptide and has a molecular weight of 1200 g/mol. A large number of hydrogen bond donors make the molecule highly polar. The trick which this molecule applies to insert into the bilayer is changing its conformation so that the hydrogen bonds are located inside the peptide structure. In addition, there are some synthetic polymers which are known to passively translocate, among them phospholipid-mimicking polymers[44,45] and PEG-containing polymeric surfactants.[46] The translocation process of non-ionic polymers was studied theoretically for homopolymers,[47] block copolymers, and polymers with a random distribution of hydrophilic and hydrophobic units.[48] Translocation is predicted to occur when the polymers have a balanced amphiphilicity. An experimental study of this phenomenon is the topic of this project.
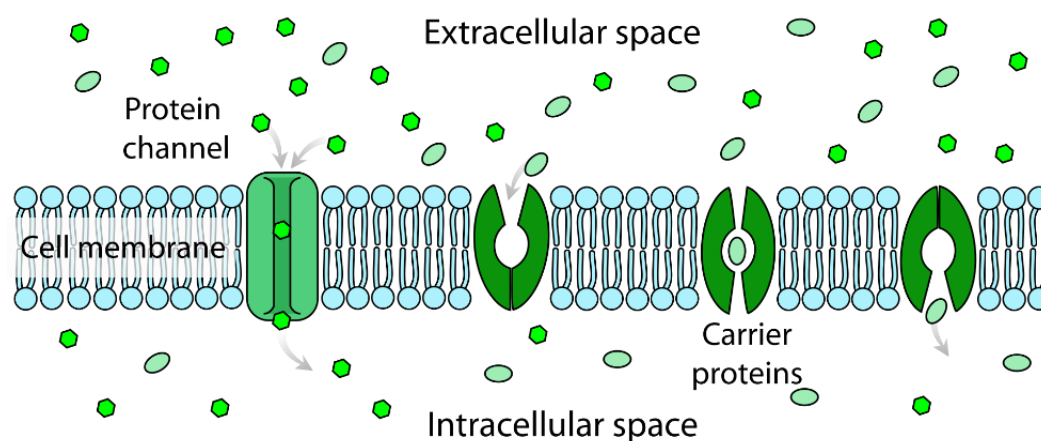

Figure 2.15 Mechanism of facilitated diffusion.[49]

For charged molecules and ions the lipid bilayer is almost impermeable by simple diffusion. Even small ions like Na^+ and K^+ have very small permeation coefficients in the order of 10^{-14} cm/s.[50]

For such molecules cells use other translocation mechanisms, e.g. via protein channels (Figure 2.15). This method is called facilitated diffusion.[51] Similar to simple diffusion it is a passive mechanism, so it does not require external energy and the translocation is driven only by the concentration gradient. The proteins which permit facilitated diffusion are usually selective, which is obtained by pore size and charge variation. Additionally, to control the translocation rate by other means than the concentration gradient, cells often have mechanisms to close or open the gate of the transport protein. This can be done by change of membrane potential (voltage-gating) or by chemical binding of molecules which triggers the opening or closing of the protein gate (ligand-gating).

Some large and charged molecules can create pores in the membrane to enter the cell interior. Some peptides, bacteria and viruses use this method which can be harmful to the cells as it creates leaks in the membrane for other unwanted molecules.[52]

Unlike passive transport mechanisms, active ones can transport molecules against the concentration gradient by using external energy. This can be done by various proteins which act as "pumps" or by encapsulating molecules into vesicles made of the cell membrane (endocytosis and exocytosis). [51]
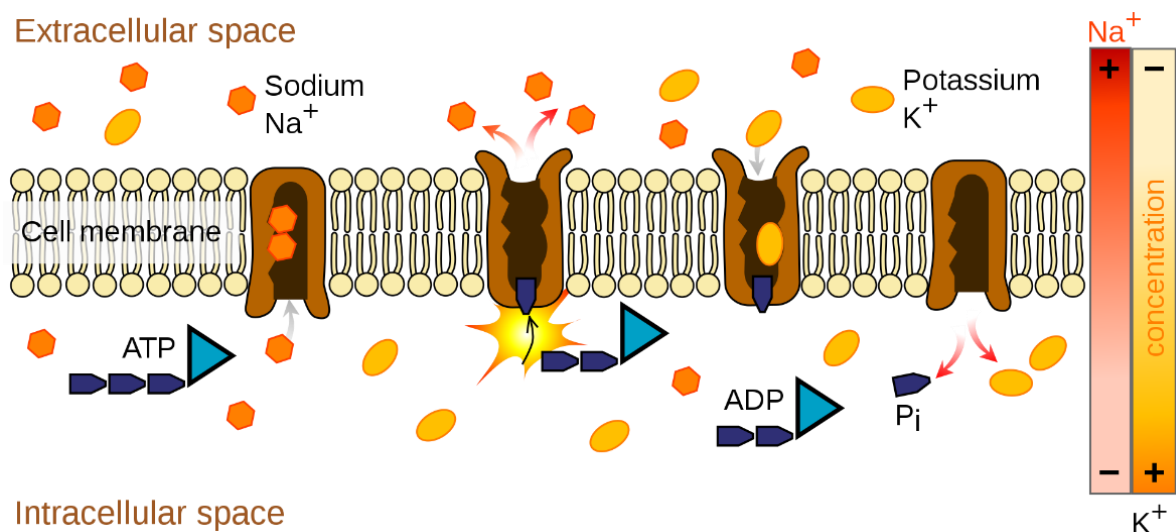
Figure 2.16. Mechanism of the sodium-potassium pump as an example of the primary active transport process.[53]

Primary active transports use the chemical energy of adenosine triphosphate (ATP). One example of such transports is the sodium-potassium exchange pump (Figure 2.16).[54] It uses energy released from "breaking" of one ATP molecule to move three sodium ions out of the cell and two potassium ions into the cell, against the concentration gradient for both ions. Secondary active transport is also known as co-transport because it uses the concentration gradient of the

first molecules created by the primary active transport to transfer other molecules in or out of the cell, often against their concentration gradient.

Endocytosis

| Phagocytosis | Pinocytosis | Receptor-mediated endocytosis |

solid particle

Extracellular fluid

Plasma membrane

Pseudopodium

Coated pit   Receptor

Phagosome (food vacuole)

Vesicle

cytoplasm

Coat protein

Coated vesicle
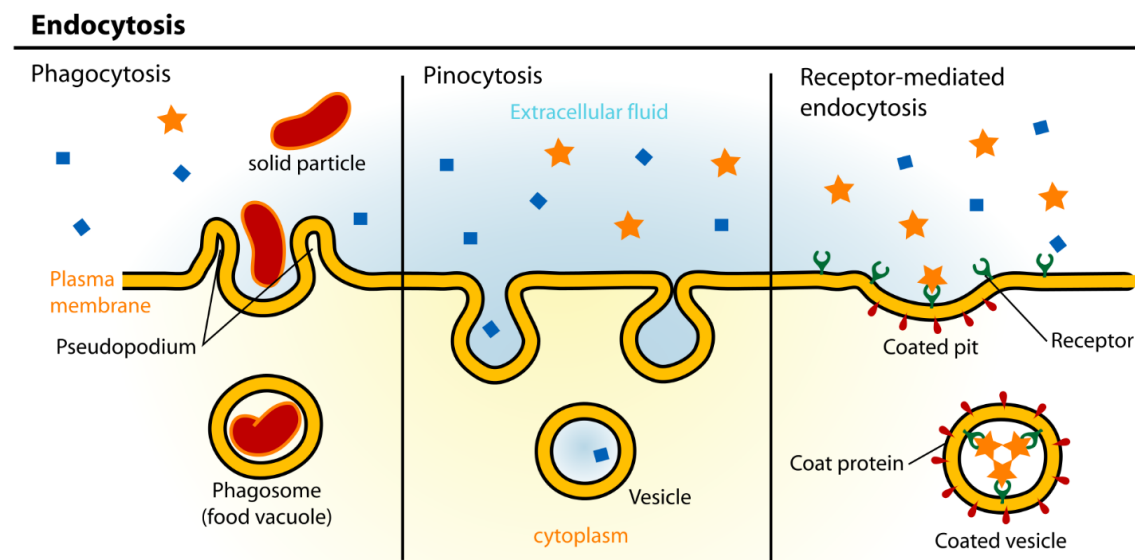
Figure 2.17 Different mechanisms of endocytosis.[55]

Simple diffusion in most cases works only for small molecules, the transport proteins also cannot transfer very large molecules due to their restricted size. For transportation of large molecules cells use endocytosis and exocytosis.[56] The difference between them is the direction of travel, in and out of the cell, respectively. The process of enveloping a molecule into the cell membrane is energy consuming for the cell, therefore this process is also classified as active. Figure 2.17 shows different ways of enveloping molecules. Vesicular transport is used not only for transportation in and out of the cell but it is also the main transport for large molecules inside the cell between different organelle.

2.5   References

[1]   M. Doi, S. F. Edwards, *The Theory of Polymer Dynamics*, Oxford University Press, USA, Oxford, **1988**.

[2]   M. R. and R. H. Colby, *Polymer Physics*, Oxford University Press, **2003**.

[3]   K. Kamide, T. Dobashi, *Physical Chemistry of Polymer Solutions : Theoretical Background*, Elsevier Science BV, **2000**.

[4]   P. J. Flory, *J. Chem. Phys.* **1942**, *10*, 51–61.

[5]   I. Teraoka, *Polymer Solutions : An Introduction to Physical Properties*, Wiley, **2002**.

[6]   H. Tompa, *Trans. Faraday Soc.* **1949**, *45*, 1142–1152.

[7]   Frakir, "Flory-Huggins theory: Mixture of polymers and solvent on a lattice," can be found under https://commons.wikimedia.org/wiki/File:Wpp1.jpg, **2010**.

[8]   R. Nagarajan, E. Ruckenstein, *Langmuir* **1991**, *7*, 2934–2969.

[9]   R. Nagarajan, K. Ganesh, *J. Chem. Phys.* **1998**, *90*, 5843.

[10]   J. Noolandi, K. M. Hong, *Macromolecules* **1983**, *16*, 1443–1448.

[11]   A. Halperin, S. Alexander, *Macromolecules* **1987**, *20*, 1146–1152.

[12]   A. Halperin, *Macromolecules* **1987**, *20*, 2943–2946.

[13]   E. Alami, M. Almgren, W. Brown, J. François, *Macromolecules* **1996**, *29*, 2229–2243.

[14]   T. Zinn, L. Willner, K. D. Knudsen, R. Lund, *Macromolecules* **2017**, *50*, 7321–7332.

[15]   K. Uramoto, R. Takahashi, K. Terao, T. Sato, *Polym. J.* **2016**, *48*, 863–867.

[16]   M. Ueda, A. Hashidzume, T. Sato, *Macromolecules* **2011**, *44*, 2970–2977.

[17]   C. Heitz, S. Pendharkar, R. K. Prud'Homme, J. Kohn, *Macromolecules* **1999**, *32*, 6652–6657.

[18]   C. Heitz, R. K. Prud'Homme, J. Kohn, *Macromolecules* **1999**, *32*, 6658–6667.

[19]   T. Horiuchi, K. Rikiyama, K. Sakanaya, Y. Sanada, K. Watanabe, M. Aida, Y. Katsumoto, *J. Oleo Sci.* **2020**, *69*, 449–453.

[20]   T. Horiuchi, T. Sakai, Y. Sanada, K. Watanabe, M. Aida, Y. Katsumoto, *Langmuir* **2017**, *33*, 14649–14656.

[21]   K. Rikiyama, T. Horiuchi, N. Koga, Y. Sanada, K. Watanabe, M. Aida, Y. Katsumoto, *Polymer (Guildf).* **2018**, *156*, 102–110.

[22]   N. A. Hadjiantoniou, A. I. Triftaridou, D. Kafouris, M. Gradzielski, C. S. Patrickios, *Macromolecules* **2009**, *42*, 5492–5498.

[23]   N. A. Hadjiantoniou, T. Krasia-Christoforou, E. Loizou, L. Porcar, C. S. Patrickios, *Macromolecules* **2010**, *43*, 2713–2720.

[24]   C. C. De Silva, P. Leophairatana, T. Ohkuma, J. T. Koberstein, K. Kremer, D. Mukherji, *J. Chem. Phys.* **2017**, *147*, 64904.

[25]   V. Hogouvieux, M. A. V. Axelos, M. Kolb, *Macromolecules* **2009**, *42*, 392–400.

[26]   V. Hugouvieux, M. A. V. Axelos, M. Kolb, *Soft Matter* **2011**, *7*, 2580–2591.

[27]   I. R. Cooke, D. R. M. Williams, *Macromolecules* **2003**, *36*, 2149–2157.

[28]   S. Li, C. Yu, Y. Zhou, *Sci. China Chem.* **2019**, *62*, 226–237.

[29]   C. C. De Silva, P. Leophairatana, T. Ohkuma, J. T. Koberstein, K. Kremer, D. Mukherji, *J. Chem. Phys.* **2017**, *147*, 64904.

[30]   S. Slomkowski, J. V. Alemán, R. G. Gilbert, M. Hess, K. Horie, R. G. Jones, P. Kubisa, I. Meisel, W. Mormann, S. Penczek, R. F. T. Stepto, *Pure Appl. Chem.* **2011**, *83*, 2229–2259.

[31]   A. Uzman, H. Lodish, A. Berk, L. Zipursky, D. Baltimore, *Biochem. Mol. Biol. Educ.* **2000**, *29*, Section 1.2The Molecules of Life.

[32]   T. D. Pollard, W. C. Earnshaw, J. Lippincott-Schwartz, G. T. Johnson, *Cell Biology: Third Edition*, Elsevier Inc., **2016**.

[33]   G. M. Cooper, *The Cell: A Molecular Approach. 2nd Edition.*, Sinauer Associates, **2000**.

[34]   M. S. Almén, K. J. V. Nordström, R. Fredriksson, H. B. Schiöth, *BMC Biol.* **2009**, *7*, 50.

[35]   LadyofHats, "Animal cell structure," can be found under https://commons.wikimedia.org/wiki/File:Animal_cell_structure_en.svg, **2006**.

[36]   Hbf878, "Membrane Lipids," can be found under https://commons.wikimedia.org/wiki/File:Membrane_Lipids.svg, **2017**.

[37]   B. T. R. Koynova, *OA Biochem.* **2013**, *1.1*, 1–9.

[38]   R. B. Gennis, in *Biomembr. Mol. Struct. Funct.* (Ed.: R.B. Gennis), Springer New York, **1989**, pp. 36–84.

[39]   D. Marsh, *Biochim. Biophys. Acta - Biomembr.* **2010**, *1798*, 40–51.

[40]   L. R. Arriaga, I. López-Montero, F. Monroy, G. Orts-Gil, B. Farago, T. Hellweg, *Biophys. J.* **2009**, *96*, 3629–3637.

[41]   M. J. Janiak, D. M. Small, G. G. Shipley, *J. Biol. Chem.* **1979**, *254*, 6068–6078.

[42]   G. G. Chernik, *Adv. Colloid Interface Sci.* **1995**, *61*, 65–129.

[43]   C. A. Lipinski, F. Lombardo, B. W. Dominy, P. J. Feeney, *Adv. Drug Deliv. Rev.* **1997**, *23*, 3–25.

[44]   T. Goda, Y. Miyahara, K. Ishihara, *J. Mater. Chem. B* **2020**, *8*, 7633–7641.

[45]   N. Morimoto, M. Wakamura, K. Muramatsu, S. Toita, M. Nakayama, W. Shoji, M. Suzuki, F. M. Winnik, *Biomacromolecules* **2016**, *17*, 1523–1535.

[46]   F. Mathot, A. Schanck, F. Van Bambeke, A. Ariën, M. Noppe, M. Brewster, V. Préat, *J. Control. Release* **2007**, *120*, 79–87.

[47]   M. Werner, J.-U. Sommer, V. A. Baulin, *Soft Matter* **2012**, *8*, 11714.

[48]   M. Werner, J. U. Sommer, *Biomacromolecules* **2015**, *16*, 125–135.

[49]   LadyofHats, "Scheme facilitated diffusion in cell membrane," can be found under https://commons.wikimedia.org/wiki/File:Scheme_facilitated_diffusion_in_cell_membrane-en.svg, **2007**.

[50]   D. Papahadjopoulos, S. Nir, S. Ohki, *Biochim. Biophys. Acta - Biomembr.* **1972**, *266*, 561–583.

[51]   M. H. Friedman, *Principles and Models of Biological Transport*, Springer New York, **2008**.

[52]   M. D. Peraro, F. G. Van Der Goot, *Nat. Rev. Microbiol. 2015 142* **2015**, *14*, 77–92.

[53]   LadyofHats, "Scheme sodium-potassium pump," can be found under https://commons.wikimedia.org/wiki/File:Scheme_sodium-potassium_pump-en.svg, **2007**.

[54]   M. V. Clausen, F. Hilbers, H. Poulsen, *Front. Physiol.* **2017**, *8*, 371.

[55]   LadyofHats, "Endocytosis types," can be found under https://commons.wikimedia.org/wiki/File:Endocytosis_types.svg, **2007**.

[56]   M. Marsh, *Endocytosis*, Oxford University Press, **2001**.

3   Experimental methods

3.1   Small angle scattering

Small angle scattering (SAS) usually considers the scattering of x-ray or neutron radiation from a sample. Because of their small wavelength in the order of 1 Å, they are suitable to study substances in the mesoscopic length scale (1nm – 1 um).[1] The typical SAS experiment setup is shown in Figure 3.1.[2] Here the monochromatic and collimated radiation beam scatters from the sample and the detector measures the intensity which came to each of its pixels. The pixel positions are then converted to a scattering vector q which is given as a difference between the incident and a scattered wave vectors $\bar{q} = \bar{k}_s - \bar{k}_i$. In the case of elastic scattering where $|\bar{k}_s| = |\bar{k}_i|$ and which is considered in diffractometry the q value can be calculated as

$$q = \frac{4\pi}{\lambda}\sin\theta$$
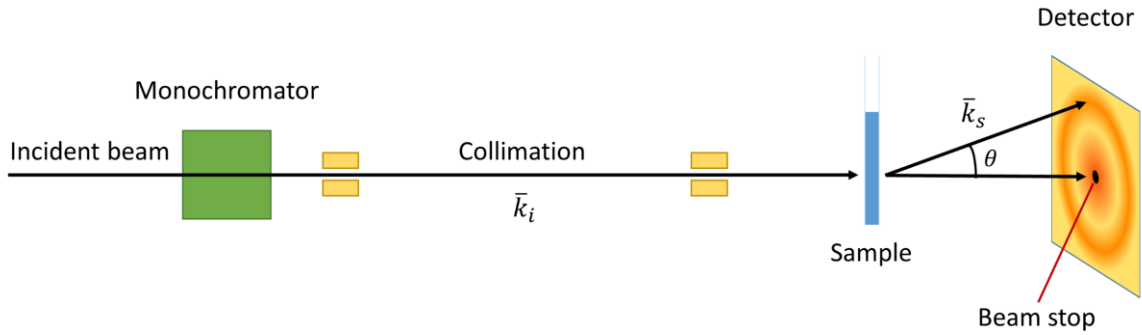
Figure 3.1 Schematic representation of small angle scattering experiment

The sample contains a huge number of scatterers (atoms) that we describe by the scattering length density $\rho_s(\bar{r})$. The scattering amplitude at a detector can be calculated as a coherent superposition of the scattering from all points within a sample[3]

$$A(\bar{q}) \sim A_0 \int_{V_s} \rho_s(\bar{r})e^{i\bar{q}\bar{r}}d\bar{r}$$

Here $\bar{q}\bar{r} = \Delta\Phi$ is a phase difference between the wave scattered at the origin of coordinated and at a point at the vector $\bar{r}$ from it, A_0 is the amplitude of the incident wave field, $\rho_s(\bar{r})$ is the scattering length density (SLD) which contains the full information about the sample which can be obtained from the scattering experiment. However, in the scattering experiment we can measure only the scattered intensity which is

$$I(\bar{q}) = |A(\bar{q})|^2 = A(\bar{q}) \cdot A^*(\bar{q}) = A_0^2 \iint_V \rho_s(\bar{r})\rho'_s(\bar{r'})e^{i\bar{q}(\bar{r}-\bar{r'})}d\bar{r}d\bar{r'}$$

The phase information here is lost meaning that the full reconstruction of $\rho_s(\bar{r})$ via Fourier transform is not possible. The equation for $I(\bar{q})$ can be simplified if we assume a sample to consist of equal spherical particles with volume V_p and a scattering length density difference $\Delta\rho$ relative to the medium between the particles. For a dilute solution the simplified equation can be written as

$$I(q) = cV_p^2\Delta\rho^2\left[\int_{V_p} e^{iqr}dr\right]^2 = cV_p^2F(q)$$

Where c is the particle number density and $F(q) = \Delta\rho^2\left[\int_{V_p} e^{iqr}dr\right]^2$ is the particle form factor, which describes the scattering from a single particle and contains information about the inner structure of the particles. At higher concentrations the spatial distribution of the particles needs to be considered which is done by including the structure factor $S(q)$ in the equation:

$$I(q) = cV_p^2F(q)S(q)$$

The exact function of the structure factor depends on the type of the interaction between the particles, but approaches 1 at infinitely small concentrations to result in the above limit for dilute solutions.
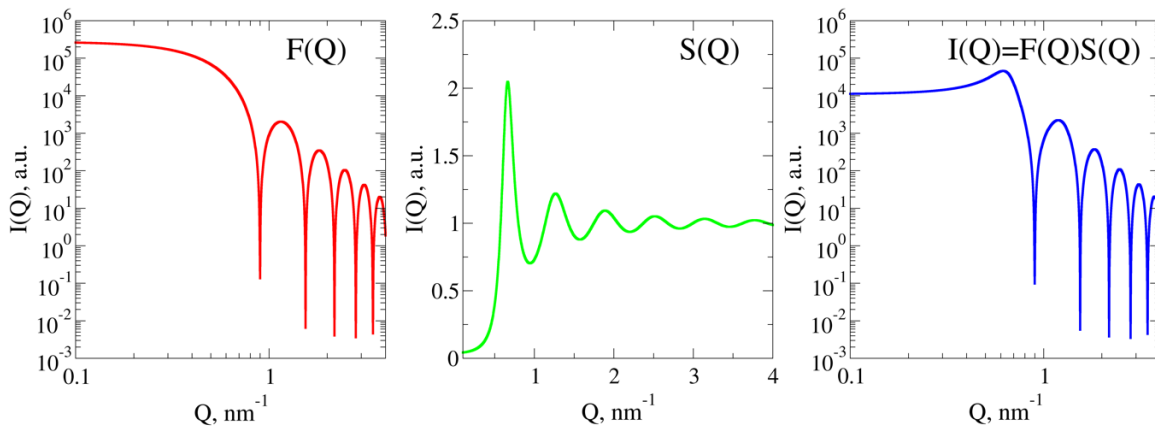
Figure 3.2. Example of form factor F(Q), structure factor S(Q) and I(Q)=F(Q)S(Q) of hard monodispersed spherical particles of radius R = 4 nm and a volume fraction of 0.4, having only sterical interaction.

In SAS of solutions finding the right form factor of particles is usually the main goal of the experiment. The functions of form factors were already calculated for various particles, from a simple sphere or Gaussian coil to multilamellar vesicles or inhomogeneous core-shell decorated with Gaussian coils, and can be calculated for other specific cases. The model complexity is basically limited only by computation power which is needed to fit experimental data with the

desired model. As an example $F(Q)$, $S(Q)$ and $I(Q)=F(Q)S(Q)$ of highly concentrated hard monodispersed spherical particles are shown in Figure 3.2.

For studying more complex particles the method of contrast variation is widely used in scattering techniques, particularly in neutron scattering. The difference between X-ray and neutron scattering is their sensitivity to light elements. Because x-ray radiation interacts with electron clouds of atoms, its scattering probability (or scattering cross section) increases with going from light to heavy elements of the periodic table. Neutrons interact only with the nuclei and their scattering cross section varies along the periodic table in a completely different way and it is different for two isotopes of one atom (Figure 3.3). The huge difference in scattering cross section between hydrogen and deuterium is very useful for contrast variation in soft matter physics.[1,4] Its principle is shown in Figure 3.4. Deuteration chemistry and biochemistry are rather developed nowadays, which opens huge possibilities for contrast variation experiments by neutron scattering.
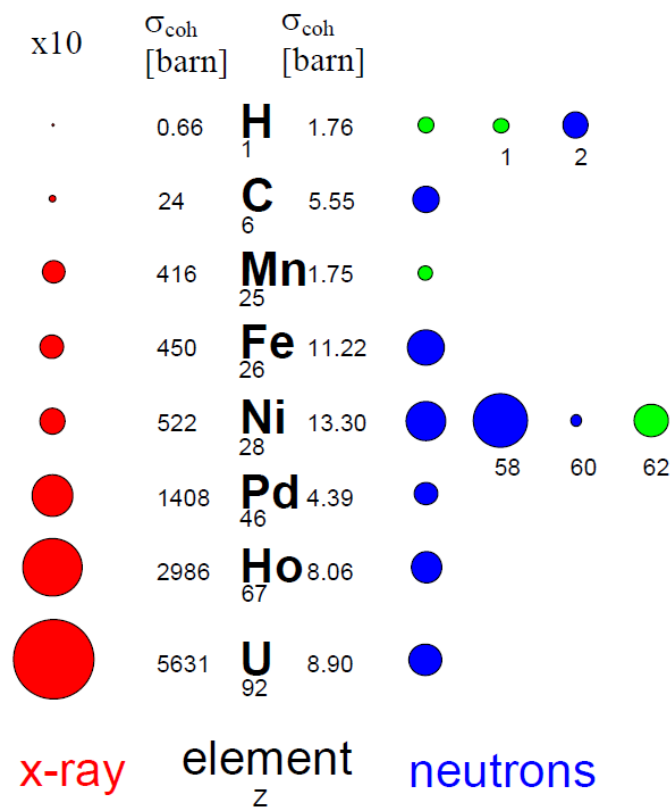
Figure 3.3 Comparison of scattering cross-sections (σ_{coh}) of selected elements for X-rays and neutrons. The area is proportional to cross section, which in the case of x-rays is scaled down 10 times. For neutrons different isotopes are shown for some atoms, and the blue and green color discriminates scattering with 180 degree phase shift. Only the values for coherent scattering are shown. The image is taken from [1].
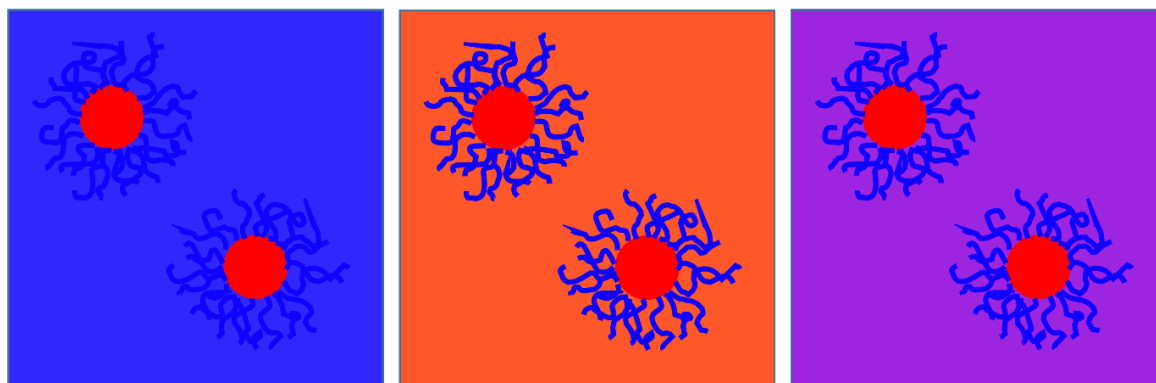
Figure 3.4 Principle of contrast variation and contrast matching by the example of core-shell particles. Variation of solvent SLD allows to contrast match different parts of the particles or the particle on average.

3.2 Neutron reflectometry

The neutron reflectometry (NR) technique is similar to SANS but instead of the scattered neutrons, the reflected neutrons are measured.[5] Because neutrons are reflected mainly at very shallow angles, only the intensity at low-q values is measured.

Figure 3.5 shows a basic principle of a neutron reflectometer. The collimated neutron beam hits the sample under a shallow angle and the reflected beam is measured by the detector. Unlike in SAS where we measure in transmission mode, here the beam hits the sample almost horizontally. The NR can discriminate between two types of information. Specular refraction contains information about structure in the z-direction, whereas off-specular refraction is only sensitive to a lateral structure if there is one.[6] Specular NR is a very precise method to study a profile of layered structures. The interaction of the beam with the layered structure is schematically shown in Figure 3.5 (insert). When the beam hits the sample, part of it is directly reflected from the surface and part penetrates to the next layer, where the same happens. Finally, all the beams interfere with each other and the interference pattern can be seen in the detector. It depends on the thicknesses of the layers and their SLD. For the ideally smooth surfaces only the parallel beams come to the detector (specular reflection). If the sample has a roughness, the beam will not always be reflected at the same angle causing the off-specular reflection. Analyzing the off-specular signal might be particularly interesting when the "roughness" is an ordered lateral structure. In the case of specular signal roughness is averaged over the whole sample area. It can be included in the specular NR by mathematically smoothing the SLD profile with the error function. The phase problem can also influence the real-space reconstruction in NR. However, performing NR experiments at different contrasts solves this

problem and makes the outcome information very precise. It allows, for example, to discriminate the location of some proteins or drugs in a single lipid membrane.
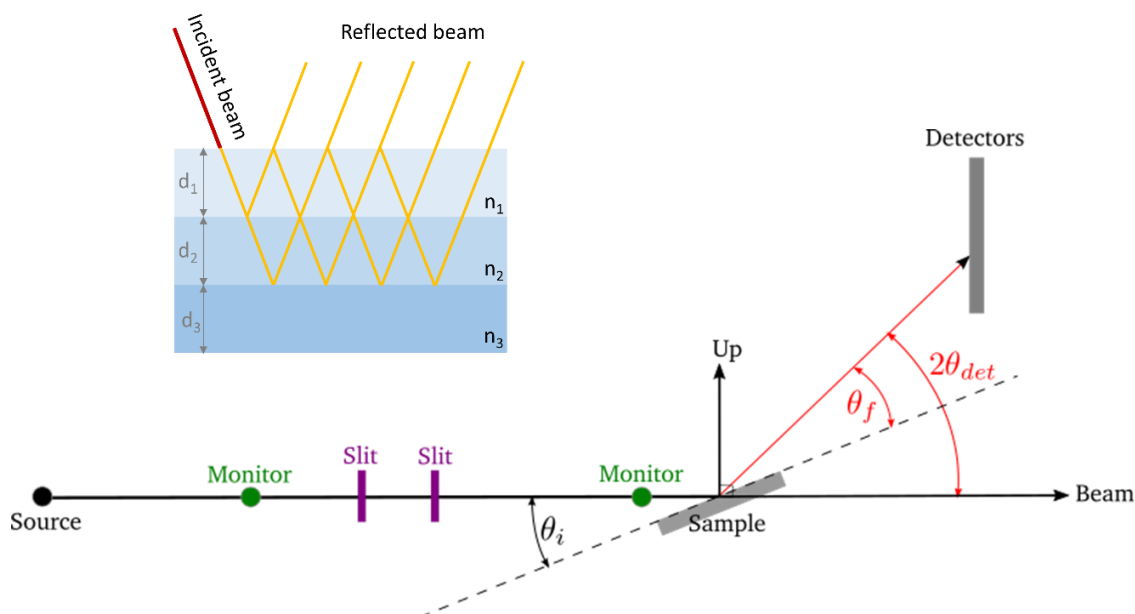
Figure 3.5 Principle of Neutron Reflectometry.[7] Insert: multiple reflections of the neutron beam from the layered structure. For simplicity of illustration the changes in refracted beam orientation are neglected and the layers' thicknesses are drowned similarly.

Figure 3.6 shows a schematic representation of neutron reflectometer MARIA located at the MLZ.[8] The neutron beam goes through the velocity selector to choose the desired wavelength. It can also be done by the Fermi chopper. It gives neutrons with smaller wavelength distribution, which leads to a better resolution but also to a smaller flux. After the wavelength selection neutrons can be polarized if, for example, the magnetic properties of the sample are needed to be measured. Then the beam is collimated by two slits, reflects from the sample and is measured by the detector. The q-vector is changed by changing the sample angle, which is done by a hexapod. The lipid bilayers were measured in temperature-controlled custom liquid cells.[9] Here the bilayer is created by a vesicle fusion on the surface of ultra-polished silica crystal covered by a thin layer of silicon oxide. The crystal surface area is 75 cm^2 and the cell volume is about 5 mL. MARIA has a sample holder for three of such cells and a flow-through option with the automatic switch between the flowing solutions.

① Neutron Guide NL5-N
② Velocity selector
③ Fermi chopper
④ Polariser
⑤ Slit pair
⑥ Hexapod sample table
⑦ Polarisation analyser (³He)
⑧ Detector
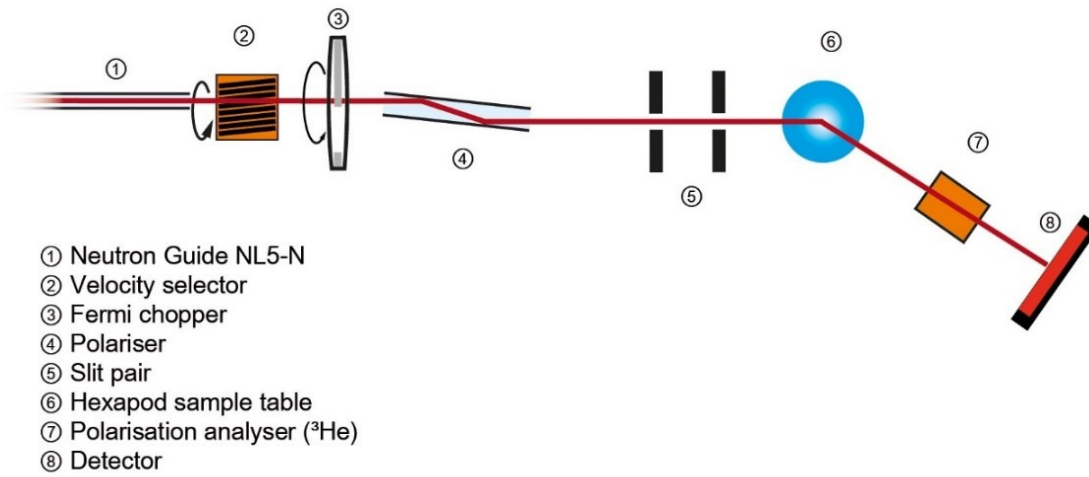
Figure 3.6 Schematic illustration of MARIA reflectometer located at MLZ.[10]

3.3   Pulsed field gradient NMR

3.3.1   Basics of PFG NMR

The nuclei having non-zero spin also have a nuclear magnetic moment, which aligns along the direction of the external magnetic field. The energy of such nuclei splits in the external magnetic field and the distance between the energy levels is proportional to the value of the magnetic field. For protons in a constant homogeneous magnetic field H_0 there are two energy levels:

$$E_{1,2} = \pm\frac{1}{2}\gamma\hbar H_0$$

Where γ is the gyromagnetic ratio and $\hbar$ is the Plank constant. The frequency of electromagnetic radiation which is needed to initiate the transition between the levels is Larmor frequency $\omega_0 = \gamma H_0$, and the distance between the two levels is $\Delta E = \hbar\omega_0$. In thermal equilibrium, the population difference between the levels is given by

$$\frac{n_1}{n_2} = e^{-\frac{\hbar\omega_0}{kT}}$$

Where n_1 and n_2 are the populations of upper and lower energy levels respectively, k is the Boltzmann constant, and T is the absolute temperature. This difference generates the net magnetic momentum, which amplitude is proportional to the total number of spins in the system. Applying the oscillating magnetic field (RF-field) in the transverse direction will cause oscillations of populations and the appearance of magnetic momentum in the transverse direction. Switching off the RF field will lead to relaxation to the thermal equilibrium state with characteristic relaxation times T_1 (for longitudinal relaxation) and T_2 (for transverse relaxation). Applying special RF pulse sequences and measuring the return to thermal equilibrium allows to

calculate the two relaxation times which contain various information about the sample properties. If the external field is not homogeneous, ΔE in different parts of the sample will be different. In Pulsed Field Gradient (PFG) NMR over two short time intervals the constant magnetic field is superimposed by an inhomogeneous field provided by the field gradient pulses of amplitude G. The Larmor frequencies during the gradient pulses are thus seen to become space dependent, following the relation[11]

$$\omega(\bar{r}) = \gamma(H_0 + \bar{G}\bar{r})$$

In this way the gradient pulse "marks" the spins.
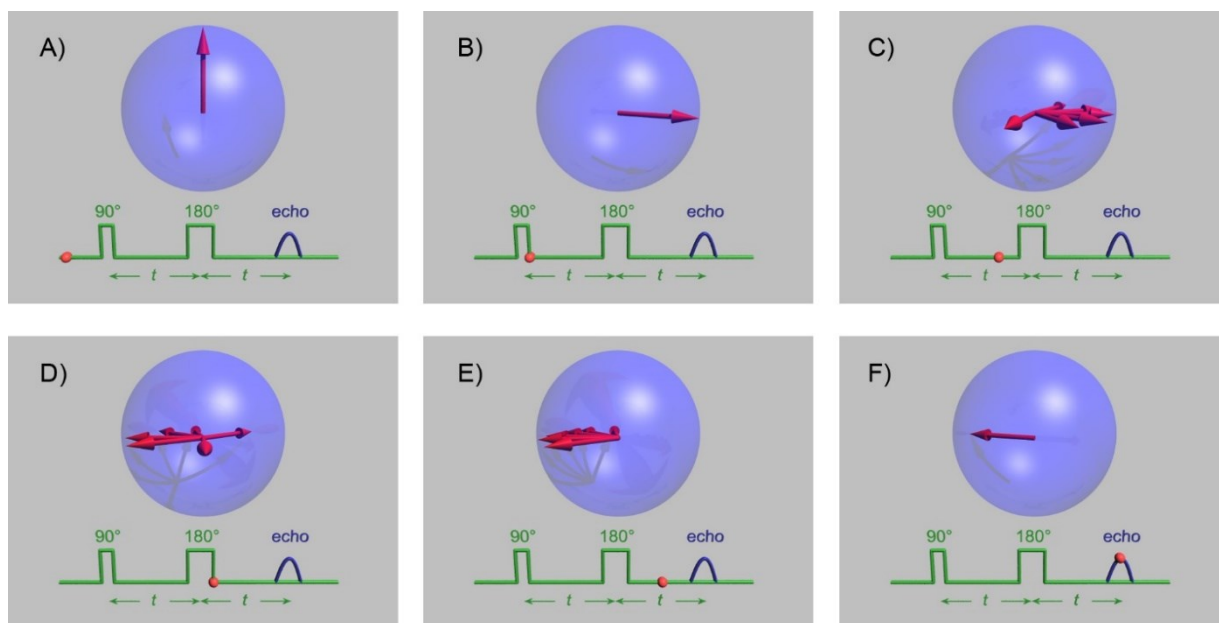
Figure 3.7 Schematic principle of spin echo given by an example of 90º-180º RF pulse sequence. The red arrow represents the magnetic moments of nuclei, and the red point shows the part of the sequence corresponding to a given distribution of magnetic moments.[12]

To better understand the principle of PFG NMR, it is useful to start from the principle of spin echo, which was first discovered and explained by Erwin Hahn in 1950.[13] Figure 3.7 shows a principle of spin echo signal appearance. At the first moment, the average magnetic moment of the spins is oriented parallel to the external constant magnetic field Figure 3.7A). The first RF pulse turns it in the perpendicular direction where the spins might slightly change the frequencies because of the magnetic field inhomogeneity in a sample volume, which will cause a signal decay (Figure 3.7B,C). After time *t* a 180º pulse is applied which "inverts the time", and after the same time *t* the spins recover the same orientation, causing a strong increase of signal intensity which is called echo signal (Figure 3.7D-F).

Now, if we apply additionally a magnetic field gradient after the first 90º pulse for a short time, we will "label" the z-position of all the spins. If the spins diffuse from their z-positions during the

time interval t between the two pulses, the 180° pulse in combination with the gradient phase of effectively opposite polarity will not give the echo signal of the same intensity as it was without the gradient. The described sequence is called the pulsed field gradient spin echo (PFGSE) sequence and it is shown in Figure 3.8. Increasing the gradient or the time between pulses will lead to a stronger decay of the echo signal, which can be used to measure the diffusion basically in every liquid sample. For the PFGSE sequence, the echo intensity can be calculated as

$$I = I_0 e^{-\frac{2\Delta}{T_2}} e^{-\gamma^2 G^2 \delta^2 D(\Delta - \frac{\delta}{3})}$$

By performing a series of measurements where G is changing at the fixed Δ and δ, one can calculate the diffusion coefficients of the spins.
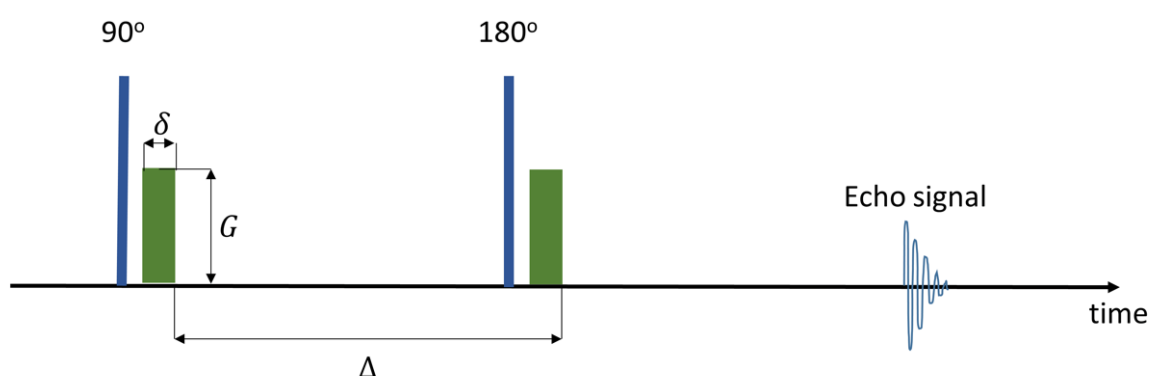
Figure 3.8 Pulsed field gradient spin echo (PFGSE) NMR sequence. The blue lines indicate RF pulses of 90° and 180°, and the green rectangles represent the gradient pulses of amplitude G and duration δ. The second gradient pulse follows the first one after time Δ.

The main weakness of the described sequence is that the spins in transverse orientation decay due to the T_2 relaxation described above, which leads to the additional decay of the echo signal. T_2 relaxation is usually quite fast for macromolecules, whereas T_1 relaxation is normally slow enough to not influence the measurements. To minimize the effect of T_2 relaxation the 180° pulse can be split into two 90° pulses (Figure 3.9). In this case, no T_2 relaxation will happen during the time period t_2, which would allow to increase Δ and, consequently, the lower limit of diffusion coefficients which can be achieved. Unlike PFGSE, this sequence produces five echo signals which can be observed at the time intervals $2t_1$, $2t_1+t_2$, $2t_2$, t_1+2t_2, $2(t_1+t_2)$.[14] For the measurements the echo appearing at the time of $2t_1+t_2$ is used, which is called stimulated echo. The ability to perform measurements at a wide range of Δ is useful for investigating diffusion in the restricted volume or various exchange processes. If the diffusion is restricted as, for example, in porous materials, the apparent diffusion coefficient will decrease when measuring at a longer observation time Δ. The PFG NMR is widely used to study the effects of confinements on

diffusive motion. The exchange process can be observed in the two-phase systems like hollow vesicles and some molecules which are able to interact or translocate through them. In these case the translocating molecule have two types of diffusions: free diffusion and diffusion together with vesicles. The typical experimental curve in this case is shown in Figure 3.10A. If the exchange process between the free and the incorporated states has a characteristic time in the order of Δ (10 ms – 1 s), the exchange time can be precisely measured by PFG NMR. In this case, the longer Δ would lead to a larger averaging between the two diffusions. It is easy to understand by imagining the diffusion of a single molecule at different observation times Δ. If the Δ is much smaller than the exchange time t_{ex}, then on average every molecule stayed at the single state (free or incorporated) during this time and the two slopes of the plot would correspond to the diffusion coefficients corresponding to each state separately (Figure 3.10A). If $\Delta \sim t_{ex}$ every molecule in average had time to stay both in free and in an incorporated state, therefore the diffusion coefficient for two states will be influenced by each other (Figure 3.10B). And if one waits long enough that $\Delta \gg t_{ex}$ all molecules will exchange so many times that two diffusion coefficients will average completely (Figure 3.10C). A theory for extracting the exchange time from the measurements at different Δ was described by Kaerger[15] and used in many studies, sometimes including the influence of T_1 and T_2 relaxation.[16]
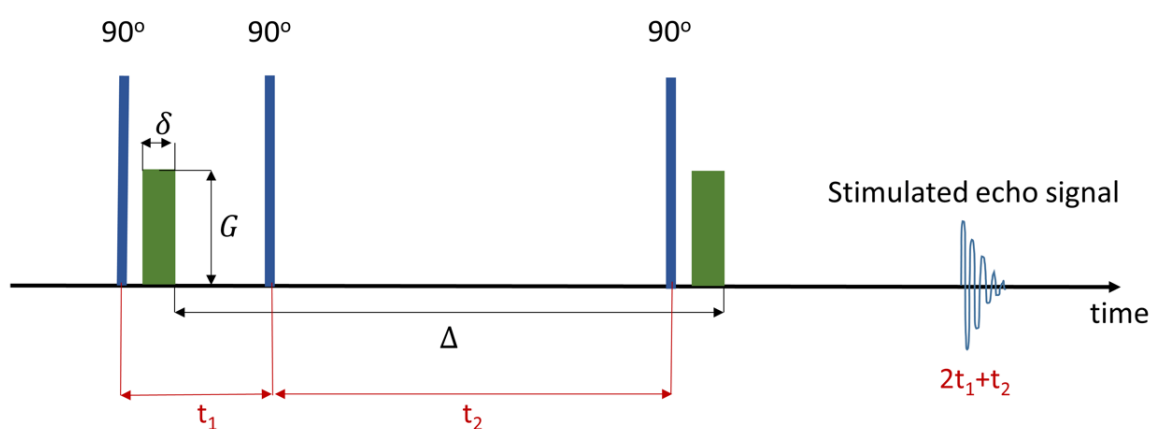
Figure 3.9 Pulsed field gradient stimulated echo (PFGSTE) NMR sequence. The blue lines indicate three RF pulses of 90°, where the duration between the first and the second is t_1 and between the second and third t_2. The echo signal appears at the time $2t_1+t_2$ after the first signal. The green rectangles represent the gradient pulses of amplitude G and duration δ. The second gradient pulse follows the first one after time Δ.
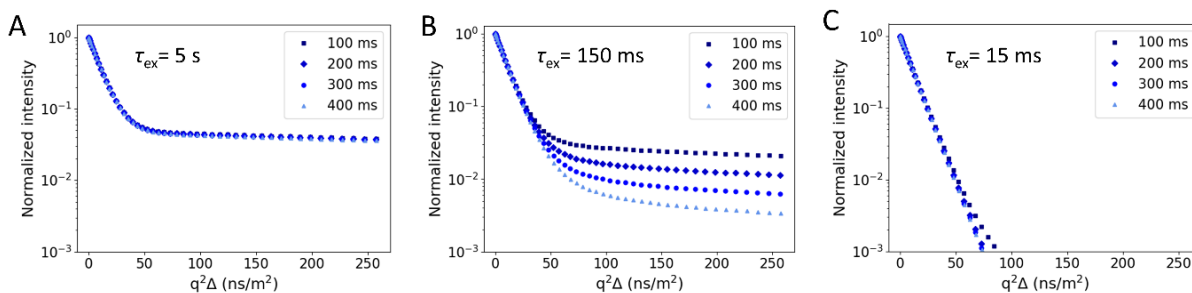
Figure 3.10. Model curves of the PFG NMR experiment at different Δ for systems of different exchange times: 5s (A), 150 ms (B), and 5 ms (C). The curves were modeled using diffusion coefficient of fast component 10^{-10} m^2/s, of slow component 10^{-12} m^2/s, the population of the slow component of 5%, and the gradient pulse duration δ = 2 ms.

The PFG NMR pulse sequences described above are good to explain the basic principle of the method but nowadays there are many modifications of those sequences which work more efficiently for some applications.[17] For example, all the measurements described in the following chapters were performed using the sequence shown in Figure 3.11. It is a DOSY gradient compensated stimulated echo sequence with spin lock and convection compensation (DgcsteSL_cc).[18,19] Apart from the two main gradient pulses for diffusion measurement the sequence has a number of gradients for compensation of different instrumental imperfections. The two homospoil gradients which are applied along the z-axis dephase the remaining transverse magnetization of the sample after the second and the fourth 90° RF pulses. The convection effect in the sample can seriously affect the diffusion measurements, particularly at temperatures different from ambient. Practically, this effect can be seen as additional oscillations on top of the signal decay and in some cases can be mistaken with fast diffusion decay. For the compensation of this effect, the sequence of two RF and two gradient pulses is added. The six compensation gradients of opposite orientation are applied to compensate for the eddy-current effect. The spin lock is a long pulse allowing to keep magnetization in the transverse orientation for a longer time.
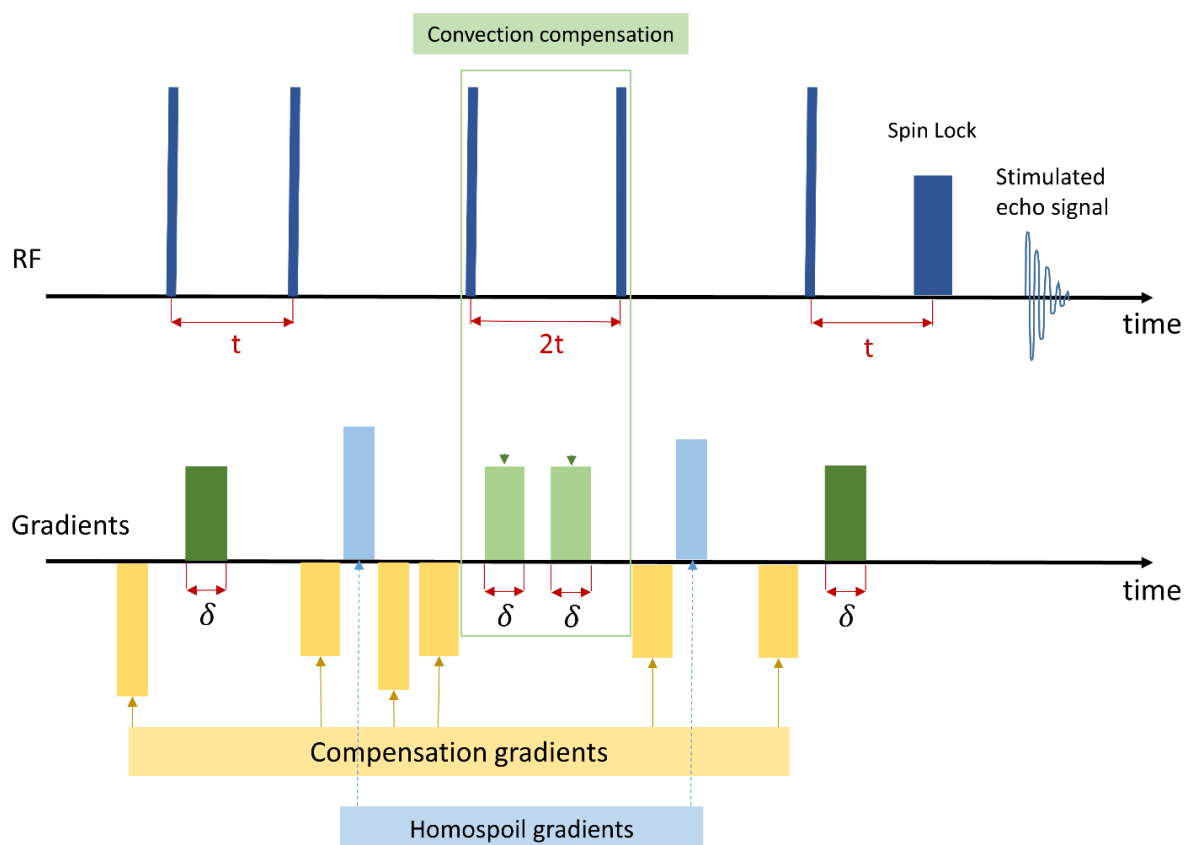
Figure 3.11. DOSY Gradient Compensated Stimulated Echo with Spin Lock and Convection Compensation (DgcsteSL_cc) sequence.

3.3.2 Kinetic PFG NMR

Unfortunately, the maximum value of Δ is limited by the T_1 relaxation and by instrumental imperfection. Normally, measurements at Δ larger than a few seconds make no sense due to the noisy NMR signal. The exchange processes with larger exchange times sometimes can be studied by measuring the time evolution of the slower diffusion component.[20] It works well for the system with vesicles plus slowly translocating molecules and even have some advantages compared to the classical PFG NMR. The intensity of the slow component extrapolated to G = 0 is proportional to the number of molecules in the incorporated state. So, if the mixing of molecules with vesicles is done at zero time, the kinetic process of their incorporation into the vesicles can be measured. The kinetic measurements are performed at a fixed gradient which is chosen such that the faster diffusion component had already decayed. The experimental scheme is presented in Figure 3.12.
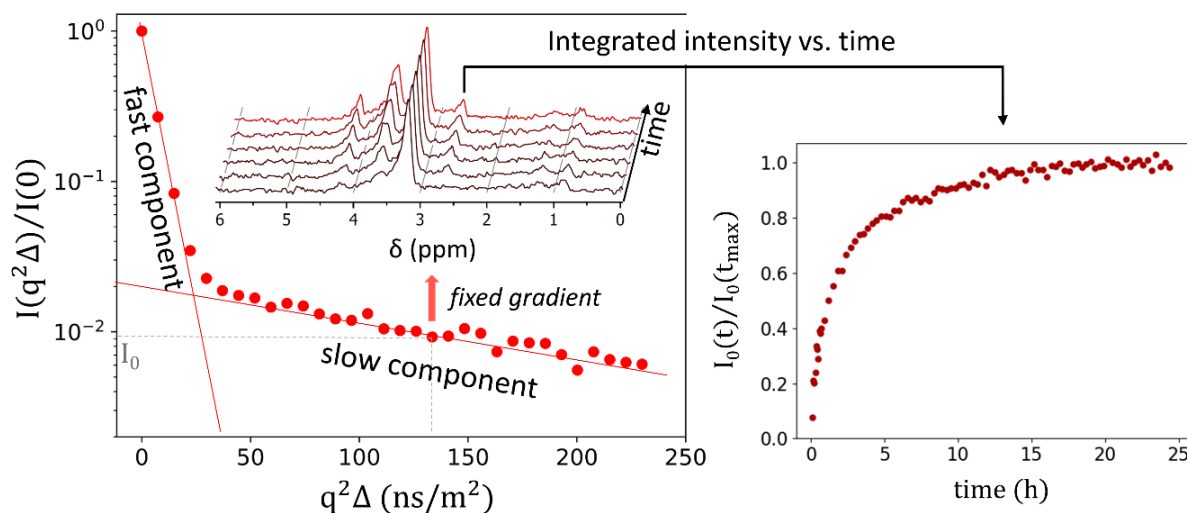
Figure 3.12. Principal of kinetic PFG NMR. Conventional PFG NMR decay of a molecule having a slow exchange between the free and encapsulated states normalized to I(q²Δ=0). The amplitude of the slow component is proportional to the number of molecules in the slow phase and the kinetics of its growth can be detected by performing PFG NMR measurements at a single gradient point (marked by red arrow).

If the translocation process is similar to the translocation through the infinitely thin membrane, the kinetic curve can be fitted by a simple exponential function and the translocation time can be extracted:

$$I = I_0 e^{-t/t_{ex}}$$

For more complex translocation processes one needs to solve a system of differential equations, describing the time evolution of molecule concentration in every state. It can be outside volume, membrane and inner vesicle volume, or sometimes different states of molecules in the membrane can be additionally discriminated. The application of the kinetic PFG NMR to the system of lipid vesicles plus polymers will be described in detail in the following chapters.

3.4   Fluorescence microscopy

The measurements presented in this work were performed by confocal laser-scanning microscopes. The difference of such microscopes from the standard light microscopes is that the light beam is focused only on a small spot of the sample.[21] It increases the resolution and allows to scan a sample also in z-direction. The schematic principle of the confocal microscope is presented in Figure 3.13. In the case of a laser-scanning microscope, the light source is a laser. Some microscopes have the possibility to switch between different wavelengths of the laser to enable an efficient excitation of various fluorescent molecules. In the case of fluorescence confocal microscopes the wavelength range which is read by the detector can be tuned

depending on the emission spectra of the used fluorescence dye. Some microscopes have several detectors which can detect at different wavelengths simultaneously.
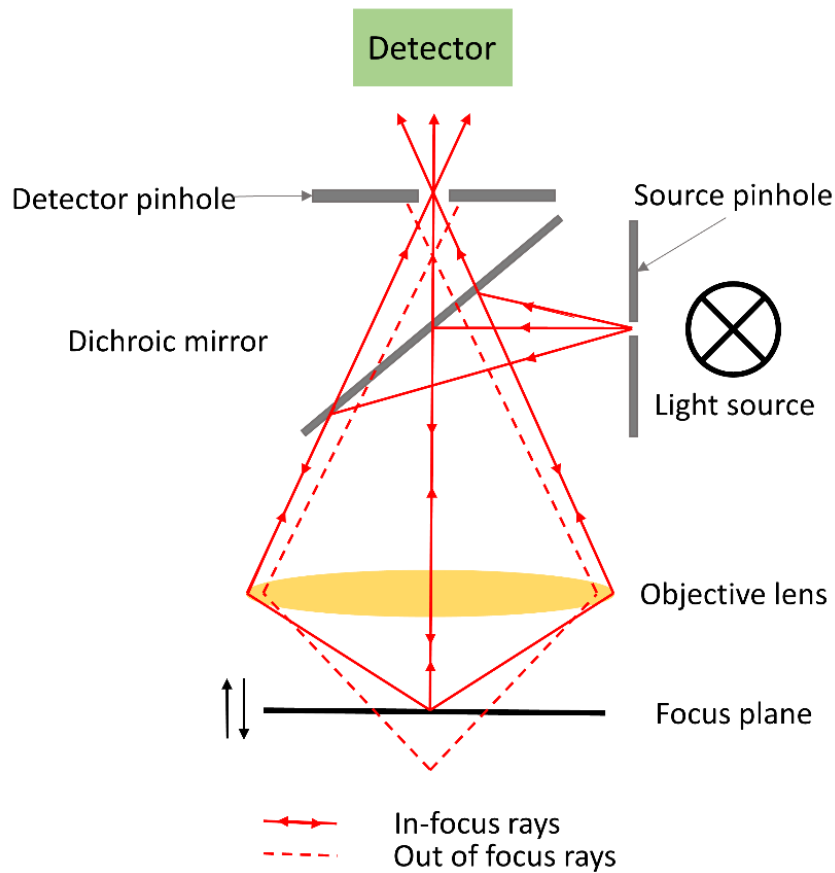
Figure 3.13 Principle of a confocal microscope.

3.5   References

[1]   T. Brückel, S. Förster, R. Zorn, G. Roth, *JCNS Lab. Course 2017* **2017**.

[2]   I. Grillo, in *Soft-Matter Charact.*, Springer Science+Business Media, LLC, **2008**, pp. 723–777.

[3]   A. Guinier, G. Fournet, *Small-Angle Scattering of X-Rays*, Wiley, **1955**.

[4]   F. Damay, D. Bazin, M. Daudon, G. André, *Comptes Rendus Chim.* **2016**, *19*, 1432–1438.

[5]   F. Cousin, G. Fadda, *EPJ Web Conf.* **2020**, *236*, 04001.

[6]   R. Pynn, S. M. Baker, G. Smith, M. Fitzsimmons, *J. Neutron Res.* **1999**, *7*, 139–158.

[7]   "ISIS Reflectometry documentation," can be found under https://docs.mantidproject.org/nightly/techniques/ISIS_Reflectometry.html, **n.d.**

[8]   S. Mattauch, A. Koutsioubas, U. Rücker, D. Korolkov, V. Fracassi, J. Daemen, R. Schmitz, K. Bussmann, F. Suxdorf, M. Wagener, P. Kämmerling, H. Kleines, L. Fleischhauer-Fuß, M. Bednareck, V. Ossoviy, A. Nebel, P. Stronciwilk, S. Staringer, M. Gödel, A. Richter, H. Kusche, T. Kohnke, A. Ioffe, E. Babcock, Z. Salhi, T. Bruckel, *J. Appl. Crystallogr.* **2018**, *51*, 646–654.

[9]   A. Koutsioubas, *J. Phys. Chem. B* **2016**, *120*, 11474–11483.

[10]   "MARIA / MLZ," can be found under https://mlz-garching.de/maria, **n.d.**

[11]   J. Kärger, M. Avramovska, D. Freude, J. Haase, S. Hwang, R. Valiullin, *Adsorption* **2021**, *27*, 453–484.

[12]   G. W. Morley, "Sequence of still images from spin echo animation," can be found under https://commons.wikimedia.org/wiki/File:SpinEcho_GWM_stills.jpg, **2011**.

[13]   E. L. Hahn, *Phys. Rev.* **1950**, *80*, 580.

[14]   D. Burstein, *Concepts Magn. Reson.* **1996**, *8*, 269–278.

[15]   J. Kärger, *Adv. Colloid Interface Sci.* **1985**, *23*, 129–148.

[16]   S. Himmelein, N. Sporenberg, M. Schönhoff, B. J. Ravoo, *Langmuir* **2014**, *30*, 3988–3995.

[17]   W. S. Price, W. S. Price, *NMR Studies of Translational Motion: Principles and Applications*, Cambridge University Press, **2009**.

[18]   Varian, Inc, *High-Resolution Diffusion-Ordered Spectroscopy (DOSY) User Guide*, Varian, Inc., **2010**.

[19]   A. Jerschow, N. Müller, *J. Magn. Reson.* **1997**, *125*, 372–375.

[20]   A. Leson, S. Hauschild, A. Rank, A. Neub, R. Schubert, S. Förster, C. Mayer, *Small* **2007**, *3*, 1074–1083.

[21]   S. W. Paddock, *Mol. Biotechnol. 2000 162* **2000**, *16*, 127–149.

4 Controlled LCST Behavior and Structure Formation of Alternating Amphiphilic Copolymers in Water

Abstract

Amphiphilic polymers show a rich variety of self-assembly behavior in aqueous solutions. In experimental studies, statistical copolymer or block copolymer architectures are usually investigated, because of their ease of synthesis or their structural analogy to surfactants. A copolymer structure that links the two architectures is an alternating copolymer, which is easily accessible by polycondensation reactions. Using alternating hydrophilic and hydrophobic building blocks with varying lengths allows a systematic variation between statistical and multi-block architectures. We synthesized alternating amphiphilic copolymers as polyesters using hydrophobic dicarboxylic acids ($C_4 - C_{20}$) and hydrophilic polyethylene glycol (PEG) units ($EG_3 - EG_{1000}$). Copolymers with long EG units were made accessible with the help of a newly developed esterification process. The solution properties of the amphiphilic copolymers feature a lower critical solution temperature (LCST) behavior in water, which can be systematically varied over a wide range from $0 - 100°C$ by adjusting the lengths of the C_n- and EG_m–units. We find that the transition temperature depends linearly on the hydrophobic unit length C_m and logarithmically on the hydrophilic length EG_n. In the one-phase region the PEG copolymer coils are more compact compared to the respective PEG homopolymers due to hydrophobic interactions between the hydrophobic units leading to loop formation. For shorter PEG-units the copolymers form micellar structures consisting only of a few copolymer chains. The micellar cores consist of hydrophobic regions containing only a few dicarboxylic acid units, embedded in a PEG-rich and water-poor matrix. The cores are surrounded by a diluted corona of PEG chains. Further decreasing the PEG unit length leads to the formation of highly swollen gels consisting of networks of interconnected micelles. These can self-assemble to form highly ordered liquid crystalline cubic phases. The study demonstrates how the structure of alternating amphiphilic

copolymers can be systematically varied to adjust thermal solution properties such as the LCST over a wide range, as well as the self-assembly properties varying between single chains, micelles, gels and highly ordered lyotropic liquid crystals.

4.1 Introduction

Amphiphilic polymers have been largely investigated in aqueous media with respect to micellization or interfacial properties. They play an important role in many applications. So far, from the structural standpoint, the focus was on diblock- and triblock- along with comb-shaped polymers and hydrophilic polymers, end-capped with low molecular weight hydrophobic units.[1,2] Less focus has been given to alternating amphiphilic copolymers (AAPs), because their synthesis is restricted to special monomers or yields polymers with a broad molecular weight distribution (MWD). In aqueous media, these polymers frequently form complex structures.

The hydrophobic and hydrophilic units in AAPs can be low molecular weight monomers or large polymeric blocks. In the latter case multiblock copolymers are formed. AAPs with monomeric hydrophobic and hydrophilic units are accessible for example via alternating polymerization of maleic anhydride with styrene or vinyl ether monomers.[3–5] The anhydride hydrolysis yields ionic moieties under basic conditions and the hydrophobic functionality frequently is located in the co-monomer side chains. Alternatively, polycondensation reactions of dicarboxylic acids with dialcohols or diamines of opposite polarity have been applied to synthesize AAPs.[6–10] Other procedures like click chemistry have been reported in rare cases.[11] The access to AAPs with polymeric hydrophilic and hydrophobic units is limited to a small number of methods. Condensation reactions, as outlined above, were used to synthesize AAPs, containing for example alternating ethylene oxide (EO) and propylene oxide (PO) units.[12–14] In a different approach, controlled radical polymerization techniques were applied to produce AAPs of hydrophobic and hydrophilic methacrylate monomers.[15,16]

AAPs were examined in aqueous media with respect to their solution behavior and structure formation. If the hydrophilic units dominate, water-soluble polymers are obtained, which frequently show a lower critical solution temperature (LCST) behavior.[6,15,16] Furthermore, the formation of micelles was reported. Mostly various flower-like structures were found.[3,4,9,10,12–16] A few studies reported nanotube or vesicle formation.[7,11] In agreement with the experimental results, different simulation studies predicted the existence of globular or expanded free chains and a large variety of complex micellar structures like uni- and multi-flower-like or worm-like micelles and micellar chains.[17–21] In addition, the formation of gels was

reported.[19] The structures formed strongly depend on solvent quality and the sizes and the size ratio of the hydrophobic units.

Thermo-responsive polymers are highly desirable in a wide range of applications.[22,23] For example, they have a significant presence in drug delivery applications.[23–25] Many polymers are used with other molecules to obtain co-functionalities and build multifunctional materials.[26] One of the most versatile and popular polymers in this regard is poly(N-isopropylacrylamide) (PNIPAM) and PNIPAM derivatives.[27–29] Poly(2-oxazoline)s[30] as well as random copolymers of EO with comonomers like propylene oxide[31] and other epoxide monomers[32] allow to vary the LCST behavior over a broad temperature range by modifying the monomer side groups or polymer composition. The same holds for AAPs, where the selection of the hydrophobic and hydrophilic units may predict the LCST behavior.[33]

In this work we synthesized polyesters from commercially available dicarboxylic acids and PEG units. These AAPs show a LCST behavior, which can be predetermined by the selection of the hydrophilic and hydrophobic moieties. Using small angle neutron scattering (SANS) and small angle X-ray scattering (SAXS) techniques, the structures formed in water were studied over a broad range of unit sizes and compositions.

4.2   Results and discussion

Synthesis

The AAPs $P(C_mEG_n)$ used in this work contain alternating hydrophobic and hydrophilic units. Dicarboxylic acids (C_m) were used as hydrophobic units and polyethylene glycols (EG_n) as the hydrophilic ones (see Figure 4.1). The total number of carbon atoms in the diacids is given by m and the number of EG repeat units in the PEGs is specified by n. PEGs contain two alcohol end groups and except tri- and tetraethylene glycol have a molecular weight distribution (MWD). The molecular weight (MW) characterization of the compounds used is summarized in Table 4.1.
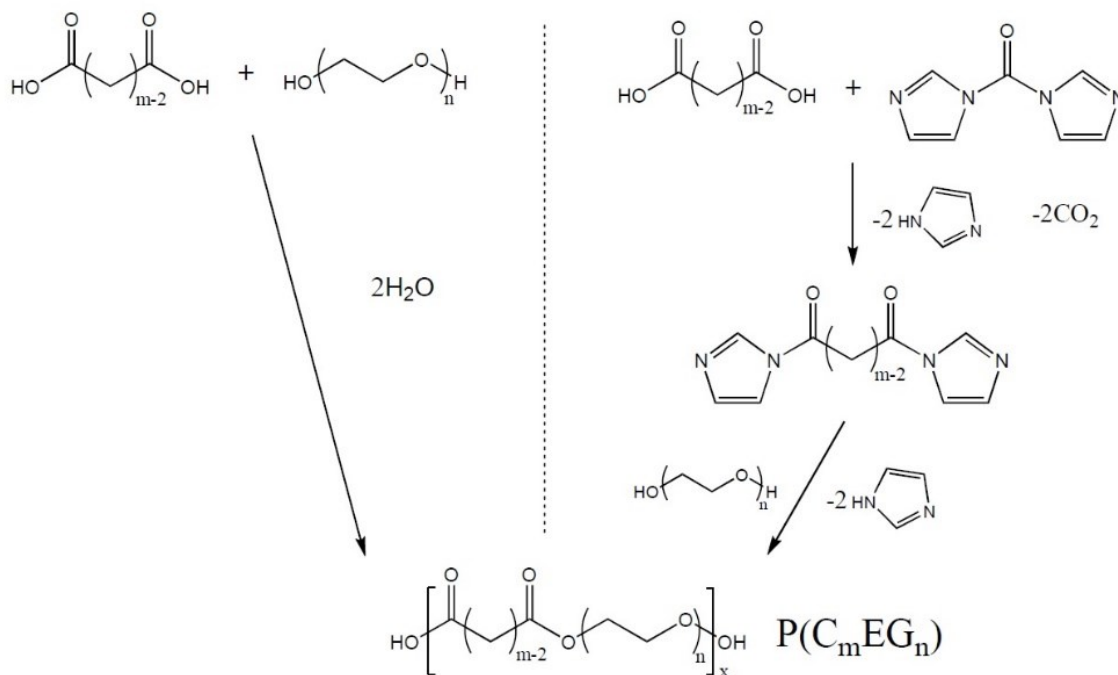
Figure 4.1. Synthesis of AAPs via polycondensation using hydrophobic dicarboxylic acids and hydrophilic polyethylene glycols as monomers. The polymer chain ends are equipped with carboxylic acid and alcohol groups in a random fashion.

Table 4.1. Hydrophobic and hydrophilic units used for the synthesis of the AAPs.

dicarboxylic acid (m)		MW	PEG (n)		M_n, g/mol	M_w/M_n
succinic acid	(C_4)	118	triethylene glycol	(EG_3)	150	
glutaric acid	(C_5)	132	tetraethylene glycol	(EG_4)	194	
adipic acid	(C_6)	146	PEG 300	(EG_6)	284	n.d.
suberic acid	(C_8)	174	PEG 400	(EG_9)	400	n.d.
sebacic acid	(C_{10})	202	PEG 600	(EG_{13})	599	1.05
dodecanedioic acid	(C_{12})	230	PEG 1k	(EG_{22})	986	1.04
tetradecanedioic acid	(C_{14})	258	PEG 2k	(EG_{47})	2,110	1.04
eicosanedioic acid	(C_{20})	343	PEG 4.5k	(EG_{103})	4,530	1.03
			PEG 10k	(EG_{240})	10,600	1.01
			PEG 45k	(EG_{1000})	44,200	1.04

Most of the AAP syntheses were achieved by polycondensation of succinic anhydride (C_4) or C_5 to C_{12} dicarboxylic acids with the lower MW PEGs up to EG_{22}. In these processes the reaction water was removed via azeotrope distillation or vacuum. *p*-Toluenesulfonic acid (TsOH) was used as catalyst (Figure 4.1, left side). The synthetic details are given in the SI. The MW characterization by SEC/LS as well as the average number of hydrophobic-hydrophilic repeat

units per polymer chain (x) is summarized in Table 4.2. In addition, the polymers were characterized by ^{1}H-NMR. The details are given in the Appendix Figure A2.

Table 4.2. SEC/LS characterization results for the non-fractionated AAPs; x represents the number of hydrophobic/hydrophilic repeat units.

	M_n, g/mol	M_w/M_n	x
$P(C_4EG_3)$	8,790	1.82	53.8
$P(C_4EG_4)$	19,360	1.95	66.3
$P(C_4EG_6)$	6,590	1.58	17.9
$P(C_5EG_3)$	3,760	1.28	15.2
$P(C_5EG_4)$	7,220	1.75	24.8
$P(C_5EG_6)$	11,700	1.51	30.7
$P(C_5EG_{13})$	6,390	1.52	9.2
$P(C_6EG_6)$	8,700	1.59	22.0
$P(C_8EG_6)$	5,610	1.65	13.2
$P(C_8EG_9)$	5,130	1.87	9.5
$P(C_8EG_{13})$	6,790	1.58	9.1
$P(C_8EG_{22})$	11,400	2.08	10.1
$P(C_{10}EG_{13})$	6,040	1.46	7.9
$P(C_{10}EG_{22})$	10,100	1.49	8.7
$P(C_{12}EG_{13})$	5,270	1.66	6.6
$P(C_{12}EG_{22})$	20,100	1.63	17.0
$P(C_{14}EG_{47})$	91,100	1.45	38.7
$P(C_{14}EG_{103})$	168,000	1.47	35.1
$P(C_{20}EG_{47})$	60,000	1.68	24.6
$P(C_{20}EG_{103})$	114,000	1.47	23.5
$P(C_{20}EG_{240})$	231,000	1.21	21.2
$P(C_{20}EG_{1000})$	537,000	1.68	12.1

For larger PEG units (EG_{47} and higher), the polyester synthesis via water removal failed. Only oligomeric products were obtained because of the increasingly lower concentrations of reactive groups. The replacement of dicarboxylic acid by the acid chloride analog did not improve the situation. Only the activation of the carboxylic acid with the help of CDI proved successful. The activation of carboxylic acids with CDI for esterification or amidation reactions is a standard procedure in organic synthesis.[34] In this approach, a dicarbonylimidazole is formed intermediately (see Figure 4.1, right side), which reacts with PEG under formation of the AAP. As a result, polymerization degrees between 20 to 40 hydrophobic-hydrophilic repeat units could be achieved (Table 4.2). The same procedure was applied for the synthesis of a $P(C_{10}EG_{22})$ polymer in order to obtain samples of higher polymerization degrees. The CDI activation procedure demands dry reaction conditions because of the water sensitivity of CDI. In addition, the exact stoichiometry is required of all three components dicarboxylic acid, PEG, and CDI. This

becomes more challenging with increasing PEG MW, due to the limited precision of the MW determination. NMR end-group analysis in pyridine-d_5 proved to be the most precise method for this purpose.[35]
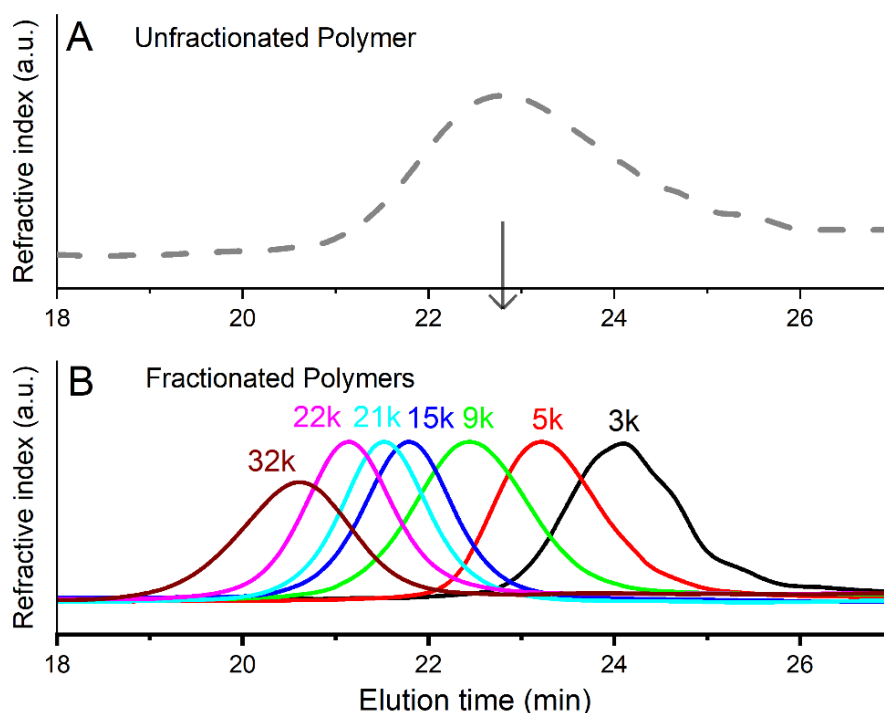
Figure 4.2. A: SEC trace of P(C$_8$EG$_{13}$) after the polymerization reaction. B: SEC traces of P(C$_8$EG$_{13}$) samples after fractionation; molecular weights corresponding to the sample names from Table 3 are shown above each curve.

Most of the polymerizations based on CDI were executed in a one-pot synthesis by first activating the dicarboxylic acid and then adding the PEG. Only the synthesis of P(C$_{20}$EG$_{1000}$) was carried out in a modified way. Because of the high MW of the PEG unit of about 45k, the concentration of reactive groups is about the same as the water concentration of a dry solvent. Therefore, the dicarboxylic acid was first activated with an excess of CDI and the dicarbonylimidazole intermediate product was isolated and purified prior to the polymerization with PEG. In addition, 1,8-diazabicyclo[5.4.0]undec-7-en (DBU) was added as a catalyst[36,37] in the polymerization step. The polymerization products exhibit a broad MWD by nature. Some of the raw products were fractionated in order to obtain polymers with different MW and narrower MWD. The fractionations were carried out either in a single solvent by exploiting the temperature dependent solubility of the polymer or by using a solvent/non-solvent pair. As a result, fractions of several grams were obtained, most of them having a MWD between 1.1 and 1.2. The details are described in the SI. Exemplarily, the SEC traces of the P(C$_8$EG$_{13}$) polymerization product

before fractionation and the fractionated samples are shown in Figure 4.2. The MW characterization of the samples fractionated in this way is listed in Table 4.3 (left).

All AAPs containing PEG units of 2k and higher exhibit high MWs. In this case, molecular weight fractionation is difficult due to the small MW dependence of the solubility. For this reason, these polymers were only fractionated in a simple approach by adding stepwise non-solvent to a diluted polymer solution and fractions with MWDs between 1.2 and 1.7 were obtained. The synthetic details are described in the SI. The MW characterization is listed in Table 4.3 (right)

Table 4.3. Left: SEC/LS characterization results of the fractionated AAPs; Right: SEC/LS characterization results for the AAPs containing PEG units of 2k and longer; x represents the number of hydrophobic/hydrophilic repeat units.

	M_n, g/mol	M_w/M_n	x		M_n, g/mol	M_w/M_n	x
$P(C_4EG_4)33k$	33,100	1.29	119.7	$P(C_{14}EG_{47})98k$	98,100	1.37	41.7
$P(C_4EG_4)21k$	20,800	1.13	75.2	$P(C_{14}EG_{47})41k$	41,400	1.17	17.6
$P(C_4EG_4)11k$	10,500	1.10	37.9	$P(C_{14}EG_{47})16k$	15,600	1.26	6.6
$P(C_4EG_4)4k$	4,140	1.08	14.9				
$P(C_4EG_4)2k$	2,070	1.05	7.4	$P(C_{14}EG_{103})174k$	174,000	1.40	36.3
$P(C_5EG_6)80k$	80,200	1.15	202.5	$P(C_{14}EG_{103})48k$	47,900	1.59	10.0
$P(C_5EG_6)40k$	39,500	1.10	99.7				
$P(C_5EG_6)26k$	25,500	1.15	64.4	$P(C_{20}EG_{47})113k$	113,000	1.32	46.4
$P(C_5EG_6)18k$	18,400	1.10	46.5	$P(C_{20}EG_{47})79k$	78,500	1.31	32.2
$P(C_5EG_6)12k$	11,800	1.10	29.8	$P(C_{20}EG_{47})32k$	31,900	1.48	13.1
$P(C_5EG_6)7k$	6,600	1.11	16.7				
$P(C_5EG_6)4k$	4,400	1.10	11.1	$P(C_{20}EG_{103})161k$	161,000	1.20	33.2
$P(C_5EG_6)2k$	2,400	1.07	6.1	$P(C_{20}EG_{103})81k$	81,400	1.30	16.8
$P(C_8EG_{13})33k$	32.600	1.22	44.2	$P(C_{20}EG_{103})49k$	49,300	1.20	10.2
$P(C_8EG_{13})22k$	22,100	1.18	29.9				
$P(C_8EG_{13})21k$	20,700	1.17	28.0	$P(C_{20}EG_{240})228k$	228,000	1.32	20.9
$P(C_8EG_{13})15k$	15,100	1.15	20.5				
$P(C_8EG_{13})9k$	8,790	1.16	11.9	$P(C_{20}EG_{1000})663k$	663,000	1.75	14.9
$P(C_8EG_{13})5k$	4,720	1.17	6.4	$P(C_{20}EG_{1000})168k$	168,000	1.51	3.8
$P(C_{10}EG_{22})65k$	65,100	1.19	55.7				
$P(C_{10}EG_{22})47k$	47,300	1.11	40.5				
$P(C_{10}EG_{22})35k$	34,900	1.07	29.9				
$P(C_{10}EG_{22})25k$	25,400	1.07	21.7				
$P(C_{10}EG_{22})13k$	13,300	1.15	11.4				

Hydrolytic stability of the AAPs

Ester bonds are susceptible to hydrolysis. In the case of polymers this can cause chain scission reactions and decomposition of the polymer structure. For this reason, the hydrolytic stability of narrowly distributed $P(C_8EG_{13})22k$ (see Table 4.3 left) was tested by taking samples of aqueous solutions after different times. The samples were freeze-dried and examined by SEC. The results

are shown in Figure 4.3. At room temperature the hydrolytic degradation is very slow. Even after 6 weeks the signal shape remained almost unchanged. The small shift to higher elution times might indicate a minimal degree of hydrolysis. On the contrary, the degradation process is visibly faster at 40 °C. At this temperature, the SEC examination revealed a small low MW tailing already after 2 weeks and a visibly reduced MW after 6 weeks. At 60 °C first signs of hydrolysis appear within the first week. After 6 weeks the refractive index signal vanished almost completely. These hydrolysis results show that the polymers are sufficiently stable in aqueous solution in the temperature and time range of our measurements. Only at high temperature is there a need to consider degradation.
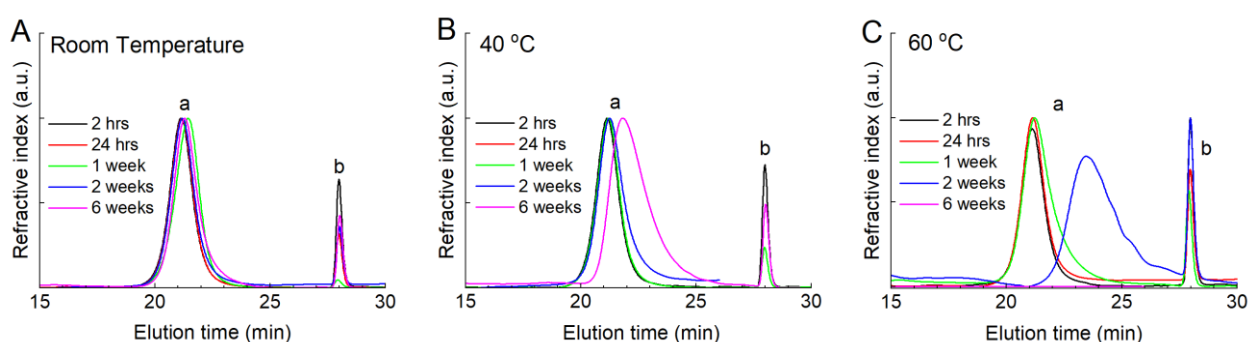

Figure 4.3. Hydrolytic stability tests in aqueous solution measured by SEC. P(C$_8$EG$_{13}$)22k of the concentration 10 mg/mL in water was used for the experiments. Signal "a" represents the polymer signal, sighnal "b" represents a flow rate marker. The experiments were performed at three different temperatures: A: Room temperature, B: 40 °C, C: 60 °C.

Solubility and thermal behavior of the polymers in water

The water solubility of the AAPs was first measured by screening experiments over a broad range of polymer compositions using the non-fractionated polymers listed in Table 4.2. The results for a polymer concentration of 10 mg/mL are collected in Figure 4.4, where the chain length of the dicarboxylic acid is plotted against the PEG ethoxylation degree. The results show that the polymers are only fully water-soluble if the PEG fraction dominates. However, they are not soluble over the whole temperature range but show a pronounced LCST behavior. With increasing ethoxylation degree and overall hydrophilicity of the polymers, the measured CPT moves to higher temperatures. Larger dicarboxylic acid units require increasingly longer PEG units in order to keep the polymers water-soluble. For C$_{14}$ an EG$_{47}$ unit (M$_n$ = 2,110 g/mol) is needed and in the case of C$_{20}$, EG$_{240}$ (M$_n$ = 10,600 g/mol) units are required to obtain at least solubility at low temperatures. Interestingly, the LCST behavior still exists for the highest PEG unit investigated in this work of EG$_{1000}$ (M$_n$ = 44,200 g/mol). Although the fraction of the

hydrophobic unit in P($C_{20}EG_{1000}$) is below 1 mass-%, the CPT of this material is 82°C. Pure PEG for comparison exhibits a LCST value above 100 °C.[38]
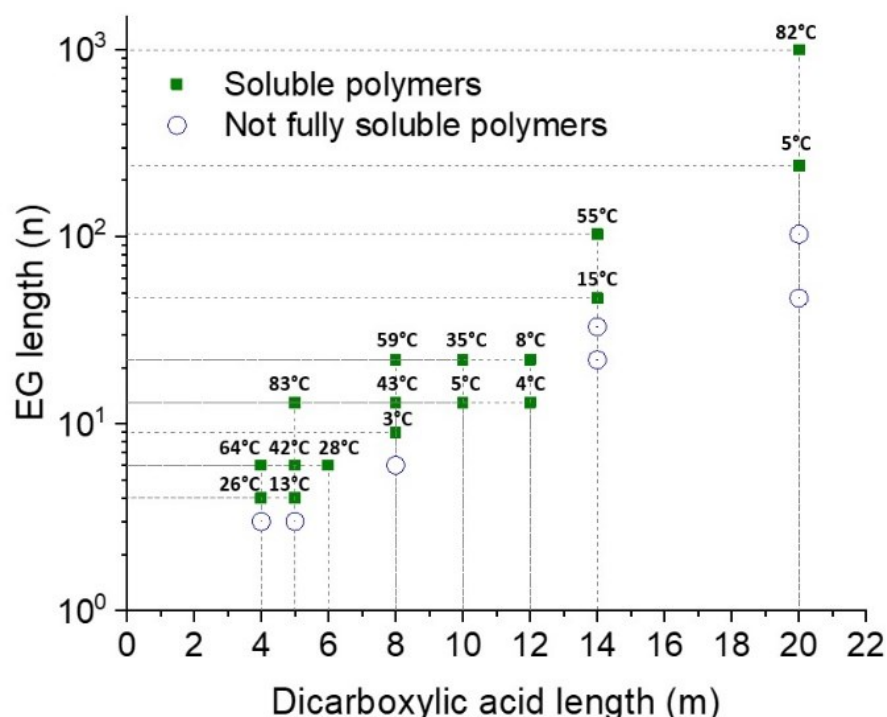

Figure 4.4. Illustration of solubilities and cloud points for different lengths of the hydrophobic and the hydrophilic units at a concentration of 10 mg/mL in water. For fully water-soluble polymers the CPT is indicated above the corresponding point.

The CPT depends strongly on the molecular weight and the concentration. This is shown exemplarily for P(C_4EG_4) with fractionated samples of different molecular weights (Table 4.3 left) in Figure 4.5A. At lower numbers of hydrophilic-hydrophobic repeat units there is a strong temperature dependence, which approaches almost constant at higher chain lengths. The same holds for the concentration dependence which was measured between 5 and 100 mg/mL. Similar behavior was observed previously for alternating amphiphilic copolymers.[6],[12],[33] For other polymer compositions we tested, the thermal behavior is qualitatively similar (see Figure 4.5B).

The thermal examination of the non-fractionated samples (Figure 4.4) was done with polymers of very different molecular weights (Table 4.2). As the thermal properties strongly depend on the molecular weight, the question arises, whether the CPTs for the different polymers are comparable. As these polymers were not fractionated they exhibit a broad MWD. As the CPTs were determined as the temperature of the turbidity onset, they correspond to the highest MW fractions, which get insoluble first (see Figure S4.1). Accordingly, for all the fractionated polymers

the CPT of the highest chain lengths are in good agreement with the values measured for the broadly distributed samples and therefore are close to the LCST values.
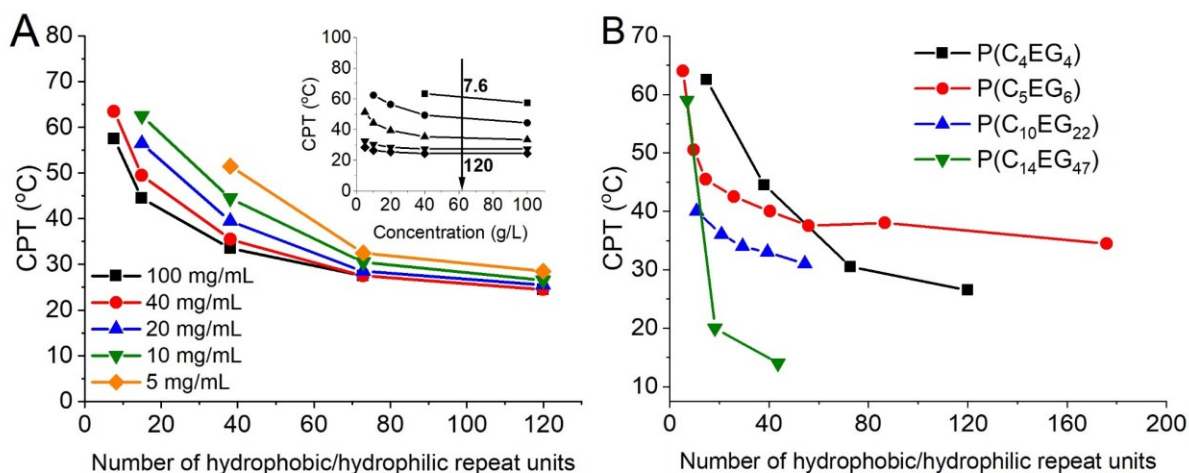

Figure 4.5. A: Dependence of the CPT on the number of hydrophobic/hydrophilic repeat units and concentration for P(C₄EG₄) polymer; insert: the same data presented as a phase diagram. The arrow indicates the increase of the number of hydrophobic/hydrophilic repeat units; B: Dependence of the CPT on the number of hydrophobic/hydrophilic repeat units for different polymer compositions at a concentration of 10 mg/mL.
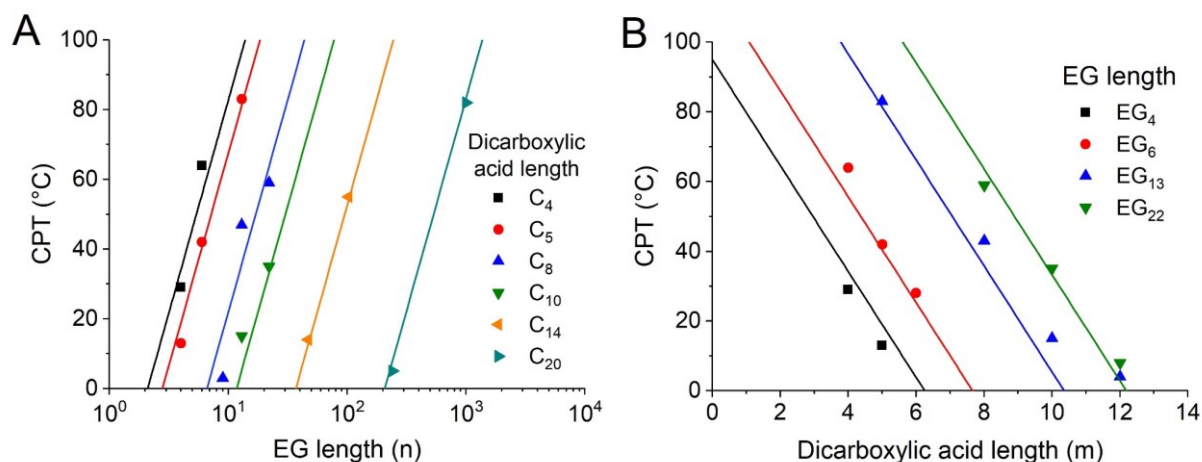
Figure 4.6. A: Dependence of the CPT on the EG unit length at fixed dicarboxylic acid length. Lines represent the fit results assuming the same slope for all the curves; B: Dependence of the CPT on the dicarboxylic acid length at fixed EG length. Lines are calculated from equation 3.1.

More details are illustrated in Figure 4.6, showing CPT as a function of the number of the EG length, and the dicarboxylic acid length. The dependence of the CPT on the EG length is logarithmic, whereas the dependence on the dicarboxylic acid length is stronger and shows a linear behavior (Figure 4.6). As a consequence, to obtain water-soluble polymers or to stay at the same LCST, the ratio of the EG and C numbers must be considerably increased with increasing the C number. From the data shown in Figure 4.6 the CPT can be calculated as a function of C_m

and EG_n. Assuming the same slope for all the dicarboxylic acid lengths (m) in Figure 4.6A, and a linear dependence of the intercept on m, we get the following equation for the CPT determination:

$$CPT = 53.0[\pm4.1] \cdot ln(n) - 15.2[\pm1.2] \cdot m + 21.6[\pm4.3] \qquad (4.1)$$

The lines in Figure 4.6B are calculated from this equation with fixed PEG lengths n. This empirical finding might be related to the Gibbs free energy of mixing.[39] In the Gibbs free energy the entropy of the polymer chain is described by a logarithmic contribution dependent on the chain length. In our case the entropic term is dominated by the EG unit length. The enthalpy contribution is proportional to the interaction between polymer and solvent. The interaction energy between the hydrophobic units and water is much larger compared to the other interactions in this system leading to the linear dependence on m.

It is interesting to notice that a very similar dependence of the CPT on the hydrophobic unit length was observed for the other methylene-PEG based amphiphilic polymers,[33] where the slope values were 15.01[±0.24] and 15.66[±0.31] for different polymer compositions. In summary, the AAP solubility in water strongly depends on the lengths of the hydrophilic and hydrophobic units, the composition as well as the MW and the concentration. With the knowledge of the compositional influence on the thermal behavior, the LCST properties of a polymer can be tuned basically between the freezing and the boiling point of water. The only limiting factor is the reduced long-term hydrolytic stability at high temperatures.

When the PEG units are not long enough to keep the polymers water-soluble, the polymers form micellar structures or macroscopic gels. A detailed structural description is given in the next section. The water adsorption of non-soluble polymers equipped with short hydrophilic units is small, e.g. 70% of the polymer weight for $P(C_8EG_6)$. However, the water uptake for polymers containing C_{14} and especially C_{20} hydrophobic units increases drastically due to the much longer PEG units. The maximum swelling degrees for the polymers equipped with C_{14} and C_{20} hydrophobic units are shown in Figure 4.7A. For these experiments, the polymer fractions with the highest MWs were used. The swelling degree is calculated as the ratio of the gel weight to the weight of the dry polymer. For polymers containing shorter PEG units, the water uptake is not so pronounced, however, the gels formed are mechanically fairly stable. More information is given in the SI (Figure. S4.3). With longer PEG units, the swelling degree increases strongly, reaching a value of 37 for $P(C_{20}EG_{240})228k$. Due to the high water content, the mechanical stability of this gel is poor, which makes it soft and mechanically unstable. The same behavior is

observed for the C_{14} polymers, which generally show a higher swelling degree than the C_{20} materials.

The gels always coexist with a soluble fraction. The amount of soluble polymer depends on the composition and the molecular weight (Figure 4.7B). The more the PEG units dominate and the lower the overall MW is, the higher is the soluble fraction. Generally, the molecular weight of the soluble polymer fraction is visibly lower than that of the starting material. This MW fractionation is demonstrated with the SEC analysis for P($C_{20}EG_{103}$)81k in the SI (Figure S5.2). More detailed information about the soluble fractions and the swelling degrees of all the examined polymers can be found in the SI (Table. S4.1).
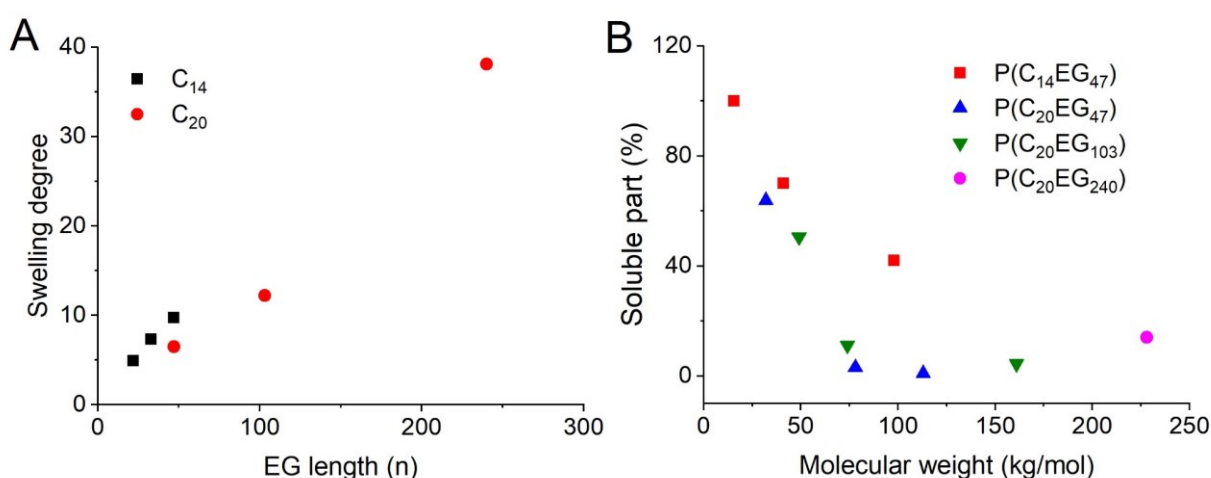
Figure 4.7. Gel forming AAPs. A: Dependence of the swelling degree on the EG length. The fractions with the highest molecular weights were used for each composition; B: Dependence of the soluble fraction on the composition and molecular weight.

Structural properties of the polymers in water

Soluble polymers

The alternating structure of the polymers and their LCST behavior raise the question of which structures such polymers can form in water. We performed a detailed study of the structural properties covering various polymer compositions, molecular weights and temperatures.

As a first step, the structure formation of AAPs in water was examined by dynamic light scattering (DLS). The concentration was always 5 mg/mL, which is below the overlap concentration for all the investigated polymers, and only the temperatures below the CPT were taken into account. For most of the examined AAP solutions, only a very small fraction of large-scale aggregates (>100 nm) was detected, which was also observed for pure PEG.[40] The main fraction was attributed to single polymer chains with a reasonable hydrodynamic radius as shown in Figure

4.8 for different compositions. The hydrodynamic radius of a polymer in solution generally depends on the polymer molecular weight $R_h \sim MW^\nu$ where ν is the Flory interaction parameter.[41] Polymer compositions $P(C_5EG_6)$ and $P(C_8EG_{13})$ are close to theta-solvent conditions with $\nu \approx 0.5$ and $P(C_4EG_4)$ shows good solvent behavior with $\nu \approx 0.6$ leading to more expanded coils. $P(C_{10}EG_{22})$ with $\nu \approx 0.4$ seems to be partially collapsed like in a bad solvent.

Another intriguing observation in Figure 4.8 is the clear change of the hydrodynamic size with the composition. The hydrodynamic radius increases with the unit sizes for the compositions $P(C_4EG_4)$, $P(C_5EG_6)$ and $P(C_8EG_{13})$. This might be related to an increased hydrophilic/hydrophobic unit ratio and, consequently, more "PEG-like" behavior. The $P(C_{10}EG_{22})$ polymer declines to smaller sizes than the trend suggests. This is an indication of the hydrocarbon units interaction which leads to the formation of loops (see Figure 4.15) with a smaller hydrodynamic radius as discussed in the explanations related to Figure 4.10.

In order to examine the change of ν on approaching the CPT, we studied the dependence of the solvent quality on temperature. In particular we analyzed the temperature dependence of ν for the $P(C_8EG_{13})$ (see Figure 4.8 insert). The maximum temperature is determined by the CPT of the largest molecular weight polymer so most of the polymers were well below the CPT. We found that there is no significant change in ν, respectively in the solvent quality, in the measured temperature range.
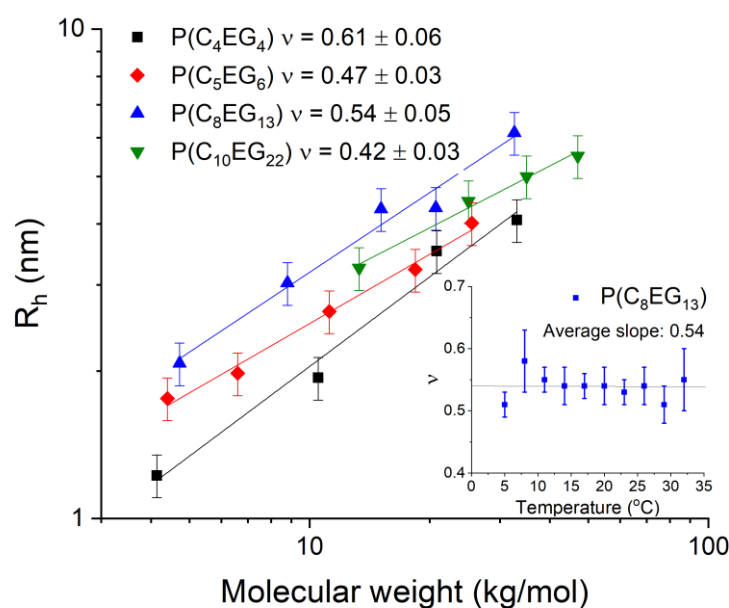

Figure 4.8. Dependence of the hydrodynamic radius (R_h) on the molecular weight for different polymer compositions at 25C. Solid lines represent the fits using $R_h \sim MW^\nu$. Insert: Dependence of the Flory parameter ν on temperature for the polymer composition $P(C_8EG_{13})$.

To examine the molecular structure of the polymers and the temperature behavior in more detail, we performed SANS measurements with an extended Q-range for polymers $P(C_8EG_{13})$ and $P(C_4EG_4)$ at several temperatures. Figure 4.9 shows SANS data for two molecular weights of $P(C_8EG_{13})$ from well below to well above the CPT. At low temperatures the scattering pattern indicates a single chain behavior well described by a Debye-like function at lower Q. The aggregation, as indicated by an increase of intensity at low Q, starts slightly below the measured CPT, (CPT = 41°C for 21 kg/mol, CPT = 60°C for 4.7 kg/mol). Extracting the radius of gyration R_g (see Figure 4.9B, inset) of the single chain component we observe first a slight drop in R_g at the CPT, which is followed by a significant drop above the measured CPT. This indicates the expected collapse of the single chain structure.
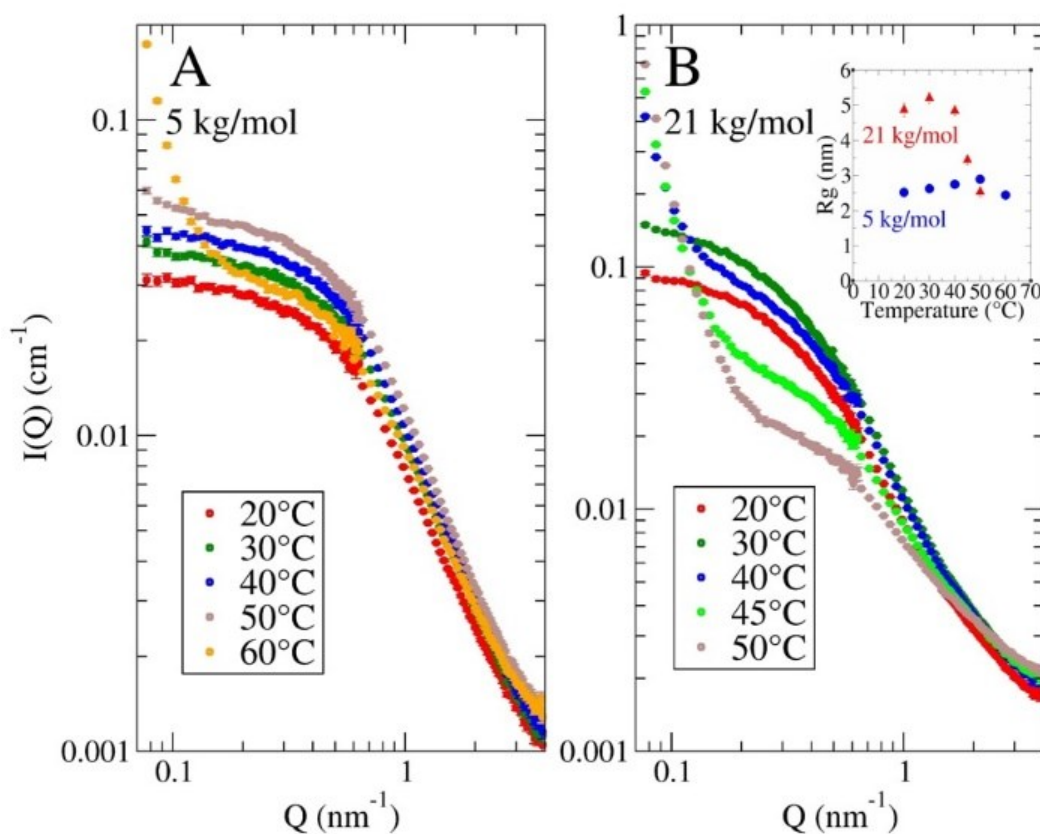
Figure 4.9. SANS data for the AAPs at different temperatures for a concentration of 10mg/mL in D_2O. A: $P(C_8EG_{13})5k$; B: $P(C_8EG_{13})21k$. The inset shows the temperature dependence of R_g for both AAPs. The values are obtained from fits with the wormlike-chain model complemented by a low Q power law contribution to describe the aggregation as described in the SI. The fits are shown in Figure S4.4.

Taking a closer look at the high Q behavior in a Kratky plot $I(Q)Q^2$ vs. Q demonstrates a quite complex structure on length scales of unit sizes that deviates from simple polymer behavior (Figure 4.10). The scattering pattern clearly deviates from a simple Gaussian polymer behavior. For a Gaussian polymer in a Kratky representation, a constant value for $I(Q)Q^2$ is expected, which

reflects a power law ~Q^{-2} for intermediate Q-values. Instead, we observe a remarkable structural peak around 1 nm^{-1} followed by a plateau-like behavior at intermediate Q in some cases and finally a linear increase at high Q. As presented in Figure 4.10A for low MWs of P(C$_4$EG$_4$) and P(C$_8$EG$_{13}$) we observe a continuous smooth increase to high Q, while for larger MW a plateau is observed. For the longest P(C$_4$EG$_4$) chains with MW of 33 kg/mol an additional peak is visible. The broken lines show a fit with a wormlike chain model.[42] The wormlike chain model considers a persistence length that describes the local stiffness of the chain. This leads to the linear increase at high Q which is independent of MW. The resulting persistence lengths for the lowest MW are in the range of 0.7 – 1 nm which is slightly larger than the value of 0.6 nm found for PEG. However, we cannot completely exclude that there is no influence of the loops which can affect the fit results. Figure 4.10B shows the temperature series from Figure 4.9A with the corresponding fits to the wormlike chain model. For lower temperatures we observe excellent agreement with the data, while for T=50°C a plateau comparable to high MW seems to evolve. The plateau value decreases for 60°C, indicating an increase of the segment length[43] above the transition temperature. For 50°C and 60°C the high Q slope is stronger increasing compared to low temperatures. Figure 4.10C shows a temperatures series for P(C$_8$EG$_{13}$) MW of 21k with a pronounced plateau. With increasing temperature the plateau is first rising with a clear peak, decreases above 30°C and vanishes on a lower level above 45˚C. While increasing intensity indicates reduced segment length, vice versa, the peak with the following plateau is characteristic for loops or branched structures.[43] We fitted correspondingly the most pronounced structure at T=30°C with a polymer ring model[44] including polydispersity as a proof of concept for the loops to describe the peak and the following plateau. From the fit an R$_g$ value of 3.9 nm was calculated and a polydispersity of 0.6 nm. Polymer models that include the loops and the wormlike chain behavior at higher Q are not available. We conclude that the plateau and corresponding peaks as a deviation from the wormlike chain model is due to loop formation of the polymer chain with itself due to attractive interaction between hydrophobic units (Figure 4.15). The loop formation depends on the attraction strength between the hydrophobic units but also on the ability of the polymer to bend. As the effect seems to be smaller for low MW we conclude that these chains are too short to form loops at least at lower temperatures. It should be mentioned that the high Q increase in a Kratky plot expected for polymer models with excluded volume (including polymer ring models) alone cannot explain the observed linear increase. Nevertheless excluded volume effects might partially contribute.

With increasing the hydrophobic unit length, a strong extension of the PEG units is required to make the polymers fully water-soluble (see Figure 4.4 and SI, Table S1). Even the polymers having very hydrophobic C_{14} or C_{20} units can be solubilized in combination with large enough PEG units as single chains. For example, the $P(C_{14}EG_{47})$ and $P(C_{20}EG_{240})$ are not fully soluble in water at room temperature whereas the $P(C_{14}EG_{103})$ and $P(C_{20}EG_{1000})$ solubilize completely.
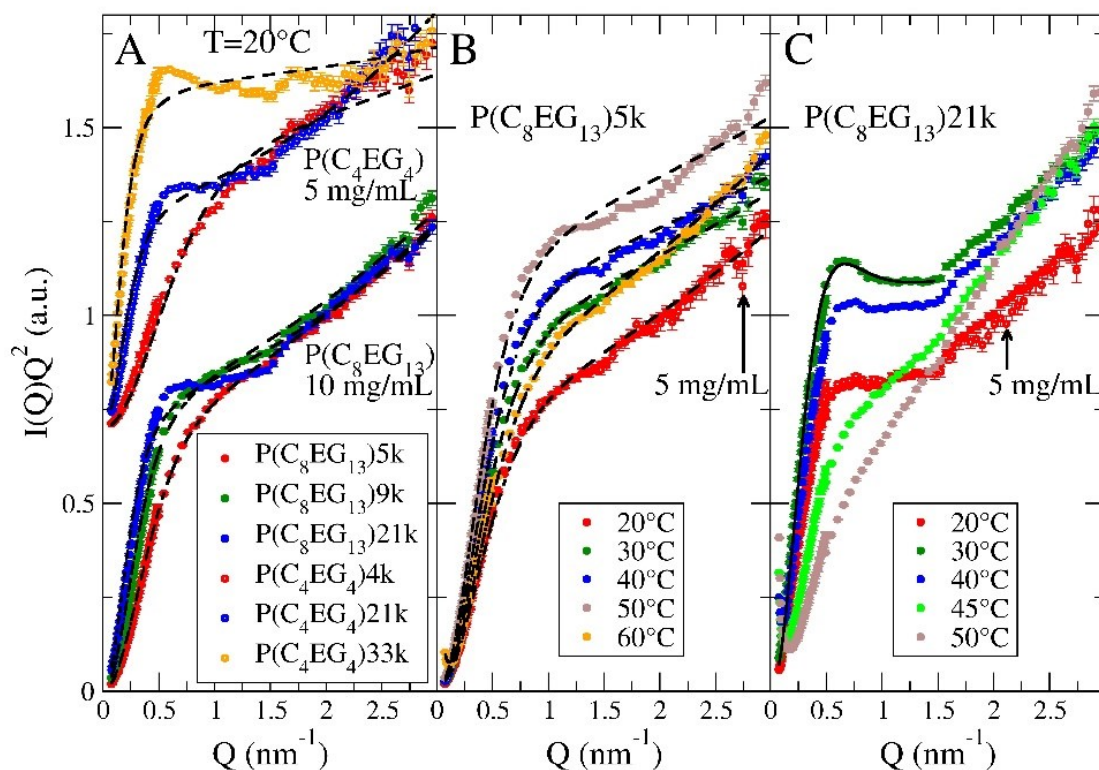
Figure 4.10 Kratky plots of the SANS data in D₂O at a concentration of 10 mg/mL and 5 mg/mL as indicated. A: Different molecular weights for the polymers P(C₄EG₄) and P(C₈EG₁₃) at 20˚C; B: P(C₈EG₁₃)5k at indicated temperatures.; C: P(C₈EG₁₃)21k at indicated temperatures. Solid lines represent fits with a polymer ring model. Broken lines represent in all plots fit results from a wormlike chain model.

Micellar structures

When we gradually decrease the EG length while still keeping the polymers water-soluble, the polymers tend to form more compact structures which depend both on the hydrophobic unit length and the hydrophilic/hydrophobic unit length ratio. Figure 4.11 represents the SAXS results for polymers with C_{14} and C_{20} hydrophobic units. $P(C_{14}EG_{103})48k$ represents an example of a water-soluble polymer which shows the behavior of worm-like chains (see Figure 4.11). Decreasing the hydrophilic unit by about half leads to the polymer $P(C_{14}EG_{47})$. Here only the

fraction with the MW=16 kg/mol is fully water soluble. This polymer shows more compact structures characterized by the intensity drop at high Q which is more pronounced above 0.8 nm^{-1} in the Kratky plot. In the intermediate Q-range the scattering curve indicates less compact structures compared to the spheres. Although the Guinier region is not reached for this sample, the overall structure size is larger than the size corresponding to the minimas at the Kratky plot. Therefore, we assume the formation of small, mostly hydrophobic regions connected to each other by PEG units and forming a partially collapsed polymer chain as a whole (see Figure 4.15). Increasing the hydrophobic length to C_{20} leads to the polymer P($C_{20}EG_{47}$). As all the P($C_{20}EG_{47}$) polymers are not fully water-soluble, the soluble part of the polymer P($C_{20}EG_{47}$)32k was taken for the measurement. The molecular weight of this polymer is 16 kg/mol and the concentration is 6 mg/mL. For this polymer the scattering pattern is more distinct than for the P($C_{14}EG_{47}$) polymers and can be well described by a micellar core-shell structure with an inhomogeneous core (see SI). Fitting with this model (black line) gives the core size of 3.7 nm and a diffuse shell with low contrast of about 5 nm thickness. In order to describe the scattering intensity at high Q, inhomogeneities must be included in the core. A core having the size of 3.7 nm cannot be built exclusively from the hydrophobic units only. We assume that it consists of the hydrophobic units, which form high contrast inhomogeneities and are embedded in a PEG-rich, low contrast matrix. We assume that the shell consists of a few PEG chains which are either loops or chain ends. However, an estimation of the shell density is difficult due to a low contrast of PEG to water for SAXS. As the radius of gyration of a respective 16 kg/mol PEG in water is about 6 nm,[45] we expect no more than a few polymer chains per micelle. A schematic view of the described micelle is presented in Figure 4.15. The soluble fractions of the polymers P($C_{20}EG_{103}$) and P($C_{20}EG_{240}$) also show the formation of micellar structures, similar to P($C_{20}EG_{47}$). A more precise model for the core is given later in the part about polymer gels. The soluble part of polymer P($C_{20}EG_{47}$)32k was additionally investigated by cryo-TEM, where micelles with a diameter of ~7 nm were observed (Figure 4.12). This is in good agreement with the micellar core size obtained from SAXS.
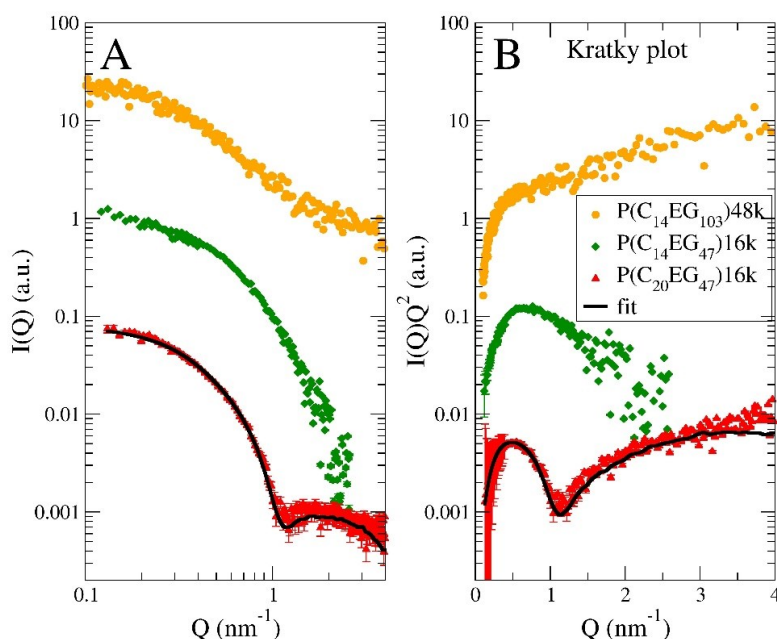
Figure 4.11. A: SAXS curves for the polymers with long hydrophilic and hydrophobic units. The polymers were measured in water at concentration of 10 mg/mL for P(C$_{14}$EG$_{103}$) and P(C$_{14}$EG$_{47}$), and 6 mg/mL for P(C$_{20}$EG$_{47}$). The intensity is scaled for convenience. The black lines show the fits with the core-shell model containing inhomogeneous cores. B: the same data are shown in a Kratky representation.
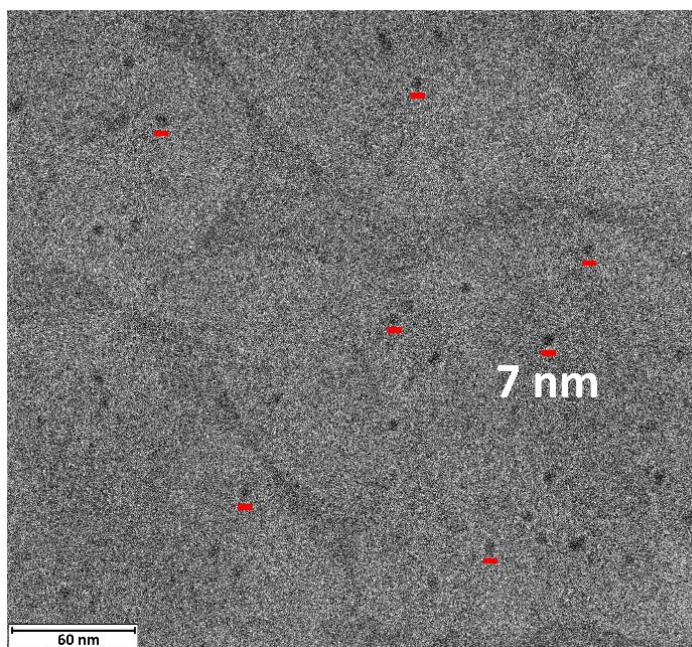
Figure 4.12. Cryo-TEM image of the polymer P(C$_{20}$EG$_{47}$)32k in water. The polymer was mixed with water in concentration 10 mg/mL and the soluble part having the MW of 16 kg/mol and co concentration of 6 mg/mL was taken for the investigation. The red lines have size of 7 nm and show some of the micelles. The micellar size coinsides with the core size calculated from SAXS.

Gels

We studied the gel samples of various polymer concentrations and compositions by SAXS. Figure 4.13 compares the experimental SAXS results for the polymers $P(C_{20}EG_{47})$, $P(C_{20}EG_{103})$ and $P(C_{20}EG_{240})$. The scattering results can be described on the basis of inhomogeneous core-shell particles as in the cases of micellar solutions. The resulting form factor $F(Q)$ was combined with the Percus-Yevick structure factor $S(Q)$ which describes the particle arrangement in a fluid order leading to structure factor peaks. For the $P(C_{20}EG_{47})113k$ polymers a size polydispersity of the cores had to be included to describe the scattering pattern. For the other polymers the shape anisotropy had to be included in order to suppress the higher order structure factor peaks. The increase at low Q can be described by domain scattering, which was added as a low-Q power law *G(Q)* (see SI for details). The final scattering function was calculated as

$$I(Q) = S(Q)F(Q) + G(Q) \tag{4.2}$$

In the dry state, the polymers are organized in a lamellar structure which is formed by the crystalline PEG and the hydrocarbon layers in between (see Figure S4.5). However, already at a water content of 50 wt% the core-shell structures evolve and can be fitted by the model described above (see Figure 4.13 A1 and A2). The two peaks of the experimental data correspond to the first structure factor peaks. At this concentration the distance between the cores is almost equal to the core size, so the structure factor has a very small value at low Q. The first order peak position is very similar to the position of the form-factor minima at about 1 nm^{-1}, which give very high and distinct peaks of $S(Q)F(Q)$. The second order peak indicates a more ordered structure and therefore is not satisfactorily described by the Percus-Yevick structure factor. Figure 4.13 A3 shows the 50 wt% gels varying the PEG length. The peak positions shift to lower Q with increasing PEG length due to a larger distance between the cores. Taking into account the same polymer concentration and the same intensity drop at the left side of the peaks we can conclude that the distance between the cores changes mainly due to the increased size of the cores. We explain the decrease of the scattering intensity with increasing PEG length by the reduced hydrocarbon unit fraction in the polymer chains and, consequently, the lower contrast of the cores. Figure 4.13 B1 and B2 show the gel model for the fully swollen $P(C_{20}EG_{47})113k$ polymer at a concentration of 15 wt%. Although the scattering pattern looks different compared to the 50 wt% sample, it can be described with the same model. At higher swelling, the volume fraction of the cores decreases which leads to a higher value of the S(Q) at low Q and the peaks shift to lower Q compared to the F(Q) minima. This results in a first order S(Q) peak overlapping with the

F(Q) shoulder and a well pronounced second order S(Q) peak. Figure 4.13 B3 again shows the polymers having different PEG lengths at a concentration of 15 wt%. The first order peak again shifts to lower Q as expected, and the second order peak vanishes for the polymers with longer PEG units. Figure 4.13 C1 and C2 show the gel model for the polymer $P(C_{20}EG_{103})161k$ at maximum swelling which corresponds to a polymer concentration of 8 wt%. The second order S(Q) peak also disappears. Increased shape anisotropy of the cores with increasing the PEG unit length leads to a suppression of all higher order peaks of the S(Q).[46] Figure 4.13 C3 shows the changes for increasing PEG length. The first order peak shows a shift and becomes less pronounced which is expected for low core volume fractions at high swelling. We notice that both, the core size and the structural arrangement of the cores are independent of the polymer MW. This is reasonable because in a macroscopic gel the polymer extension is larger than the core-core distance, allowing the polymer chain to interconnect cores.

In order to estimate the water content and the number of hydrophobic/hydrophilic repeat units inside a core we chose a model for the fully swollen $P(C_{20}EG_{47})113k$ gel (Figure 4.13 B1 and B2). The form factor gives a core radius of 3.3 nm and a core volume fraction of 35%. Taking into account the polymer concentration of 15% at the maximum swelling degree we find that the concentration of the polymer in the core is 43%. This allows us to estimate the number of hydrophobic/hydrophilic units per core. Considering the volume of such a unit of 3.3 nm^3, we calculated 19.6 hydrophobic/hydrophilic units per core. For the polymer $P(C_{20}EG_{47})113k$ which makes the strongest gel, this value corresponds to 0.41 polymer chains. Therefore, the cores must be strongly interconnected by the polymer chains, which explains the high mechanical stability we observe for these gels (see Figure S4.3).

We also found that the polymer $P(C_{20}EG_{47})113k$ can form crystalline structures at high concentration (Figure 4.14). At some measurements at 50 wt% concentration we observed a highly ordered crystalline structure with peaks up to 4th order (bcc or simple cubic) which melts at higher temperatures.
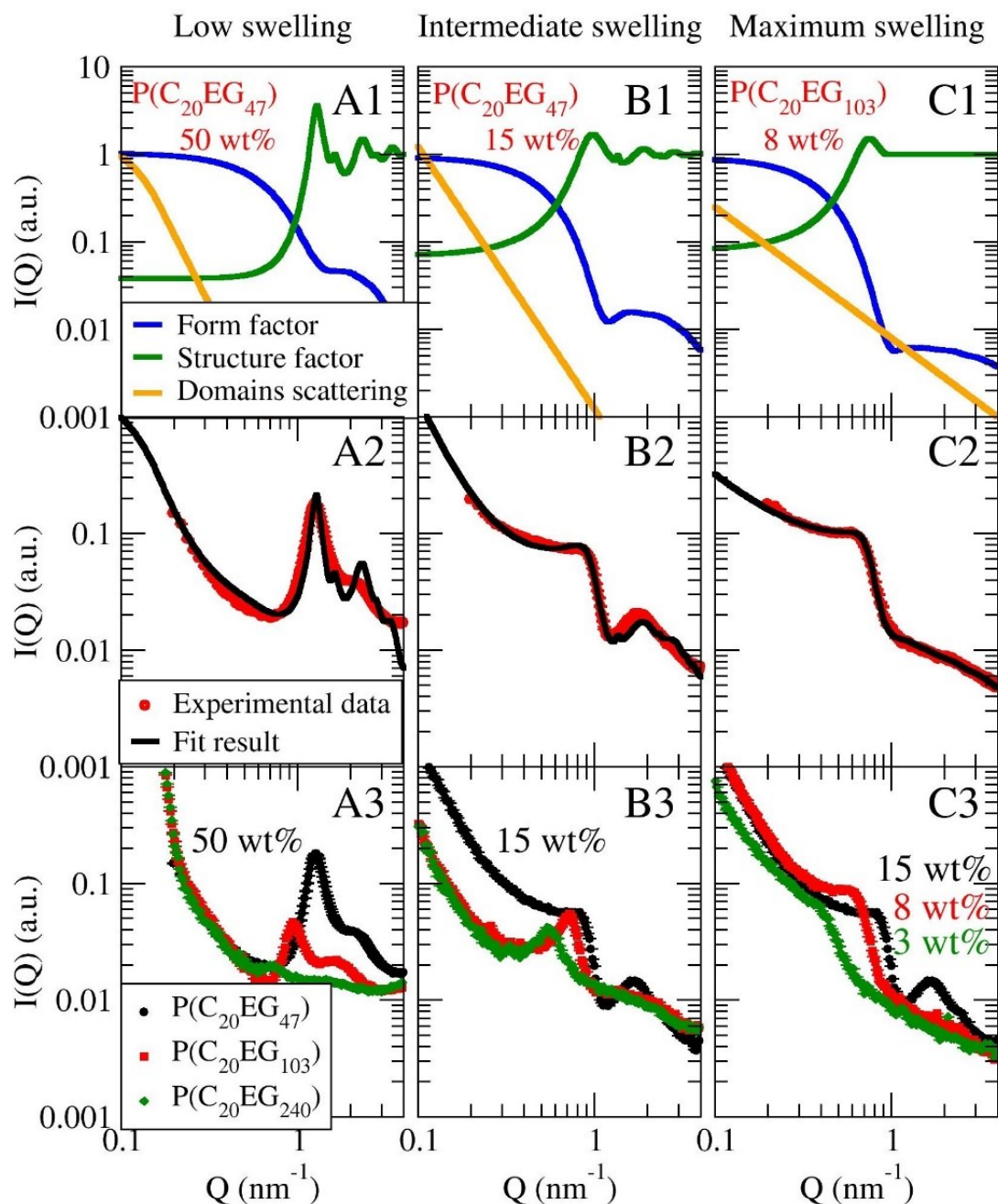
Figure 4.13. SAXS curves and gel models for three different polymer concentrations and compositions. A1, A2: model for the polymer P(C$_{20}$EG$_{47}$)113k of the concentration 50 wt%. A3: Comparison of the SAXS curves for the polymers with different EG lengths at 50 wt% concentration. B1, B2: model for the polymer P(C$_{20}$EG$_{47}$)113k at 15 wt% concentration. B3: Comparison of the SAXS curves for the polymers with different EG lengths at 15 wt% concentration. C1, C2: model for the polymer P(C$_{20}$EG$_{103}$)161k at 8 wt% concentration. C3: Comparison of the SAXS curves for the polymers with different EG lengths at 8 wt% concentration (maximum swelling).
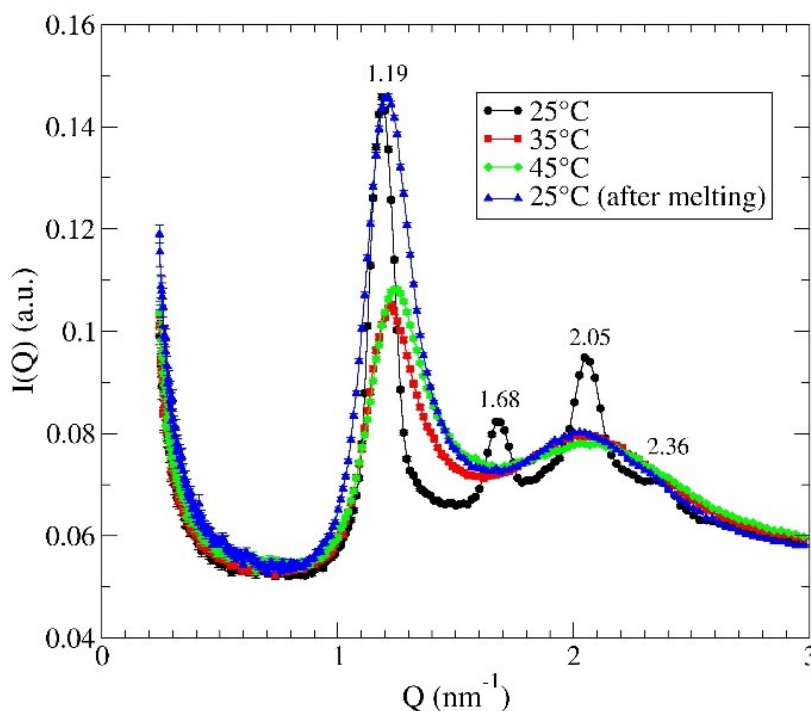
Figure 4.14. SAXS curves for the polymer P(C$_{20}$EG$_{47}$)113k at different temperatures for the polymer concentration of 50 wt%. Peak positions for the temperature of 25°C are indicated. The sample was recooled to 25°C after melting.

Discussion of the structural properties

Exceeding a certain threshold for the EG unit length, the AAPs solubilize as free chains with a slightly larger persistence length than that for PEG.[47] Intrachain loop formation is observed for these polymers (see Figure 4.15). We suppose that the ability of AAPs to form at least metastable loops is attributed to attractive interactions between the hydrophobic units. As AAPs may form inner loops between any of the hydrophobic units of a chain, the probability for loop formation increases with increasing polymer molecular weight. The opposite effect of the molecular weight was found for telechelic polymers,[48] where micellar loop formation is related to end-end loops which is less probable for longer chains. Due to loop formation, the AAPs form less extended coils than expected for a Gaussian chain. An increased loop formation with increasing temperature close to the transition point shows that the phase transition of the AAPs is a continuous process which starts before the chain collapse occurs.

Increasing the length of the hydrophobic unit leads to stronger hydrophobic interactions and requires a dramatic increase of the EG unit to keep the polymers water-soluble. When the EG unit is not long enough, the hydrophobic interactions provoke the formation of micelles containing multiple hydrophobic contacts. As a result, the micellar core consists of several small hydrophobic regions incorporated in a PEG-rich matrix, containing only a small amount of water

(Figure 4.15). In order to understand such behavior, we compare our micelles with telechelic polymers studies by Alami et. al.[48] In this work PEGs were used which contain hydrocarbon units at the chain ends. The ability to form loops, which leads to the formation of micelles, is related to the change in free energy which can be estimated[48] as

$$\Delta G \approx 1.5 RT ln(n) - 0.4 RT m \qquad (4.3)$$

where n is the number of EG monomers in the hydrophilic unit and m is the number of CH_2 groups at a chain end. The first term is attributed to the entropy loss of the PEG chains due to the loop formation, and the second term describes the gain in free energy when the hydrophobic tails associate. This implies that, at short alkyl chains and long enough PEG the entropy term dominates which leads to free polymer chains. At longer alkyl chains and/or shorter PEG, when the second term dominates, strong hydrophobic interactions lead to the formation of stable flower-like micelles. It was reported[49] that in the intermediate state, when the entropy term dominates but the formation of loops still has a reasonable probability, the micelle formation takes place but not all of the hydrophobic chain ends are located in the micellar core.

The AAP $P(C_{20}EG_{47})$ forming the most defined micelles can be described as a sequence of telechelic $C_{10}EG_{47}C_{10}$ units. ΔG for this polymer has a positive value, which explains why the AAP micelles have no single hydrophobic core. Furthermore, water molecules are highly polar. Their dipole moment is 1.84 debye, compared to a value of 1.04 debye for a monomer unit in PEG.[50] This makes the observed PEG-rich core structure of the AAP micelles more favorable compared to the structure where the hydrophobic regions are embedded in a water-rich environment.

Similar structures were found in simulation studies. Depending on the segment lengths, their ratio, the solvent quality as well as other criteria, a large variety of micellar structures were found,[17,18,51] among them multi-core micelles, where the cores are surrounded by a rather dense shell of the hydrophilic polymer. In experimental studies, such structures have not been reported so far, to our knowledge. This also applies to AAPs having polymeric hydrophobic and hydrophilic units. The closest examples to the structure we found contain two complex forming polymers.[52] In this case the structure formation is driven by positive interactions between the different polymers, whereas in our case the structure formation is the result of the lesser incompatibility between the hydrophilic and hydrophobic units compared to the incompatibility between the hydrophobic units and water. In a study where alternating amphiphilic PEO/PPO multiblock copolymers were used, which contain polymeric hydrophobic PPO blocks,[14] the multiblock copolymers form flower-like structures under loop formation of the PEO blocks. This

is understandable as the hydrophobic interactions are stronger and the spacial restrictions for loop formation are smaller than in the case of low MW hydrophobic units.
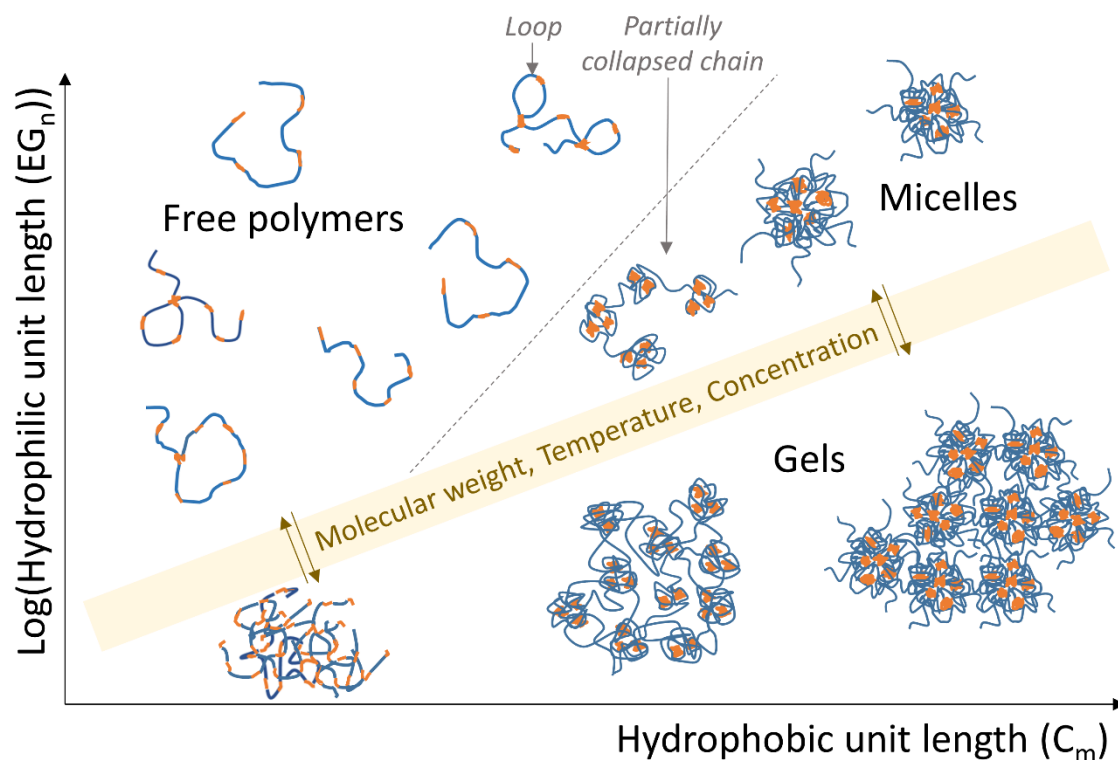
Figure 4.15. Diagram representing structures of the AAP in water depending on the hydrophobic/hydrophilic unit lengths.

It is interesting to observe that the gels formed by the AAPs with long hydrophobic and hydrophilic units have the same structural features as in the micelles (Figure 4.15). Moreover, these structures are independent of the polymer molecular weight. Our calculations show that there are about 20 hydrophobic/hydrophilic repeat units per one core. Especially for the polymers having a large number of hydrophobic/hydrophilic repeat units, one chain is located in more than one micellar core, increasing the number of crosslinks. The crosslinks between the cores are much stronger than for the telechelic polymers, where only the chain ends must be pulled out of the core. This leads to a much higher mechanical stability and elasticity of the AAP gels compared to the gels made by telechelic polymers. The details are given in the SI. The gels always coexist with the micelles or free polymers of smaller molecular weight. In the case of free micelles the number of polymer chains per core is about 2.5, which allows them to stay single. A qualitatively similar phase diagram for the AAPs was reported in the simulation work by Hugouvieux V. et al.[53]

4.3   Conclusions

The synthesis of polyesters from dicarboxylic acids and PEG monomers represents a simple procedure to gain access to AAPs, making a broad range of hydrophilic and hydrophobic unit lengths and compositions accessible. The variation of the lengths of the hydrophilic and hydrophobic blocks allows tuning the LCST between 3 and 83°C. For large PEG-units the copolymers are soluble as single chains. For longer hydrophobic units, i.e. C_{14} and C_{20}, micelle and gel formation is observed. The formation of a pure alkyl micellar core is hindered by the conformational restrictions resulting from the alternating arrangement of the hydrophilic and hydrophobic units. As a consequence, the micellar cores consist of several small hydrophobic regions embedded in a PEG-rich and water-poor matrix. The micellar cores represent the nodes of the network structure of the macroscopic gels. The strongly swollen gels show a high degree of mechanical stability. We also found that the polymer forms lyotropic liquid crystals as demonstrated for $P(C_{20}EG_{47})113k$ at 50 wt% concentration. We observe a highly ordered crystalline structure with peaks up to 4th order (bcc or simple cubic) which melts at higher temperatures). This makes the material interesting for rheological experiments as this allows quenching of e.g. shear oriented structures. The study demonstrates how the structure of alternating amphiphilic copolymers can be systematically varied to adjust the hydrophilic/hydrophobic balance and thus the solution and self-assembly properties. Copolymers with a larger hydrophobic fraction are expected to be compatible with hydrophobic environments such as lipid membranes, which can be utilized in biological applications.[54]

4.4   Acknowledgments

4.5   Materials and methods

Polymer synthesis

The AAPs were synthesized as polyesters using dicarboxylic acids and polyethylene glycols. The products were obtained by direct esterification of the diacids and diols under the removal of water or by activating the diacid first with the help of 1,1'-carbonyldiimidazole (CDI). Some of the polymers were fractionated to obtain samples with narrow molecular weight distributions. All synthetic procedures are described in detail in the Supplementary Information (SI).

Polymer Characterization

Size-exclusion chromatography (SEC) experiments were carried out using an Agilent 1260 Infinity SEC instrument equipped with a Wyatt DAWN Heleos II light scattering (LS) detector, an Optilab T-rex differential refractive index (RI) detector and with three PolyPore columns at 50 °C. The solvent was a mixture of THF, DMA, and acetic acid (84:15:1 by volume) at a flow rate of 1 mL/min. The dn/dc values were calculated using the ASTRA software (Wyatt) from the RI signal intensities using the calibrated RI detector and known sample concentrations. Molecular weights and molecular weight distributions were also calculated using the ASTRA software. NMR spectra were collected on a Bruker Avance III 600 MHz spectrometer equipped with a Prodigy cryoprobe with a 5 mm PFGAutoX DB probe. Samples were measured at 295 K. The molecular weights of the PEG units were determined from ^{1}H-NMR spectra in pyridine-d_5. M_n values were calculated from the signal intensities of the methylene units next to the alcoholic end groups at 3.95 ppm and the rest of the PEG signals between 3.5 and 3.7 ppm.[35] The polyesters products were also characterized by 1H-NMR spectroscopy in pyridine-d_5.

Cloud point temperature (CPT) determination

Non-fractionated polymers were dissolved in deionized water at a concentration of 10 mg/mL. Samples of about 5 mL were gradually heated in a thermostated shaker with a step of 1°C and visually inspected. The temperature where turbidity appeared was taken as the CPT. For the fractionated samples the CPT was measured by dynamic light scattering (DLS). The polymers were dissolved in deionized water in a concentration of 10 mg/mL and analyzed in a wide temperature range with a step of 1°C. CPT was detected as the appearance of large aggregates correlated to a strong increase in scattered intensity appearing over ~1 °C. All the DLS measurements were performed with a Malvern Zetasizer Nano ZS apparatus with a backscattering set up (θ = 173°) and a He-Ne laser of the wavelength λ = 633 nm.

Hydrodynamic radius (R_H) determination

The R_H of the AAPs was determined using the Malvern Zetasizer Nano ZS instrument described above. The R_H value was obtained by analyzing autocorrelation functions using a built-in algorithm of the instrument.

Small Angle Neutron Scattering (SANS)

SANS experiments were performed at the instrument KWS-1[55,56] operated by the Jülich Centre for Neutron Science (JCNS) at Heinz Meier-Leibnitz Zentrum (MLZ) in Garching, Germany. The incident neutron wavelength λ was 0.5 nm (Δλ/λ = 10%). The data were obtained from two different detector and collimation distances: the detector distances of 1.5 m with a collimation distance of 4 m and 8 m with a collimation distance of 8 m. The resulting Q-range was 0.06 – 4 nm^{-1}. Here Q is the magnitude of the scattering wave vector defined as $Q = (\frac{4\pi}{\lambda})\sin(\theta)$, where 2θ is the angle between the incident and scattered beam. The polymers were dissolved in D_2O at a concentration of 5 or 10 mg/mL and measured in quartz cells with a beam path of 1 mm. The temperature was controlled by a thermostat. The data presented here were converted to an absolute intensity unit of cm^{-1} taking into account the sample thickness, transmission, the scattering from a standard sample and the background from electronic noise, the solvent and the quartz cell. Data reduction was done using the QtiKWS software[57] and data analysis has been done using the Python-based project Jscatter.[58]

Small angle X-ray Scattering (SAXS)

SAXS experiments were performed the Jülich Centre for Neutron Science (JCNS) at Forschungszentrum Jülich, Germany. The instruments "Ganesha-Air" from SAXSLAB/XENOCS and Gallium Anode Low-Angle X-ray Instrument (GALAXI)[59] were used. The X-ray source of the laboratory-based "Ganesha-Air" system is a D2-MetalJet (Excillum) with a liquid metal anode operating at 70 kV and 3.57 mA with Ga– Kα radiation (wavelength λ = 0.13414 nm). The beam is further focused with a focal length of 55 cm, using specially made X-ray optics (Xenocs) to provide a very narrow and intense beam at the sample position. Two pairs of scatterless slits are used to adjust the beam size depending on the detector distance. The data were acquired with a position-sensitive detector (PILATUS 300 K, Dectris). After calibration with silver behenate, the distance from the sample to the detector was set to 950 and 350 mm resulting in a Q-range 0.13 – 6 nm^{-1}. The GALAXI X-ray source is a liquid anode of a GaInSn alloy operating at 70 keV with Ga– Kα radiation (wavelength λ = 0.134 nm). Two four-segment slits which are separated by 4 m distance collimate the beam and confine the size to about 0.7 × 0.7 mm^2. A third slit reduces the

scattering from the edges of the second one. A sample-to-detector distance of 1285 mm calibrated using Bragg reflections from silver behenate resulting in a Q-range of 0.09–4 nm^{-1} was used. All samples were sealed in glass capillaries of 2 mm inner diameter. Data analysis was done using the Python-based project Jscatter.[58]

4.6 Supporting information

Cloud point temperatures for the AAPs with broad MW distribution

As the CPTs were determined as the temperature of the turbidity onset, they correspond to the highest MW fractions, which get insoluble first. This is demonstrated in the following experiment. A sample of $P(C_8EG_{13})$ was heated at a concentration of 10 mg/mL to 44 °C, one degree above its CPT. At this temperature the turbid mixture was centrifuged to separate the precipitated material. SEC traces of the precipitate and the still soluble polymer are shown in Figure S4.1. The precipitate corresponds to 3% of the overall sample and exhibits a M_n of 19,700 kg/mol compared to M_n = 6,790 kg/mol for the starting material.
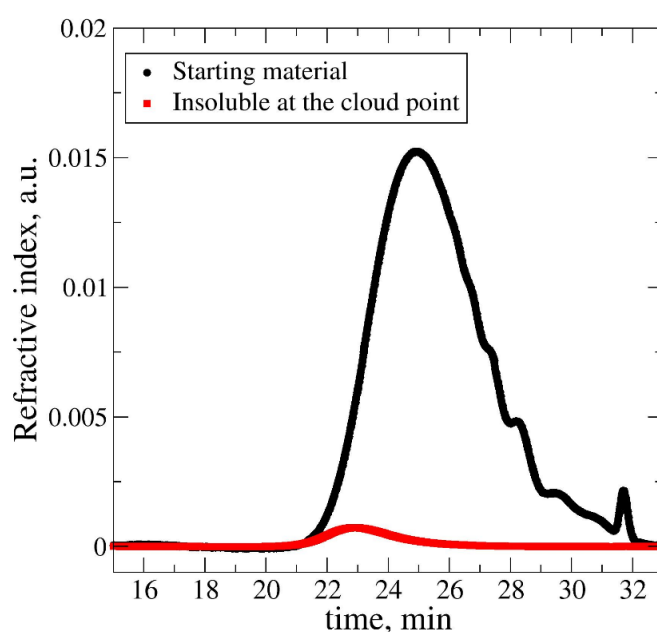
Figure S4.1. SEC traces of the polymer $P(C_8EG_{13})$. Black: starting material; red: Precipitated fraction produced at the cloud point. The refractive index signals are normalized by the weight fractions of starting and precipitated polymer.

Soluble polymer fractions in gels.

All the samples for the following experiments (Figure S4.1 and Table S4.1) were prepared by mixing 100-200 mg of polymer with water in the mass ratio 1:100. The mixtures were stirring during 4 days at 5 °C and for 2 hours at room temperature afterwards. Than the precipitated and soluble fractions were separated, the weight of the fully swollen gel was measured and both fractions were separately freeze dried. The swelling degree was determined as the mass of the fully swollen gel divided by the mass of the dry gel fraction.
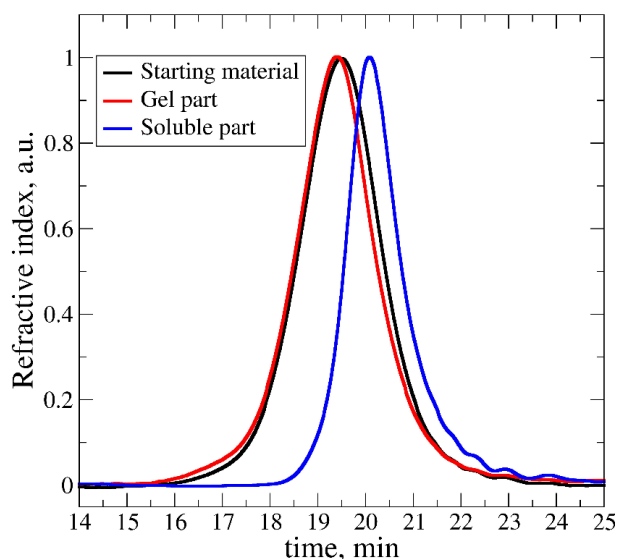
Figure S4.2. SEC traces of the polymer P(C$_{20}$EG$_{103}$)81k, showing that the soluble part in the phase separated material always have smaller molecular weight compared to the starting material, and the gel phase – the higher molecular weight. The mass ratio of soluble and insoluble fractions for this material was 11:89 (Table S6). M$_n$ of the soluble fraction obtained from LS trace was 53.0 kg/mol and of the gel fraction 88.5 kg/mol.

Table S4.1. Solubility and swelling degree for different polymer compositions and molecular weight.

Polymer structure	M$_n$, kg/mol	CPT, °C	soluble fraction	gel fraction	swelling degree
P(C$_8$EG$_6$)	17.9	<0	2.4%	97.6%	1.7
	98.1	14	42.0%	58.0%	8.7
P(C$_{14}$EG$_{47}$)	41.4	20	70.0%	30.0%	9.7
	15.6	59	100.0%		
P(C$_{14}$EG$_{103}$)	174.0	55	100.0%		
	47.9	72	100.0%		
	113.0	<0	0.9%	99.1%	6.5
P(C$_{20}$EG$_{47}$)	78.5	<0	3.1%	96.9%	7.7
	31.9	<0	63.8%	36.2%	5.4
	161.0	<0	4.4%	95.6%	12.2
P(C$_{20}$EG$_{103}$)	81.4	<0	11.1%	88.9%	13.0
	49	<0	50.5%	49.5%	13.8
P(C$_{20}$EG$_{240}$)	228.0	~5°C	14.0%	86.0%	38.1
P(C$_{20}$EG$_{1000}$)	663.0	82	100.0%		

Shape stability of the AAP gels

With increasing the hydrocarbon chain length or decreasing the PEG length the gel becomes

more mechanically stable. In order to demonstrate the gel stability, we tested the fully swollen gel of polymer P(C$_{20}$EG$_{47}$)113k (Figure S3.3). The cylindrical shape was obtained by centrifugation inside a Teflon mold. The piece of gel was kept in a closed container at 100 % humidity to avoid drying of the polymer.
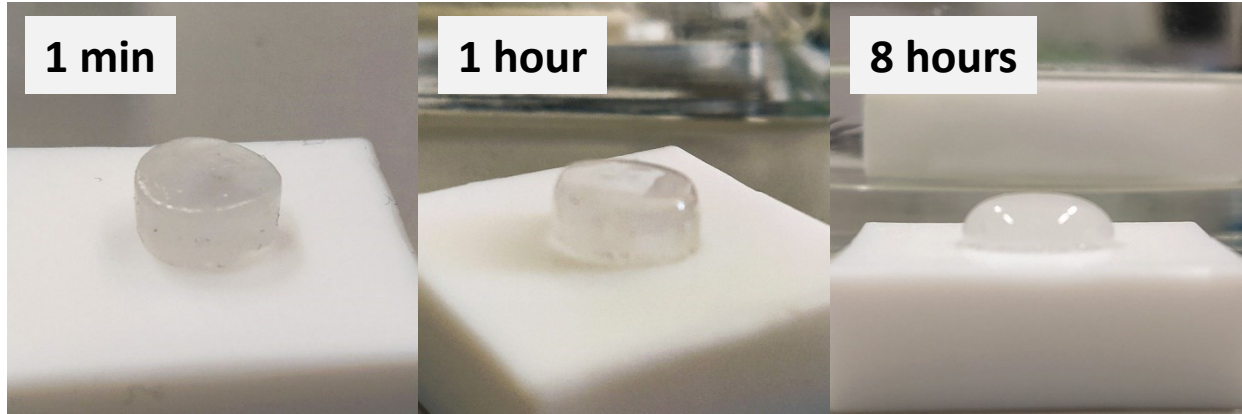
Figure S4.3. Shape stability of the fully swollen gel of P(C$_{20}$EG$_{47}$)113k corresponding to a concentration of 15 wt%.

Models used to describe the scattering data

Ring polymer

The ring polymer form factor is according to Hammouda[44]

$$F(q) = s\int_0^1 ds(1-s)\, e^{-q^2 a^2 N^{2\nu} s^{2\nu}(1-s^{2\nu})/6}$$

With segment length a and number of segment N in the ring.

Wormlike chain

The wormlike chain model for a chain with N segments of segment length a is described by Kholodenko as[42]

$$S_{wc}(Q) = 2/x[I_1(x) - 1/xI_2(x)] \quad \text{with} \quad x = 3N/2a \quad \text{and} \quad I_n = \int_0^x z^{n-1}(z)$$

for

$$Q \leq \frac{3}{2a}: f(z) = \frac{1}{E}\frac{\sinh(Ez)}{\sinh(z)} \quad \text{with } E^2 = 1 - \left(\frac{2}{3}aQ\right)^2$$

$$Q > \frac{3}{2a}: f(z) = \frac{1}{\bar{E}}\frac{\sinh(\bar{E}z)}{\sinh(z)} \quad \text{with } \bar{E}^2 = \left(\frac{2}{3}aQ\right)^2 - 1$$

Characteristic is a linear decrease at high Q representing the linear character of segments on length scales smaller than the segment length.

The corresponding radius of gyration R_g is[60]

$$R_g^2 = \frac{aN}{6}(1 - \frac{3a}{2N} + \frac{3a^2}{2N^2} - \frac{3a^3}{4N^3}(1 - e^{-2N/a}))$$

The model is be complemented by an additional power law $S_p(Q) = AQ^{-d}$ to represent the additional scattering at lower Q caused by larger aggregates described by the Porod exponent d.

d ranges from $\frac{5}{3}$ for polymer chains with excluded volume effects over 2 for Gausisan chains to 2-4 for mass fractals or surface fractals[61]. The composed model accounting for wormlike chains and possoble aggregates results in

$$S(Q) = S_{wc}(Q) + S_p(Q)$$

Core shell particle with inhomogeneous core

The model describes a spherical core-shell particle with the core filled with small random positioned particles as drops or Gaussian coils to approximate inhomogeneities in the core. If the added drop volume extends to the outside of the core this is not cut to represent shape inhomogeneities/surface roughness.

The model consists of 3 scattering amplitudes $F_a(q)$ for core $F_{a,core}(q)$, shell $F_{a,shell}(q)$ and drops $F_{a,drop}(q)$ with core and shell centered at the origin r=0 and the drops at random position r_i inside of the core ($|r_i| < R_{core}$). The scattering amplitude of the inhomogeneous core shell particle is

$$F_{a,inhomCS}(q) = F_{a,core}(q, R_{core}, \rho_c) + F_{a,shell}(q, R_{core} + d, \rho_s) + \sum_{i=1}^{N} e^{iqr_i} F_{a,drop}(q, R_d, \rho_d)$$

and the form factor $F_{inhomCS}(Q)$ is

$$F_{inhomCS}(q) = F_{a,inhomCS}(q) \cdot F_{a,inhomCS}^*(q)$$

with * for complex conjugation. R are respective radii, d is the shell thickness. ρ is the respective scattering length density difference to the solvent (contrast) for shell and core and the contrast to the core for the drops. Respective scattering amplitudes are classical sphere and shell scattering amplitudes for core and shell as[62]

$$F_{a,sphere}(q, R, \rho) = 4\pi\rho^2 V^2 \left[\frac{3(\sin(qR) - qR\cos(qR))}{q^3 R^3}\right]$$

$$F_{a,shell}(q, R, d, \rho) = F_{a,sphere}(q, R + d, \rho) - F_{a,sphere}(q, R, \rho)$$

or scattering amplitudes of a Gaussian coil with radius of gyration R_g according to Hammouda for the drops[63]

$$F_a(q, R_g, \rho) = \rho^2 V_{chain}^2 (1 - e^{-x})/x \text{ with } x = q^2 R_g^2$$

The inhomogeneous core shell form factor is implemented in Jscatter for drops as Gaussian coils, Gaussian function and spherical drops[58]. It should be noted that the drops might be an ordered lattice resulting in high q peaks or disordered to represent irregular inhomogenities. If the q range covers only the Guinier region of small drops the model represents undefinded inhomogenities covering the high q form factor structure of the larger core-shell particle.

Any polydispersity as e.g. core size polydispersity can be accounted for by integration over a respective distribution varying the repective parameter.

Gel Model

Our gel like structures are described by

$$I(Q) = S(Q)F(Q) + G(Q)$$

with the structure factor S(Q) as the classical Percus-Yevick structure factor of hard core particles as an approximation[64]. The form factor is the above described inhomogeneous particle. The scattering of domains or large scale inhomogeneities is described by a power law function $G(q) = Aq^{-\alpha}$ with $2 < \alpha < 4$. In the limit of flat domain interfaces one finds $\alpha = 4$ for Porod scaattering while fractal domain surfaces or fractal aggregates show smaller exponents.

The structure factor is influenced by particle size polydispersity and shape anisotropy which can be taken into account by the anisotropy factor $\beta(Q)$ as described by Kotlarchyk[46] with

$$\beta(Q) = \frac{|\langle F(Q) \rangle|^2}{\langle |F(Q)|^2 \rangle}$$

and

$$S_\beta(Q) = 1 + \beta(Q)(S(Q) - 1)$$

The factor $\beta(Q)$ is calculated within the form factor calculation.

Fit of the SANS data
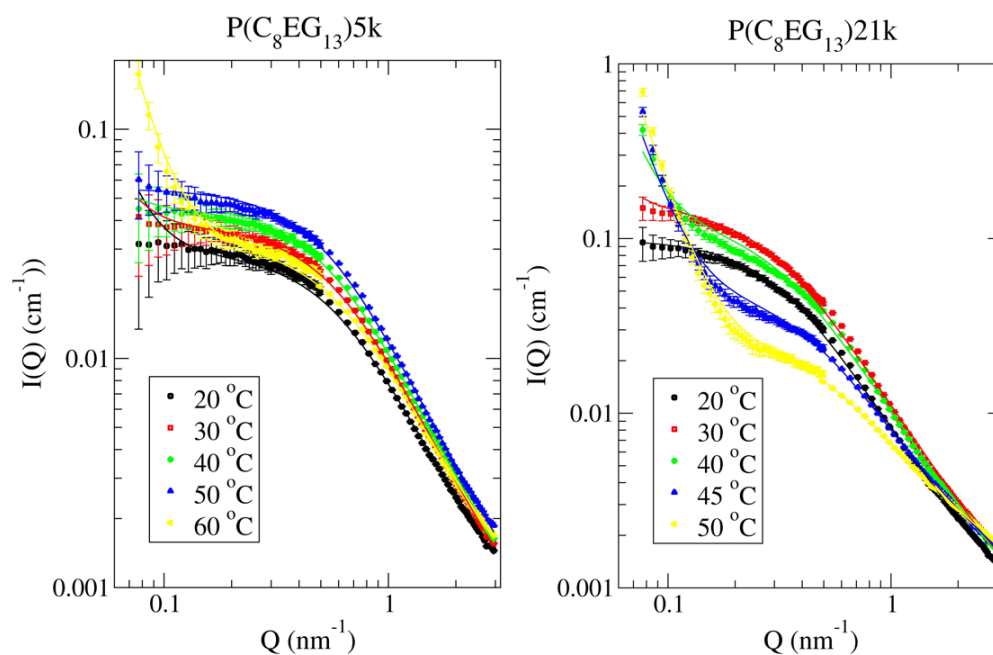
Figure S4.4. SANS data for the AAPs at different temperatures for a concentration of 10mg/mL in D₂O. A: P(C₈EG₁₃)5k; B: P(C₈EG₁₃)21k. The solid lines represent the fits using the wormlike-chain model.
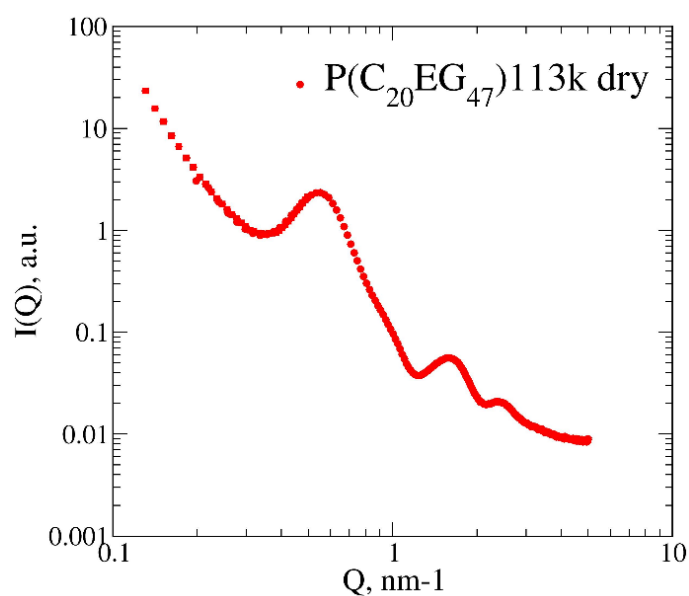
SAXS of the dry P(C20EG47)113k

Figure S4.5. SAXS curve for the polymer P(C₂₀EG₄₇)113k in a dry state. The polymers are organized in a lamellar structure which is formed by the crystalline PEG and the hydrocarbon layers in between.

4.7   References

[1]   S. J. Holder, N. A. J. M. Sommerdijk, *Polym. Chem.* **2011**, *2*, 1018–1028.

[2]   R. Lund, L. Willner, M. Monkenbusch, P. Panine, T. Narayanan, J. Colmenero, D. Richter, *Phys. Rev. Lett.* **2009**, *102*, 188301.

[3]   K. Uramoto, R. Takahashi, K. Terao, T. Sato, *Polym. J.* **2016**, *48*, 863–867.

[4]   M. Ueda, A. Hashidzume, T. Sato, *Macromolecules* **2011**, *44*, 2970–2977.

[5]   E. Di Cola, N. Plucktaveesak, T. A. Waigh, R. H. Colby, J. S. Tan, W. Pyckhout-Hintzen, R. K. Heenan, *Macromolecules* **2004**, *37*, 8457–8465.

[6]   M. Rackaitis, K. Strawhecker, E. Manias, **2002**, DOI 10.1002/polb.10284.

[7]   K. G. Goswami, S. Mete, S. S. Chaudhury, P. Sar, E. Ksendzov, C. Das Mukhopadhyay, S. V. Kostjuk, P. De, *ACS Appl. Polym. Mater.* **2020**, *2*, 2035–2045.

[8]   L. M. Tomalino, A. Voronov, A. Kohut, W. Peukert, *J. Phys. Chem. B* **2008**, *112*, 6338–6343.

[9]   C. Heitz, S. Pendharkar, R. K. Prud'Homme, J. Kohn, *Macromolecules* **1999**, *32*, 6652–6657.

[10]   C. Heitz, R. K. Prud'Homme, J. Kohn, *Macromolecules* **1999**, *32*, 6658–6667.

[11]   Q. Xu, S. Li, C. Yu, Y. Zhou, *Chem. - A Eur. J.* **2019**, *25*, 4255–4264.

[12]   T. Horiuchi, K. Rikiyama, K. Sakanaya, Y. Sanada, K. Watanabe, M. Aida, Y. Katsumoto, *J. Oleo Sci.* **2020**, *69*, 449–453.

[13]   T. Horiuchi, T. Sakai, Y. Sanada, K. Watanabe, M. Aida, Y. Katsumoto, *Langmuir* **2017**, *33*, 14649–14656.

[14]   K. Rikiyama, T. Horiuchi, N. Koga, Y. Sanada, K. Watanabe, M. Aida, Y. Katsumoto, *Polymer (Guildf).* **2018**, *156*, 102–110.

[15]   N. A. Hadjiantoniou, A. I. Triftaridou, D. Kafouris, M. Gradzielski, C. S. Patrickios, *Macromolecules* **2009**, *42*, 5492–5498.

[16]   N. A. Hadjiantoniou, T. Krasia-Christoforou, E. Loizou, L. Porcar, C. S. Patrickios, *Macromolecules* **2010**, *43*, 2713–2720.

[17]   C. C. De Silva, P. Leophairatana, T. Ohkuma, J. T. Koberstein, K. Kremer, D. Mukherji, *J. Chem. Phys.* **2017**, *147*, 64904.

[18]   V. Hogouvieux, M. A. V. Axelos, M. Kolb, *Macromolecules* **2009**, *42*, 392–400.

[19]   V. Hugouvieux, M. A. V. Axelos, M. Kolb, *Soft Matter* **2011**, *7*, 2580–2591.

[20]   I. R. Cooke, D. R. M. Williams, *Macromolecules* **2003**, *36*, 2149–2157.

[21]   S. Li, C. Yu, Y. Zhou, *Sci. China Chem.* **2019**, *62*, 226–237.

[22]   Y. K. Sung, S. W. Kim, *Biomater. Res.* **2020**, *24*, 1–12.

[23]   S. Chatterjee, P. C. L. Hui, C. wai Kan, *Polymers (Basel).* **2018**, *10*, 480.

[24]   M. Sponchioni, U. Capasso Palmiero, D. Moscatelli, *Mater. Sci. Eng. C* **2019**, *102*, 589–605.

[25]   N. Vanparijs, L. Nuhn, B. G. De Geest, *Chem. Soc. Rev.* **2017**, *46*, 1193–1239.

[26]   E. M. Frazar, R. A. Shah, T. D. Dziubla, J. Z. Hilt, *J. Appl. Polym. Sci.* **2020**, *137*, 48770.

[27]   A. Halperin, M. Kröger, F. M. Winnik, *Angew. Chemie - Int. Ed.* **2015**, *54*, 15342–15367.

[28]   F. A. Plamper, W. Richtering, *Acc. Chem. Res.* **2017**, *50*, 131–140.

[29]   D. Roy, W. L. A. Brooks, B. S. Sumerlin, *Chem. Soc. Rev.* **2013**, *42*, 7214–7243.

[30]   C. Weber, R. Hoogenboom, U. S. Schubert, *Prog. Polym. Sci.* **2012**, *37*, 686–714.

[31]   A. Louai, D. Sarazin, G. Pollet, J. François, F. Moreaux, *Polymer (Guildf).* **1991**, *32*, 703–712.

[32]   C. Mangold, B. Obermeier, F. Wurm, H. Frey, *Macromol. Rapid Commun.* **2011**, *32*, 1930–1934.

[33]   S. Samanta, D. R. Bogdanowicz, H. H. Lu, J. T. Koberstein, *Macromolecules* **2016**, *49*, 1858–1864.

[34]   A. Armstrong, W. Li, in *Encycl. Reagents Org. Synth.*, John Wiley & Sons, Ltd, **2007**.

[35]   C. H. Hövelmann, S. Gooßen, J. Allgaier, *Macromolecules* **2017**, *50*, 4169–4179.

[36]   P. J. Dunn, W. Hoffmann, Y. Kang, J. C. Mitchell, M. J. Snowden, *Org. Process Res. Dev.* **2005**, *9*, 956–961.

[37]   Z. Peng, J. W. Wong, E. C. Hansen, A. L. A. Puchlopek-Dermenci, H. J. Clarke, *Org. Lett.* **2014**, *16*, 860–863.

[38]   S. Saeki, N. Kuwahara, M. Nakata, M. Kaneko, *Polymer (Guildf).* **1976**, *17*, 685–689.

[39]   H. Tompa, *Trans. Faraday Soc.* **1949**, *45*, 1142–1152.

[40]   B. Hammouda, D. L. Ho, S. Kline, *Macromolecules* **2004**, *37*, 6932–6937.

[41]   M. Doi, S. F. Edwards, *The Theory of Polymer Dynamics*, Oxford University Press, USA, Oxford, **1988**.

[42]   A. L. Kholodenko, *Macromolecules* **1993**, *26*, 4179–4183.

[43]   H. Benoît, J. F. Joanny, G. Hadziioannou, B. Hammouda, *Macromolecules* **1993**, *26*, 5790–5795.

[44]   B. Hammouda, *J. Res. Natl. Inst. Stand. Technol.* **2016**, *121*, 139–164.

[45]   S. Kawaguchi, G. Imai, J. Suzuki, A. Miyahara, T. Kitano, K. Ito, *Polymer (Guildf).* **1997**, *38*,

2885–2891.

[46]   M. Kotlarchyk, S.-H. Chen, *J. Chem. Phys.* **1983**, *79*, 2461.

[47]   H. Lee, R. M. Venable, A. D. MacKerell, R. W. Pastor, *Biophys. J.* **2008**, *95*, 1590–1599.

[48]   E. Alami, M. Almgren, W. Brown, J. François, *Macromolecules* **1996**, *29*, 2229–2243.

[49]   T. Zinn, L. Willner, K. D. Knudsen, R. Lund, *Macromolecules* **2017**, *50*, 7321–7332.

[50]   N. Yamaguchi, M. Sato, *Polym. J. 2009 418* **2009**, *41*, 588–594.

[51]   I. R. Cooke, D. R. M. Williams, *Macromolecules* **2003**, *36*, 2149–2157.

[52]   P. Hebbeker, A. A. Steinschulte, S. Schneider, F. A. Plamper, *Langmuir* **2017**, *33*, 4091–4106.

[53]   V. Hugouvieux, M. A. V. Axelos, M. Kolb, *Soft Matter* **2011**, *7*, 2580–2591.

[54]   M. Werner, J. U. Sommer, *Biomacromolecules* **2015**, *16*, 125–135.

[55]   H. Maier-Leibnitz Zentrum Forschungszentrum Jülich, H. Maier-Leibnitz Zentrum, *J. large-scale Res. Facil.* **2015**, *1*, 28.

[56]   A. V. Feoktystov, H. Frielinghaus, Z. Di, S. Jaksch, V. Pipich, M. S. Appavou, E. Babcock, R. Hanslik, R. Engels, G. Kemmerling, H. Kleines, A. Ioffe, D. Richter, T. Brückel, *J. Appl. Crystallogr.* **2015**, *48*, 61–70.

[57]   V. Pipich, "QtiKWS," can be found under http://www.qtisas.com/qtikws, **n.d.**

[58]   R. Biehl, *PLoS One* **2019**, *14*, DOI 10.1371/journal.pone.0218789.

[59]   E. Kentzinger, M. Krutyeva, U. Rücker, *J. large-scale Res. Facil. JLSRF* **2016**, *2*, 61.

[60]   X. Zhang, Y. Jiang, B. Miao, Y. Chen, D. Yan, J. Z. Y. Chen, *Soft Matter* **2014**, *10*, 5405–5416.

[61]   B. Hammouda, *J. Appl. Crystallogr.* **2010**, *43*, 1474–1478.

[62]   A. Guinier, G. Fournet, *Small-Angle Scattering of X-Rays*, Wiley, **1955**.

[63]   B. Hammouda, *J. Polym. Sci. Part B Polym. Phys.* **1992**, *30*, 1387–1390.

[64]   M. S. Wertheim, *Phys. Rev. Lett.* **1963**, *10*, 321–323.

5 Passive macromolecular translocation mechanism through lipid membranes

The biggest part of the following chapter was published in Journal of American Chemical Society:
Kostyurina, E. et al., J. Am. Chem. Soc. 144, 33, 15348–15354, 2022. Reprinted with permission from ACS Publications. Copyright 2022 American Chemical Society.

Abstract

The translocation of biological active macromolecules through cell membranes is of vital importance for cells and a key process for drug delivery. Proteins exploit specific conformational changes in their secondary structure to facilitate membrane translocation. For the large class of biological and synthetic macromolecules, where such conformational adaptions are not possible, guidelines to tailor monomer and macromolecular structure to aid membrane translocation and cross membrane drug delivery would be highly desirable. Here we use alternating amphiphilic macromolecules to systematically investigate the relation between polarity, polymer chain length, lipid chain length, polymer concentration and temperature on membrane partition and translocation rate. We employed Pulse Field Gradient NMR and confocal fluorescence microscopy to determine membrane adsorption and desorption rate constants, and partitioning coefficients. We find that translocation is a two-step process involving a fast adsorption and membrane insertion process, and a slower desorption process. Membrane insertion is a key step that determines the molecular weight, concentration and temperature dependences. Passive translocation is possible on time scales from minutes to hours. Macromolecules with different adapted hydrophilic/hydrophobic co-monomer sequences show the same translocation rate, indicating that common optimized translocation conditions can be realized with a variety of monomer chemical structures. The investigated copolymers are biocompatible, biodegradable and capable of transporting a hydrophobic payload through the lipid membrane. This detailed understanding of the macromolecular translocation mechanism enables to better tailor the delivery of active agents using macromolecular carriers.

5.1 Introduction

The main component of a cell membrane is the lipid bilayer that separates the cell from its environment. The translocation of macromolecules across the bilayer mostly occurs via active

processes requiring specific channels or pumps, via pore formation involving a strong local disruption of the cellular membrane, or via endocytosis.[1,2] The polarity of the molecules plays an important role in the translocation process. Polar molecules are well soluble in water, but the hydrophobic interior of the lipid bilayer blocks the transportation of polar molecules through the membrane. Hydrophobic molecules can be solubilized in the bilayer, but require a carrier due to their low solubility in water.[3,4]

Passive translocation can play an important role in the delivery of drugs and other biologically active agents across the cell membrane. Therefore, there is a large interest in the relation between the structure of molecules and the efficiency and time scale of their translocation through lipid membranes. Passive translocation for small molecules mostly occurs for molecules with moderate polarity.[1,5] For macromolecules the ability to translocate across a lipid bilayer is dramatically decreased. An exception is cell-penetrating peptides (CPP).[6,7] A well-studied example is Cyclosporin A, which changes its conformation inside the membrane in order to reduce the polarity of the molecular surface.[7] There are only a few synthetic polymers which are known to translocate, among them phospholipid-mimicking polymers[8,9] and PEG-containing polymeric surfactants.[10] As synthetic polymers can act as carriers for therapeutic agents, and because their molecular structure can be well adapted to the polarity of the bilayer, there is an increasing interest in the translocation of synthetic polymers.

Nonionic polymers are ideally suited for membrane translocation due to minimal interaction with other biomolecules, in particular proteins. The translocation process of non-ionic polymers was studied theoretically for homopolymers,[11] block copolymers, and polymers with a random distribution of hydrophilic and hydrophobic units.[12] Translocation is predicted to occur when the polymers have a balanced amphiphilicity, while more hydrophilic polymers cannot penetrate the membrane and more hydrophobic polymers are trapped in the hydrophobic membrane interior. These theoretical predictions were verified experimentally for polymers containing alternating hydrophilic and hydrophobic repeat units but had a more hydrophilic nature to obtain water solubility.[13]

Alternating copolymers enable to balance the polarity via the polarity of the two alternating repeat units. For example, for alternating amphiphilic copolymers, the polarity can be adjusted via the lengths of the alternating hydrophilic and hydrophobic repeat units. This parallels the structure of proteins, where the presence of both hydrophilic and hydrophobic amino acid residues is one of the most general features of both membrane and soluble proteins. Alternating amphiphilic copolymers thus employ the same structural concept as proteins to adjust the

polarity, and can be synthesized over a wide range of repeat unit lengths and total chain length for systematic studies of membrane translocation.

In the present work, we systematically investigate the translocation behavior of non-ionic alternating polyester and polyether amphiphilic copolymers (AAPs) through phosphatidylcholine model lipid membranes. We determine adsorption and desorption rates, as well as the amount of polymer in the lipid bilayer as a function of temperature, concentration, and molecular weight. We find that the translocation process occurs via a two-step process, where the slower desorption process is the rate limiting step. The translocation rates of amphiphilic copolymers with membrane-adapted polarity represent an upper limit for translocation rates that can be achieved if no specific conformational changes (e.g. helix formation of CPP) are involved such as for membrane-penetrating proteins.

5.2   Results and discussion

We examined the translocation process of AAPs through phosphatidylcholine lipid membranes. The AAPs were synthesized as polyesters containing hydrophobic dicarboxylic acids and hydrophilic polyethylene glycol oligomers ($P(C_mEG_n)$) or as polyethers where the hydrophobic units were replaced by alkanediols ($PE(C_mEG_n)$, see Figure 5.2A). Samples with different molecular weights (MW) and narrow molecular weight distributions were obtained by fractionation (see Appendix Table S5.1). The AAP show a lower critical solution temperature (LCST) behavior (see SI Figure S5.1).[14] Because of their amphiphilic nature we tested one AAP with respect to its biocompatibility as an elementary prerequisite for medical applications. A 48 hours treatment of HeLa cells with the AAP did not decrease cell viability (Figure 5.1).
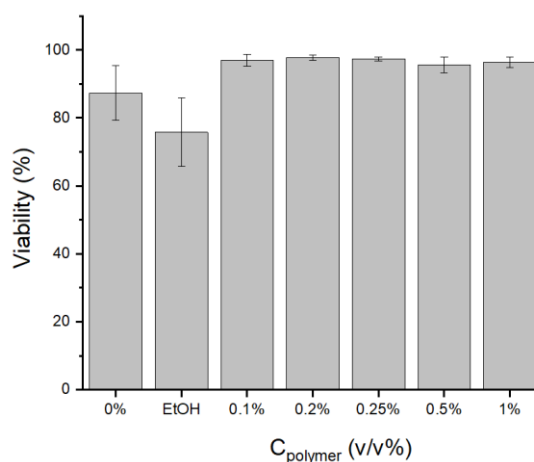

Figure 5.1. HeLa cell viability upon 48 h treatment with $P(C_4EG_4)6k$ at variing concentrations from 0.1 to 1 v/v%. As control samples, cells without any treatment and cells incubated with ethanol (2.5 v/v%) were used. Data were collected from three independent experiments. Bars show mean ± s.d.

We examined the interaction and translocation kinetics of AAPs with lipid membranes by mixing aqueous AAP solutions with solutions of large unilamellar vesicles (LUV, diameter ≈ 90 nm). Time-evolution pulse field gradient NMR (PFG-NMR) (see Figure 5.2B,C) allowed us to determine the amount of AAP integrated into the LUVs by binding to the membrane and translocating to the inner LUV volume (see Figure 5.3A). PFG-NMR provides access to the molecular mobility of all components containing specific resonance nuclei (typically hydrogen) by variation of the observation time Δ in a range from ten to a few hundreds ms.[15,16] With this the distinction between the hydrogens of the external phase (free polymer) and the phase interacting with the liposome (integrated polymer) is possible (see Figure 5.2B). Observing the time evolution in a kinetic PFG NMR experiment with exclusive detection of the integrated fraction by using fixed pulsed gradient value gives direct access to the permeation process.[17]
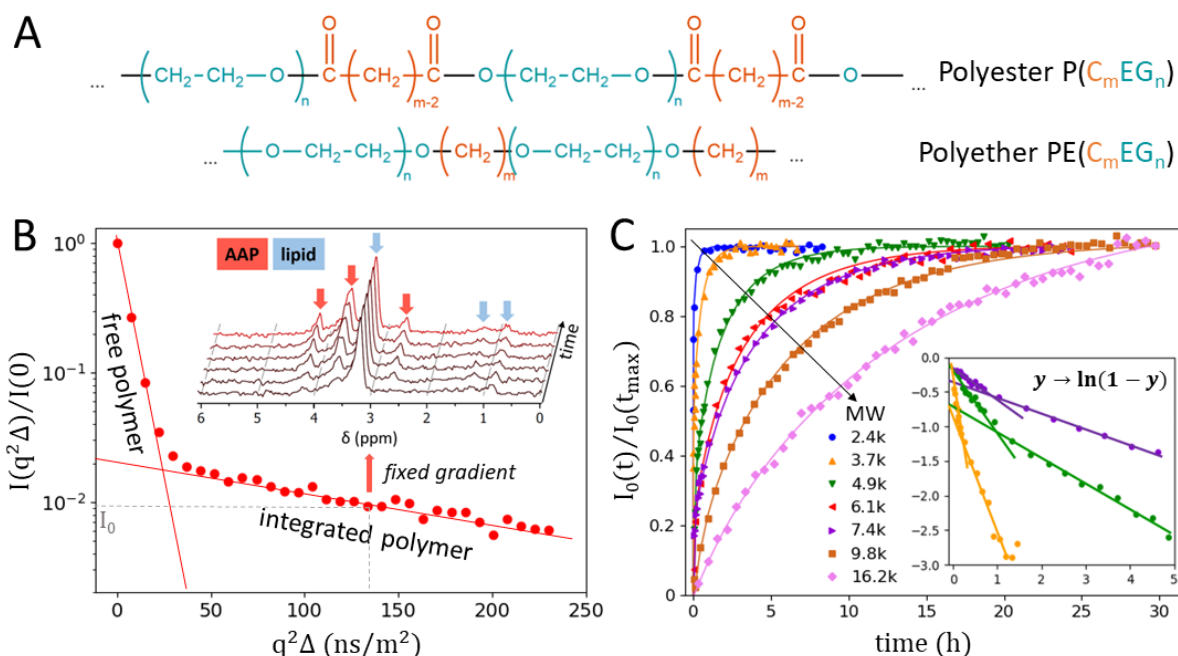
Figure 5.2. A: Chemical structure of AAPs synthesized as polyesters and polyethers. B: Conventional PFG NMR decay of an AAP-LUV mixture normalized to $I(q^2\Delta=0)$: with increasing time $q^2\Delta$ one observes first the fast diffusion of free AAP and later the slower diffusion of LUV-(POPC) integrated AAP for an AAP specific peak. The amplitude of the slow component is proportional to the amount of LUV-integrated AAP (membrane bound and inside of the vesicle). Inset: NMR peaks of AAP (increasing with time) and lipid (constant). C: Time-evolution PFG NMR of $P(C_4EG_4)$ at T=25ºC after AAP addition to the LUV solution. For a fixed $q^2\Delta$ after full relaxation of free AAP (red arrow in A) the AAP peak-integral shows an increasing amount of integrated AAP. Data are normalized to the long-time equilibrium of saturated integrated AAP. With increasing molecular weight of AAP the kinetics becomes slower. Inset: selected data scaled to y -> ln(1-y) unveiling a two-step process for translocation indicated by two slopes (same colors as in the main plot). LUV were monitored using the same method examining the lipid peak (≈ 3.2ppm) and showed no changes during the experiments (see SI Figure S5.3).

Due to the limited inner LUV volume the adsorption and the desorption processes can be separated by analysis of the kinetic process. The time evolution of the NMR intensity shows a strong dependence on the AAP molecular weight. The time-dependence of the data clearly reveals a two-step process (Figure 5.2C and inset) which we interpret as fast adsorption to the membrane and slower desorption of AAP to the inside LUV volume. To describe the observation we apply a model which takes into account the limited inner LUV volume and limited polymer concentration in the membrane.

The kinetics of the system can be described by a set of rate equations describing changes in the total number of AAP molecules in the outside volume (po), in or adsorbed to the membrane (pm), and inside the vesicles (pi) as (see Figure 5.3A):

$$\frac{dn_{po}}{V_o dt} = k_d \cdot \frac{n_{pm}}{V_m} - k_a \cdot c_{po} \cdot \left(1 - \frac{n_{pm}}{n_{pmax}}\right) \tag{5.1}$$

$$\frac{dn_{pm}}{V_m dt} = k_a \cdot c_{po} \cdot \left(1 - \frac{n_{pm}}{n_{pmax}}\right) - 2 \cdot k_d \cdot \frac{n_{pm}}{V_m} + k_a \cdot \frac{n_{pi}}{V_i}\left(1 - \frac{n_{pm}}{n_{pmax}}\right) \tag{5.2}$$

$$\frac{dn_{pi}}{V_i dt} = k_d \cdot \frac{n_{pm}}{V_m} - k_a \cdot \frac{n_{pi}}{V_i}\left(1 - \frac{n_{pm}}{n_{pmax}}\right) \tag{5.3}$$

where k_a and k_d are the translocation rates for the adsorption and desorption processes respectively, n_j and c_j indicate the respective numbers and number concentration of AAP molecules in the respective volumes V_j. $c_{pmax} = \frac{n_{pmax}}{V_m}$ is the maximum number concentration in the membrane. Because of the small total liposome volume of about 4%, the final equilibrium c_{po} was regarded to be constant over the whole measurement time. The system of rate equations can be solved numerically (boundary condition t=0: $c_{pi} = 0; c_{pm} = 0, c_{po} = const$) and is normalized to the final equilibrium integrated number $n_{pm} + n_{pi}$. We note that a simpler system of rate equations, e.g. two equations neglecting the membrane volume, cannot reproduce the observed two step behavior. To describe the measured data, we fit k_a, k_d and n_{pmax}. The equilibrium value of n_{pm} is recovered by modeling the kinetic curves with the fitted values without normalization. It should be noted that accessing the LUV integrated AAP amount together with the limited V_i allows to discriminate between adsorption, desorption and c_{pm}, which cannot be achieved by other methods.

The dependence of the translocation rates and the concentration of P(C$_4$EG$_4$)5k in the bilayer on the outside AAP concentration is presented in Figure 5.3B,C. The rate constants k_a and k_d show no dependence on the concentration. k_a is much larger than k_d. c_{pm} presents a linear

dependence on c_{po} corresponding the partition coefficient c_{pm}/c_{po} of AAP between membrane and water.[18]

The observed linear dependence of c_{pm} as a function of c_{po} in Figure 5.3C is in agreement with the kinetic scheme (Eq. 4.1). In equilibrium the scheme yields

$$\frac{c_{pm}}{c_{po}} = \frac{k_a}{k_d}\left(1 - \frac{n_{pm}}{n_{pmax}}\right) \tag{5.4}$$

which describes the balance between rates and concentrations corrected for the limited concentration inside the membrane. c_{pm}/c_{po} consequently reflects the difference in rates up to a factor that approaches zero if $n_{pm} \approx n_{pmax}$. As from Figure 5.3B the ratio $\frac{k_a}{k_d} \approx 100$ and from Figure 5.3C we have $\frac{c_{pm}}{c_{po}} \approx 2$, we have $n_{pm} \approx n_{pmax}$, i.e. nearly maximum partitioning of the AAPs in the lipid membrane.
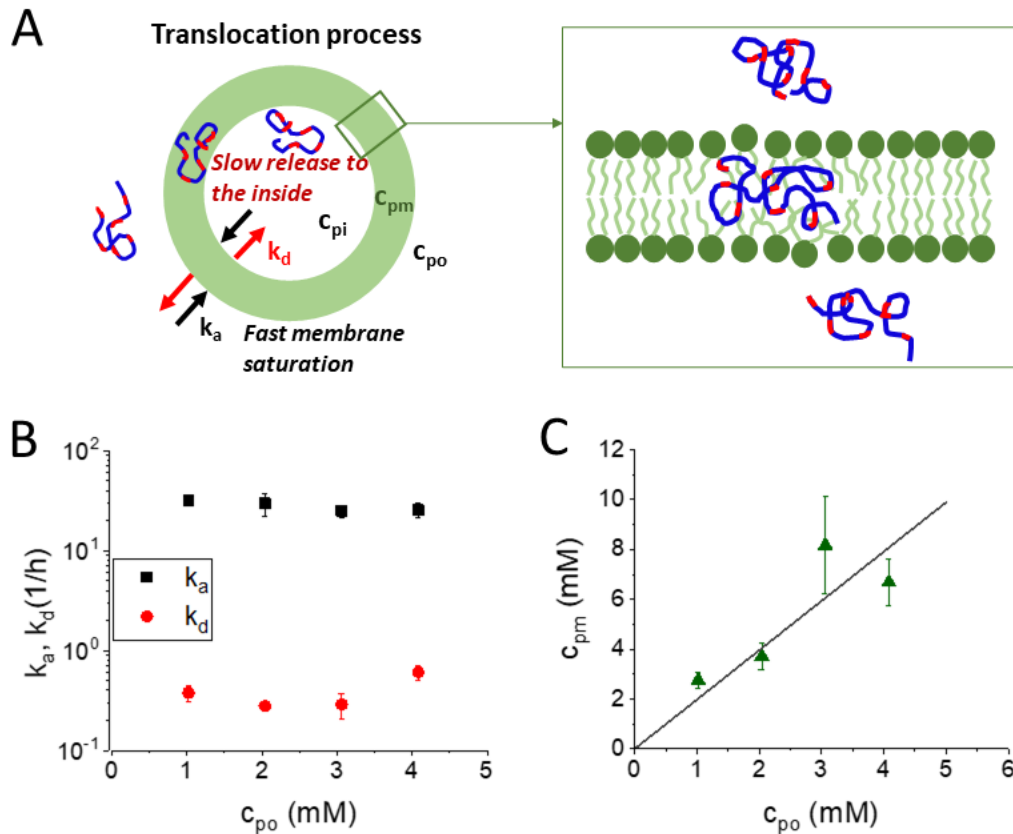
Figure 5.3 A: The translocation process as described by the kinetic modeling with the adsorption and desorption rates k_a, k_d, the AAP concentration outside of the vesicles c_{po}, inside of the vesicles c_{pi} and in the membrane c_{pm}. B: Dependence of the rate constants k_a and k_d on the AAP number concentration for P(C$_4$EG$_4$)5k using POPC vesicles at T=25ºC. C: c_{pm} vs. c_{po} for the same data as B; solid line: fit with the $y = Ax$, the resulting $A = 1.98 \pm 0.25$;

Figure 5.4 presents the molecular weight dependence of the translocation rates and the partition coefficients for different AAP copolymer compositions. For all investigated AAPs we observe the same decrease of the partition coefficient c_{pm}/c_{po} with increasing molecular weight (see Figure 3A). Figure 5.4B shows the molecular weight dependence of the rate constants k_a and k_d. We observe a decrease of k_a with increasing molecular weight, whereas k_d is nearly independent of molecular weight. The very small molecular weight dependence of k_d is supported by additional measurements for $P(C_4EG_4)$ at different temperatures (see SI Figure S5.6). The observed decrease of the partitioning ratio c_{pm}/c_{po} with the decreasing ratio k_a/k_d is in agreement with Eq. (4.4), i.e. higher molecular weight copolymers adsorb at a slower rate, whereas the desorption rate stays constant, resulting in a reduced membrane partition of the copolymers. Remarkably, both processes are independent of the copolymer composition, which varied across $PE(C_4EG_3)$, $PE(C_4EG_6)$, $P(C_4EG_4)$ and $P(C_8EG_{13})$.
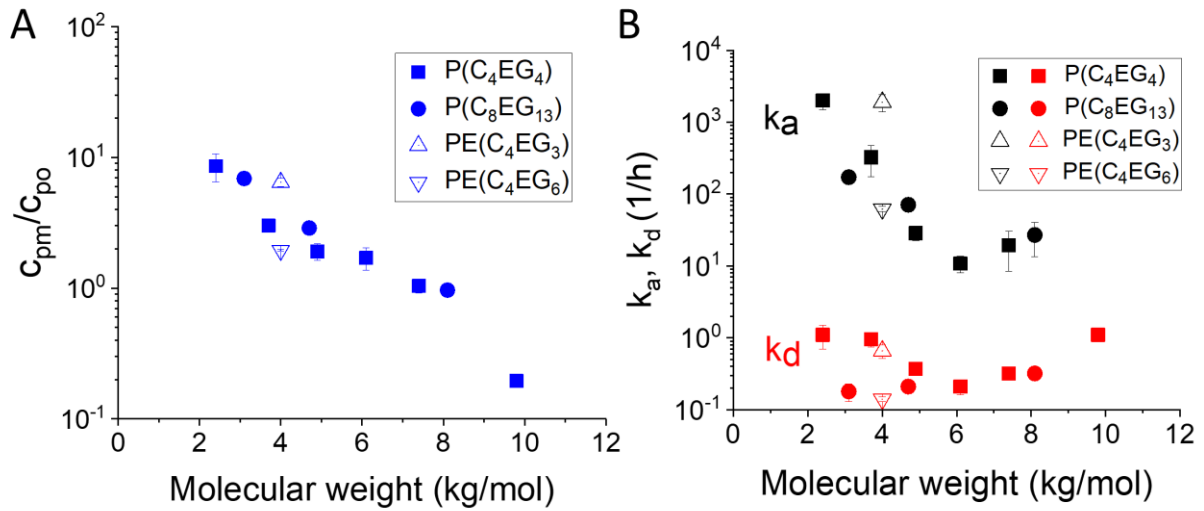
Figure 5.4. A: Dependence of c_{pm}/c_{po} on the AAP molecular weight; B: Dependence of k_a and k_d on the AAP molecular weight. For all AAPs the measurements were performed at T=25ºC and constant mass concentration of 10 mg/mL (≈2mM for 5 kg/mol).

Transition state theory relates rates k to the free energy of activation $\Delta G = \Delta H - T\Delta S$ by[19]

$$\mathrm{k} = \frac{\kappa k_B T}{h} e^{\frac{-\Delta G}{RT}} \tag{5.5}$$

where κ is the transmission coefficient, T is the absolute temperature, k_B, h and R are the Boltzmann, Plank and gas constants, respectively. The value of ΔG and its temperature dependence provide valuable insights into the mechanism of the adsorption (k_a) and desorption (k_d) processes. We therefore systematically determined the translocation rates of $P(C_4EG_4)$ copolymers as a function of temperature as shown in Figure 5.5. We note that for all investigated temperatures the lipid membrane stayed in the fluid phase.

In Figure 5.5 we present Eyring plots of the logarithm of the rates k_a (Figure 5.5A) and k_d (Figure 5.5.B) as a function of the inverse temperature $1/T$ for different molecular weights for the P(C$_4$EG$_4$) copolymer series. As the data in this representation scale nearly linearly, we can calculate the respective free enthalpies of activation ΔH for both rate constants from the slopes ($-\Delta H/R$) for all investigated molecular weights. The intercepts correspond to a weighted sum of the logarithm of the transmission coefficients κ and the activation entropies ΔS.
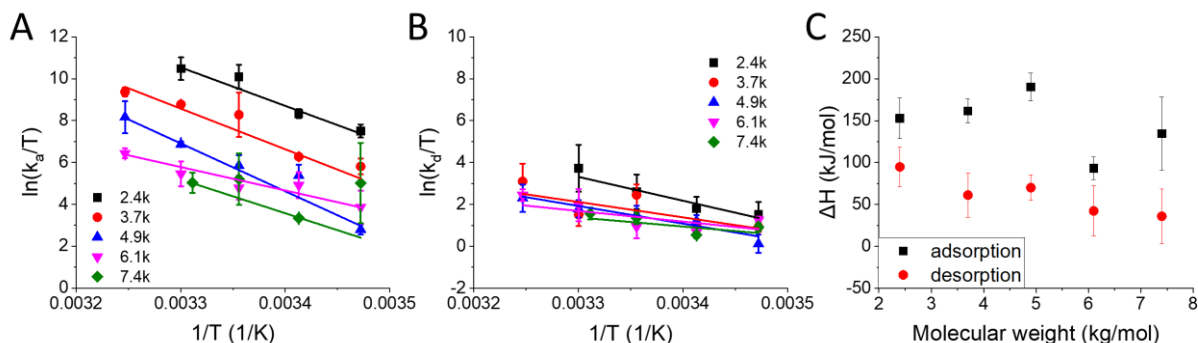

Figure 5.5. A: Eyring plots of the adsorption rate constants for POPC vesicles for different molecular weights of P(C$_4$EG$_4$), in the temperature range 15-35 ºC (POPC melting point is -2 ºC). B: Same for the desorption rate. C: Enthalpies of activation calculated from the Eyring equations for adsorption and desorption; AAPs with a cloud point below 35 °C were studied in a reduced temperature range.

For the different copolymers we calculate activation enthalpies in the range of 50 – 150 kJ/mol. For both adsorption and desorption processes the corresponding ΔH-values do not show a significant dependence on molecular weight. On average, the values for the desorption rate constant are approximately half compared to the adsorption rate constant (Figure 5.5C). Therefore, opposite to the observed relation $k_a \gg k_d$ which requires $\Delta G_a < \Delta G_d$, we observe a relation $\Delta H_a > \Delta H_d$ for all investigated P(C$_4$EG$_4$) copolymers. The minimum values of ΔG estimated from the rate constants using $\kappa = 1$ in eq. 4.5 are in the order of 100 kJ/mol. It leads to the relation $\Delta S_a > 0 > \Delta S_d$. Assuming same entropy for the polymer in water before and after translocation means that the entropy of the polymer-membrane mixture is larger than that of the polymer-water mixture. This can only be explained if tail entropy makes a significant contribution to the entropy of the polymer-membrane mixture.

Large positive ΔH_a- and ΔS_a-values are characteristic for the breakage of attractive interactions and the disruption of the molecular assembly in lipid bilayer assembly.[20] This indicates that the adsorption process involves the insertion of the copolymers into the lipid bilayer. This process, representing a barrier for adsorption, was already described by Sommer using MD simulations

and is the reason why the maximum translocation occurs for more hydrophobic polymers.[12] The desorption step involves the permeation and translocation of the polymer chain across the bilayer, which on its way requires only a little change of the disordered state of the lipid tails.
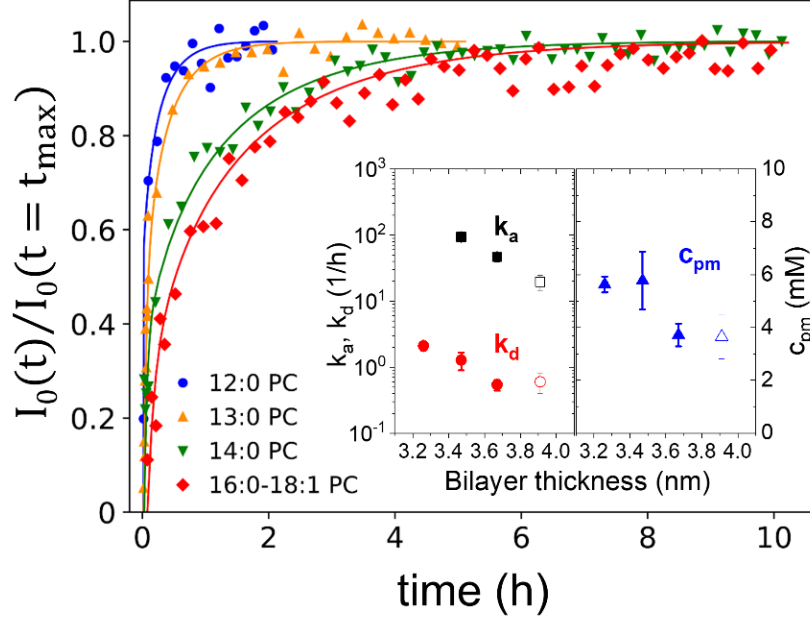

Figure 5.6. Kinetic curves for P(C₄EG₄)6k at T=30ºC for lipids 12:0 PC (DLPC), 13:0PC, 14:0 PC (DMPC) and 16:0-18:1 PC (POPC) (unsaturated) with bilayer thicknesses of 3.26, 3.47, 3.67 and 3.91 nm and melting temperature -2, 14, 24 and -2 ºC, respectively.[21] Insert: k_a, k_d and c_{pm} plotted against bilayer thickness of the lipids. k_a for DLPC cannot be determined due to the weak NMR signal.

From the experiments we observe a clear decrease of the adsorption rate constant k_a with increasing molecular weight, which corresponds to an increasing ΔG-value with increasing molecular weight. Since the ΔH-values do not show a significant molecular weight dependence, as shown in Figure 5.5C, the ΔS-values must be increasing with decreasing molecular weight, consistent with the parallel down-shift of the curves in Figure 5.5A. The observation of larger ΔS-values for shorter polymer chains is in agreement with Flory Huggins theory, where the entropy of mixing (ΔS_m) polymers with small molecules decreases with increasing molecular weight since an increasing chain connectivity reduces the number of realizable states. It is also in agreement with the observed reduction of the LCST-temperature for the higher molecular weight.[14] Therefore, the observed molecular weight dependence of the adsorption rate constant k_a and of the LCST-temperature are both consistent with predictions of the Flory Huggins theory for the mixing entropy ΔS_m, demonstrating that the mixing step when the polymer inserts into the lipid bilayer is a key step for polymer translocation. The insertion process requires the formation of a

disordered volume in the lipid bilayer to accommodate the polymer chain. This would both lead to the observed large positive ΔH_a- and ΔS_a-values, in line with the so-called $\Delta H - \Delta S$-compensation known for cross cell membrane transport.[20]

Since the lipid structure and assembly play a significant role in the translocation process, we investigated the influence of lipid chain length and lipid phase transition temperature on the translocation process, as presented in Figure 5.6 and Figure 5.7. From the measurements at one temperature we observe that the translocation rates and the lipid partition decrease with increasing lipid chain length and bilayer thickness, indicating an increased ΔG. This dependence is not affected by the use of saturated and unsaturated lipids resulting in different melting temperatures. c_{pm} decreases with increasing membrane thickness which can be related to the balance between rates and concentrations described above.
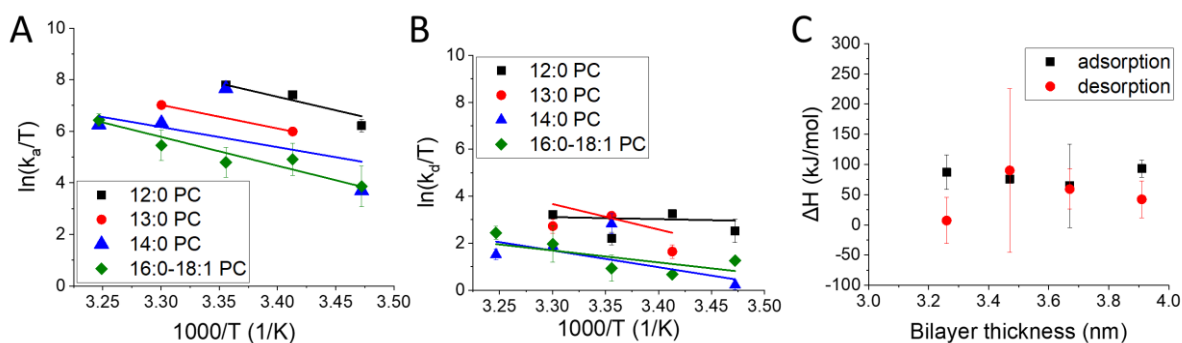

Figure 5.7. A: Eyring plots of the adsorption rate constants for P(C₄EG₄)6k to the vesicles made of different lipids, in the temperature range 15-35 ºC. B: Same for the desorption rate. C: Enthalpies of activation calculated from the Eyring equations for adsorption and desorption.

In Figure 5.7A,B we present Eyring plots for the rates k_a and k_d for P(C₄EG₄)6k measured using different lipids. The free enthalpies of activation ΔH were calculated for both rate constants (Figure 5.7C). Similar to molecular weight dependence presented in Figure 5.5C the average ΔH for desorption is approximately twice smaller than for adsorption, which is attributed to the large contribution of lipid tail entropy for the entropy of polymer-lipid mixture. The parallel down-shift visible in Figure 5.7A indicates a decrease of activation entropy of adsorption with increasing tail length, similar to the molecular weight dependence depicted in Figure 5.5A. This is consistent with a reduction of lipid tail entropy and consequently the polymer-membrane mixing entropy with increasing tail length. For the DMPC membrane the translocation was measured both above and below the lipid melting temperature of 24ºC. Surprisingly, the transition of the membrane to the gel phase did not reduce the translocation rates dramatically (Figure 5.7A,B), which is opposite to translocation of small molecules.[22] We conclude that the energy required for locally

melting the membrane is small compared to the polymer-membrane free energy of mixing, that might be opposite for small molecules. Close to the melting temperature, the adsorption rate showed a significant increase. This might be an effect of the membrane thickness ondulations in the "ripple" phase P_β,[23–25] and is an interesting subject for further investigations. The desorption rate shows a slight trend towards decrease with increasing membrane thickness (Figure 5.7B), consistent with the results at 30ºC in Figure 5.6 and might also be the result of the decreasing tail entropy.

To verify the translocation of the copolymers with a payload across the bilayer, we labeled the P(C$_4$EG$_4$)6k copolymer with the hydrophobic fluorescent label 7-(diethylamino)coumarin (P(C$_4$EG$_4$)6k-coumarin). The translocation process was followed by confocal laser scanning fluorescence microscopy using giant unilamellar vesicles (GUV) made from DLPC. A sequence of fluorescence microscopy images is presented in Figure 5.8 showing the increasing fluorescence intensity inside of the GUV after the addition of the coumarin labeled AAP. This result proves that AAPs can be used to transport hydrophobic molecules through lipid membrane. Although the coumarin moiety is hydrophobic, we observe only a small enrichment of the labeled polymer in the membrane which coincides qualitatively with the partition coefficient of the unlabeled AAP from the PFG NMR measurement. For comparison, the low molecular weight 7-(diethylamino)coumarin compound is predominantly located in the membrane (see Figure S5.7).
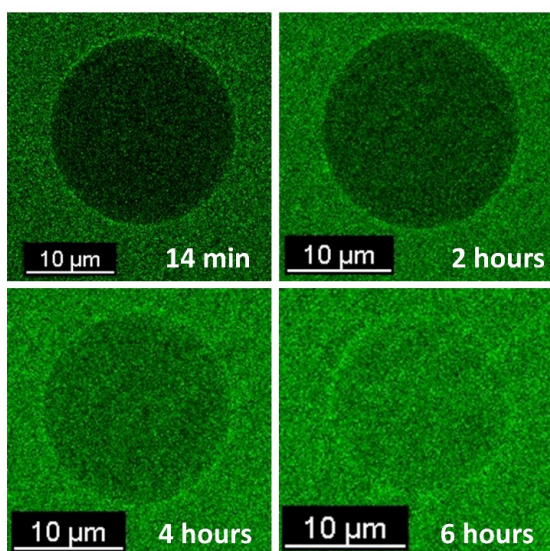

Figure 5.8. Sequence of fluorescence microscopy images of a GUV prepared from DLPC after the addition of P(C$_4$EG$_4$)6k-coumarin at T=25ºC.

5.3   Conclusion

We have shown by PFG-NMR experiments that the translocation of amphiphilic macromolecules across lipid bilayer membranes is a two-step process involving fast adsorption and membrane insertion process, and a slower desorption process. The time-evolution PFG NMR study using liposomes with a restricted inner volume allows to access independently adsorption and desorption processes, and the concentration of the translocating species in the membrane. The insertion of the copolymers into the bilayer mainly determines the molecular weight, concentration and temperature dependence. Membrane insertion involves large enthalpy and entropy changes, where the lipid membrane/copolymer mixing entropy determines the molecular weight dependence. We find this in agreement with classical Flory-Huggins theory, with the observed thermal solution phase behavior of the copolymers, and with recent MD-simulations. We furthermore observe that copolymers with different adapted hydrophilic/hydrophobic co-monomer sequences show the same translocation rate. The alternating amphiphilic architecture thus provides a route to tune the overall AAP polarity to keep it water-soluble and compatible with the hydrophobic interior of the membrane. In addition, we show by confocal fluorescence microscopy, that the copolymers are capable to translocate hydrophobic molecules across lipid membranes. We anticipate that this detailed understanding of the macromolecular translocation mechanism enables to better tailor the delivery of active agents using macromolecular carriers.

5.4   Acknowledgments

5.5   Materials and Methods

Materials

1-palmitoyl-2-oleoyl-sn-glycero-3-phosphocholine (POPC), 1,2-dimyristoyl-sn-glycero-3-phosphocholine, (DMPC), 1,2-ditridecanoyl-sn-glycero-3-phosphocholine (13:0 PC) and 1,2-dilauroyl-sn-glycero-3-phosphocholine (DLPC) were purchased from Avanti Polar Lipids and used without further purification. Polymer synthesis is described in Appendix. Characterization of polymers used in this work is presented in Table S1

Table S5.1. Characterization of AAP fractions used for the translocation experiments. Number average molecular weight (M_n) and molecular weight distribution (M_w/M_n) are obtained by SEC/LS. Chain end to end distance values (R_{ee}) for the AAP in water were calculated from the measured hydrodynamic radii (R_h)[14] as $R_{ee} = 3.6R_h$, d_{POPC} is the POPC bilayer thickness set to be 4.0 nm.[21] The ratio R_{ee}/d_{POPC} is a measure for the spacial restrictions of the AAP inside the membrane. Strong compression of the AAP in a two-dimensional environment causes a strong entropic penalty. As R_{ee} in the membrane might differ from R_{ee} in water, the ratio R_{ee}/d_{POPC} is only a rough estimate.

Fraction	M_n (SEC/LS), kg/mol	M_w/M_n.(SEC/LS)	R_{ee}, nm	R_{ee}/d_{POPC}
P(C$_4$EG$_4$)2k	2.4	1.08	3.1	0.8
P(C$_4$EG$_4$)4k	3.7	1.07	4.0	1.0
P(C$_4$EG$_4$)5k	4.9	1.07	4.8	1.2
P(C$_4$EG$_4$)6k	6.1	1.09	5.4	1.4
P(C$_4$EG$_4$)7k	7.4	1.11	6.1	1.5
P(C$_4$EG$_4$)10k	9.8	1.05	7.2	1.8
P(C$_4$EG$_4$)16k	16.2	1.08	9.8	2.5
P(C$_5$EG$_6$)2k	2.4	1.07		
P(C$_5$EG$_6$)4k	4.4	1.10		
P(C$_5$EG$_6$)7k	6.6	1.11		
P(C$_5$EG$_6$)12k	11.8	1.10		
P(C$_8$EG$_{13}$)3k	3.1	1.14		
P(C$_8$EG$_{13}$)5k	4.7	1.15		
P(C$_8$EG$_{13}$)8k	8.1	1.18		
PE(C$_4$EG$_3$)	4.0	1.50		
PE(C$_4$EG$_6$)	4.0	1.28		

Cell viability analysis

Cell culture

Experiments were performed on HeLa cells purchased from (Sigma-Aldrich, Taufkirchen, Germany). They were maintained in DMEM-F12 supplemented with 10% fetal bovine serum (FBS) and 10,000 units penicillin and 10 mg/ml streptomycin (Sigma-Aldrich). During culture as well as experiment, cells were kept at 37 °C and 5% CO_2 in a saturated humid atmosphere. Cell density never exceeded 80% confluence. For cell viability analyses 10,000 cells/well were seeded on 98 well plates one day before the experiments.

Viability analysis

Prior to experiments, AAP stock solutions were diluted with DMEM-F12 (Sigma-Aldrich) without serum supplement at a concentration of 0.1 w/w%, 0.2 w/w%, 0.25 w/w%, 0.5 w/w%, and 1 w/w% and cells were incubated in AAP solutions for 48 h at 37 °C. As control samples, cells without any treatment were used. Subsequently, cells were washed with PBS followed by treatment with 0.04 % trypsin/EDTA for 3 min at 37°C and 5% CO_2. The optained suspensions of single cells were incubated with 0.5 µl of LIVE/DEAD fixable cell staining (ThermoFischer Scientific, Waltham, MA, USA) for 30 min at 37°C to detect vital cell populations by flow cytometry (CytoFLEX S from BeckmanCoulter Life Sciences, Brea, CA, USA). For dye excitation, 488 nm solid state laser was used. For signal detection, the band pass filter 585/42 was used. To distinguish between healthy and dead cell populations, cells without treatment were compared with cells treated with 2.5 v/v% ethanol for 30 min.

Pulsed-Field Gradient NMR experiments

Sample preparation

Dry lipids were dispersed in D2O at concentration of 20 mg/mL for 30 min above lipid transition temperature, followed by 5 freeze/thaw cycles. Large Unilamellar vesicles (LUV) were prepared from this dispersion using an Avanti miniextruder. The vesicles were extruded 21 times through a 100 nm polycarbonate membrane and afterwards 21 times through a 50 nm membrane, while the lipid was above its phase-transition temperature. AAPs were dissolved in D2O and added to LUV solution directly before measurements.

Method

The PFG NMR is a powerful and promising approach to study the mobility and exchange processes on molecular scale. The method provides an access to the molecular mobility of all components containing specific resonance nuclei (typically hydrogen) by variation of the

observation time Δ in a range from ten to a few hundreds ms.[15,16] With this the distinction between the hydrogens of the external phase (free polymer) and the phase interacting with the liposome (integrated polymer as membrane bound and located inside of the vesicle) is possible. A kinetic PFG NMR experiment with exclusive detection of the integrated fraction by using fixed pulsed gradient value gives direct access to the permeation process.[17]   This technique is applied for the exchange processes with a characteristic time larger than maximal possible Δ.
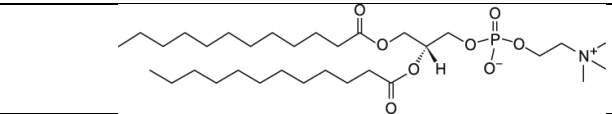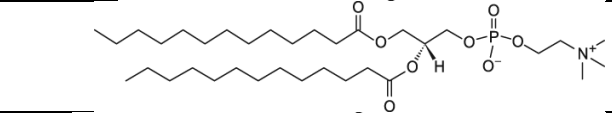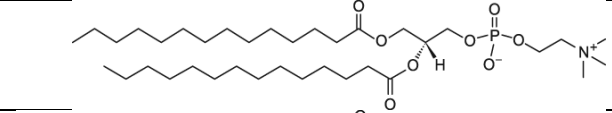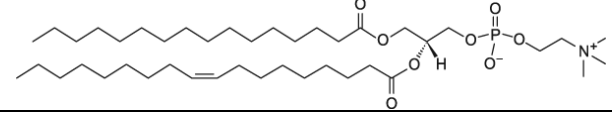
The PFG NMR measurements were performed using a Varian 600 MHz system equipped with diffusion ^{1}H probe head. The attenuation of the spin echo signal from a pulse sequence containing a magnetic field gradient pulse is used to measure the translational diffusion of the molecules (hydrogens) in the sample at the time scales from ten to a few hundreds milliseconds. During this time hydrogens are able to overcome the distances of order of hundreds of nanometers. Diffusion spin echo decays were measured using a standard stimulated echo (STE) pulsed field gradient sequence[26] with convection compensation in the temperature range from 15 to 35 °C Observation times Δ were equal to 100 ms. The gradient pulse length δ was 2 ms. The kinetic PFG NMR measurements were performed at gradient pulse amplitude G chosen such that only the integrated polymer is observed. Number of scans per point were chosen depending on the kinetic rates, from 4 scans for the fastest processes to 128 scans for the slowest. The amplitude of spin echo was determined as a function of time.

For all polymers and liposome, the self-diffusion coefficients were measured in separate conventional PFG-NMR experiments on their aqueous solutions prior to the translocation experiments. The relaxation times T_1 and T_2 have typical values of 1 and 0.5 s for all sample types allowing conventional diffusion measurements at the time scale of order of 0.5-1 s.

Fit method of kinetic data

The PFG-NMR data were fitted using Bayesian inference using the Markov Chain Monte Carlo (MCMC) method as implemented in the Python package *emcee*.[27] An uninformative prior was used. It allows to look for a probability distribution of all possible solutions which can be visualized using the Python module *corner.py* module. As an example Figure S5.4 shows the Corner plot of the fit for P(C$_4$EG$_4$)5k to identify dependencies and errors. Radii of LUVs and bilayer thicknesses used for the fits are shown in Table 2.

Table 5.2. Characterization of phospholipids and LUVs made of them. Tc is the lipid transition temperature, d is the bilayer thickness,[21] R is the LUV radius. R was measured by DLS (Malvern Zetasizer Nano ZS apparatus with a backscattering set up (ϑ = 173°) and a He-Ne laser of the wavelength λ = 633 nm). The LUV were dilluted by D_2O to the concentraion of 1 mg/mL and measured at 25°C. Additional measurements in the temperature range of 15 − 35 °C proved that R changes in this range only marginally.

Lipid	Chemical structure	T_c, ºC	d, nm	R, nm
12:0 PC (DLPC)		-2	3.26	35
13:0 PC		14	3.47	37
14:0 PC (DMPC)		24	3.67	39
16:0-18:1 PC (POPC)		-2	3.91	44

Fluorescent microscopy

Giant unilamellar vesicles (GUV) preparation

GUVs were prepared by electroswelling.[28] Two indium tin oxide coated glass slides were covered by 40 uL of 1 mg/mL DLPC solution in chloroform containing about 1% of 1,1'-dioctadecyl-3,3,3',3'- tetramethylindodicarbocyanine (DiD). The DiD was used to fluorescently label the bilayer but was not always needed in the experiments. After chloroform was evaporated under vacuum, two slides were placed vertically in a Teflon holder with ~2mm spacer in between. The volume between the slides was filled with 150 mM sucrose solution in water. The electroswelling took place under AC voltage of 10 Hz frequency and 1.1 V amplitude during 1.5 hours.

Synthesis of P(C4EG4)6k –coumarin

The 7-(diethylamino)-coumarin functionalized polymer P(C4EG4)6k-coumarin was synthesized following a procedure described in literature.[29] Polymer P(C4EG4)6k was first dried under high vacuum conditions for 3 days. This polymer contains according to the ^{1}H-NMR analysis 63 % of OH-end groups and 37 % of carboxylic acid end groups. A sample of 468 mg (0.120 mmol OH-end groups, 0.071 mmol COOH-end groups) was dissolved in 2.38 g of dry toluene inside a glove box.

A separate flasks equipped with a Teflon stopcock was charged inside a glove box with 7-

(diethylamino)-coumarin-3-carbonylazid (Sigma-Aldrich, ≥95%) (6.2 mg, 0.0217mmol) and 1.96 g of dry toluene. The mixture was frozen in liquid nitrogen and the argon gas was pumped off at a vacuum line. Then the mixture was heated to 100 °C for 12 min. in order to carry out the rearrangement to 7-(diethylamino)-coumarin-3-isocyanate. 1.71 g of the 7-(diethylamino)-coumarin-3-isocyanate solution was added to the polymer solution. The mixture was stirred at 50 °C for 18 h and then cooled to 0 °C, where it became turbid. After centrifugation, the lower orange colored phase was isolated and washed 4 times with 10 mL of diethyl ether and 3 times with 8 mL of ethanol. The product $P(C_4EG_4)6k$-coumarin was finally dried under high vacuum conditions. Figure S5.5 shows the SEC refractive index and UV detector traces of $P(C_4EG_4)6k$-coumarin, proving the linkage of the 7-(diethylamino)-coumarin unit to polymer chains. Missing UV intensity at an elution time of ~30 min shows the quantitative removal of non-polymer bound low MW 7-(diethylamino)-coumarin compounds.

Fluorescent microscopy measurements

The fluorescence experiments were performed using Leica-manufactured Sp8i confocal laser scanning microscope. Five detectors (2 hybrid detectors *HyD* and 3 photomultiplier tubes *PMT*) allow for the simultaneous detection of different, user-selectable wavelengths while the white-light laser can provide up to 8 lines for excitation, along with a 405 nm UV laser diode. Sampling frequency and resolution are selectable using the Leica LAS X software. For imaging of 7-(diethylamino)coumarin the excitation wave length was 405 nm (UV laser diode), the emitted light was detected with the PMT detector in the wavelength range of 420-455 nm.

5.6 Supporting Information

LCST behavior of AAP in water
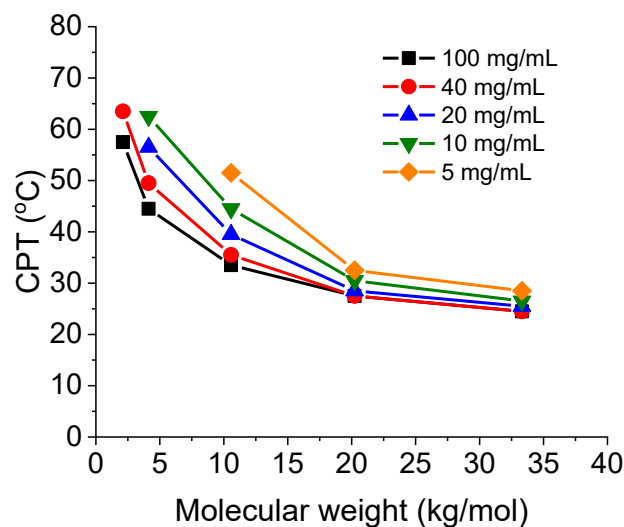
Figure S5.1. Dependence of cloud point temperature (CPT) on the molecular weight for P(C₄EG₄) at different concentrations.

Unilamellarity of lipid vesicles
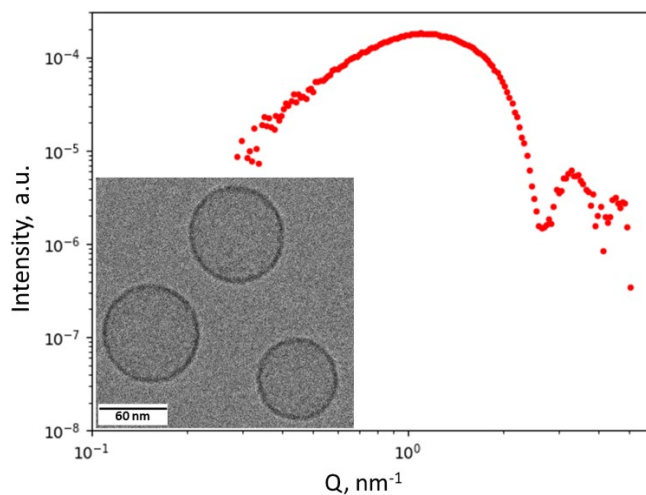
Figure S5.2. Unilamellarity of lipid vesicles was tested by SAXS and cryo-TEM. Data is shown for POPC vesicles prepares by extrusion as described above. SAXS shows smooth curve specifically below 1 nm^{-1} where SAXS is sensitive to multilamellar contributions. The inset shows cryo-TEM images of POPC vesicles.

LUV stability
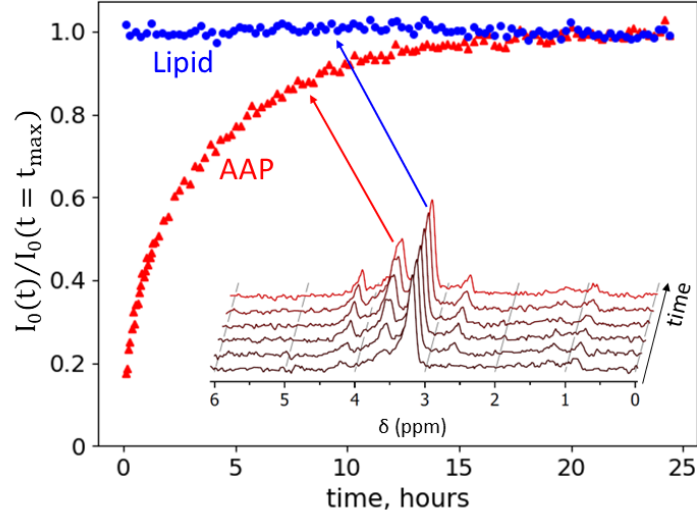
Figure S5.3. LUV stability can be monitored similar as described in the main text (see Fig 1B+C). Looking at the specific lipid peak at ≈3.2 ppm we can follow the LUV time evolution. We observe a constant value indicating that the LUV diffusion is constant over the whole experimental time. This indicates that we have a stable LUV solution without significant flocculation or fusion. We observed also no visible sign of aggregation or flocculation. The diffusion coefficient of the LUV without AAP was also measured as a reference (using full PFG NMR spectra) and was the same as for LUV in presence of AAP.

Examples of Corner plots
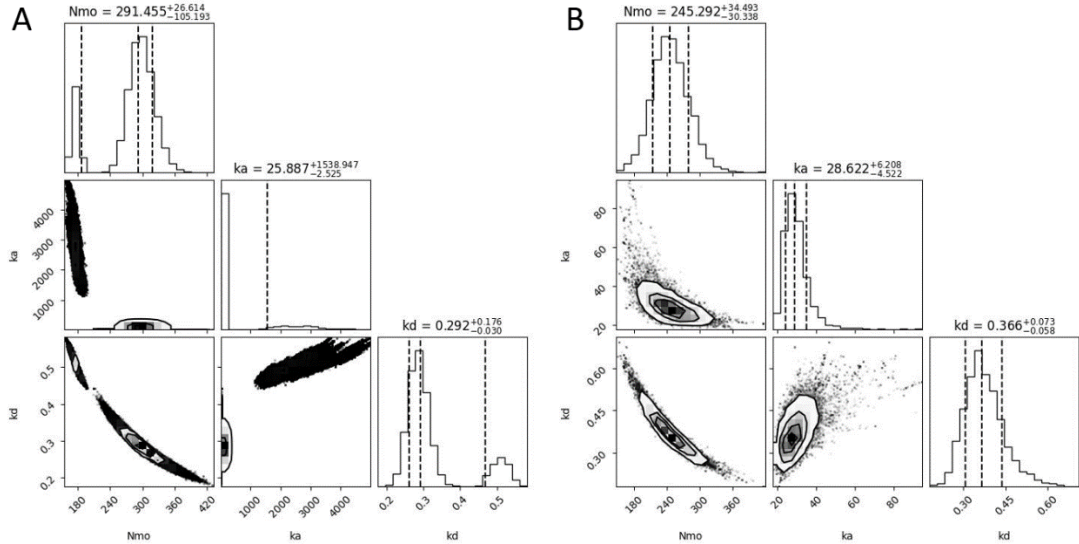
Figure S5.4. Corner plot visualization of emcee fit for the polymer P(C$_4$EG$_4$)5k in a wide range of parameters (A) and focused in the range where the most probable solutions are located (B).

SEC traces of P(C₄EG₄)6k-coumarin
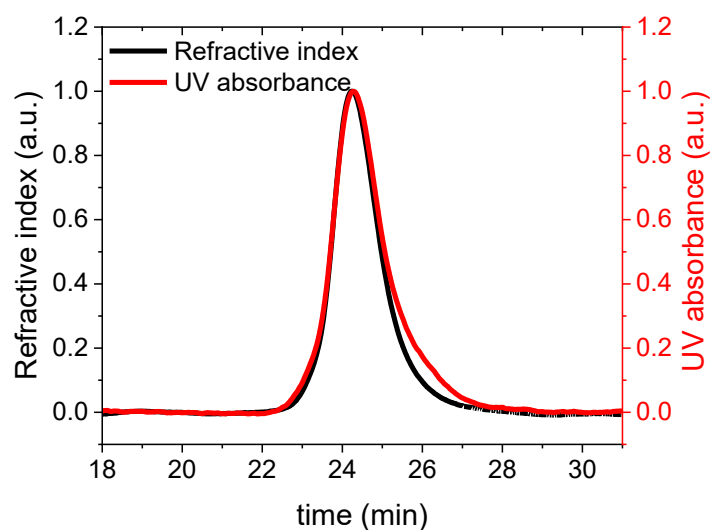
Figure S5.5. SEC traces of P(C₄EG₄)6k-coumarin; black: refractive index signal, red: UV signal at 350 nm.

Desorption rate measurements
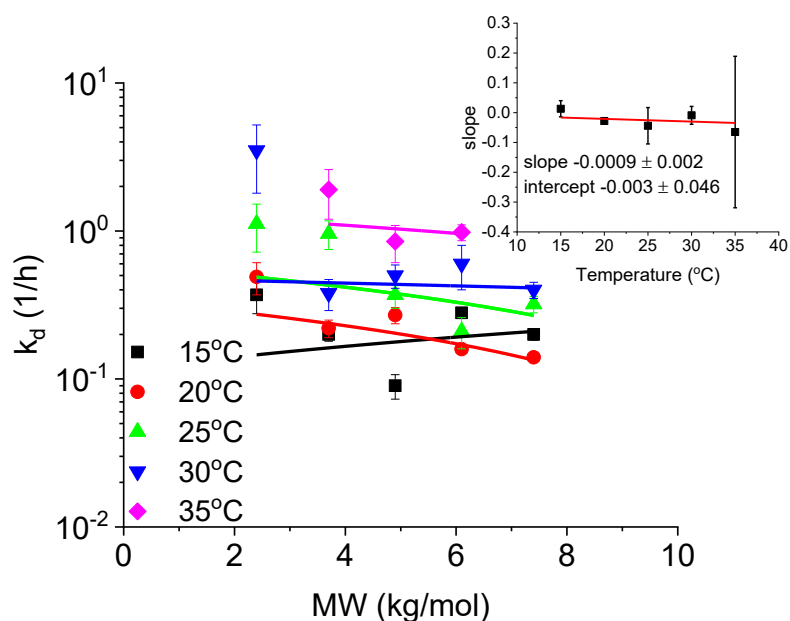
Figure S5.6 Dependence of k_d on the AAP molecular weight measured for different temperatures, the solid lines represent fits with linear function; the insert shows slope values obtained from the fits at different temperatures, the linear fit of it proves that k_d shows not more than a slight dependence on the AAP MW.

Fluorescent microscopy of GUV with 7-(diethylamino)coumarin
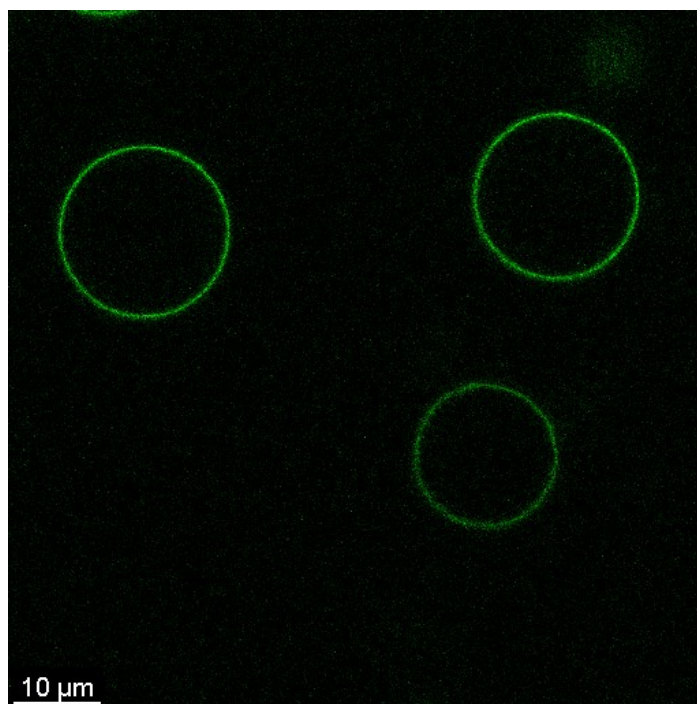
Figure S5.7 Fluorescence microscopy image of a GUV prepared from DMPC after the addition of 7-(diethylamino)coumarin at T=25ºC.

Fluorescent microscopy of GUV with 7-(diethylamino)coumarin

5.7   References

[1]   N. J. Yang, M. J. Hinner, *Methods Mol. Biol.* **2015**, *1266*, 29–53.

[2]   D. Pei, *Acc. Chem. Res.* **2022**, *55*, 309–318.

[3]   R. O. Ryan, *Expert Opin. Drug Deliv.* **2008**, *5*, 343–351.

[4]   L. Colombeau, S. Acherar, F. Baros, P. Arnoux, A. M. Gazzali, K. Zaghdoudi, M. Toussaint, R. Vanderesse, C. Frochot, *Top. Curr. Chem.* **2016**, *370*, 113–134.

[5]   C. A. Lipinski, F. Lombardo, B. W. Dominy, P. J. Feeney, *Adv. Drug Deliv. Rev.* **1997**, *23*, 3–25.

[6]   S. A. Wheaten, F. D. O. Ablan, B. L. Spaller, J. M. Trieu, P. F. Almeida, *J. Am. Chem. Soc.* **2013**, *135*, 16517–16525.

[7]   P. G. Dougherty, A. Sahni, D. Pei, *Chem. Rev.* **2019**, *119*, 10241–10287.

[8]   T. Goda, Y. Miyahara, K. Ishihara, *J. Mater. Chem. B* **2020**, *8*, 7633–7641.

[9]   N. Morimoto, M. Wakamura, K. Muramatsu, S. Toita, M. Nakayama, W. Shoji, M. Suzuki, F. M. Winnik, *Biomacromolecules* **2016**, *17*, 1523–1535.

[10]   F. Mathot, A. Schanck, F. Van Bambeke, A. Ariën, M. Noppe, M. Brewster, V. Préat, *J. Control. Release* **2007**, *120*, 79–87.

[11]   M. Werner, J.-U. Sommer, V. A. Baulin, *Soft Matter* **2012**, *8*, 11714.

[12]   M. Werner, J. U. Sommer, *Biomacromolecules* **2015**, *16*, 125–135.

[13]   J. B. Schneider, G.; Allgaier, J.; Fleury, *Translocation of Synthetic Polymers by Lipid Membranes*, **n.d.**, European Patent WO2018065583, April, 12, 2018.

[14]   E. Kostyurina, J. U. De Mel, A. Vasilyeva, M. Kruteva, H. Frielinghaus, M. Dulle, L. Barnsley, S. Förster, G. J. Schneider, R. Biehl, J. Allgaier, *Macromolecules* **2022**, *55*, 1552–1565.

[15]   W. S. Price, W. S. Price, *NMR Studies of Translational Motion: Principles and Applications*, Cambridge University Press, **2009**.

[16]   P. T. Callaghan, *Principles of Nuclear Magnetic Resonance Microscopy*, Clarendon Press, **1993**.

[17]   A. Leson, S. Hauschild, A. Rank, A. Neub, R. Schubert, S. Förster, C. Mayer, *Small* **2007**, *3*, 1074–1083.

[18]   W. Nernst, *Zeitschrift für Phys. Chemie* **1891**, *8U*, 110–139.

[19]   a. D. Mc Naught, A. Wilkinson, *Compendium of Chemical Terminology-Gold Book*, International Union Of Pure And Applied Chemistry (IUPAC), **2012**.

[20]   M. Sogami, S. Era, M. Murakami, Y. Seo, H. Watari, N. Uyesaka, *Biochim. Biophys. Acta -*

Biomembr. **2001**, *1511*, 42–48.

[21]   N. Kučerka, M.-P. Nieh, J. Katsaras, *Biochim. Biophys. Acta - Biomembr.* **2011**, *1808*, 2761–2771.

[22]   J. Frallicciardi, J. Melcr, P. Siginou, S. J. Marrink, B. Poolman, *Nat. Commun. 2022 131* **2022**, *13*, 1–12.

[23]   K. Akabori, J. F. Nagle, *Soft Matter* **2015**, *11*, 918.

[24]   K. Sengupta, V. A. Raghunathan, J. Katsaras, *Phys. Rev. E* **2003**, *68*, *031710*

[25]   K. Honda, H. Kimura, *J. Phys. Soc. Jpn.* **2013**, *60*, 1212–1215.

[26]   E. O. Stejskal, J. E. Tanner, *J. Chem. Phys.* **2004**, *42*, 288.

[27]   D. Foreman-Mackey, D. W. Hogg, D. Lang, J. Goodman, *Publ. Astron. Soc. Pacific* **2013**, *125*, 306–312.

[28]   D. S. Dimitrov, M. I. Angelova, *J. Electroanal. Chem. Interfacial Electrochem.* **1988**, *253*, 323–336.

[29]   K. Kuramochi, S. Yukizawa, S. Ikeda, T. Sunoki, S. Arai, R. Matsui, A. Morita, Y. Mizushina, K. Sakaguchi, F. Sugawara, M. Ikekita, S. Kobayashi, *Bioorg. Med. Chem.* **2008**, *16*, 5039–5049.

6 Influence of polymer properties on translocation

Abstract

In the previous chapter, it was shown that the translocation mechanism is similar for all the investigated alternating amphiphilic polymers (AAPs). It consists of two steps: relatively fast adsorption to the lipid membrane and slower desorption of the polymer molecules from it. Moreover, the adsorption rate and equilibrium concertation of the AAP in the membrane strongly depend on its molecular weight. It also was shown that the translocation depends on temperature and lipid composition and a thermodynamic model of the translocation process was developed. In this chapter, the influence of the AAP hydrophobic/hydrophilic unit lengths and of the overall AAP polarity on the translocation behavior is systematically examined using Pulsed-Field Gradient (PFG) NMR. The increase of the AAP unit length leads to faster adsorption and a larger number of adsorbed polymer chains, but to a slower desorption process. The AAPs with the longest units show behavior similar to triblock copolymers having one hydrophobic and two hydrophilic blocks. On the other side, the increase of the AAP polarity leads to the decreasing rate of both translocation steps as well as of the concentration in the membrane. Neutron reflectometry experiments allowed to obtain information about the interaction of the polymer with the membrane on the molecular level and to compare the adsorption behavior of the AAP having short units with the one of the amphiphilic triblock copolymer. It was shown that the triblock copolymer adsorbs to the membrane only by its hydrophobic part leaving the hydrophilic chains outside, whereas the AAP fully solubilizes in the hydrophobic interior of the membrane. Understanding the influence of the polymer properties on translocation opens the abilities to tune the AAP for use in a wide range of biomedical applications.

6.1 Introduction

Based on the knowledge of membrane translocation mechanisms, mostly small molecules of moderate polarity can cross lipid membranes passively, whereas macromolecules translocate through the membrane mostly via endocytosis pathways. However, amphiphilic polymers of the right polarity were shown to be an exception. A couple of synthetic polymers were reported to translocate through the lipid membrane.[1–3] However, apart from the computer simulation studies,[4,5] only in our work the influence of polymers and membrane properties on translocation were systematically studied.[3] We showed that non-ionic alternating amphiphilic polymers (AAP) generally can passively cross lipid bilayers. The translocation process was found

to consist of fast adsorption to the membrane and slow desorption. The adsorption rate and the concentration of polymers in the membrane were shown to strongly decrease with increasing polymer molecular weight, whereas the desorption rate stayed constant. The lipid membrane composition and temperature we also found to influence the translocation, and the temperature measurements helped to understand the basic thermodynamics of the translocation process. A unique advantage of AAPs compared to most other polymers is the ability to tune their polarity continuously and over a very broad range by varying the length ratio of the hydrophobic and hydrophilic units. The variation of the overall segment lengths yields polymers with a homogeneous polarity profile for short segments. For larger segments, the products are more block copolymer like. This ability is useful not only for applications but also for a general understanding of the macromolecular translocation mechanisms and mechanisms of interaction with a lipid membrane.

The first aspect which is studied is the length of the hydrophobic/hydrophilic units. The AAPs with short units have a nearly homogeneous polarity profile along the chain (e.g. compared to membrane thickness or tail length), whereas the increase of the hydrophobic and hydrophilic units leads to a more distinct polarity profile. It is expected to influence the translocation because increasing the hydrophobic unit leads to a stronger interaction with the lipid bilayer and therefore stronger adsorption. However, the increase of the hydrophilic units yields polymers for which entering the bilayer interior is energetically less favorable. This might slow down or even restrict both the adsorption and translocation. The extreme case are di- and triblock copolymers which interact with lipid membranes via the hydrophobic blocks,[6] but only some diblocks with rather short hydrophilic chains were reported to translocate.[2] We studied the influence of AAP unit length using amphiphilic triblock copolymer as a limiting case. In order to get more precise information on the interaction of polymers with the membrane, we studied the polymer-membrane system by neutron reflectometry (NR) and small angle neutron scattering (SANS).

It was shown in the previous chapter that the AAPs show an LCST behavior that can be tuned in a wide range by varying hydrophobic/hydrophilic unit length and unit length ratio.[7] The LCST, therefore, is a measure of the overall polarity of the AAP. Because in medical applications there is a need for the compounds to work at body temperature, AAPs with LCST values above 40 degrees are required. Additionally, if there is a need to connect hydrophobic molecules to the AAP in order to increase their water solubility and transport them through the membrane, AAPs

with higher LCSTs are useful so that the adduct stays water soluble. Therefore, we study how AAP hydrophilicity (or LCST) influences translocation behavior.

6.2   Results and discussions

To study the influence of AAP unit length on translocation through lipid membranes we examined the translocation kinetics of five AAPs having different unit lengths and of EO/PO triblock copolymer (Pluronic-F127) as a limiting case (Table 6.1 left). The measurements were performed by time-resolved PFG NMR as described in Chapter 4 using POPC vesicles of 44 nm radius.

Table 6.1. AAP compositions and corresponding LCST values used for the translocation experiments for studying the effect of the hydrophobic/hydrophilic unit length (left) and of the polymer polarity (right).

AAP composition	LCST, °C	AAP composition	LCST, °C
$P(C_4EG_4)$	26	$P(C_4EG_4)$	26
$P(C_5EG_6)$	42	$P(C_4EG_9)$	64
$P(C_8EG_{13})$	43	$P(C_5EG_6)$	75
$P(C_{10}EG_{22})$	35		
$P(C_{14}EG_{47})$	60		
Pluronic-F127			

Figure 6.1A shows kinetic curves for three different polymers having similar molecular weights. The signal intensity is proportional to the sum of polymers attached to the membrane and translocated to the inside of the vesicle. Fitting the results allows to separate these two contributions as shown in Figure 6.1B. The two AAPs $P(C_4EG_4)$ and $P(C_{10}EG_{22})$ show similar behavior with slower translocation and larger adsorption for the AAP having longer hydrophilic and hydrophobic units ($P(C_{10}EG_{22})$). Surprisingly, Pluronic also clearly shows a slow translocation behavior, which was never reported before. Number of polymers in the inner part of the vesicle changes similarly for Pluronic and $P(C_{10}EG_{22})$13k. However, taking much higher Pluronic density at the lipid membrane into account (Figure 6.1B), its desorption rate is much smaller. This small translocation rate might be a reason why the translocation of Pluronic was not observed in other experiments.
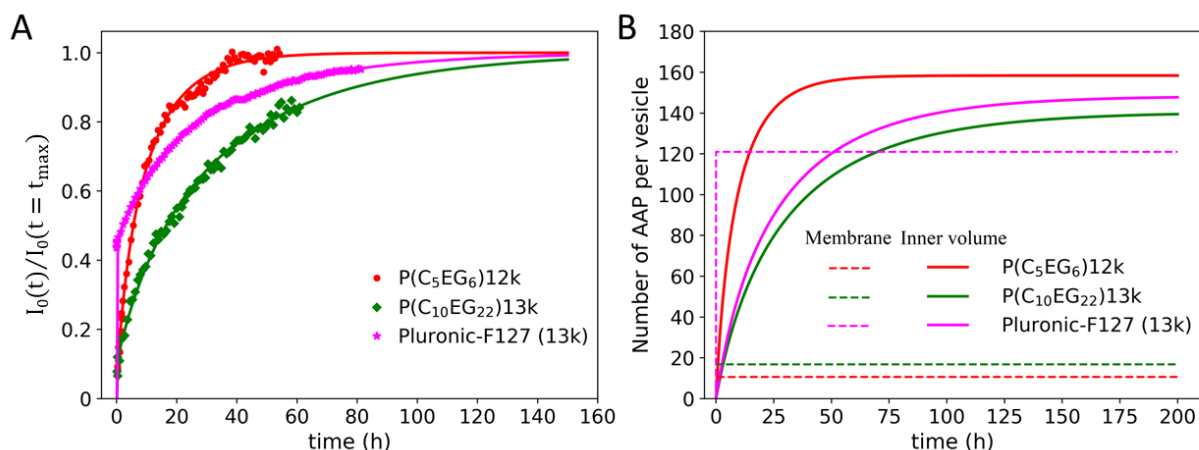
Figure 6.1. A: Translocation kinetics for two different AAPs and Pluronic-F127 measured by time resolved PFG NMR. B: Kinetics of membrane and inner LUV volume saturation reconstructed after the fit of kinetic curves from Figure A. The curves show the polymer number in the membrane and in the inner volume per vesicle. The membrane is saturated after less than an hour.

Figure 6.2 shows the desorption rate k_d for polymers of different compositions. It was shown in the previous chapter that k_d shows no more than a small dependence on the AAP molecular weight. Therefore, for the polymers $P(C_4EG_4)$, $P(C_5EG_6)$, and $P(C_8EG_{13})$ average error-weighted values of k_d were used for the comparison of different AAP compositions (Figure 6.2). The average k_d values of these polymers show a small trend towards reduction of k_d with increasing the AAP unit lengths (Figure 6.2B). The effect gets increasingly stronger for $P(C_{10}EG_{22})$, $P(C_{14}EG_{47})$, and Pluronic, so we can conclude that increasing the unit lengths leads to slower desorption. For $P(C_{10}EG_{22})$, $P(C_{14}EG_{47})$ only one MW could be measured because smaller molecular weight AAPs having these long units have only a few repeat units per chain, whereas larger molecular weight AAPs have too slow kinetics.

The adsorption rates k_a for the AAPs $P(C_4EG_4)$, $P(C_5EG_6)$, and $P(C_8EG_{13})$ show a strong dependence on the polymer molecular weight, but no significant difference from each other (Figure 6.3A). However, a trend of decreasing slope with increasing unit length can be observed. Both $P(C_{14}EG_{47})16k$ and the EO/PO triblock show the k_a value similar to the ones of 3-5 kg/mol AAPs with shorter units. For the AAPs of the molecular weight larger than 8-9 kg/mol, other than $P(C_{14}EG_{47})$, the k_a cannot be determined because of the relatively small concentration in the membrane and the small signal-to-noise ratio of the first measurement points.
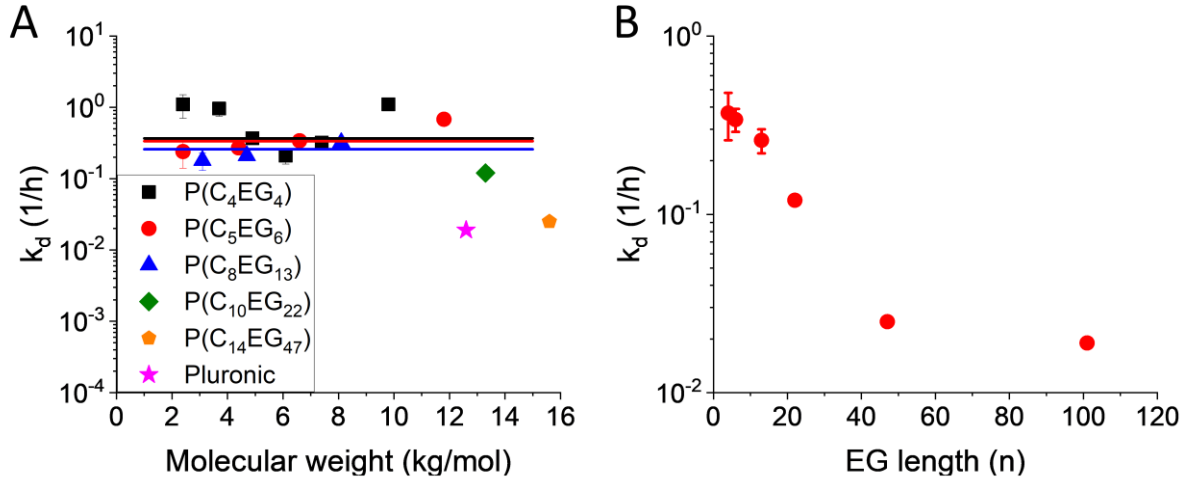
Figure 6.2. A: Dependence of k_d on polymer molecular weight for different polymer compositions. Solid lines: fits of the data assuming no MW dependence. B: Dependence of the average k_d values obtained from Figure A as a function of the hydrophilic unit length (given as the polymerization degree of the polyethylene glycol units).

The partitioning of polymers between membrane and water strongly depends on polymer MW (Figure 6.3B). For the polymer concentration in water of 1 wt% the corresponding concentrations in the membrane vary in the range of 0.1 – 10 wt%. Fitting the dependences with the same slope gives intercepts which slightly increase with unit lengths, meaning larger interaction with the membrane for polymers equipped with longer units. P($C_{10}EG_{22}$), P($C_{14}EG_{47}$), and Pluronic follow this trend. In order to understand the dependences of the polymer unit length on the translocation parameters, we study the polymer location in the membrane by reflectometry and SANS.
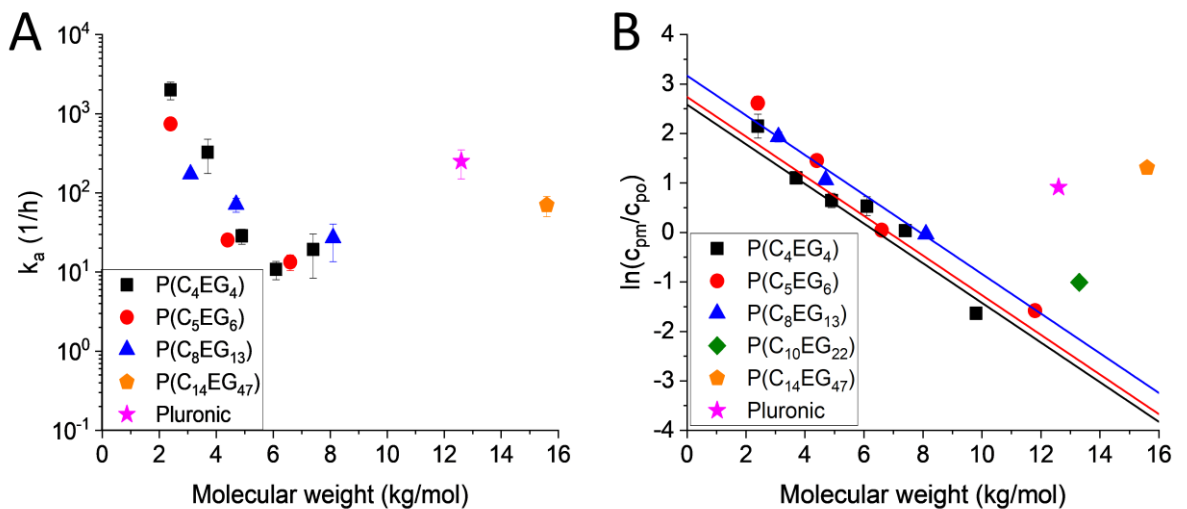
Figure 6.3. Dependence of k_a (A) and of polymer concentration in the membrane (B) on polymer molecular weight for different polymer compositions. For P($C_{10}EG_{22}$) the data quality does not allow to access the reliable value of k_a.

The location of the polymers at the membrane was examined by neutron reflectometry which allows us to get the scattering length density (SLD) profile of the membrane and detect the polymer location in it. $P(C_4EG_4)$ and EO/PO triblock were examined as extreme cases. The membrane was prepared by vesicle fusion on Si/SiO substrate. High contrast between the polymer and membrane was obtained by using deuterated lipids (POPC-d82) and hydrogenous polymers in D_2O. The polymer in or at the membrane reduces the SLD of the lipid region or of the adjacent solvent significantly dependent on its location. The experiments at different concentrations show that $P(C_4EG_4)2k$ is fully solubilized in the hydrophobic interior of the membrane (see Figure 6.4). The concentration of polymer in the tail region calculated from the SLD profile is 4% and 25% for the outside polymer concentration of 1% and 5% respectively. These values are approximately in agreement with the values obtained from the PFG NMR. In contrast, Pluronic enters the membrane by its hydrophobic middle block and leaves the hydrophilic outer blocks in the aqueous environment (see Figure 6.5). Therefore, only a fraction of the polymer is located in the membrane and more polymer chains can be adsorbed without losing much entropy. Again the results are in agreement with the high pluronic concentration in the membrane obtained by the PFG NMR (Figure 6.3B).

Figure 6.4. A: Neutron reflectivity curves (symbols) and fits (lines) for a fully deuterated POPC lipid bilayer in D_2O (green) and after incubation with $P(C_4EG_4)2k$ of 1 wt% and 5 wt% concentration (blue and red respectively). Solid lines represent the fits with a solvent penetration model. B: Scattering length density profiles obtained from the fit. We observe that the AAP is mostly localized in the tail region of the membrane and homogeneously distributed there.
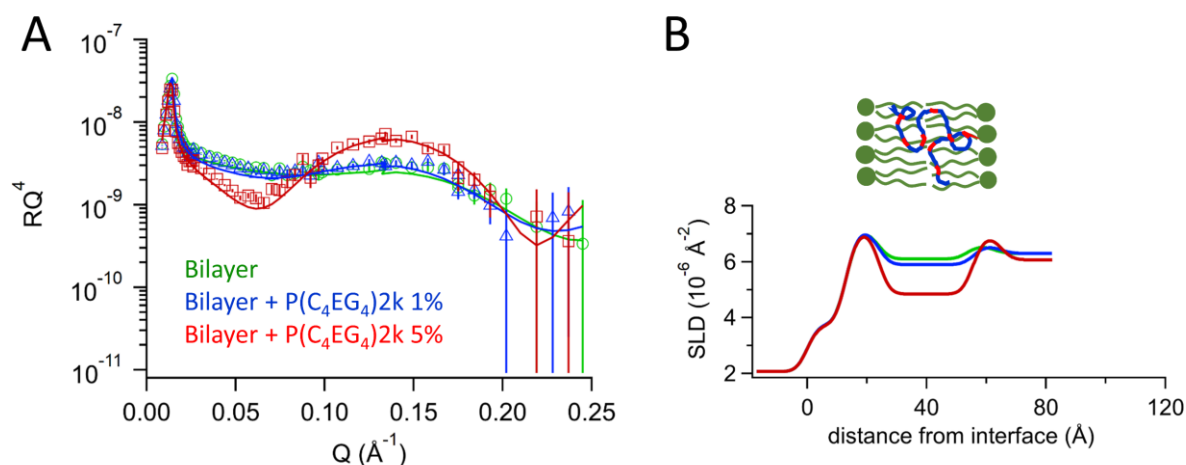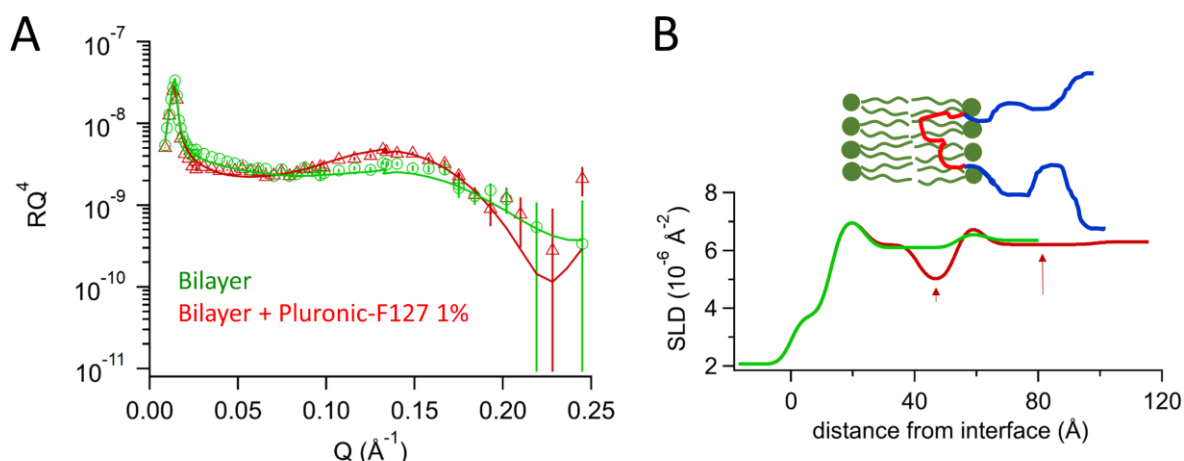
Figure 6.5. Neutron reflectivity curves (symbols) and fits (lines) for a fully deuterated POPC lipid bilayer in D_2O (green) and after incubation with Pluronic-F127 of 1 wt% concentration (red). Solid lines represent the fits with a solvent penetration model. B: Scattering length density profiles obtained from the fit. We observe a 36 Å extended layer with a reduced SLD at the outer surface of the bilayer and a remarkable reduction at the outer tail region.

The strong interaction of $P(C_{14}EG_{47})$ with the lipid membrane can now be explained on the basis of the neutron reflectivity results. The long PEG units of this polymer are expected to prevent solubilization of the whole chains inside the hydrophobic membrane interior. On the other hand, for AAPs with increasing length of the hydrophilic units loop formation is entropically less disfavored. This makes configurations where some EG units are outside of the membrane more favorable and increases the number of attached polymers as we observe it in the PFG-NMR study (Figure 6.3B). In this way also the large k_a value of $P(C_{14}EG_{47})$ can be explained if it firstly is adsorbed by only one hydrophobic unit, similar to Pluronic. Both the adsorption rate and the partition coefficient of $P(C_{14}EG_{47})$ are even larger than those of Pluronic. The reason for this might be the smaller size of the AAP hydrophobic units than the PPO block of Pluronic, as well as their different interaction energies with water and with the membrane interior.

In the cause of AAP with small units the hydrophilic chains can solubilize in the membrane interior together with hydrophobic units. Therefore, the chain translocate as a whole, firstly solubilizing in the membrane and then desorbing. However, in the case of pluronic its hydrophilic blocks are located mostly outside of the membrane and cannot fully solubilize in the membrane interior. Together with very low translocation rate it lets us assume that the translocation for pluronic happens in three steps: adsorption, flip-flop of a hydrophilic units to the opposite side, and finally desorption. The lipid flip-flop rate in model membranes is rather slow ($> 1\ h^{-1}$),[8] however, Pluronics are known to increase lipid flip-flop dramatically by disordering the lipid membrane.[9] For a disordered membrane with a high lipid flip-flop rate, the chances of Pluronic

to flip-flop, and thereby translocating, also increase. For Pluronic, one of the hydrophilic chains has to flip-flop first and therefore Pluronic will be trapped in the membrane until the second chain follows, which adds additional time to the translocation process. We assume that with increasing the length of the hydrophilic units a similar situation happens and stepwise hydrophilic units flip-flop. Although the number of flip-flops per AAP chain needs to be larger, the smaller EG units compared to the ones of investigated Pluronic, make the process easier. If the units are small enough the picture changes from a chain of individual units to a chain with an average hydrophobicity that can easier be distributed inside of the tail region.

In addition, we used SANS to study the changes in the bilayer structure caused by the incorporated polymer. To achieve the best contrast conditions we measured vesicles made of tail deuterated lipids in D_2O in combination with hydrogenous polymers. The strong spatial correlation between the hydrogenous lipid head groups results in strong bilayer correlation peaks at high Q (first order peak at 1 - 2 nm^{-1}; second order peak at 2.5 - 4 nm^{-1}). Nevertheless, such measurements are still very challenging because of the strong incoherent neutron scattering background at the respective Q range. For all AAPs and Pluronic the second order correlation peak was suppressed, and an additional increase of the intensity above 4 nm^{-1} was observed (Figure 6.6B,C). This effect can be described by including thickness fluctuations in the model of unilamellar vesicles (Figure 6.6A). For the longest AAP (P(C_4EG_4)10k) a Debye-Waller like factor had to be included additionally to the thickness fluctuations to describe the data at high Q. The Debye-Waller like factor is widely used in crystallography to describe uncorrelated atom displacements due to thermal fluctuations, defects and any other distortions. In the case of the lipid membranes, it describes the local loss of correlations in the bilayer, whereas the thickness fluctuation parameter described correlated fluctuations. The values for obtained thickness fluctuations are presented in Table 6.2. Generally, there is a trend towards increasing thickness fluctuations with increasing polymer size. Considering that the hydrophobic part of Pluronic-F127 which is inserted in the bilayer has a molecular weight of 3.3 kg/mol, the thickness fluctuations that are causes roughly follow the AAP trend. The increased thickness fluctuations of the lipid bilayer are an indication of a distorted bilayer interior and a reason for the increased probability of lipid and, consequently, the flip-flops of polymers with long hydrophilic units.
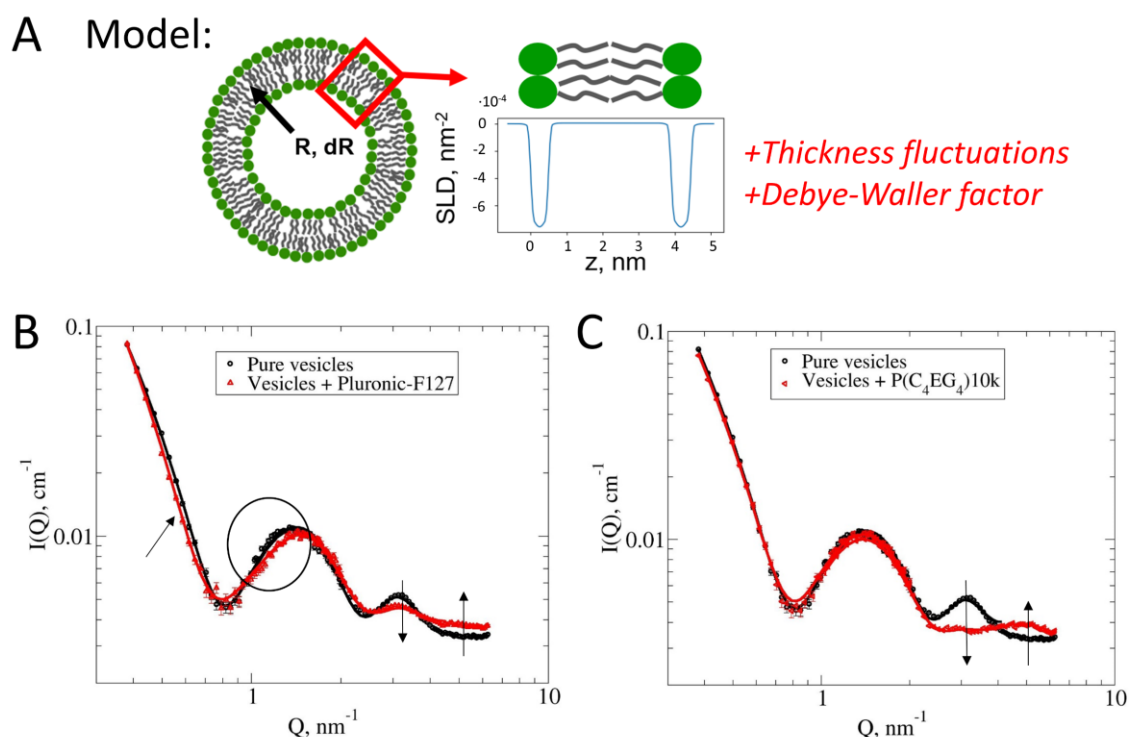
Figure 6.6. A: Model of lipid vesicles used to fit experimental SANS data. B: SANS data (symbols) and the best fits (lines) obtained with the model described above for pure solution of lipid vesicles and for vesicles with Pluronic. C: SANS data (symbols) and the best fits (lines) obtained with the model described above for pure solution of lipid vesicles and for vesicles with $P(C_4EG_4)10k$.

Table 6.2. Values for thickness fluctuations obtained from the fit of SANS curves.

System	Thickness fluctuations, nm
Pure vesicles	0.14 ± 0.05
Vesicles + $P(C_4EG_4)2k$	0.41 ± 0.01
Vesicles + $P(C_4EG_4)10k$	0.68 ± 0.01
Vesicles + $P(C_5EG_6)5k$	0.43 ± 0.01
Vesicles + Pluronic-F127	0.48 ± 0.02

The scattering curve of Pluronic has some additional features compared to the ones of the AAPs, such as additional asymmetry of the bilayer peak and changed curvature at lower Q (marked in Figure 6.6B). The minimal model which describes these features is the model from Figure 6.6A including one additional layer at the outside of the vesicle, having a slightly lower SLD than that of water. The fit curve which is shown in Figure 6.6B for Pluronic corresponds to this model. This is an indication of hydrophilic units located outside of the bilayer, similar to the scenario observed in neutron reflectometry. The other modifications of the model, like a similar layer on the inner surface of the membrane, or an asymmetric SLD profile of the tail region do not additionally improve the fit but do not exclude such possibilities.

Although these SANS results reported above fit to the general picture, they could not be reproduced later in a similar experiment. In that experiment, we observed no changes in SANS curves after the addition of AAP, as well as Pluronic.

Simulation studies predict the maximum translocation rate of amphiphilic polymer to occur at the point where the polymer hydrophobicity is balanced with the membrane. On both sides from this point, the translocation rate is predicted to decrease dramatically.[4,5] However, applications might require more hydrophilic membrane translocating polymers to keep a good water solubility at a higher temperature. In order to study the influence of polymer hydrophilicity on translocation, we measured the MW dependences of AAPs having different LCSTs (Figure 6.7). The hydrophobic unit of the polymers was kept the same and the hydrophilicity was changed by changing the length of the EG unit (Table 6.1 right). The polymers $P(C_4EG_4)$, $P(C_4EG_6)$, and $P(C_4EG_9)$ were measured having LCST of 26, 64, and 75 °C, respectively. From the study described above (Figure 6.2 and Figure 6.3) the unit length does not have a big influence in this range of unit lengths, therefore, the differences in Figure 6.7 come mostly from the LCST.

The decrease of k_a with increasing polymer LCST is resulting from the increase of free energy of adsorption ΔG_a (Figure 6.7C). With increasing LCST the polymer entropy is not expected to change a lot when the temperature is well below LCST, so the main effect comes from enthalpy changes. The polymers having larger LCSTs are better soluble in water and less soluble in the membrane interior. Therefore, the interaction parameter for them with water is smaller and with the membrane interior is larger, which lead to the increase of the adsorption enthalpy and consequently of the free energy. The desorption rate k_d shows a weak decrease with increasing LCST (Figure 6.7D). The reason for this effect is not clear yet. One of the possible explanations is the effect of the EG unit length which was shown above. This effect can be more pronounced for the more hydrophilic polymers.

The partition coefficient c_{pm}/c_{po} relates to k_a and k_d by[3]

$$\frac{c_{pm}}{c_{po}} = \frac{k_a}{k_d}\left(1 - \frac{n_{pm}}{n_{pmax}}\right)$$

This equation describes the balance between rates and concentrations corrected for the limited concentration inside the membrane. Here n_{pm} is the number of polymers in the membrane in equilibrium and n_{pmax} is the maximum number of polymers in the membrane, or membrane capacity. The observed behavior of the partition coefficients is in agreement with this equation and with the fact that more hydrophilic polymers are less soluble in hydrophobic environments.

Change from $P(C_4EG_4)$ (LCST = 26°C) to $P(C_4EG_9)$ (LCST = 75 °C) causes lower membrane solubility and slower adsorption and desorption processes. As a result the translocation process is slower by a factor of 10. But the hydrophilic polymer still translocates and can be used to transport hydrophobic molecules through the membrane.
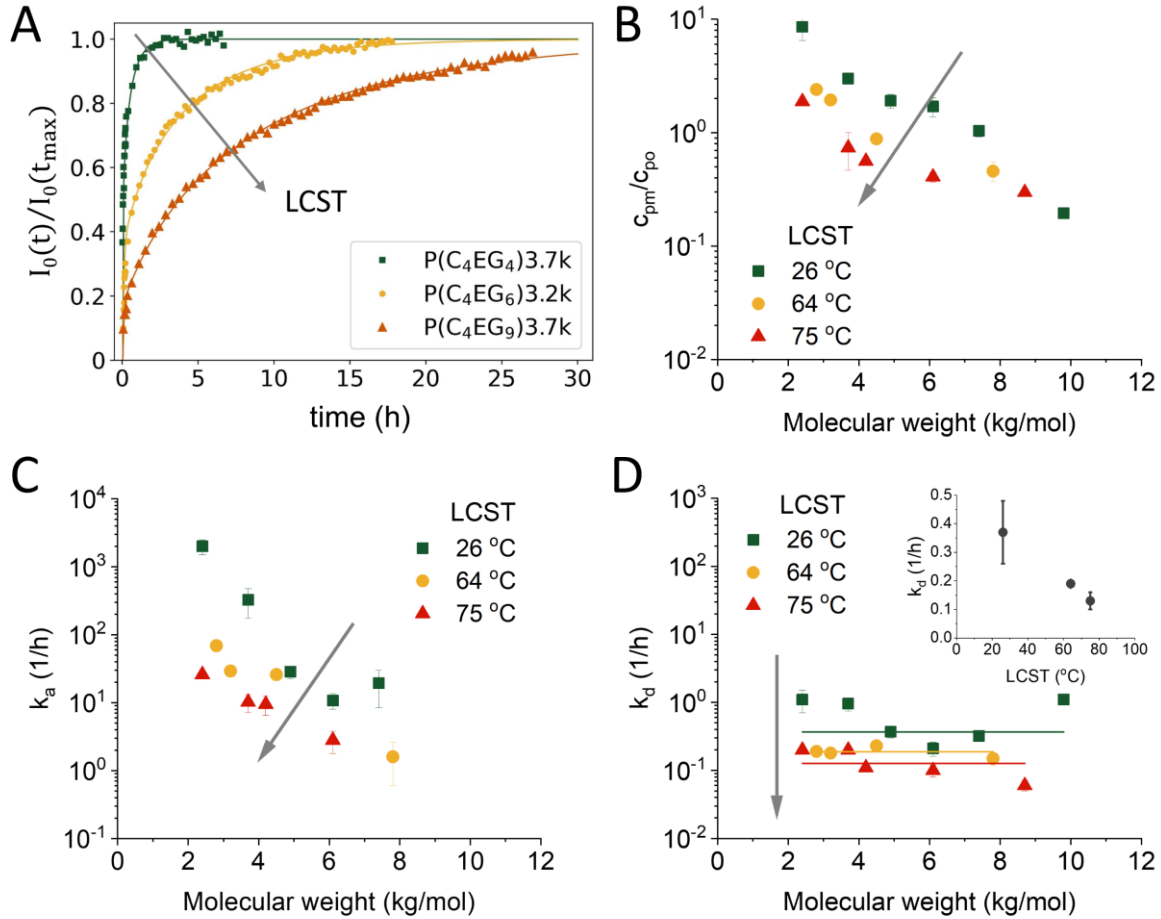
Figure 6.7. Dependence of polymer LCST on its translocation through POPC lipid membranes at t = 25°C. The polymers corresponding to the indicated LCSTs are $P(C_4EG_4)$, $P(C_4EG_6)$, and $P(C_4EG_9)$ having LCST of 26, 64, and 75 °C respectively. A: Kinetic curves for AAPs having similar MW and different LCST. B: Dependence of the partition coefficient c_{pm}/c_{po} on polymer MW for polymers having different LCSTs. C: Dependence of the adsorption rate k_a on polymer MW for polymers having different LCST. D: Dependence of the desorption rate k_d on polymer MW for polymers having different LCSTs The insert shows the dependence of the average k_d of polymer LCST. The grey arrow in all the plots shows the direction of LCST increase.

6.3   Conclusion

The presented results show that the translocation of the AAP through lipid membrane happens for a very wide range of AAP properties. Both the hydrophobic/hydrophilic unit length and the hydrophobicity influence the translocation parameters but do not restrict translocation completely, at least in the studied range of parameters. The increase of the hydrophobic/hydrophilic unit lengths leads to an increased adsorption to the lipid membrane in

combination with a decreased translocation rate. Also the triblock copolymer Pluronic, which was proven to passively translocate through the lipid membrane, follows this trend. These findings correlate with the simulation results on random amphiphilic copolymers.[5] Random copolymers where the maximum unit length is fixed to a small value behave similarly to homopolymers, which show smaller adsorption to the membrane and larger translocation rate around the point of balanced hydrophobicity. On the opposite, random copolymers containing longer hydrophobic and hydrophilic units better adsorb to the membrane due to the ability of loop formation at the membrane surface. The decrease of the adsorption and translocation with increasing polymer hydrophilicity also goes along with the simulation studies, although the direct comparison of the hydrophobicity values for the real and the simulated polymers is difficult. These findings suggest that the translocation phenomenon is general for all linear non-ionic amphiphilic polymers, which opens great abilities for tuning the translocating polymers for a wide range of biomedical applications.

6.4   Materials and methods

Materials

1-palmitoyl-2-oleoyl-sn-glycero-3-phosphocholine (POPC) was purchased from Avanti Polar Lipids and used without further purification. 1-Palmitpyl-*d*31-2-oleoyl-*d*33-*sn*-glycero-3-phosphocholine (POPC-d64) and 1-Palmitoyl-d31-2-oleoyl-d33-*sn*-glycero-d5-3-phosphocholine-d13 (POPC-d82) were purchased from ANSTO national deuteration facility. The synthetic procedures for producing them are published.[10] Pluronic-F127 was purchased from Sigma Aldrich and used without further purification. All AAP were synthesized as described in Appendix.

Pulsed-Field Gradient NMR

Sample preparation

Dry lipids were dispersed in D2O at concentration of 20 mg/mL for 30 min above lipid transition temperature, followed by 5 freeze/thaw cycles. Large Unilamellar vesicles (LUV) were prepared from this dispersion using an Avanti miniextruder. The vesicles were extruded 21 times through a 100 nm polycarbonate membrane and afterwards 21 times through a 50 nm membrane, while the lipid was above its phase-transition temperature. AAPs were dissolved in D2O and added to LUV solution directly before measurements.

Method

The PFG NMR measurements were performed using a Varian 600 MHz system equipped with diffusion ^{1}H probe head. The attenuation of the spin echo signal from a pulse sequence containing a magnetic field gradient pulse is used to measure the translational diffusion of the molecules (hydrogens) in the sample at the time scales from ten to a few hundreds milliseconds. During this time hydrogens are able to overcome the distances of order of hundreds of nanometers. Diffusion spin echo decays were measured using a standard stimulated echo (STE) pulsed field gradient sequence[11] with convection compensation in the temperature range from 15 to 35 °C Observation times Δ were equal to 100 ms. The gradient pulse length δ was 2 ms. The kinetic PFG NMR measurements were performed at gradient pulse amplitude G chosen such that only the integrated polymer is observed. Number of scans per point were chosen depending on the kinetic rates, from 4 scans for the fastest processes to 128 scans for the slowest. The amplitude of spin echo was determined as a function of time.

For all polymers and liposome, the self-diffusion coefficients were measured in separate conventional PFG-NMR experiments on their aqueous solutions prior to the translocation

experiments. The relaxation times T_1 and T_2 have typical values of 1 and 0.5 s for all sample types allowing conventional diffusion measurements at the time scale of order of 0.5-1 s.

Fit method of kinetic data

The PFG-NMR data were fitted using Bayesian inference using the Markov Chain Monte Carlo (MCMC) method as implemented in the Python package *emcee*.[12] An uninformative prior was used. It allows to look for a probability distribution of all possible solutions which can be visualized using the Python module *corner.py* module. Radius of LUVs and bilayer thicknesses used for the fits were 44 nm and 4 nm respectively.

Neutron reflectometry

Method

Neutron reflectivity data were acquired at the MARIA neutron reflectometer operated by Jülich Centre for Neutron Science at Heinz Maier-Leibnitz Zentrum in Garching (Germany).[13] Custom temperature-regulated liquid cells was used to perform measurements of supported lipid bilayers.[14] The measurements were performed using two different wavelengths, 10 Å for the low-q region and 5 Å for the high-q region up to 0.25 Å^{-1}, with a 10% wavelength spread. The change of solvent contrast in the liquid cells was performed using a combination of valves and a peristaltic pump, at small flow rates ~0.5 mL/min. All the fit were performed with the Igor PRO based software Motofit.[15]

Preparation of supported lipid bilayer

Two Andreas-Holm GmbH ultra-polished Si blocks (r.m.s. roughness 1-2 Å, dimensions 150x50x20 mm) were cleaned with water and ethanol and treated with an UV-ozone plasma etching (Novascan technologies) for 10 minutes 2 times. Then the liquid cells were assembled immediately and H_2O was injected in the cell. The liquid cell is made of boronglas and sealed by a Viton o-ring.[14] After alignment of the sample in respect of the beam the thickness and roughness of the silicon oxide layer was characterized. The liposomes were prepared in H_2O similar to PFG NMR and had a concentration of 6 mg/mL. The vesicles were kept for 10 minutes at 35 °C to fuse on the substrate. Afterwards the remaining liposomes were flushed out with H_2O. Now the samples were measured first in H_2O and afterwards in D_2O to enable precise characterization of the lipid bilayer SLD profile by the simultaneous fit of the two contrasts. The polymers were solubilized in water at desired concentration and manually injected into the cells by a syringe.

Small Angle Neutron Scattering (SANS).

SANS experiments were performed at the instrument KWS-1[16,17] operated by the Jülich Centre for Neutron Science (JCNS) at Heinz Meier-Leibnitz Zentrum (MLZ) in Garching, Germany. The incident neutron wavelength λ was 0.5 nm (Δλ/λ = 10%). The data were obtained from two different detector distances, 1.5 m and 4 m with a collimation distance of 4 m for each. The resulting Q-range was 0.4 − 6.7 nm^{-1}. Here Q is the magnitude of the scattering wave vector defined as $Q = (\frac{4\pi}{\lambda})\sin(\theta)$, where 2θ is the angle between the incident and scattered beam. The samples were prepared similar to PFG NMR. The data presented here were converted to an absolute intensity unit of cm^{-1} taking into account the sample thickness, transmission, the scattering from a standard sample and the background from electronic noise, the solvent and the quartz cell. Data reduction was done using the QtiKWS software[18] and data analysis has been done using the Python-based project Jscatter.[19]

6.5 References

[1]   T. Goda, Y. Miyahara, K. Ishihara, *J. Mater. Chem. B* **2020**, *8*, 7633–7641.

[2]   F. Mathot, A. Schanck, F. Van Bambeke, A. Ariën, M. Noppe, M. Brewster, V. Préat, *J. Control. Release* **2007**, *120*, 79–87.

[3]   E. Kostyurina, J. Allgaier, M. Kruteva, H. Frielinghaus, A. Csiszár, S. Förster, R. Biehl, *J. Am. Chem. Soc.* **2022**, *2022*, 15348–15354.

[4]   M. Werner, J.-U. Sommer, V. A. Baulin, *Soft Matter* **2012**, *8*, 11714.

[5]   M. Werner, J. U. Sommer, *Biomacromolecules* **2015**, *16*, 125–135.

[6]   W. Zhang, K. J. Haman, J. M. Metzger, B. J. Hackel, F. S. Bates, T. P. Lodge, *Langmuir* **2017**, *33*, 12624–12634.

[7]   E. Kostyurina, J. U. De Mel, A. Vasilyeva, M. Kruteva, H. Frielinghaus, M. Dulle, L. Barnsley, S. Förster, G. J. Schneider, R. Biehl, J. Allgaier, *Macromolecules* **2022**, *55*, 1552–1565.

[8]   M. Nakano, M. Fukuda, T. Kudo, N. Matsuzaki, T. Azuma, K. Sekine, H. Endo, T. Handa, *J. Phys. Chem. B* **2009**, *113*, 6745–6748.

[9]   A. A. Yaroslavov, N. S. Melik-Nubarov, F. M. Menger, *Acc. Chem. Res.* **2006**, *39*, 702–710.

[10]   N. R. Yepuri, T. A. Darwish, A. M. Krause-Heuer, A. E. Leung, R. Delhom, H. P. Wacklin, P. J. Holden, *Chempluschem* **2016**, *81*, 315–321.

[11]   E. O. Stejskal, J. E. Tanner, *J. Chem. Phys.* **2004**, *42*, 288.

[12]   D. Foreman-Mackey, D. W. Hogg, D. Lang, J. Goodman, *Publ. Astron. Soc. Pacific* **2013**, *125*, 306–312.

[13]   S. Mattauch, A. Koutsioubas, U. Rücker, D. Korolkov, V. Fracassi, J. Daemen, R. Schmitz, K. Bussmann, F. Suxdorf, M. Wagener, P. Kämmerling, H. Kleines, L. Fleischhauer-Fuß, M. Bednareck, V. Ossoviy, A. Nebel, P. Stronciwilk, S. Staringer, M. Gödel, A. Richter, H. Kusche, T. Kohnke, A. Ioffe, E. Babcock, Z. Salhi, T. Bruckel, *J. Appl. Crystallogr.* **2018**, *51*, 646–654.

[14]   A. Koutsioubas, *J. Phys. Chem. B* **2016**, *120*, 11474–11483.

[15]   A. Nelson, IUCr, *urn:issn:0021-8898* **2006**, *39*, 273–276.

[16]   H. Maier-Leibnitz Zentrum Forschungszentrum Jülich, H. Maier-Leibnitz Zentrum, *J. large-scale Res. Facil.* **2015**, *1*, 28.

[17]   A. V. Feoktystov, H. Frielinghaus, Z. Di, S. Jaksch, V. Pipich, M. S. Appavou, E. Babcock, R. Hanslik, R. Engels, G. Kemmerling, H. Kleines, A. Ioffe, D. Richter, T. Brückel, *J. Appl. Crystallogr.* **2015**, *48*, 61–70.

[18]   V. Pipich, "QtiKWS," can be found under http://www.qtisas.com/qtikws

[19]   R. Biehl, *PLoS One* **2019**, *14*, DOI 10.1371/journal.pone.0218789.

7 From model membranes to living cells

The work for this chapter was carried out in co-operation with the Institute of Biological Information processing - Mechanobiology (IBI-2) at Forschungszentrum Jülich using the expertise of the institute on the field of cell biology and imaging.

Abstract

In the previous chapters, we showed that alternating amphiphilic polymers can translocate through model lipid membranes and carry small hydrophobic molecules with them. We have also proved the biocompatibility of AAPs synthesized as polyesters with HeLa cells. The next step towards biomedical applications is testing the translocation phenomena of the AAP in living cells. For this reason, we made tests with different cell cultures and found that the AAPs translocate through the plasma membrane of all examined cell lines. Additionally, we tested the biocompatibility of AAPs synthesized as polyethers and compared the influence of the two AAP chemistries on interaction with the cells. The research presented in this chapter is not complete and the chapter is presented as a discussion of the current results.

7.1 Introduction

Macromolecules mostly translocate into the cell via the pore formation or via endocytosis pathways.[1,2] The pore-formating molecules are usually harmful for the cells due to the strong disruption of the plasma membrane and in the case of endocytosis they require a mechanism of endosomal escape to be able to act in the cell. Passive translocation of macromolecules would be desired because it does not face these difficulties. An example of a macromolecule that was found to passively cross the cell plasma membrane and did not show cytotoxicity is a lipid-mimicking polymer containing phospholipid moieties covalently attached as side groups to the polymer backbone.[3] Such polymers showed a translocation time of several minutes and were reported to localize at the cell organelles depending on the organelle specificity of the attached fluorescent label. The linear non-ionic AAPs investigated in this research project were found to generally translocate through model lipid membranes, most likely independently of their composition.[4] The polarity of the AAPs can be tuned which allows using them for the solubilization of hydrophobic molecules in water and hydrophilic molecules in the lipid membrane and so transport molecules of different polarity through the membrane. The next

step towards possible biomedical applications is now described in this chapter by testing AAP translocation through cell plasma membranes and examining their cytotoxicity.

Molecules are identified as being cell toxic when they damage the cell function by for example generating leaks in the plasma membrane or being accumulated inside the cell and blocking cell mechanisms. The AAPs synthesized as polyesters were found to not decrease cell viability within at least 48 hours, which let us assume that this polymer type is not cell-toxic.

The biocompatibility of the AAPs was tested on the HeLa cell line. This is an immortal cancer cell line, which is quite robust to environmental changes. Moreover, the composition of the cell membranes varies in a wide range depending on the cell type. Therefore, we tested the interaction of a fluorescent-labeled AAP with different cell types: endothelial cells, astrocytes, and neurons. As endothelial cells, we used human umbilical vein endothelial cells (HUVECs) most commonly used as a laboratory endothelial cell model. Astrocytes are one of the main components of the central nervous system and one of the components of the blood-brain barrier (BBB). They have a large surface area and cover synapses and blood capillaries, performing numerous functions. Neurons are electrically excitable cells, the main component of the nervous tissues. The combination of endothelial cells and astrocytes is also a partial model of the BBB, a highly selective membrane that prevents solutes from the bloodstream from non-selective entering the extracellular fluid of the central nervous system. Because AAP translocation is not restricted to the endocytosis pathway, unlike most macromolecules, there is a chance for these polymers to pass the BBB which would be important for medical applications.

7.2   Results and discussions

The interaction of AAPs with cells was firstly studied on a HeLa cell culture using the AAP functionalized with the fluorescent label 7-(diethylamino)coumarin (P(C$_4$EG$_4$)6k-coumarin). HeLa is the oldest and the most common human immortal cancer cell line. The coumarin-labeled AAP was found to rapidly translocate through the HeLa plasma membrane into the cell interior. In order to study the translocation kinetics live imaging of the AAP uptake was performed (Figure 7.1). The AAP-coumarin was found to translocate into the cell interior within a few seconds.
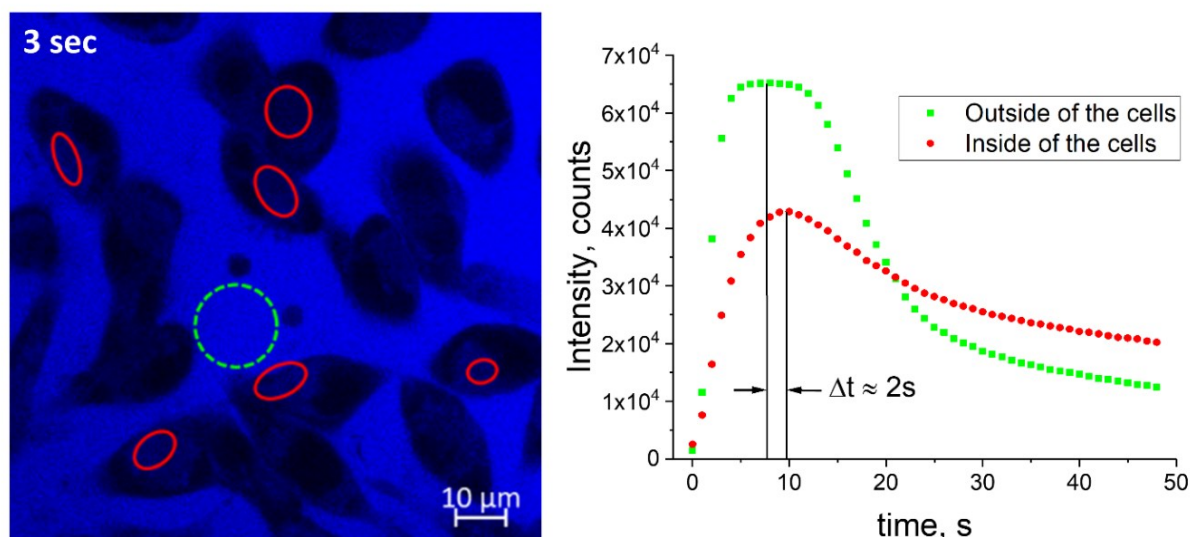
Figure 7.1. Live imaging of AAP-coumarin uptake of HeLa cells visualized by fluorescence microscopy after addition of AAP-coumarin (time=0) to the sample. The image corresponds to the time of 3 seconds after the addition of $P(C_4EG_4)6k$-coumarin. The red points show the time evolution of the average intensity inside of the cells (red areas), green points correspond to the time evolution of average intensity outside of the cells (green area). Temperature = 37ºC.

Due to the very fast kinetic process, the images were taken every second. However, this led to several side effects which complicated the quantification of the measurement. In the ideal experiment, the intensity outside of the cells stays nearly constant whereas the intensity inside of the cells must exponentially saturate. However, in the first seconds after the injection of AAP-coumarin, the intensity outside of the cells was increasing due to the polymer diffusion from the point of injection to the measurement area. Moreover, high and almost continuous irradiation of the sample led to fast bleaching of the coumarin dye and the maximum at the kinetics curves. These effects made the kinetic curves difficult to analyze, therefore, we could only roughly estimate the translocation time by comparing the intensity change inside and outside of the cells. If the translocation time is much below one second the two intensity curves must be identical. The delay between the two curves corresponds to the translocation time and was estimated from the curve maxima to be about 2 seconds. This translocation rate is about three orders of magnitude faster than that of a similar AAP through a POPC model lipid membrane at 35ºC and about two orders of magnitude faster than through the DLPC lipid membrane at 30ºC. As the translocation rate strongly depends on temperature, which was 37ºC in the case of cells, and on the lipid composition, this large difference in the translocation rates might be explained by the changes in these two parameters.

To determine the coumarin localization in the cell, fluorescent staining of the cell organelles was used. The coumarin signal was found exclusively in mitochondria with the perfect colocalization of the coumarin and mitochondria fluorescent dyes (Figure 7.2).
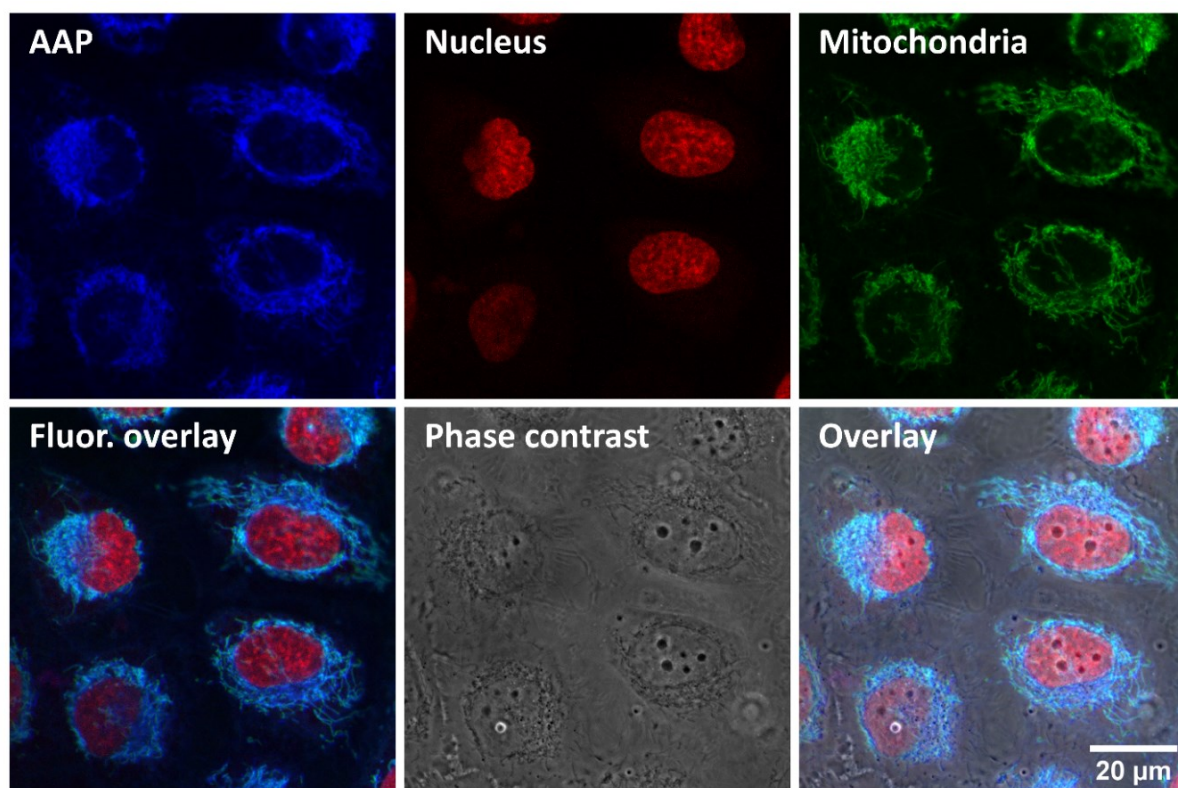
Figure 7.2. AAP-coumarin uptake of HeLa cells visualized by fluorescence and phase contrast microscopy. Upon 15 min of incubation, the AAP P(C₄EG₄)6k-coumarin (blue) was enriched in the cellular mitochondria (green) verified by signal co-localization with the mitochondrial dye MitoGreen (co-localized signal-cyan). The Phase contrast image shows a healthy morphology. Scale bare fits to all, 20 µm.

This experiment was performed on HeLa cells, which are much more robust to the environment compared to regular body cells. Moreover, the composition of the cell membranes varies in a wide range depending on the cell type, which might change the interaction properties with the AAPs. Therefore, we tested the interaction of the AAP-coumarin with a few different cell types. We chose endothelial cells, astrocytes, and neuron cells. The AAP-coumarin showed translocation into all three types of cells (Figure 7.3). The fluorescent signal of the translocated AAP-coumarin was found preferably in mitochondria, and additionally in some other parts of the cell. Within the first 30 min after the incubation with AAP-coumarin, all the cells did not show signs of degradation. After 24 hours the cells were still alive but showed morphological changes, which also could be a result of the slightly toxic Mitotrekker. Therefore, a test of the long-term AAP toxicity to the studied cell types is still required.
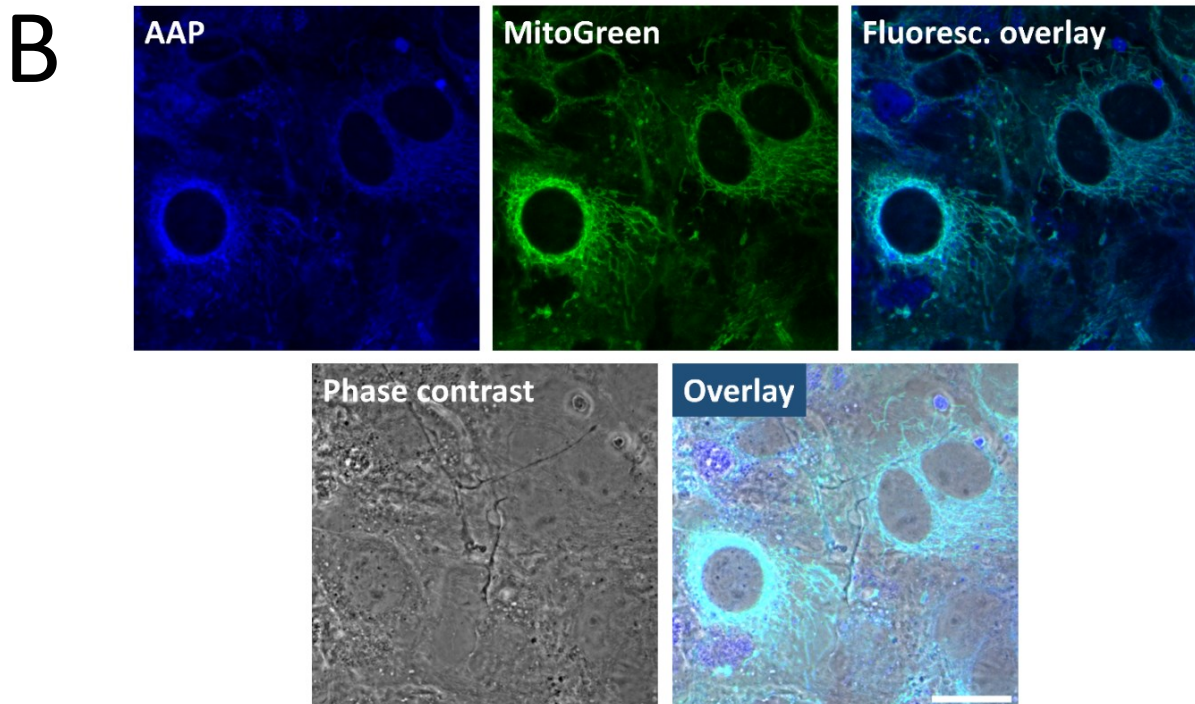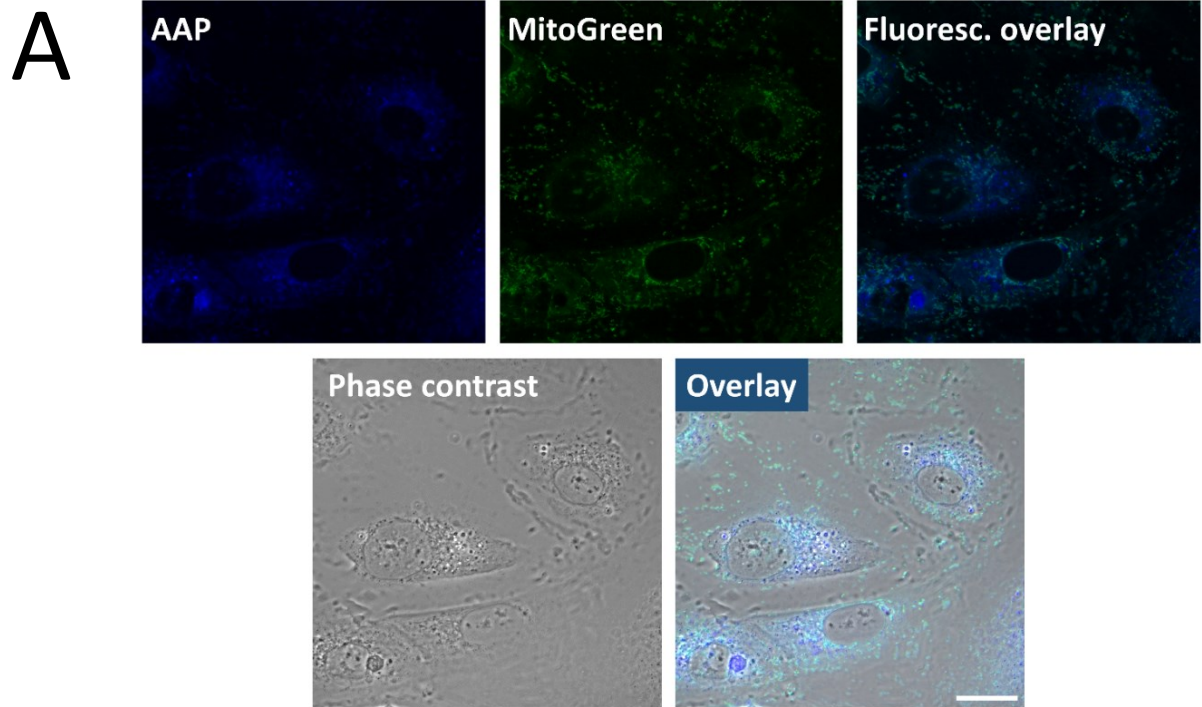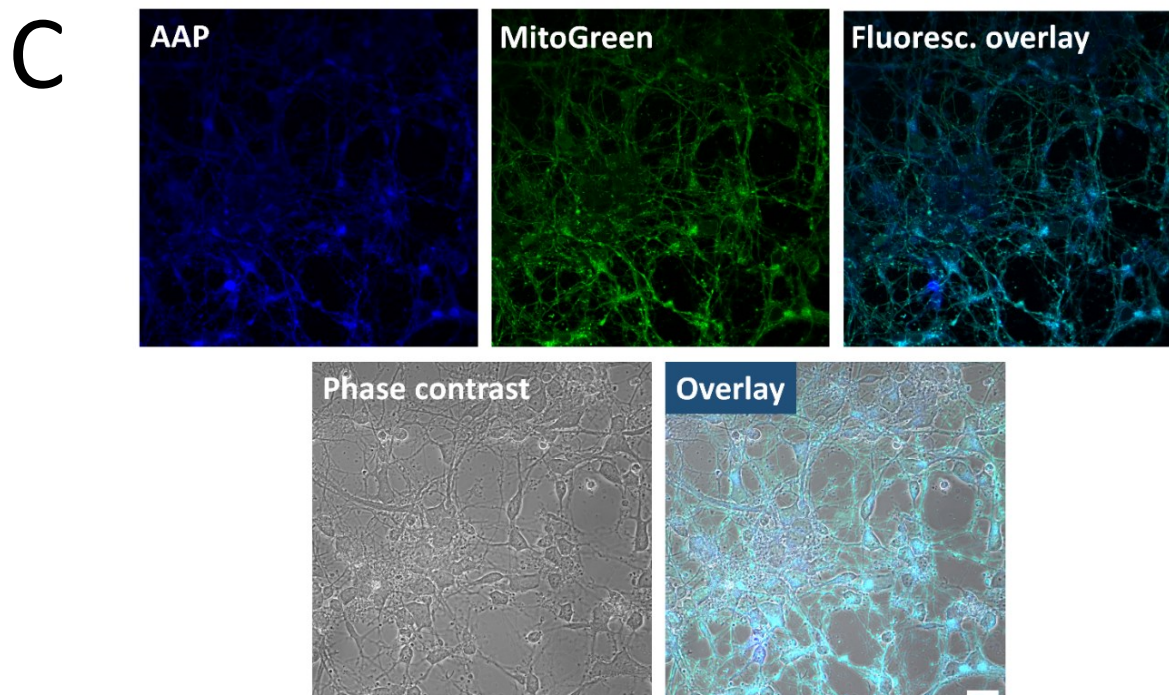
Figure 7.3. AAP uptake of HUVEC cells (A), Astrocytes (B) and Neuron cells (C) visualized by fluorescence and phase contrast microscopy. Upon 5 min of incubation, AAP (blue) was enriched in the cellular mitochondria (green) verified by signal co-localization with the mitochondrial dye MitoGreen (co-localized signal-cyan). Phase contrast image shows healthy morphology. Scale bare fits to all, 20 μm.

The AAP synthesised as polyesters were proved to not decrease the viability of HeLa cells within at least 48 hours (see chapter 5 Figure 5.1). However, the ester bonds are susceptible to hydrolysis at the time intervals of several weeks, which might complicate some biomedical applications. To avoid this effect, the AAPs can be synthesized by linking the hydrophilic and hydrophobic segments via ether bonds. We found that such polymers also translocate through lipid membranes. Therefore, their effect on HeLa cells was tested. Figure 7.4 shows the images of HeLa cells 24 hours after incubation with different AAPs. Whereas incubation with polyester does not show any significant effect on the cells, polyethers cause significant changes in the cell morphology even at a relatively low concentration of 0.1 wt%, which indicates their cell toxicity. Therefore, the biocompatibility of the polyesters most likely is a result of the ester bonds which the cell can cleave and in this way digest the polymer.
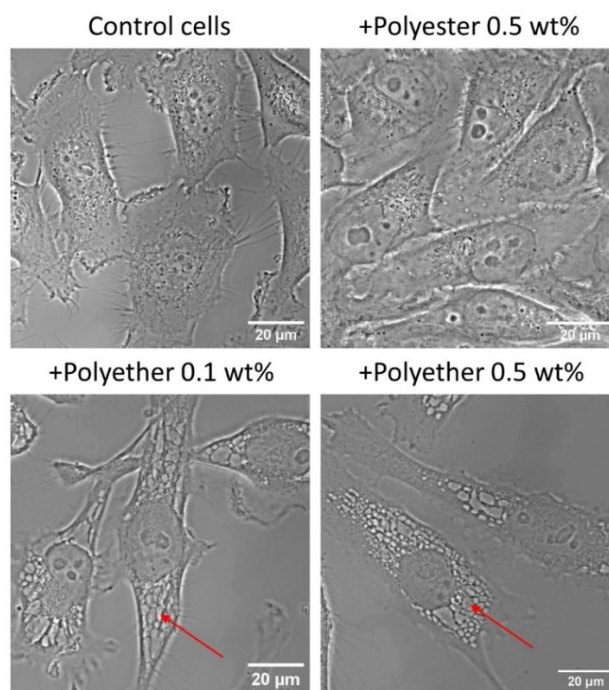
Figure 7.4. Phase contrast images of HeLa cells treated by AAP synthesized as polyester (P(C₄EG₄)6k) and polyether (PE(C₄EG₃)3k). Red errors show changes in mitochondria after treatment with AAP synthesized as polyethers.

The cells have a mechanism for cleavage of ester bonds by using the enzyme esterase. To prove that these enzymes are able to cleave the polymer ester bonds, we performed a test experiment using the enzymatic assay of esterase. Esterase splits the ester into alcohol and acid group leading to a change in pH. The assay determines the ester bond cleavage by monitoring the amount of titrant to keep a contant pH 8 of the solution upon esterase activity (Figure 7.5). AAP was found to be cleaved by the tested esterase enzyme of the porcine liver. Its kinetics was compared with one of the small reference molecules, butyric acid ethyl ester. Initially, the AAP ester bonds are cleaved about 3 times slower than those of the reference molecule (Figure 7.5A), and with time the process slows down even more (Figure 7.5B). Moreover, the titration curve for the AAP looks very different from the expected exponential one. The smaller reaction rate of the AAP most likely is caused by steric restrictions of the polymer coil. Cleavage of the ester bonds along the chain leads to shorter chains which might change the probability of the next bonds being cleaved and result in the observed kinetics.

Figure 7.5. Enzymatic assay of esterase. The plots show the time needed to compensate for a given amount of titrant by the cleaving of ester bonds by the known amount of esterase. A: titration curves for P(C₄EG₄)6k and for butyric acid ethyl ester as a reference. The solid lines represent the fits with a linear function. The AAP ester bonds are cleaved 3 times slower than the bond of the butyric acid ethyl ester. B: titration curve for P(C₄EG₄)6k after the addition of 5 times more esterase than in Figure A, collected for a longer time. 5 ti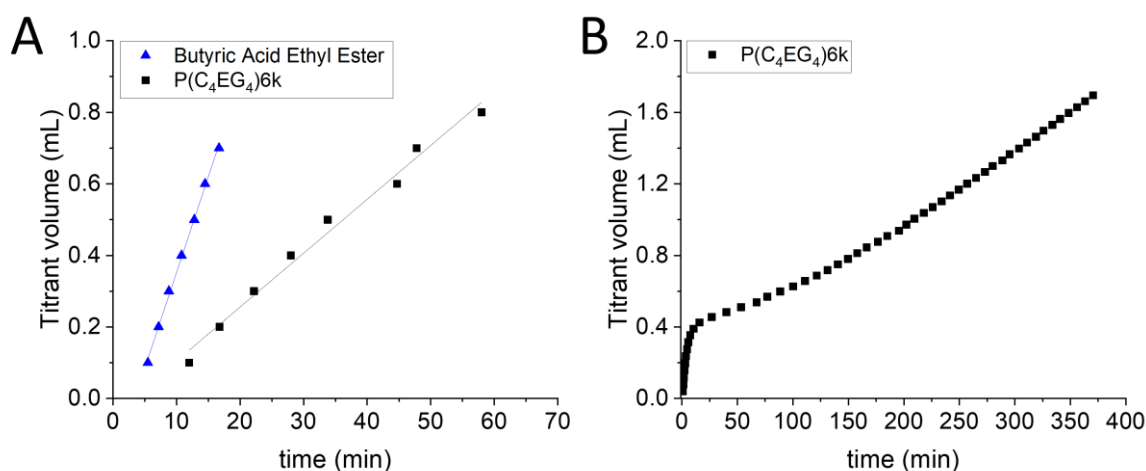mes smaller volume of 5 times more concentrated titrant solution was used in the experiment of figure B, therefore each point corresponds to the same amount of base added.

While the AAP translocation through the plasma membrane is proven by the in vivo experiments described above, its distribution and its degradation pathways in the cell cannot be directly examined. The polyester can be cleaved by the esterase inside the cell and in this way, the 7-(diethylamino)coumarin can be disconnected from a large part of the polymer chain. As coumarin is also known to enrich in mitochondria, we cannot know whether the AAP is still attached to the coumarin when we observe the fluorescent signal in mitochondria, as the rate of the ester bond cleavage inside the cells is unknown. However, the organelle which is affected most by the polyethers is the mitochondria (Figure 7.4), which suggests that the AAP are localized preferably there. It gives a hint that the localization of the polyester-coumarin complexes in mitochondria is not an effect of coumarin.

7.3   Conclusion

The AAP functionalized with 7-(diethylamino)coumarin was found to translocate through the plasma membrane of all four investigated cell types: HeLa, HUVEC, Astrocytes, and Neurons. In all the cases its fluorescent signal was found in the mitochondria of the cells, however, in HUVEC, Astrocytes, and neurons some signal was also located in other parts of the cell. We showed that the polyesters can be cleaved by the esterase, which is most likely the reason for their biocompatibility, as compared to the polyethers which were found to be cell toxic. In the case of

drug delivery applications, this mechanism can be also used for drug release.[5] Suspense of the esterification rate in the cell obscurse whether the AAP is present in mitochondria, or the fluorescent molecule was cleaved from the main AAP chain. However, degradation of the cells in the presence of polyethers is most pronounced at mitochondria and might be a hint to the preferable location of AAP in it. Although the study is not yet complete, the present results make the AAP a promising macromolecule for applications with living cells.

7.4   Materials and methods

Synthesis of P(C$_4$EG$_4$)6k –coumarin

The 7-(diethylamino)-coumarin functionalized polymer P(C$_4$EG$_4$)6k-coumarin was synthesized following a procedure described in the literature.[6] Polymer P(C$_4$EG$_4$)6k was first dried under high vacuum conditions for 3 days. This polymer contains according to the ^{1}H-NMR analysis 63 % of OH-end groups and 37 % of carboxylic acid end groups. A sample of 468 mg (0.120 mmol OH-end groups, 0.071 mmol COOH-end groups) was dissolved in 2.38 g of dry toluene inside a glove box. A separate flask equipped with a Teflon stopcock was charged inside a glove box with 7-(diethylamino)-coumarin-3-carbonylazid (Sigma-Aldrich, ≥95%) (6.2 mg, 0.0217mmol) and 1.96 g of dry toluene. The mixture was frozen in liquid nitrogen and the argon gas was pumped off at a vacuum line. Then the mixture was heated to 100 °C for 12 min. in order to carry out the rearrangement to 7-(diethylamino)-coumarin-3-isocyanate. 1.71 g of the 7-(diethylamino)-coumarin-3-isocyanate solution was added to the polymer solution. The mixture was stirred at 50 °C for 18 h and then cooled to 0 °C, where it became turbid. After centrifugation, the lower orange-colored phase was isolated and washed 4 times with 10 mL of diethyl ether and 3 times with 8 mL of ethanol. The product P(C$_4$EG$_4$)6k-coumarin was finally dried under high vacuum conditions. Characterization of the final material is given in chapter 4 Figure S5.5.

Cell cultures

HeLa and HUVEC cells were purchased from Sigma-Aldrich (Taufkirchen, Germany). They were maintained in DMEM-F12 (Sigma-Aldrich) supplemented with 10% fetal bovine serum (FBS) and 10,000 units penicillin and 10 mg/ml streptomycin (Sigma-Aldrich). Neurons and Astrocytes were isolated from embryonic rats as described by Jella-Andrea Abraham et al.[7]

During culture as well as experiment, all cells were kept at 37 °C and 5% CO$_2$ in a saturated humid atmosphere. Cell density never exceeded 80% confluence. For microscopy analyses 30,000 cells were seeded on fibronectin (BD Biosciences, San Jose, CA, USA) coated (10 µg/ml, 30 min) glass surfaces (Ø = 3.5 cm) one day before the experiment.

Prior to experiments, AAP stock solutions were diluted with DMEM medium supplemented with FBS (Sigma Aldrich) at 10%. Cells were incubated in AAP solutions for 5 – 15 min at 37 °C, unless live imaging was performed. Subsequently, AAP solutions were replaced by fresh medium and the internalized cellular fluorescence was analyzed by fluorescence microscopy immediately after treatment and 20-24 h later.

Fluorescence microscopy

Samples were imaged using a confocal laser scanning microscope (LSM 710 from Carl Zeiss MicroImaging GmbH, Jena, Germany) equipped with an argon ion laser (488 nm) and a HeNe laser (633 nm). The mitochondria staining dye MitoGreen signal was exited at 488 nm and its fluorescence emissions was detected using a band pass filter BP 495–550 nm (green channel). The nucleus staining dye DRAQ5 was excited using the 633 nm laser line and the emitted signal was detected through the long pass filter LP 650 nm. For imaging a Plan-Apochromat 40x/1.40 Ph3 (Carl Zeiss) objective was used. To maintain appropriate culture conditions, the microscope was equipped with an incubator (Incubator XL 2, Carl Zeiss). Temperature as well as CO_2 were kept constant at 37 °C and 5%, respectively. The images were analyzed using ZEN software (Carl Zeiss).

Enzymatic assay of esterase

Esterase from the porcine liver was purchased from Sigma Aldrich as ammonium sulfate suspension in the concentration of 47.3 protein/mL with 209 units/mg. The esterase solution was prepared as described in the technical documentation from Sigma Aldrich[8] to obtain a final esterase concentration in a Buffer of 50 units/mL for the experiment shown in Figure 7.5A and 200 units/mL for the experiment shown in Figure 7.5B. Butyric Acid Ethyl Ester used as a reference was purchased from Sigma Aldrich. As an AAP the $P(C_4EG_4)6k$ was used. The assay was done as described in the protocol from Sigma Aldrich.[9] The 10mM borate buffer was prepared by solubilizing of boric acid in MilliQ water and adjusting the pH to 8.0 with 1N NaOH. 0.01 N and 0.05 N NaOH solution were used as a titrant in the experiments from Figure 7.5A and Figure 7.5B respectively. The concentration of esterase was 0.2 unit/mL 2 unit/mL for the experiments from Figure 7.5A and Figure 7.5B respectively. The Butyric Acid Ethyl Ester concentration was 3.50 mg/mL, and of the AAP 4.16 mg/mL which corresponds to the same number of ester bonds in the system.

7.5   References

[1]   N. J. Yang, M. J. Hinner, *Methods Mol. Biol.* **2015**, *1266*, 29–53.

[2]   D. Pei, *Acc. Chem. Res.* **2022**, *55*, 309–318.

[3]   T. Goda, Y. Miyahara, K. Ishihara, *J. Mater. Chem. B* **2020**, *8*, 7633–7641.

[4]   E. Kostyurina, J. Allgaier, M. Kruteva, H. Frielinghaus, A. Csiszár, S. Förster, R. Biehl, *J. Am. Chem. Soc.* **2022**, *2022*, 15348–15354.

[5]   H.   Dong,   L.   Pang,   H.   Cong,   Y.   Shen,   B.   Yu, *https://doi.org/10.1080/10717544.2019.1588424* **2019**, *26*, 416–432.

[6]   K. Kuramochi, S. Yukizawa, S. Ikeda, T. Sunoki, S. Arai, R. Matsui, A. Morita, Y. Mizushina, K. Sakaguchi, F. Sugawara, M. Ikekita, S. Kobayashi, *Bioorg. Med. Chem.* **2008**, *16*, 5039–5049.

[7]   J. A. Abraham, C. Linnartz, G. Dreissen, R. Springer, S. Blaschke, M. A. Rueger, G. R. Fink, B. Hoffmann, R. Merkel, *Langmuir* **2019**, *35*, 7423–7431.

[8]   "How to Work with Enzymes Supplied as Ammonium Sulfate Suspensions," can be found under   https://www.sigmaaldrich.com/DE/en/technical-documents/technical-article/protein-biology/enzyme-activity-assays/ammonium-sulfate-suspensions

[9]   "Enzymatic   Assay   of   Esterase,"   can   be   found   under https://www.sigmaaldrich.com/DE/en/technical-documents/protocol/protein-biology/enzyme-activity-assays/enzymatic-assay-of-esterase

8 Conclusions and outlook

In this project, non-ionic alternating amphiphilic polymers (AAPs) were widely studied from different perspectives: thermal behavior, structure formation in water, and translocation through lipid membranes. Most of the AAPs used in this project were synthesized as polyesters using hydrophobic dicarboxylic acids ($C_4 - C_{20}$) and hydrophilic polyethylene glycol (PEG) units ($EG_3 - EG_{1000}$).

In chapter 3 the thermal behavior and structural properties of the AAP in water were investigated. In water the AAPs show an LCST behavior, and the critical temperature can be used as a measure of polymer hydrophilicity. It was shown that the LCST of the AAPs in water can be tuned between 0 and 100 ^{o}C by varying the length and the ratio of the hydrophobic and hydrophilic unit lengths. It was found that the transition temperature depends linearly on the hydrophobic unit length and logarithmically on the hydrophilic length. On the basis of an empirical equation, LCST values can be predicted from the AAP composition. This ability to tune the hydrophilicity and simplicity in the production of the AAPs opens a wide range of applications. Therefore it was intended to broader characterize these materials and study more properties of it. Apart from the LCST, which is attributed to the average hydrophilicity of the chain, the polymer composition allows to change the polarity profile, either by arranging it nearly homogeneous for AAPs with short units or more alternating in the case of AAPs with long units. In the next step, the dependence of the hydrophobic and hydrophilic unit lengths and unit length ratio on the structures the polymers form in water was investigated. This study was performed by small-angle x-ray and neutron scattering. As a result, the qualitative diagram was constructed, which shows that depending on the hydrophobic and hydrophilic unit lengths and unit length ratio, the AAPs can be soluble in water as free chains, form micelles or gels. The AAPs with a high hydrophilic/hydrophobic ratio solubilize in water as free chains and form single intrachain hydrophobic connections resulting in the formation of loops. For larger hydrophobic units starting with C_{14}, micelles can be formed. In this case, the number of connections between the hydrophobic units increases compared to the unimerically solubilized chains. The so formed hydrophobic domains are embedded in a PEG rich and water poor matrix. The micelle corona is formed by a smaller number of PEG end groups or internal PEG units forming loops. Because of the alternating nature of the polymer, these micelles differ structurally from micelles formed by block copolymers or surfactants. The gels are formed by interconnected micellar structures

described above, which make the gel mechanically stable. Especially at higher concentration, the micelles inside of the gel are able to arrange in a crystalline order.

As the hydrophilicity of the AAPs can be tuned in a wide range, it can be adjusted in a way to have simultaneously a solubility in water and in hydrophobic environments, for example, the interior of lipid membranes. In chapter 4 it is shown that AAP having such balanced hydrophilicity are able to passively cross lipid membranes. This translocation process was investigated by kinetic PFG NMR. It was shown that translocation is in general a slow process that happens in the time range between several minutes and several days depending on parameters, such as AAP molecular weight, lipid composition, and temperature. The translocation process consists of a relatively fast adsorption and membrane insertion process, and a slower, time limiting, desorption process. The adsorption rate and the concentration in the membrane strongly depend on polymer molecular weight, decreasing for larger polymers, whereas the desorption rate stays constant. These findings together with temperature measurements allowed us to develop a basic thermodynamic model of the translocation process. Measurements with different lipids suggest that the length of the lipid tails has a larger effect on the translocation rate than the lipid phase. This effect is opposite to the translocation of small molecules. This finding requires further investigations, which could lead to a deeper understanding of the thermodynamics principles laying behind the translocation processes in general. Additionally, the biocompatibility of the AAPs synthesized as polyesters was proved using living HeLa cells, and the ability of the AAPs to carry hydrophobic molecules through the membrane was proved by fluorescence experiments with lipid vesicles. These results are important steps towards drug delivery applications.

In chapter 5 the chemical composition of the AAPs was varied in a broad range to learn how sensitive the translocation phenomenon is towards hydrophobic/hydrophilic unit length and the AAP average hydrophilicity. It was shown that these parameters can be varied in a wide range, still maintaining the translocation properties. However, their choice influences strongly the translocation parameters. An increase of the hydrophobic and hydrophilic unit lengths leads to an increase of the adsorption rate and of the number of adsorbed AAPs but on the other hand to a decrease of the translocation rate. The triblock copolymer (Pluronic-F127) was used as a reference system and was found to translocate through lipid membranes as well, with the translocation similar to the AAP with long hydrophobic/hydrophilic units. Increasing the AAP hydrophilicity leads to a decrease of both adsorption and desorption rates as well as of the concentration in the lipid membrane. These findings suggest that the translocation phenomenon

exists general for all linear non-ionic amphiphilic polymers, which opens the ability to tune the composition of the translocating polymers for a wide range of biomedical applications.

In the last chapter, the translocation phenomenon of the AAP was studied on living cells. Using fluorescence microscopy, the translocation of the fluorescently labeled AAP through the plasma membranes was proved for four different cell types. The preferable location of the AAPs in the cells was assumed to be the mitochondria. Additionally it was shown that the chemistry of the cell-translocating AAP plays an important role for their toxicity to living cells. Changing the connection between the hydrophilic and hydrophobic units from ester bonds to ether bonds led to cell toxicity. The different toxicity behavior of the polyesters and polyethers most likely is due to the fact that the polyesters easily can be digested by the cells using esterase. In vitro experiments with an esterase showed that this enzyme attacks polymeric ester bonds.

In the scope of this work, the extended characterization of the AAP behavior in water was achieved and their translocation phenomenon both in vitro and in vivo was widely described. On the other hand, various aspects where more extended research would be desired were found. One of them is the crystallinity of the AAP gels which appeared for one measurement at a high polymer concentration. The strong crosslinking of the micelles creating these gels make the material very different from all other micelles which are known to form crystals, and therefore they are very interesting for further investigations. Currently, in a new PostDoc research, this topic is examined in more detail showing promising first results. Furthermore, it would be interesting to study the internal structure of the micelles in more detail. The translocation study can be continued in several promising directions. The next step towards applications could be to verify the location of the AAPs in the cell because the organelle specificity would make the AAPs a highly desired macromolecule for drug delivery applications for the organelle-targeted drugs. Another step could be to try transferring a pharmacologically relevant drug into the cell interior. Another direction is a deeper general understanding of the macromolecular translocation process by studying the effect of more complex membrane compositions, and polymer properties, such as charge or specific functional groups on translocation. This research might be useful for understanding the interaction and translocation process of proteins and cell-penetrating peptides and might allow to design cell-translocating polypeptides, which would be an even bigger step toward drug delivery applications.

Appendix

Synthesis of alternating amphiphilic polymers

Materials. Succinic anhydride (Sigma-Aldrich, ≥99.0%, batch purity 100.0% (GC)), glutaric acid (Sigma-Aldrich, 99%, batch purity 99.9% (GC)), adipic acid (Sigma-Aldrich, ≥99.5%, batch purity 99.9% (GC)), suberic acid (Sigma-Aldrich, 98%, batch purity 99.9% (GC)), sebacic acid (Sigma-Aldrich 99%, batch purity 98.8% (GC)), and dodecanedioic acid (Sigma-Aldrich, 99%, batch purity 99.2% (GC)) were used as received. Tetradecanedioic acid (Sigma-Aldrich, 99%, batch purity 99.9% (GC)) and eicosanedioic acid (TCI, >98.0% (T); batch purity 99.2% (titration, 95.5%(GC)) were dried prior to use under high vacuum conditions overnight. Triethylene glycol (Fluka, ≥99.0%, batch purity 99.9%), tetraethylene glycol (Sigma-Aldrich, 99%, batch purity 99.6 % (GC)), PEG 300 (Sigma-Aldrich; two batches, M_n = 284 and 298), PEG 400 (Sigma-Aldrich; M_n = 400), PEG 600 (Sigma-Aldrich; two batches, M_n = 599 and 623) were used as received. PEG 1k (Sigma-Aldrich; M_n = 986), PEG 2k (Sigma-Aldrich; M_n = 2,110), and PEG 4.6k (Sigma-Aldrich; M_n = 4,530 were dried prior to use under high vacuum conditions overnight. The PEG molecular weights were determined by ^{1}H-NMR as described in the main text. *p*-Toluenesulfonic acid monohydrate (Sigma-Aldrich, ≥99.0%), 1,1'-carbonyldiimidazole (CDI) (Sigma-Aldrich, ≥97%), anhydrous *N,N*-dimethylacetamide (DMA) (Sigma-Aldrich, 99.8%, <0.005% water), and 1,8-diazabicyclo[5.4.0]undec-7-en (DBU) (Sigma-Aldrich, ≥99.0%) were used as received. 1,4-Butanediol (Sigma-Aldrich, 99%), *p*-toluenesulfonyl chloride (Fluka, 99%) were used as received. Dry potassium hydroxide was obtained by heating the commercial product (85 % KOH) in a platinum crucible to 475 °C overnight, transferring the hot product into a glovebox and powdering it in a porcelain mortar.

Synthesis of PEG 10k and PEG 45k. The high molecular weight PEG units used in this work were synthesized by polymerizing ethylene oxide (EO) with triethylene glycol (TEG) or low MW PEG based initiators. PEG 10k was polymerized by using partially potassium metalated TEG (TEG−(OH/K)$_2$).[1] PEG 45k was polymerized in the same way but fully metalated PEG 2k (PEG−(OK)$_2$) was used and the polymerization temperature was 40 °C for 1 day and 50 °C for another day. The molecular weights were determined by NMR end-group analysis as described in the main text. For PEG 10k M_n was 10,600 g/mol and for PEG 45k 44,200 g/mol. Both polymers were dried under high vacuum conditions overnight prior to AAP synthesis.

Synthesis of polyesters

General procedures for the AAP syntheses. Most of the AAPs containing C_4 to C_{12} diacids as well as PEGs up to PEG 1k were synthesized from molar 1:1 mixtures of the carboxylic acid anhydride (C_4) or dicarboxylic acid (C_5 to C_{12}) and PEG. Using *p*-Toluenesulfonic acid as catalyst, most of the generated water was removed by azeotropic distillation with toluene or in solvent free mixtures under moderately reduced pressure. Most of the polymers were additionally heated up to 160 °C under vacuum conditions, usually for several days, to increase the molecular weight of the polymer. Some of the raw products were fractionated in order to obtain polymers with different molecular weights (MWs) and narrower molecular weight distributions (MWD). Two different procedures were used, depending on the solubility behavior of the polymers. The first one comprised solubilization of the polymer at an elevated temperature either in ethanol or in isopropanol. Stepwise reduction of the temperature effected gradual precipitation of polymer with decreasing molecular weights. In the second procedure a solvent/non-solvent pair was used. The polymers were solubilized in toluene or THF and the solvent quality was reduced by adding stepwise a non-solvent (ethanol, diisopropyl ether, or cyclohexane), which effected gradual precipitation of polymer with decreasing MWs. In some cases, prefractionations were carried out to obtain starting materials of smaller quantities and different MWs. As the fractionation efficiency is drastically reduced with increasing polymer concentration, this measure helped to obtain fractions of several grams with reasonably narrow MWDs.

The reactivity of the systems containing C_{14} and C_{20} diacids as well as PEG 2k to PEG 45k is drastically reduced because of low end group concentrations. In these cases, the diacids were first activated with the help of CDI and then reacted with PEG. In addition, the same method was applied forr the polymer, synthesized from the C_{10} diacid and PEG 1k in order to obtain samples with high polymerization degrees. DMA was identified as a suitable solvent for both, the activation and the polymerization process. The solvent quantities were reduced to a minimum. Due to the required exact stoichiometry of the compounds and the water sensitivity of CDI, all compounds had to be used in a dry state and the reactions were carried out inside a glove box. A simplified fractionation process was applied for the raw products to remove generated imidazole and to obtain fractions with different MWs. For this purpose, the reaction mixtures were diluted with dichloromethane (DCM), and under stirring slowly and stepwise diethyl ether was added. In most cases, the polymer separated as second liquid phase and stirring was continued for about one hour to reach as much as possible the thermodynamic equilibrium. Only

for $P(C_{20}EG_{1000})$ different procedures were applied due to the high MWs of the PEG starting material and the products. The details are described below.

Synthesis of P(C4EG4)-R1. The polymer was synthesized by dissolving 30.633 g of succinic anhydride (0.326 mol), 63.206 g of tetraethylene glycol (0.325 mol), and 351 mg of *p*-toluenesulfonic acid in 135 mL of toluene. The mixture was heated to the boiling point in a flask equipped with a Dean-Stark apparatus. Within 48 h 5.8 mL of water was extracted. Then the solvent was distilled off, the pressure was reduced gradually to about 10^{-2} mbar within 3 h and the temperature was increased to 120 °C. The mixture was stirred under these conditions for another 20 h. The reaction product $P(C_4EG_4)$-R1 was characterized by SEC/LS (Table S1).

Synthesis of P(C4EG4)-R2. In a second polymerzation experiment 43.874 g of succinic anhydride (0.438 mol), 85.142 g of tetraethylene glycol (0.438 mol), and 328 mg of *p*-toluenesulfonic acid were dissolved in 175 mL of toluene. With the help of a Dean-Stark apparatus 7.5 mL of water was extracted. After having removed the solvent, the temperature was increased to 160 °C. The pressure was first reduced to 50 mbar, kept for 3 days and then slowly reduced to 5 mbar within 8h. After one day the pressure was again reduced to 10^{-2} mbar for 3 days, still keeping the temperature at 160 °C. The reaction product $P(C_4EG_4)$-R2 was characterized by SEC/LS (Table S1)

Fractionation of P(C4EG4)-R1. 40.7 g of polymer $P(C_4EG_4)$-R1 was dissolved in 1.99 L of dry ethanol at about 75 °C. The temperature was reduced to 62 °C and the mixture was left at this temperature until all insoluble polymer had precipitated. After removal of the supernatant liquid, the precipitate was stirred under high vacuum conditions for 1 day and 11.4 g of $P(C_4EG_4)$-FC were obtained. The remaining ethanol solution was further cooled down and product fractions were isolated and dried as described above. At 42 °C 6.8 g of polymer $P(C_4EG_4)$4k were obtained; at 24 °C 5.7 g of polymer $P(C_4EG_4)$3k ; at 0 °C 5.2 g of polymer $P(C_4EG_4)$2k; and at -27 °C 3.5 g of polymer $P(C_4EG_4)$1k. From the remaining ethanol solution, the solvent was removed and 7.6 g of polymer $P(C_4EG_4)$1ka was obtained. Due to a broader MWD, fraction $P(C_4EG_4)$-FC was fractionated again using 1.8 L of dry ethanol. The fraction isolated at 62 °C yielded 6.6 g of $P(C_4EG_4)$9k and at 22 °C 3.2 g of $P(C_4EG_4)$5k were obtained. The SEC/LS characterization results are summarized in Table A1.

Fractionation of P(C4EG4)-R2. In order to remove lower molecular weight polymer, 51.9 g of $P(C_4EG_4)$-R2 was dissolved in 1.0 L of toluene. The temperature was raised to 55-60 °C until all material was solubilized. The solution was transferred into a separating funnel and cooled to room temperature. The phase separation occurred overnight and the lower phase was isolated. After drying under high vacuum conditions, 43 g of polymer was obtained. It was dissolved in

2.25 L of THF; 2.00 L of dry ethanol was added and the temperature was raised to 37 °C, where the mixture became clear. The mixture was transferred into a separating funnel and cooled to room temperature. The phase separation occurred overnight and the lower phase was isolated. After drying under high vacuum conditions, 21.0 g of polymer P(C$_4$EG$_4$)-FA was obtained. The upper phase (fraction P(C$_4$EG$_4$)-FB) was left in its solvent. Polymer P(C$_4$EG$_4$)-FA was dissolved in 2.50 L of THF and 1.90 L of dry ethanol was added. In this experiment the mixture became clear at 30.5 °C. It was transferred into a separating funnel and cooled to room temperature. The phase separation occurred overnight and the lower phase was isolated. After drying and stirring under high vacuum conditions, 9.1 g of polymer P(C$_4$EG$_4$)33k was obtained. The upper phase of this fractionation experiment was mixed with another 500 mL of dry ethanol, which upon heating to 32 °C became clear. The lower phase contained 6.8 g of fraction P(C$_4$EG$_4$)21k. In the next step, fraction P(C$_4$EG$_4$)FB was mixed with another 350 mL of dry ethanol, which upon heating to 29 °C became clear. The lower phase contained 3.7 g of fraction P(C$_4$EG$_4$)16k. The upper phase of this experiment was gradually cooled to 1 °C, resulting in 10.1 g of polymer P(C$_4$EG$_4$)11k. The SEC/LS characterization results are summarized in Table A1.

Table A1. SEC characterization results of P(C$_4$EG$_4$) polymers.

Sample name	M_n, g/mol	M_w/M_n
P(C$_4$EG$_4$)-R1	3,670	1.40
P(C$_4$EG$_4$)-R2	12,000	1.74
P(C$_4$EG$_4$)33k	33,100	1.29
P(C$_4$EG$_4$)21k	20,800	1.13
P(C$_4$EG$_4$)16k	15,600	1.13
P(C$_4$EG$_4$)11k	10,500	1.10
P(C$_4$EG$_4$)9k	8,680	1.13
P(C$_4$EG$_4$)5k	4,940	1.06
P(C$_4$EG$_4$)4k	4,140	1.08
P(C$_4$EG$_4$)3k	2,700	1.09
P(C$_4$EG$_4$)2k	2,070	1.05
P(C$_4$EG$_4$)1k	1,410	1.06
P(C$_4$EG$_4$)1ka	1,240	1.29

Synthesis of P(C$_4$EG$_6$)-R. 16.805 g of succinic anhydride (0.168 mol), 49.970 g of PEG 300 (M_n = 298, 0.168 mol) and 53 mg of p-toluenesulfonic acid were mixed and heated under argon overnight at 120 °C. Then, the pressure was decreased to 100 mbar and within 8 h the

temperature was raised to 160 °C. The pressure was then reduced to 20 mbar (overnight), 6 mbar (7h) and 10^{-2} mbar (3 days), still keeping the temperature at 160 °C. The reaction product $P(C_4EG_6)$-R was characterized by SEC/LS (Table A2).

Fractionation of $P(C_4EG_6)$-R. After removal of the solvent toluene, 48.8 g of the polymer was mixed with 1.8 L of dry ethanol and heated. At 64 °C the mixture became clear and was cooled to 60 °C. The phase separation occurred overnight and the lower phase ($P(C_4EG_6)$-FA) was isolated (2.2 g after drying). It was mixed with 400 mL of THF and 670 mL of dry ethanol. Upon heating to 34 °C the mixture became clear. It was cooled to 22 °C overnight and the lower phase formed was isolated ($P(C_4EG_6)$15k) (1.1 g after drying). Then the upper pase of the ethanol mixture of $P(C_4EG_6)$-R was cooled from 60 °C to 55 °C. The lower phase formed ($P(C_4EG_6)$8k) was separated (4.1 g after removal of solvent) and the new upper phase was cooled to 40 °C. Then again the lower phase ($P(C_4EG_6)$7k was separated (12.1 g after removal of solvent) and the upper phase was cooled to 35 °C. The lower phase formed ($P(C_4EG_6)$5k) was separated (1.5 g after removal of solvent) and the new upper phase was cooled to 26 °C. The precipitate was isolated ($P(C_4EG_6)$4k, 4.6 g after removal of solvent). Further cooling to 10 °C and -10 °C yielded the samples $P(C_4EG_6)$3k (7.0 g) and $P(C_4EG_6)$3ka (4.0 g), respectively. The SEC/LS characterization results are summarized in Table A2.

Table A2. SEC characterization results of $P(C_4EG_4)$ polymers.

Sample name	M_n, g/mol	M_w/M_n
$P(C_4EG_6)$-R	4,950	1.34
$P(C_4EG_6)$15k	15,200	1.14
$P(C_4EG_6)$8k	7,800	1.21
$P(C_4EG_6)$7k	6,500	1.11
$P(C_4EG_6)$5k	4,500	1.16
$P(C_4EG_6)$4k	4,400	1.09
$P(C_4EG_6)$3k	3,200	1.11
$P(C_4EG_6)$3ka	2,800	1.10

Synthesis of $P(C_4EG_9)$-R. 12.396 g of succinic anhydride (0.124 mol), 50.068 g of PEG 400 (M_n = 404, 0.124 mol) and 290 mg of *p*-toluenesulfonic acid were dissolved in 140 mL of toluene. The mixture was heated to the boiling point in a flask equipped with a Dean-Stark apparatus. Within 16 h 2.0 mL of water was extracted. Then the Dean-Stark apparatus was exchanged by a modified Dean-Stark apparatus, containing molecular sieve 0.4 nm as a drying agent (see Figure

A1), and the water extraction was continued for 6 hours. The reaction product P(C$_4$EG$_9$)-R was characterized by SEC/LS (Table A3).
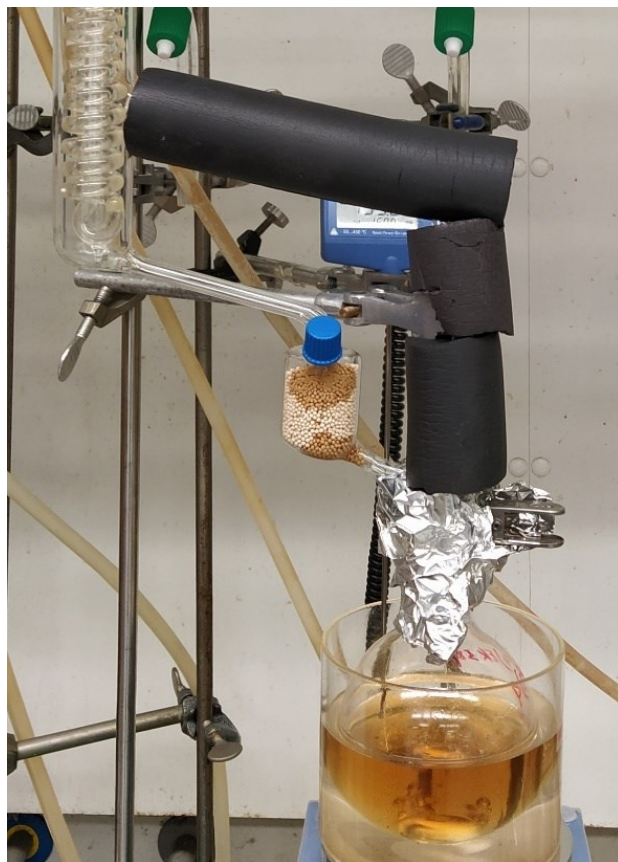

Figure A6. Modified Dean-Stark apparatus containing a molecular sieve as a drying agent. The upper glass tubing is covered for insulation purposes.

Fractionation of P(C$_4$EG$_9$)-R. After removal of most of the solvent toluene, the polymer was mixed with 2.0 L of dry ethanol and heated. At 59 °C the mixture became clear and was slowly cooled to 35 °C. The phase separation occurred overnight and the lower phase (P(C$_4$EG$_9$)-FA) was isolated. The uper phase was mixed with 100 mL of dry ethanol, warmed until the mixture became clear and then cooled to 25 °C overnight. The lower phase formed (P(C$_4$EG$_9$)6k) was separated (4.3 g after removal of solvent) and the new upper phase was cooled to 10 °C. The lower phase (P(C$_4$EG$_9$)4k was separated (6.5 g after removal of solvent) and the upper phase was mixed with 100 mL of dry ethanol and cooled to -10 °C. Again, the lower phase (P(C$_4$EG$_9$)3k was separated (3.9 g after removal of solvent)) and the upper phase was now cooled to -22 °C. The solid precipitate was isolated (P(C$_4$EG$_9$)2k, 5.2 g after removal of solvent).

In the next step, P(C$_4$EG$_9$)-FA was mixed with 1.0 L of THF and 2.6 L fo dry ethanol. The mixture became clear at 32 °C and was cooled to 24 °C overnight. The lower phase (P(C$_4$EG$_9$)16k was separated (6.9 g after removal of solvent)) and the upper phase was mixed with 1.0 L of dry

ethanol. It was heated, became clear at 30 °C and was cooled overnight to 23 °C. The lower phase was isolated (P(C$_4$EG$_9$)12k, 6.5 g after removal of solvent). The upper phase was cooled to 8 °C overnight. The lower pase formed was isolated (P(C$_4$EG$_9$)9k, 8.0 g after removal of solvent). The upper phase was further cooled to – 10 °C and the precipitate isolated the next day (P(C$_4$EG$_9$)7k, 3.7 g after removal of solvent). The SEC/LS characterization results are summarized in Table A3.

Table A3. SEC characterization results of P(C$_4$EG$_4$) polymers.

Sample name	M$_n$, g/mol	M$_w$/M$_n$
P(C$_4$EG$_9$)-R	6,070	1.65
P(C$_4$EG$_9$)16k	16,200	1.16
P(C$_4$EG$_9$)12k	12,300	1.09
P(C$_4$EG$_9$)9k	8,700	1.09
P(C$_4$EG$_9$)7k	6,700	1.05
P(C$_4$EG$_9$)6k	5,900	1.13
P(C$_4$EG$_9$)4k	4,200	1.11
P(C$_4$EG$_9$)3k	3,600	1.08
P(C$_4$EG$_9$)2k	2,400	1.09

Synthesis of P(C$_5$EG$_6$)-R1. The polymer was synthesized by dissolving 23.461 g of glutaric acid (0.178 mol), 50.138 g of PEG 300 (M$_n$ = 284, 0.178 mol), and 264 mg of *p*-toluenesulfonic acid in 70 mL of toluene. The mixture was heated to the boiling point in a flask equipped with a Dean-Stark apparatus. Within 24 h 6.2 mL of water was extracted. Then the Dean-Stark apparatus was exchanged by a modified Dean-Stark apparatus, containing molecular sieve 0.4 nm as a drying agent (see Figure A1), and the water extraction was continued for 24 hours. The reaction product P(C$_5$EG$_6$)-R1 was characterized by SEC/LS (Table A4).

Synthesis of P(C$_5$EG$_6$)-R2. Another synthesis was performed in order to get lower molecular weight samples. The polymer was synthesized by dissolving 11.57 g of glutaric acid (0.0876 mol), 24.73 g of PEG 300 (M$_n$ = 284, 0.0876 mol), and 134 mg of *p*-toluenesulfonic acid in 70 mL of toluene. The mixture was heated to the boiling point in a flask equipped with a Dean-Stark apparatus. Within 24 h 3.1 mL of water was extracted. The reaction product P(C$_5$EG$_6$)-R2 was characterized by SEC/LS (Table A4).

Fractionation of P(C$_5$EG$_6$)-R1. 70 g of P(C$_5$EG$_6$)-R1 still containing about 50 mL of toluene after the reaction was dissolved in 1.12 L of toluene and 2.3 L of dry ethanol was added. At 26 °C the mixture became clear. It was transferred into a separating funnel and cooled to room

temperature. The phase separation occurred overnight and the lower phase was isolated (P(C$_5$EG$_6$)-F1). The upper phase of this fractionation experiment was mixed with another 300 mL of dry ethanol, which upon heating to 26.5 °C became clear. After drying under high vacuum conditions, 8.6 g of polymer P(C$_5$EG$_6$)34k was obtained. Another 350 mL of dry ethanol was added and the mixture became clear at 27 °C (fraction P(C$_5$EG$_6$)26k, 12.0 g). In the upper part of this experiment another 800 mL of dry ethanol was added and the mixture became clear at 29 °C resulting to 6.0 g of fraction P(C$_5$EG$_6$)18k. The upper phase of this experiment was cooled to 5 °C, resulting in 7.3 g of fraction P(C$_5$EG$_6$)12k. Further cooling of the upper phase to -22 °C resulted in fraction P(C$_5$EG$_6$)7k (3.0 g). Fraction P(C$_5$EG$_6$)-F1 was dissolved in 1 L of Toluene and 1.9 L of dry ethanol was added. The mixture became clear at 24 °C (fraction P(C$_5$EG$_6$)80k, 5.3 g). Another 250 mL of dry ethanol was added to the upper fraction and the mixture became clear at 26 °C (fraction P(C$_5$EG$_6$)58k, 4.3 g). After adding another 450 mL of dry ethanol to the upper part the mixture became clear at 30°C, resulting to 3.5 g the fraction P(C$_5$EG$_6$)40k. The upper fraction of this experiment (P(C$_5$EG$_6$)-F12) was dryed under high vacum and kept for later fractination together with P(C$_5$EG$_6$)-R2. The SEC/LS characterization results are summarized in Table A4.

Fractionation of P(C$_5$EG$_6$)-R2. 33 g of P(C$_5$EG$_6$)-R2 still containing about 50 mL of toluene after the reaction was mixed with the fraction P(C$_5$EG$_6$)-F12 (5 g) from the fractionation of P(C$_5$EG$_6$)-R1 material and dissolved in 1 L of toluene. Then 2.6 L of dry ethanol was added. At 27 °C the mixture became clear. It was transferred into a separating funnel and cooled to room temperature. The phase separation occurred overnight and the lower phase was isolated. After drying under high vacuum conditions, 2.5 g of polymer P(C$_5$EG$_6$)28k was obtained. The upper phase of this fractionation experiment was mixed with another 700 mL of dry ethanol, which upon heating to 31 °C became clear (fraction P(C$_5$EG$_6$)20k, 6.1 g). Another 900 mL of dry ethanol was added and the mixture became clear at 29 °C. Afterwords, the solution was cooled down to 10°C and the lower fraction was collected (fraction P(C$_5$EG$_6$)16k, 12.4 g). The upper phase of this experiment was cooled to -20 °C, resulting in 4 g of fraction P(C$_5$EG$_6$)4k. Upper fraction of this experiment was dryed and dissolved in 1.5 L of dry ethanol where 1 L of distilled heptane was added. Solution became clear at 34°C. 0.7 g of polymer were collected from the walls of the separating funnel where it was precipitated (P(C$_5$EG$_6$)4ka). The upper part of this experiment which was still turbid was cooled to 3°C and 1.8 g of material were collected (P(C$_5$EG$_6$)2k). As the upper part contained only oligomers, it was not used for further fractionation. The SEC/LS characterization results are summarized in Table A4.

Table A4. SEC characterization results of P(C$_5$EG$_6$) polymers.

Sample name	M$_n$, kg/mol	M$_w$/M$_n$
P(C$_5$EG$_6$)-R1	7.7	5.4
P(C$_5$EG$_6$)-R2	2.1	7.2
P(C$_5$EG$_6$)80k	80.2	1.15
P(C$_5$EG$_6$)58k	57.7	1.11
P(C$_5$EG$_6$)40k	39.5	1.10
P(C$_5$EG$_6$)34k	34.4	1.19
P(C$_5$EG$_6$)28k	27.8	1.26
P(C$_5$EG$_6$)26k	25.5	1.15
P(C$_5$EG$_6$)20k	19.6	1.15
P(C$_5$EG$_6$)18k	18.4	1.10
P(C$_5$EG$_6$)16k	16.0	1.15
P(C$_5$EG$_6$)12k	11.8	1.10
P(C$_5$EG$_6$)7k	6.6	1.11
P(C$_5$EG$_6$)4k	4.4	1.10
P(C$_5$EG$_6$)4ka	4.0	1.25
P(C$_5$EG$_6$)2k	2.4	1.07

Synthesis of P(C$_8$EG$_{13}$)-R1. The polymer was synthesized by dissolving 17.666 g of suberic aric acid (0.101 mol), 60.742 g of PEG 600 (M$_n$ = 599 g/mol, 0.101 mol), and 142 mg of *p*-toluenesulfonic acid in 150 mL of toluene. The mixture was heated to the boiling point in a flask equipped with a Dean-Stark apparatus. In this case no water separated, but remained as an emulsion in the toluene phase. Therefore, after 5 h the toluene was distilled off and the temperature was increased to 160 °C. The pressure was first reduced to 50 mbar, kept for 1 h and then slowly reduced to 5 mbar within 24 h. After one day the pressure was again reduced to 10^{-2} mbar for 7 days, keeping the temperature at 160 °C. The reaction product P(C$_8$EG$_{13}$)-R1 was characterized by SEC/LS Table A5)

Synthesis of P(C$_8$EG$_{13}$)-R2. In a second polymerization experiment 27.713 g of suberic acic acid (0.159 mol), 99.117 g of PEG 600 (M$_n$ = 623 g/mol, 0.159 mol), and 460 mg of *p*-toluenesulfonic acid were dissolved in 235 mL of toluene. Again, no water separated during the distillation process and most of the toluene was distilled off. Then another 445 mg of *p*-toluenesulfonic acid was added and the heating and pumping process was carried out as described above, except

that the final pumping process at 10^{-2} mbar lasted only 3 days. The reaction product P(C$_8$EG$_{13}$)-R2 was characterized by SEC/LS (Table A5)

Fractionation of P(C$_8$EG$_{13}$)-R1 and P(C$_8$EG$_{13}$)-R2. 53.5 g of P(C$_8$EG$_{13}$)-R1 was dissolved in 3.3 L of toluene and 1.5 L of cyclohexane was added. After heating to 34 °C the mixture became clear. It was transferred into a separating funnel and cooled to room temperature. The phase separation occurred overnight and the lower phase was isolated. After drying under high vacuum conditions, 6.9 g of polymer (P(C$_8$EG$_{13}$)-FA) was obtained. From the upper phase the solvent was distilled off and 46.6 g of (P(C$_8$EG$_{13}$)-FB) was obtained. Next, fraction P(C$_8$EG$_{13}$)-FA was dissolved in 140 mL of dry ethanol at elevated temperature and cooled to room temperature. The lower phase contained after drying 2.9 g of fraction P(C$_8$EG$_{13}$)-FC and from the upper phase 3.9 g of fraction P(C$_8$EG$_{13}$)-FD was isolated. Fraction P(C$_8$EG$_{13}$)-FB was dissolved in 1.0 L of dry ethanol at elevated temperature and cooled to room temperature. The lower phase contained after drying 4.6 g of fraction P(C$_8$EG$_{13}$)-FE. The upper phase was diluted with one more liter of dry ethanol and cooled in two steps to 1 °C and -20 °C. After drying, fractions P(C$_8$EG$_{13}$)-FF (15.6 g) and P(C$_8$EG$_{13}$)-FG (21.2 g) were obtained.

50.5 g of P(C$_8$EG$_{13}$)-R2 was dissolved in 2.8 L of toluene and 1.9 L of diisopropyl ether was added. After heating to 37 °C the mixture became clear. It was transferred into a separating funnel and cooled to room temperature. The phase separation occurred overnight and the lower phase was isolated. After drying under high vacuum conditions, 19.8 g of polymer (P(C$_8$EG$_{13}$)-FH) was obtained. The upper phase was mixed with another 300 mL of diisopropyl ether. The mixture was heated to 35 °C, where it became clear. After cooling to room temperature, 10.9 g of (P(C$_8$EG$_{13}$)-FI was obtained from the lower fraction.

19.8 g of polymer P(C$_8$EG$_{13}$)-FH was dissolved in 2.1 L of isopropanol at 65 °C. The temperature was reduced to 50 °C and the mixture was left at this temperature until all insoluble polymer had precipitated. After removal of the supernatant liquid, the precipitate was stirred under high vacuum conditions for 1 day and 11.1 g of P(C$_8$EG$_{13}$)33k was obtained. The upper fraction of this separation experiment was combined with fractions P(C$_8$EG$_{13}$-)FI, mixed with a total of 1.9 L of isopropanol, and heated to 57 °C, where the mixture became clear. It was left at 46 °C and from the lower phase 7.1 g of fraction P(C$_8$EG$_{13}$)22k were obtained.

The upper fraction of this separation experiment was combined with fractions P(C$_8$EG$_{13}$)-FC and P(C$_8$EG$_{13}$)-FE, mixed with a total of 1.8 L of isopropanol, and heated to 50 °C, where the mixture became clear. It was left at 42 °C and from the lower phase 5.2 g of fraction P(C$_8$EG$_{13}$)21k were obtained. Further cooling of the upper phase to 37 °C resulted in fraction P(C$_8$EG$_{13}$)15k (4.2 g).

The remaining material of the upper phase was combined with fraction P(C$_8$EG$_{13}$)-FD, warmed to 45 °C until the mixture became clear and then cooled to 17 °C, where fraction P(C$_8$EG$_{13}$)9ka was isolated (6.6 g). In the next fractionation experiment fraction P(C$_8$EG$_{13}$)-FF was mixed with 500 mL of isopropanol and warmed to 65 °C, where it became soluble. After cooling to 30 °C, from the lower phase 12.8g of fraction P(C$_8$EG$_{13}$)9k was obtained. Finally, fraction P(C$_8$EG$_{13}$)-FG was mixed with 1.0 L of isopropanol and warmed to 50 °C, where it became soluble. It was cooled to room temperature and from the lower phase 12.0 g of fraction P(C$_8$EG$_{13}$)5k was obtained. From the upper phase half of the solvent was distilled of and the mixture cooled to 4 °C. From the lower phase 6.2 g of fraction P(C$_8$EG$_{13}$)3k was obtained. The SEC/LS characterization results are summarized in Table A5.

Table A5. SEC characterization results of P(C$_8$EG$_{13}$) polymers.

Sample name	M$_n$, g/mol	M$_w$/M$_n$
P(C$_8$EG$_{13}$)-R1	6,250	1.94
P(C$_8$EG$_{13}$)-R2	13,600	1.70
P(C$_8$EG$_{13}$)33k	32.600	1.22
P(C$_8$EG$_{13}$)22k	22,100	1.18
P(C$_8$EG$_{13}$)21k	20,700	1.17
P(C$_8$EG$_{13}$)15k	15,100	1.15
P(C$_8$EG$_{13}$)9k	8,790	1.16
P(C$_8$EG$_{13}$)9ka	8,780	1.28
P(C$_8$EG$_{13}$)5k	4,720	1.17
P(C$_8$EG$_{13}$)3k	3,090	1.14

Synthesis of P(C$_{10}$EG$_{22}$)-R. Inside a glove box, 9.0195 g of tetradecanedioic acid (44.596 mmol) and 14.680 g of CDI (90.536 mmol) were suspended in 70 mL of dry DMA and heated to 50 °C while stirring. Although the mixture always contained solid material, the evolution of CO$_2$ indicated the ongoing reaction. After one day 44.450 g of PEG 1k (45.081 mmol) was added and the mixture was heated to 100 °C. After 1 day the M$_n$ of the polymer measured by SEC/LS was only 11.7 kg/mol. Therefore, 170 mg of DBU (1.117 mmol) was added to the mixture to catalize the reaction.[2,3] Already after 1 hour the solution became more viscous and after one day the reaction was stoped and the mixture was cooled to room temperature. The reaction product P(C$_{10}$EG$_{22}$)-R was characterized by SEC/LS Table A6)

Fractionation of P(C$_{10}$EG$_{22}$)-R. 52.7 g of P(C$_{10}$EG$_{22}$)-R still containing about 70 mL of DMA was dissolved in 1.46 L of ethyl acetate (EE) and 1.76 L of diethyl ether was added. The mixture was stirred for 1 hour and centrifuged afterwards. The lower phase was washed with diethyl ether and then dried, resulting in 1 g of fraction P(C$_{10}$EG$_{22}$)111k. The upper phase of this fractionation experiment was mixed with another 300 mL of diethyl ether. The mixture was left stirring over night. The precipitated fraction was isolated, washed with diethyl ether and dried (P(C$_{10}$EG$_{22}$)86k, 31 g). Another 150 mL of diethyl ether was added to the soluble fraction resulting in 2.6 g of the fraction P(C$_{10}$EG$_{22}$)65k. Fractions P(C$_{10}$EG$_{22}$)47k (4.4 g), P(C$_{10}$EG$_{22}$)35k (2.7 g) and P(C$_{10}$EG$_{22}$)25k (2.0 g) were obtained by addition of 300 mL, 400 mL and 900 mL of diethyl ether respectively. The soluble phase of the last fractination experiment was cooled to +3 °C resulting in fraction P(C$_{10}$EG$_{22}$)FA, (2.5 g). The soluble fraction was cooled to -20 °C resulting to 0.5 g of fraction P(C$_{10}$EG$_{22}$)FB. P(C$_{10}$EG$_{22}$)FA and P(C$_{10}$EG$_{22}$)FB had similar MWs and broad MWDs (M$_w$/M$_n$ = 1.5), therefore, these two fractions were mixed together, dried and fractionated again with 250 mL of chloroform, 1.85 L of cyclohexane and 250 mL of n-hexane. This resulted in 1.5 g of fraction P(C$_{10}$EG$_{22}$)13k. The SEC/LS characterization results are summarized in Table A6.

Table A6. SEC characterization results of P(C$_{10}$EG$_{22}$) polymers.

Sample name	M$_n$, g/mol	M$_w$/M$_n$
P(C$_{10}$EG$_{22}$)- R	5,000	1.78
P(C$_{10}$EG$_{22}$)111k	110,900	1.35
P(C$_{10}$EG$_{22}$)86k	85,600	1.33
P(C$_{10}$EG$_{22}$)65k	65,100	1.19
P(C$_{10}$EG$_{22}$)47k	47,300	1.11
P(C$_{10}$EG$_{22}$)35k	34,900	1.07
P(C$_{10}$EG$_{22}$)25k	25,400	1.07
P(C$_{10}$EG$_{22}$)13k	13,300	1.15

Synthesis of the polymers used for cloud point determination. A series of polymers was synthesized without subsequent molecular weight fractionation. The synthetic protocols largely coincide with the ones described above. For some polymerization experiments, the initial water removal by azeotropic distillation with toluene was replaced by heating the solvent free mixtures (see Table A7). In these cases, the pressure was reduced to 10 – 20 mbar within several hours and kept for 1 – 3 days, followed by pumping at about 10^{-2} mbar, again for 1 – 3 days. The reaction procedures and the SEC/LS characterization results are summarized in Table A7.

Table A7. Synthetic details and SEC characterization results of the polymers used for cloud point determination.

Sample name	Reaction temperature during pumping process	solvent for synthesis	M_n, g/mol	M_w/M_n
$P(C_4EG_3)$	120 °C	toluene	8,790	1.82
$P(C_4EG_4)$	120 °C	toluene	3,020	1.68
$P(C_4EG_6)$	160 °C	——	6,590	1.58
$P(C_5EG_3)$	110 °C	——	3,760	1.28
$P(C_5EG_4)$	1 day 100 °C 1 day 140 °C 1 day 160 °C	——	7,220	1.75
$P(C_5EG_6)$	1 day 120 °C 4 days 160 °C	——	11,700	1.51
$P(C_5EG_{14})$	160 °C	——	6,390	1.52
$P(C_6EG_6)$	160 °C	——	8,700	1.59
$P(C_8EG_6)$	160 °C	——	5,610	1.65
$P(C_8EG_9)$	160 °C	——	5,130	1.87
$P(C_8EG_{13})$	160 °C	——	3,780	1.52
$P(C_8EG_{22})$	160 °C	toluene	11,400	2.08
$P(C_{10}EG_{13})$	160 °C	——	6,040	1.46
$P(C_{10}EG_{22})$	140 °C	toluene	10,100	1.49
$P(C_{12}EG_{13})$	160 °C	——	5,270	1.66
$P(C_{12}EG_{22})$	160 °C	——	20.100	1.63

Synthesis and fractionation of $P(C_{14}EG_{47})$. Inside a glove box, 2.4625 g of tetradecanedioic acid (9.532 mmol) and 3.1059 g of CDI (19.17 mmol) were suspended in 20 mL of dry DMA and heated to 50 °C. Although the mixture always contained solid material, the evolution of CO_2 indicated the ongoing reaction. After one day 20.153 g of PEG 2k (9.538 mmol) were added and the mixture was heated to 100 °C. It became transparent 1 h after the polymerization reaction started. After 4 days the mixture was cooled to room temperature. The raw product $P(C_{14}EG_{47})$-R was diluted with 200 mL of DCM and precipitated in 1.1 L of diethyl ether by adding the ether to the polymer solution. The polymer fraction $P(C_{14}EG_{47})$98k was isolated by centrifugation. The supernatant liquid was mixed with additional 400 mL of diethyl ether and the precipitated polymer $P(C_{14}EG_{47})$41k was isolated by centrifugation. From the remaining solution most of the DCM and diethyl ether was distilled off under reduced pressure and 400 mL of new diethyl ether

was added. The precipitated polymer P($C_{14}EG_{47}$)16k was treated as described above. All fractions were washed with diethyl ether. After drying under high vacuum conditions, 19.0 g of P($C_{14}EG_{47}$)98k, 1.7 g of P($C_{14}EG_{47}$)41k, and 0.8 g of P($C_{14}EG_{47}$)16k were obtained. The SEC/LS characterization results are summarized in Table A8.

Synthesis and fractionation of P($C_{14}EG_{103}$). The same procedure as described for P($C_{14}EG_{47}$) was applied and 1.1471 g of tetradecanedioic acid (4.440 mmol), 1.4469 g of CDI (8.923 mmol), 15 mL of dry DMA, and 20.1048 g of PEG 4.5k (4.440 mmol) were used. At the end of the polymerization reaction the mixture was cooled to room temperature. The raw product P($C_{14}EG_{103}$)-R was diluted with 200 mL of DCM and precipitated in 800 mL of diethyl ether. The polymer P($C_{14}EG_{103}$)174k was isolated by centrifugation. From the supernatant liquid most of the DCM and diethyl ether was distilled off under reduced pressure and 120 mL of new diethyl ether was added. The precipitated polymer P($C_{14}EG_{103}$)48k was treated as described above. Both fractions were washed with diethyl ether. After drying under high vacuum conditions, 17.4 g of P($C_{14}EG_{103}$)174k and 2.3 g of P($C_{14}EG_{103}$)48k were obtained. The SEC/LS characterization results are summarized in Table A8.

Synthesis and fractionation of P($C_{20}EG_{47}$). The same procedure as described for P($C_{14}EG_{47}$) was applied, except that the activation of the diacid with CDI was carried out for two days and the polymerization for 6 days. Eicosanedioic acid (3.2339 g, 9.441 mmol), 3.0757 g of CDI (18.968 mmol), 40 mL of dry DMA, and 19.7786 g of PEG 2k (9.360 mmol) were used. At the end of the polymerization reaction the mixture was cooled to room temperature. The raw product P($C_{20}EG_{47}$)-R was diluted with 220 mL of DCM and precipitated in 1.3 L of diethyl ether. The polymer fraction P($C_{20}EG_{47}$)113k was isolated by centrifugation. The supernatant liquid was mixed with additional 240 mL of diethyl ether and the precipitated polymer P($C_{20}EG_{47}$)79k was isolated by centrifugation. From the remaining solution most of the DCM and diethyl ether was distilled off under reduced pressure and 400 mL of new diethyl ether was added. The precipitated polymer P($C_{20}EG_{47}$)32k was treated as described above. All fractions were washed with diethyl ether. After drying under high vacuum conditions, 5.41 g of P($C_{20}EG_{47}$)113k, 10.8 g of P($C_{20}EG_{47}$)79k, and 4.7 g of P($C_{20}EG_{47}$)32k were obtained. The SEC/LS characterization results are summarized in Table A8.

Synthesis and fractionation of P($C_{20}EG_{103}$). The same procedure as described for P($C_{14}EG_{47}$) was applied, except that the polymerization was carried out for 5 days. Eicosanedioic acid (1.5298 g, 4.466 mmol), 1.4476 g of CDI (8.927 mmol), 25 mL of dry DMA, and 20.017 g of PEG 4.5k (4.421 mmol) were used. At the end of the polymerization reaction the mixture was cooled to room

temperature. The raw product P(C$_{20}$EG$_{103}$)-R was diluted with 300 mL of DCM and precipitated in 1.2 L of diethyl ether. The polymer fraction P(C$_{20}$EG$_{103}$)161k was isolated by centrifugation. The supernatant liquid was mixed with additional 200 mL of diethyl ether and the precipitated polymer P(C$_{20}$EG$_{103}$)74k was isolated by centrifugation. Both fractions were washed with diethyl ether. After drying under high vacuum conditions, 15.1 g of P(C$_{20}$EG$_{103}$)161k and 2.5 g of P(C$_{20}$EG$_{103}$)81k were obtained. Finally, 1.412 g of P(C$_{20}$EG$_{103}$)49k was dissolved in 30 mL of DCM and 200 mL of diethyl ether was added. The precipitated polymer was removed by centrifugation. The upper phase containing still soluble polymer was concentrated and precipitated in a large excess of diethyl ether. After centrifugation and vacuum drying 165 mg of product was obtained. The SEC/LS characterization results are summarized in Table A8.

Synthesis and fractionation of P(C$_{20}$EG$_{240}$). The same procedure as described for P(C$_{14}$EG$_{47}$) was applied, except that the polymerization was carried out for 7 days. Eicosanedioic acid (0.528 g, 1.542 mmol), 0.502 g of CDI (3.096 mmol), 9 mL of dry DMA, and 16.240 g of PEG 10k (1.531 mmol) were used. At the end of the polymerization reaction the mixture was cooled to room temperature. The raw product P(C$_{20}$EG$_{240}$)-R diluted with 160 mL of DCM and precipitated in 600 mL of diethyl ether. The polymer P(C$_{20}$EG$_{240}$)228k was isolated by centrifugation. After drying under high vacuum conditions, 16.1 g of product were obtained. The SEC/LS characterization results are summarized in Table A8.

Synthesis and fractionation of P(C$_{20}$EG$_{1000}$). As PEG 45k was available only in smaller quantities, the CDI activated eicosanedioic acid was synthesized in larger quantities in a separate experiment in order to have a more precise control over the stoichiometry of the reaction. In this reaction, 0.9721 g of eicosanedioic acid (2.838 mmol) and 1.3811 g of CDI (8.517 mmol) were suspended in 20 mL of dry DMA and heated to 50 °C inside a glove box for one day. The solvent was distilled off under high vacuum conditions at about 40 °C and the residual white solid was washed with water in order to decompose excess CDI and to remove the formed imidazole. After drying under vacuum conditions overnight, 0.86 g of the raw product was recrystallized from 30 mL of boiling toluene and dried for one day under high vacuum conditions. The yield was 0.73 g. The purity of the product, eicosanedioylimidazole, was determined by ^{1}H-NMR. The measurement revealed that less than 1% of the carboxylic acid groups remained non-functionalized.

The synthesis of the P(C$_{20}$EG$_{1000}$) polymer was carried out using 47.4 mg of eicosanedioylimidazole (0.106 mmol), 4.6838 g of PEG 45k (0.106 mmol) and 5 mL of dry DMA. In addition, 40.8 mg of DBU (0.27 mmol) was added as catalyst. Within 5 days at 100 °C the

mixture transformed into a clear solid gel. Then, 20 mL more DMA was added and the reaction continued for another 4 days. At the end of the polymerization reaction the mixture was cooled to room temperature, the solvent was distilled off and the raw product $P(C_{20}EG_{1000})$-R was stirred with 500 mL of ethyl acetate for 2 days in order to remove most of the generated imidazole. After vacuum drying the polymer was dissolved in 650 mL of chloroform and mixed with 3.15 L of cyclohexane. The turbid mixture was stirred at 30 °C for 5 hours and fraction $P(C_{20}EG_{1000})663k$ was isolated by centrifugation. The supernatant liquid was mixed with additional 400 mL of cyclohexane and the precipitated polymer $P(C_{20}EG_{1000})168k$ was isolated by centrifugation. Both fractions were dissolved in chloroform and precipitated in heptane. After drying under high vacuum conditions, 3.0 g of $P(C_{20}EG_{1000})663k$ and 0.7 g of $P(C_{20}EG_{1000})168k$ were obtained. The SEC/LS characterization results are summarized in Table A8.

Table A8. SEC characterization results of the polymers containing hydrophobic C_{14} and C_{20} units.

Sample name	M_n, g/mol	M_w/M_n	Number of repeating units
$P(C_{14}EG_{47})$-R	91,1	1.45	
$P(C_{14}EG_{47})98k$	98,100	1.37	41.7
$P(C_{14}EG_{47})41k$	41,400	1.17	17.6
$P(C_{14}EG_{47})16k$	15,600	1.26	6.6
$P(C_{14}EG_{103})$-R	168,000	1.47	
$P(C_{14}EG_{103})174k$	174,000	1.40	36.3
$P(C_{14}EG_{103})48k$	47,900	1.59	10.0
$P(C_{20}EG_{47})$-R	60,000	1.68	
$P(C_{20}EG_{47})113k$	113,000	1.32	46.4
$P(C_{20}EG_{47})79k$	78,500	1.31	32.2
$P(C_{20}EG_{47})32k$	31,900	1.48	13.1
$P(C_{20}EG_{103})$-R	114,000	1.47	
$P(C_{20}EG_{103})161k$	161,000	1.20	33.2
$P(C_{20}EG_{103})81k$	81,400	1.30	16.8
$P(C_{20}EG_{103})49k$	49,300	1.20	10.2
$P(C_{20}EG_{240})$-R	231.000	1.21	
$P(C_{20}EG_{240})228k$	228,000	1.32	20.9

P(C$_{20}$EG$_{1000}$)-R	537.000	1.68	
P(C$_{20}$EG$_{1000}$)663k	663,000	1.75	14.9
P(C$_{20}$EG$_{1000}$)168k	168,000	1.51	3.8

Polyethers synthesis

The polyethers were synthesized from 1,4-butanediol di-(p-toluene sulfonate) and polyethylene glycol oligomers. The tosylated 1,4 butanediol was synthesized by, reacting 1,4-butanediol with p-toluenesulfonyl chloride in the presence of KOH. For this 50.55 g of 1,4-butanediol (0.561 mol) and 232.04 g of p-toluenesulfonyl chloride (1.22mol) were dissolved in 1.1 L of THF. The solution was cooled to 5°C in an ice bath and 292.72g of solid KOH (85 %) was slowly added during 1.5 h keeping the temperature in the flask below 15°C. The mixture was left warming up under stirring overnight. After the insoluble material was removed by centrifugation and filtration through a paper filter, THF was removed under reduced pressure. Remaining salt was removed by dissolving the raw product in 1.5 L of dichloromethane and washing with 0.3 L of water. After removal of the solvent, the final purification was done by recrystallization from ethanol at 5°C.

PE(C$_4$EG$_3$) was synthesized in a glove-box under argon atmosphere from 15.00 g of 1,4-butanediol di-(p-toluene sulfonate) (37.64 mmol) and 5.65 g of triethyleneglycol (37.64 mmol) in the presence of 10.55 g of dry KOH (188.20 mmol). First, the activated butandiol and triethyleneglycol were dissolved in 50 mL of dry THF. Dry KOH was slowly added under stirring, and another 75 mL of THF were added during this process in order to keep the mixture liquid. The reaction took place at 50 °C during 5 days. Afterwards, the solvent was removed and the the dry mixture was dissolved in 200 mL of water. The water solution was neutralized by 0.5 mL of half concentrated HCl, and salt was removed by extraction of the polymer into chloroform. After removal of the solvent at reduced pressure, 5.2 g of dry material was obtained and washed in 2-propanol at -20°C to remove the low MW oligomers and non-reacted starting compounds. Finally, 3.9 g of product PE(C$_4$EG$_3$) was obtained having M_n = 4.0 kg/mol and M_w/M_n = 1.50.

PE(C$_4$EG$_6$) was synthesized in a glove-box under argon atmosphere from 10.01 g of 1,4-butanediol di-(p-toluene sulfonate) (25.2 mmol) and 7.51 g of PEG300 (25.1 mmol) in the presence of 8.1 g of solid KOH. The activated butanediol, PEG300 and KOH were mixed in 50 mL of dry THF. The reaction took place at 50 °C during 5 days, Then THF was removed at reduced pressure. The reaction mixture was dissolved in water and the polymer was extracted into dichlorometane. The organic phase was dried with MgSO$_4$. After removal of the solvent at reduced pressure, 4.7 g of dry material was obtained and washed 2 times in 2-propanol at -20°C

to remove the low MW oligomers and non-reacted starting compounds. Finally, 3 g of product PE(C$_4$EG$_6$) was obtained having M$_n$ = 4.0 kg/mol and M$_w$/M$_n$ = 1.28.

Characterization of the AAPs by ^{1}H-NMR

Additionally to SEC/LS the synthesized polymers were characterized by ^{1}H-NMR. The spectra for P(C$_8$EG$_{13}$)9k is shown as an example in figure A2.The ratio of the EG to the dicarboxylic acid monomers calculated from the integral values is 1.03, which is very close to the expected ratio of 1.00. The small mismatch results from the imbalance of the monomer units. For this reason, the intensity ratio of the signals 1' and 12' is not 1:1.
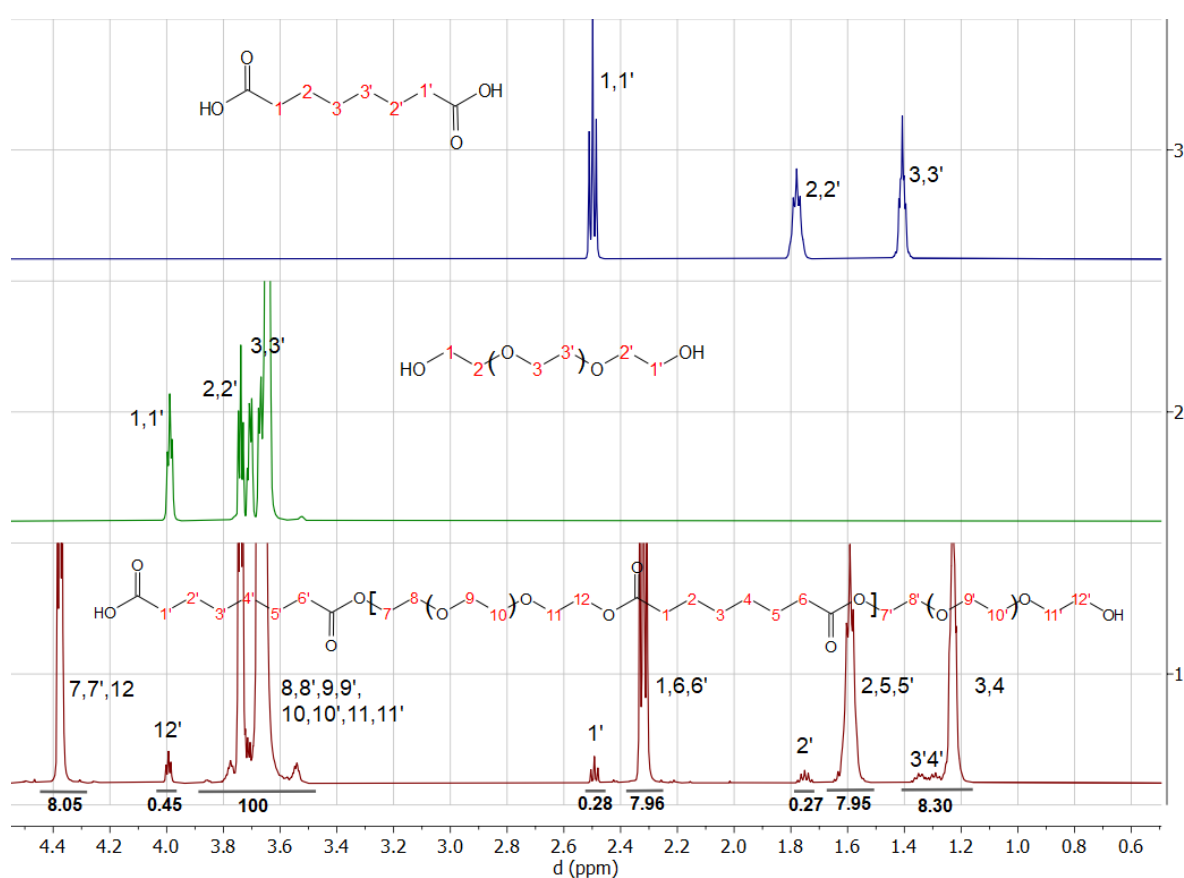
Figure A2. ^{1}H-NMR of P(C$_8$EG$_{13}$)9k (bottom) and its starting compounds PEG600 (middle) and suberic acid (top). Values below the grey lines indicate the integrals of the corresponding signals.

References

[1]   C. H. Hövelmann, S. Gooßen, J. Allgaier, *Macromolecules* **2017**, *50*, 4169–4179.

[2]   P. J. Dunn, W. Hoffmann, Y. Kang, J. C. Mitchell, M. J. Snowden, *Org. Process Res. Dev.* **2005**, *9*, 956–961.

[3]   Z. Peng, J. W. Wong, E. C. Hansen, A. L. A. Puchlopek-Dermenci, H. J. Clarke, *Org. Lett.* **2014**, *16*, 860–863.

Acknowledgments

Curriculum Vitae

Personal Details

Name: Ekaterina Kostyurina

Date of birth: 26.01.1995

Place of birth: Moscow region, Russia

Education

2018 – today	PhD Physical Chemistry
	Jülich Centre for Neutron Science (JCNS-1), Forschungszentrum Jülich GmbH & Institute of Physical Chemistry, RWTH Aachen
2016 – 2018	Applied Mathematics and Physics M.Sc.
	Moscow Institute of Physics and Technology (MIPT)
2012 – 2016	Applied Mathematics and Physics B.Sc.
	Moscow Institute of Physics and Technology (MIPT)
2009 – 2012	High School Moscow Chemical Lyceum (Lyceum 1303)